

Chapter 6

Hybrid Copper–Chlorine Cycle

Abstract In this chapter, the hybrid copper–chlorine (Cu–Cl) cycle for hydrogen production is examined in detail. The historical perspective of this cycle development is presented in Sect. 6.1. A precursor of the cycle was proposed in 1974, which uses a non-electrochemical, non-thermochemical disproportionation of cuprous chloride; this process is based on complexation and chelating schemes that generate the desired products. Electrochemical hydrogen generation from hydrochloric acid and cuprous chloride electrolysis is one of the latest cycle developments for engineering scale-up. This process simplifies the separation steps and it has been proven by test-bench experiments. Two reactors were mainly studied for the hydrolysis reaction, which is a crucial cycle step: fluidized bed and spray reactor. Both are interesting schemes proposed for scaling up the cycle. At the University of Ontario Institute of Technology, a scaled up laboratory facility has been developed for each cycle step.

In total, seven cycle variants are examined in this chapter. The variants, including a copper electrowinning step, were studied mostly since 2003; much progress has been made in the development of the processes. Because electrowinning implies difficult separation of chemicals, it appears less feasible for large-scale implementation.

This chapter presents a detailed treatment of all relevant processes, such as electrochemical disproportionation, electrochemical chlorination, complexation, dehydration, drying, crystallization, hydrolysis, fluidized bed hydrodynamics and heat transfer, spray drying hydrodynamics and heat transfer, multiphase processes in reactors, thermochemical chlorination, thermolysis, heat recovery from molten salt, and special heat exchangers, as well as system integration of the unit operations.

Integration of the chemical plant with heat pumps and heat engines may have promising potential to substantially increase the overall hydrogen production efficiency. An interesting option is to use integrated heat pumps based on thermochemical processes such as a steam–methane reaction, or vapor compression heat pumps with CuCl as a working fluid.

Material research is also important for cycle development. Several corrosion-resistant coatings were developed—as explained in the chapter—and assessed experimentally by various methods. Various auxiliary systems are required for a full-scale plant. One item of major interest is separation of hydrochloric acid from an HCl/steam mixture exiting the hydrolysis reactor for purposes of recycling; this aspect is also detailed in a section of this chapter. Various concepts for a full-size plant and its equipment are presented, as well as simulation results with ASPEN Plus software. Other aspects are also discussed such as reliability, control, safety, environmental impact, and life cycle assessment. The overview in this chapter concludes that the Cu–Cl cycle is a promising candidate for large-scale hydrogen production with nuclear reactors.

6.1 Introduction

The analysis presented in the previous chapter shows that the most commonly encountered chemical compounds in hybrid thermochemical cycles are those of chlorine and copper. According to Fig. 5.24, chlorine compounds are present in 40 % of significant hybrid cycles while copper in 32 % of them. In general, the raw materials from which copper and chlorine can be produced are relatively cheap and widely available. Electrolytic processes involving copper or chlorine are relatively well understood and used in various industries. These are some of the reasons in favor of selecting a hybrid copper–chlorine thermochemical water-splitting cycle to generate hydrogen with nuclear energy. The low temperature requirement of these cycles—around 800 K—represents their strongest advantage. A lower temperature level allows for linking the thermochemical plant with a wider range of nuclear reactors including those of intermediate temperature—such as supercritical water-cooled reactor (SCWR)—and those of high temperature as well—for example, the helium-cooled high-temperature reactor (HTGR), modular temperature reactor (MHR), very-high-temperature reactor (VHTR), etc.

The copper–chlorine thermochemical cycle—with several variants—is under development in several institutions around the world. The US Department of Energy envisages the use of this cycle in conjunction with concentrated solar power systems to generate hydrogen. In Canada, Atomic Energy of Canada Limited (AECL) is interested in this cycle development for their planned SCWR which generates heat at 800–900 K. In France, CEA (Commissariat à l'Énergie Atomique et aux Énergies Alternatives) has conducted research on this cycle both for concentrated solar and nuclear energy purposes.

A precursor of the hybrid copper–chlorine cycle was proposed by Wentorf from General Electric and a collaborator Hanneman (1974). They developed a process that includes a cuprous chlorine disproportionation step which is described by the same chemical reaction as the electrolytic step in the standard 5-step copper–chlorine cycle (the Cu–Cl-A cycle listed in Chap. 5, Table 5.16). However, in the approach proposed by Wentorf and Hanneman (1974), this reaction is

conducted by physicochemical means rather than electrochemically as per Cu–Cl–A. Namely, the disproportionation of CuCl is performed in two steps: (1) complexation of CuCl according to $4\text{CuCl} + \chi \rightarrow 2\text{Cu} + 2\text{CuCl}_2 \cdot \chi$, followed by (2) thermal decomposition of the CuCl_2 complex $2\text{CuCl}_2 \cdot \chi \rightarrow 2\text{CuCl}_2 + \chi$, where χ is a chelating agent. As proposed, the complexation is performed with propylenediamine which acts as a chelating agent that selectively dissolves CuCl_2 . Another proposed agent suggested by Wentorf and Hanneman (1974) for complexation of CuCl is aqueous hydrochloric acid with a moderate concentration so that hydrolysis is prevented and the solubility of CuCl is reduced. The third suggested process in Wentorf and Hanneman (1974) is to use an ion-exchange resin capable of absorbing copper ions and to regenerate CuCl_2 by a hydrochloric acid solution. Such physicochemical processes for the disproportionation step may have the advantage of not requiring electricity, although some mechanical work consumption is still necessary for separation and extraction processes. The possibility of using an electrochemical process for the disproportionation step was not envisioned in the early work by Wentorf and Hanneman (1974).

A copper–chlorine cycle comprising an electrochemical process was first proposed by Dokyia and Kotera (1976) as a two-step cycle comprising an electrolytic process of cathodic reduction of hydrochloric acid to generate hydrogen, and oxidation of metallic copper at the anode from Cu^+ to Cu^{2+} . The closure reaction is thermo-hydrolysis of cupric chloride which evolves oxygen at 823 K. This hydrolysis was demonstrated experimentally by Dokyia and Kotera (1976) in a small glass reactor with an attached chromatograph that showed the oxygen evolution. Dokyia and Kotera (1976) suggested also that the hydrolysis reaction can be performed as a two-step process, namely, by thermolysis of cupric chloride followed by a reverse Deacon reaction. If these reaction steps are implemented in two separate reactors, then the cycle becomes a three-step hybrid cycle with one electrochemical and two thermochemical steps.

Further analysis of the hydrolysis reaction of cupric chloride was performed at the Institute of Gas Technology (IGT) by the end of the 1970s. As reported by Carty et al. (1981), they studied hydrolysis of cupric chloride with the aim of reducing the reaction temperature of ferrous chloride hydrolysis within their iron–copper–chloride cycle B-16. In this cycle, ferrous chloride is hydrolyzed in the presence of solid cupric chloride to form a mixed copper oxide–cupric chloride which is a coordination complex, namely, $\text{CuO} \cdot \text{CuCl}_2$. In their first set of experiments with this reaction, ferric chloride was not used and only the hydrolysis of cupric chloride was performed. It was found that the conversion of cupric chloride to mixed copper oxide–cupric chloride (also denoted as copper oxychloride) was essentially complete at 675 K. Thereafter, IGT proposed an oxygen evolution step by thermolysis of copper oxychloride at 800 K. However, according to Carty et al. (1981), oxygen evolution was not confirmed experimentally at IGT at that time, although the thermodynamic analysis showed that the reaction appears feasible. This process was confirmed by experimental work performed much later at the Argonne National Laboratory (ANL) by Lewis et al. (2003).

Furthermore, an electrochemical process was proposed by IGT for cuprous chlorine disproportionation which generates solid copper and cupric chlorine. The process performs electrochemically the same reaction as suggested by Wentorf and Hanneman (1974) through complexation or ion-absorption techniques. This reaction was not tested experimentally by IGT, which only stated that the reaction might be workable with electrochemistry, although the reaction configuration is unknown (Carty et al. 1981). With this electrochemical reaction, the hydrolysis of cupric chloride, thermolysis of mixed copper oxychloride, and a hydrogen evolution reaction, IGT formulated the hybrid cycle denoted as H-6, which is essentially the same as the five-step copper–chlorine cycle adopted later for development at ANL and UOIT. The hydrogen evolution reaction in cycle H-6 is a chlorination of metallic copper with hydrochloric acid which also produces cuprous chloride.

IGT screened 200 over thermochemical cycles and found that only five thermochemical and six hybrid cycles were potential viable candidates for linkage to nuclear energy. The copper–chlorine cycle, H-6, was selected as a promising cycle. Carty et al. (1981) estimated that the maximum attainable cycle efficiency of a Cu–Cl plant coupled with high-temperature nuclear reactors is 38 %, whereas the overall hydrogen production process efficiency is 26 % when the thermochemical plant is coupled to a helium-cooled high-temperature reactor (helium is supplied at 875 K and returned at 365 K). If molten lithium is used as a coolant for the nuclear reactor with a 975 K supply temperature and 625 K return flow temperature, then the overall hydrogen production process efficiency estimated by Carty et al. (1981) becomes 28 %.

In his book, Williams (1980) proposed a purely thermochemical copper–chlorine cycle (also called US-Chlorine) which involves three chemical reactions: a reverse Deacon reaction as hydrolysis which evolves oxygen, cuprous chloride chlorination as the hydrogen evolving reaction, and thermolysis of cupric chlorine as a reaction for recycling of intermediate reagents. The reactions of this cycle are listed in Table 5.10. In the 1990s, the Korean Institute of Energy Research (KIER) identified pure thermochemical cycles with copper and chlorine compounds. Three of the cycles proposed at KIER by Sim et al. (1993) have reactions similar to those in hybrid versions (e.g., hydrolysis of CuCl_2 and chlorination of CuCl) but all steps are thermochemical (see cycles KIER-2, KIER-A, KIER-B in Table 5.10). However, none of the purely thermochemical copper–chlorine cycles are suitable for linkage with nuclear reactors due to their higher temperature requirement (above 1,100 K).

Beginning in the 2000s, research on the hybrid copper–chlorine cycle was reinvigorated at ANL where laboratory investigations were performed for each of the reaction steps. In a seminal paper, Lewis et al. (2003) conducted a comprehensive experimental study to establish the thermodynamic feasibility of the cycle, determine the preliminary kinetic data, and assess the importance of side reactions.

The first interest of ANL was toward the IGT H-5 version of the cycle. Vilim (2004) at ANL studied an integrated system consisting of a sodium-cooled fast reactor of 840 MWth (design PRISM/Mod B) and the copper–chlorine thermochemical cycle. The nuclear heat is used in a proportion of 25 % to drive the

thermochemical reactions and 75 % to generate power via a steam-based Rankine plant. According to the results of Vilim (2004), the nuclear reactor vessel is 1,400 m³ while the chlorination reactor represents about half and the oxygen-evolving reactor is about one-quarter in size, whereas the associated costs with the reactor vessels and copper inventory represent less than 10 % of the power plant cost.

A comparative study of four hybrid cycles by ANL concluded that the copper–chlorine cycle is a main candidate for further development because the efficiency is reasonable high, the chemistry experiments have proven the reactions as feasible, and the temperature level for heat input is compatible with next-generation reactors (see Lewis et al. 2005a, b) collaborated with IGT to develop a proof-of-principle demonstration of the electrolytic step which produces metallic copper at the cathode. The main challenges that were identified for electrochemical copper generation are related to the membrane development (to impede undesired crossover of ionic species), finding of suitable electrode materials, and determination of operating conditions to generate a well-concentrated cupric chloride solution at the anode and small dendritic copper particles at the cathode.

The solubility of CuCl in water can be increased by the addition of HCl in order to concentrate the CuCl₂ in the output stream. A flow-sheet analysis developed in ASPEN Plus, which included model data validated by chemical lab experiments, was presented in Lewis et al. (2005b). For a production scale of 40,000 N m³ hydrogen per day, the flow-sheet analysis revealed an efficiency of 63 % based on the higher heating value (HHV) of hydrogen. This figure corresponds to the assumption that electricity is generated with 50 % efficiency and all heat rejected by the cycle is recovered and reused internally. A more realistic flow-sheet efficiency was also presented by Lewis et al. (2005b) based on a pinch analysis which reveals that the cycle efficiency is around 50 % (based on HHV).

Miller (2005) reported AECL's interest in the development of the copper–chlorine cycle in view of integration with future CANDU reactors in collaboration with ANL. The focus at AECL was primarily on the development of the electrolytic step for direct production of hydrogen by CuCl/HCl electrolysis. A first set of results on the electrolytic step developed at AECL was reported by Suppiah et al. (2005). They obtained a current density of ~800 A/m² at ~0.7 V with a copper cathode and platinum anode when a solution of 0.3 mol/L CuCl in 4 mol/L HCl was electrolyzed.

The researchers in University of Nevada at Las Vegas (UNLV) performed simulation work and process analysis (Khan and Chen 2005). According to the APEN Plus simulations performed at UNLV, the flow sheet-based efficiency of hydrogen production was 33 %, assuming that the electricity is produced with 50 % energy efficiency.

The University of Ontario Institute of Technology (UOIT) began a long-term program on the copper–chlorine thermochemical cycle development in 2006. The UOIT team published numerous papers since that time, covering general analyses of the hybrid cycle, experimental unit operations, and a scaled-up hydrogen production plant. An integrated engineering-scale demonstration unit of 50 Nm³

hydrogen per day is presently under development at UOIT. A UOIT-led international team on this cycle development comprises eight institutions, five countries, and six industrial partners (see Table 5.21). This consortium and some selected main research results are summarized in Chap. 5, Sect. 5.10.3.3.

In this chapter, the hybrid copper–chlorine cycle is analyzed in detail. Seven versions of the cycle are identified. The physicochemical properties and their prediction are discussed. Each major cycle step is examined extensively. Heat recovery and reuse are reported. Also, scaled-up design and plant simulations are included.

6.2 Copper–Chlorine Cycle Versions

In past literature, a total of seven versions of the copper–chlorine cycle were reported: 1 cycle with two-step, 2 versions of three-step, 2 cycles with four-step, and 1 five-step cycle. In this section, each of these cycle versions is introduced and diagrams are presented. The knowledge of the processes is essential for cycle analysis and design. There are seven main classes of processes that are encountered in the copper–chlorine cycles. Their nature is thermochemical, electrochemical, physicochemical, or thermophysical. Table 6.1 lists the main classes of processes encountered in copper–chlorine cycles and shows definitions. These classes of processes are complexation, chlorination, oxychlorination, hydrolysis, thermolysis, and drying.

Past literature results show that for the copper–chlorine cycles, the following 12 processes occur: (1) electrochemical disproportionation of CuCl , (2) four distinct hydrolysis reactions, (3) two chlorination reactions of which one is thermochemical and one is electrochemical, (4) one oxychlorination reaction, (5) two thermolysis reactions, and (6) two dehydration processes of hydrated cupric chloride, of which one occurs via spray drying and one is based on crystallization. Table 6.2 presents the 12 distinct processes based on which copper–chlorine cycles can be formed.

Process #1 in Table 6.2 is the electrochemical disproportionation of cuprous chloride which is conducted in an aqueous solution in the presence of hydrochloric acid. In this process, a complexation of cupric chloride occurs, namely, hydrated cupric chloride is produced in the form of the complex $\text{CuCl}_2 \cdot n\text{H}_2\text{O}$ which is present in the aqueous phase (dissolved). At the same time, copper precipitates as solid particles of micron size.

Processes #2 to #5 are hydrolysis processes. The hydrolysis that evolves at the lowest temperature is process #2 which requires 650 K and combines $2\text{CuCl}_2 \cdot n\text{H}_2\text{O(s)}$, a hydrated cupric chloride in solid form, with steam to form copper oxychloride and hydrochloric acid. During the process, the moisture from CuCl_2 is released as steam. Process #3 is similar to #2; however it uses dried cupric chloride as a reactant and thus no steam is released. The highest temperature hydrolysis process of CuCl_2 is process #3 which is conducted at 823 K. This process uses hydrated cupric chloride as reactant and generates oxygen, hydrochloric acid, and molten cuprous chloride.

Table 6.1 Main processes encountered in copper–chlorine thermochemical cycles

Process	Nature	Definition and remarks
Complexation	Physicochemical	Reaction that forms a chemical complex by loose association of two or more molecular entities with bonds weaker than a covalent bond. In the Cu–Cl cycle, complexation of CuCl and CuCl ₂ occurs. ^a
Chlorination	Thermochemical Electrochemical	Reaction of a chemical compound with chlorine. In the Cu–Cl cycle, chlorine is sourced from HCl. Electrolysis of CuCl/HCl is an electrochemical chlorination of CuCl. Chlorination of Cu is conducted thermochemically.
Oxychlorination	Thermochemical	Chlorination in the presence of oxygen. In the Cu–Cl cycle, oxygen is derived from water during oxychlorination of the complex CuCl ₂ ·H ₂ O.
Disproportionation	Electrochemical ^b	Reaction during which a molecule is transformed in two dissimilar chemical compounds. In the Cu–Cl cycle, CuCl is disproportionated electrochemically to form metallic copper and cupric chloride.
Hydrolysis	Thermochemical	Reaction of a chemical compound with water. Depending on the version, Cu–Cl cycle hydrolysis can be conducted at lower temperature when CuO·CuCl ₂ is formed, or at higher temperatures when oxygen is released.
Thermolysis	Thermochemical	Chemical reaction of thermal decomposition of a molecule. In Cu–Cl cycles, thermolysis of CuO·CuCl ₂ or CuCl ₂ is encountered.
Drying	Thermophysical	Removing moisture from a material. In the Cu–Cl cycle, water is removed from the coordination complexes of cupric chloride with water (CuCl ₂ · <i>n</i> H ₂ O) either by spray drying or crystallization methods.

^aThermochemically conducted disproportionation exists, but is not in the scope of the hybrid Cu–Cl cycle

^bIn the Cu–Cl cycle, a coordination complex CuO·CuCl₂ is also formed during hydrolysis or oxychlorination; also the hydrated complex of CuCl₂, namely, CuCl₂·*n*H₂O, is generated in the anolyte of the electrochemical cell

In addition, steam from the moisture content of CuCl₂ is released. There is also a hydrolysis process of chlorine—encountered in the three-step cycle of Dokyia and Kotera (1976)—which is a reverse Deacon reaction at 1,073 K, noted in Table 6.2 as process #5. A thermochemical chlorination of copper is used in three of the versions of the copper–chlorine cycle as will be described below. Chlorination of copper is performed with hydrochloric acid according to process #6.

Process #7 is an electrochemical process of chlorination in which cuprous chloride is reacted with hydrochloric acid in an aqueous electrolyte. The electrochemical reaction generates hydrogen at the cathode. A complexation process occurs in the electrolyte and forms a hydrated cupric chloride complex in the aqueous phase at the anode, namely, CuCl₂ · *n*H₂O(aq), *n* > 0. Electrochemical cells for this reaction are in development at UOIT, ANL, AECL, and Gas Technology Institute (GTI, USA). Process #8 is oxychlorination, having as the sole reactant

Table 6.2 Main processes and chemical reactions in copper–chlorine thermochemical cycles

ID	Process	Chemical reactions	<i>T</i> (K)
1	CuCl disproportionation	$E : 4\text{CuCl}(s) + n\text{H}_2\text{O}(l) \rightarrow 2\text{Cu}(s) + 2\text{CuCl}_2 \cdot n\text{H}_2\text{O}(aq), \text{ in presence of HCl}$	350
2	CuCl ₂ hydrolysis, low <i>T</i>	$T : \text{H}_2\text{O}(g) + 2\text{CuCl}_2 \cdot n\text{H}_2\text{O}(s) \rightarrow \text{CuO} \cdot \text{CuCl}_2(s) + 2\text{HCl}(g) + n\text{H}_2\text{O}(g)$	650
3	CuCl ₂ hydrolysis, dry	$T : \text{H}_2\text{O}(g) + 2\text{CuCl}_2(s) \rightarrow \text{CuO} \cdot \text{CuCl}_2(s) + 2\text{HCl}(g)$	673
4	CuCl ₂ hydrolysis, high <i>T</i>	$T : \text{H}_2\text{O}(g) + 2\text{CuCl}_2 \cdot n\text{H}_2\text{O}(s) \rightarrow 0.5\text{O}_2(g) + 2\text{HCl}(g) + 2\text{CuCl}(l) + n\text{H}_2\text{O}(g)$	823
5	Chlorine hydrolysis	$T : \text{H}_2\text{O}(g) + \text{Cl}_2(g) \rightarrow 0.5\text{O}_2(g) + 2\text{HCl}(g)$	1,073
6	Copper chlorination	$T : 2\text{Cu}(s) + 2\text{HCl}(g) \rightarrow \text{H}_2(g) + 2\text{CuCl}(l)$	723
7	CuCl chlorination ^a	$E : n\text{H}_2\text{O}(l) + 2\text{CuCl}(s) + 2\text{HCl}(aq) \rightarrow \text{H}_2(g) + 2\text{CuCl}_2 \cdot n\text{H}_2\text{O}(aq)$	<473 ^b
8	Oxychlorination	$T : 2\text{CuCl}_2 \cdot n\text{H}_2\text{O}(s) \rightarrow \text{CuO} \cdot \text{CuCl}_2(s) + 2\text{HCl}(g) + (n - 1)\text{H}_2\text{O}(g)$	800
9	CuO·CuCl ₂ thermolysis	$T : \text{CuO} \cdot \text{CuCl}_2(s) \rightarrow 0.5\text{O}_2(g) + 2\text{CuCl}(l)$	800
10	CuCl ₂ thermolysis	$T : 2\text{CuCl}_2 \cdot n\text{H}_2\text{O}(s) \rightarrow 2\text{CuCl}(l) + \text{Cl}_2(g) + n\text{H}_2\text{O}(g)$	773
11	Drying (spray)	$T : 2\text{CuCl}_2 \cdot n\text{H}_2\text{O}(s) \rightarrow 2\text{CuCl}_2 \cdot m\text{H}_2\text{O}(s) + (n - m)\text{H}_2\text{O}(g), \quad n > m$	<530
12	Drying (crystallization)	$T : 2\text{CuCl}_2 \cdot n\text{H}_2\text{O}(aq) \rightarrow 2\text{CuCl}_2(s) + n\text{H}_2\text{O}(l)$	<373

ID process identification number, *E* electrochemical, *T* thermochemical

^aThis is an electrochemical chlorination process, also denoted as CuCl/HCl electrolysis

^b473 K in process by Dokyia and Kotera (1976); ~350 K in other implementations(see Naterer et al. 2011a)

the complex $\text{CuCl}_2 \cdot n\text{H}_2\text{O}(\text{s})$. In this reaction, copper oxychloride is formed together with gaseous hydrochloric acid. The thermolysis of copper oxychloride is described by process #9 in Table 6.2. This is a thermal decomposition that releases oxygen and forms molten cuprous chloride. Thermolysis of hydrated cupric chloride is also encountered as described by process #10.

Dehydration of wet cupric chloride can be achieved by spray drying, in which the moisture content is reduced partially or totally as indicated in Table 6.2 by process #11. This process requires heat at temperature below 573 K. A crystallization process is also possible at lower temperatures, namely, below 373 K. In this case, anhydrous cupric chloride is obtained according to process #12, listed in Table 6.2.

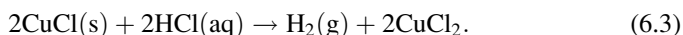
There are some simplified forms to describe processes #1 to #12 listed in Table 6.2 which can be found in various sources. For example, the electrolytic process #1—disproportionation—is described by the following simplified equation:



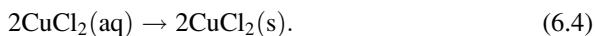
The reaction is conducted in an aqueous solution of HCl. Equation (6.1) does not indicate how many molecules of water are made in the complexation of cupric chloride. This detail is not necessary for a screening of the cycle; however it is important for accurate analysis and design. In the same manner, processes #2, #3, #4, and #8 can be simplified by the following equation, which corresponds exactly to process #3:



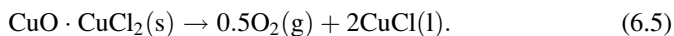
Process #7 can be written as



Moreover, the dehydration processes #10 and #11 can be represented by the following simplified equation, namely:



The five-step hybrid cycle can be described in a non-detailed manner using (6.1)–(6.4) and (6.5) as follows:

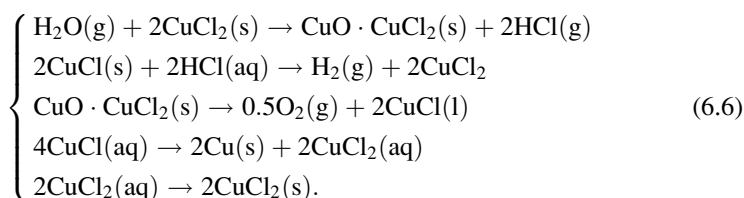


Therefore, the five-step hybrid copper–chlorine cycle is characterized by the following set of simplified equations:

Table 6.3 Definitions of copper–chlorine thermochemical cycles and their main processes

Cycle ID	Process ID (see Table 6.2)											
	1	2	3	4	5	6	7	8	9	10	11	12
Cu–Cl-2	No	No	No	Yes	No	No	Yes	No	No	No	No	No
Cu–Cl-3A	Yes	No	No	Yes	No	Yes	No	No	No	No	No	No
Cu–Cl-3B	No	No	No	No	No	No	Yes	Yes	Yes	No	No	No
Cu–Cl-3C	No	No	No	No	Yes	No	Yes	No	No	Yes	No	No
Cu–Cl-4A	Yes	No	No	No	No	Yes	No	Yes	Yes	No	No	No
Cu–Cl-4B	No	No	Yes	No	No	No	Yes	No	Yes	No	No	Yes
Cu–Cl-5	Yes	Yes	No	No	No	Yes	No	No	Yes	No	Yes	No
Enc. (%)	43	14	14	28	14	43	57	28	57	14	14	14

Enc. processed encountered with respect to the total number of cycles (7); e.g., process 1 encountered in three cycles which is 43 % of the total number of cycles



In this five-step thermochemical cycle, water is fed in the gaseous phase (as steam) to the hydrolysis reaction. In the process, all the intermediate reagents are recycled, but steam, which is consumed, and hydrogen and oxygen are delivered as products. All versions of the copper–chlorine cycle proposed in past literature are described compactly in Table 6.3 where the processes are indicated for each cycle. An identification coding for the cycles is shown in Table 6.3 which consists of “Cu–Cl” followed by the number of steps and a letter “A,” “B,” or “C” to indicate the cycle version. For example, as indicated in the table, cycle Cu–Cl-2 is a two-step version consisting of processes #4 and #7; the processes are those listed in Table 6.2. Cycle Cu–Cl-3A is a three-step cycle with the steps being processes #1, #4, and #6. The Cu–Cl-5 cycle, also described by simplified equation (6.6), comprises processes #1, #2, #6, #9, and #11.

It can be observed from Table 6.3 that the processes which are encountered mostly in copper–chlorine cycle versions are #7, namely, the electrochemical chlorination of CuCl with hydrochloric acid, and process #9, namely, the thermolysis of copper oxychloride. These processes occur in four of seven cycle versions. The electrochemical process of CuCl/HCl electrolysis (namely, #7) is used in four cycles while the other electrochemical process (CuCl disproportionation, process #1) is encountered in only three cycles.

Table 6.4 lists for each of the cycles the proponent, main references, and alternative cycle identifications as proposed in past literature. As indicated in the table, the cycle Cu–Cl-2 was proposed by Dokyia and Kotera (1976) and it has an alternative identification in Lewis and Masin (2009) as Cu–Cl-C. The three-step cycle Cu–Cl-3A is also called ANL-287 in Abanades et al. (2006), as UNLV-191 in

Table 6.4 Cycle proponents and alternative identifications of Cu–Cl cycle versions

ID	T_{\max} (K)	Proponent	Alternative identifications
Cu–Cl-2	823	NCLI, Dokyia and Kotera (1976)	Cu–Cl-C, in Lewis and Masin (2009)
Cu–Cl-3A	800	ANL, Perret et al. (2005)	ANL-287 in Abanades et al. (2006) UNLV-191 in Perret et al. (2005) Three-step cycle (UOIT) in Wang et al. (2009)
Cu–Cl-3B	800	AECL and ANL, Suppiah et al. (2005)	Cu–Cl-B in Lewis and Masin (2009) Three-step cycle (UOIT) in Naterer et al. (2010)
Cu–Cl-3C	1,073	NCLI, Dokyia and Kotera (1976)	UNLV-56, in McQuillan et al. (2010) Cu–Cl-D in Lewis and Masin (2009)
Cu–Cl-4A	800	UOIT, Wang et al. (2009)	Four-step cycle (UOIT) in Wang et al. (2009)
Cu–Cl-4B	800	UOIT, Naterer et al. (2010)	Four-step cycle (UOIT) in Naterer et al. (2010)
Cu–Cl-5	800	IGT, Carty et al. (1981)	H-5 in Carty et al. (1981) ALTC-1 in Lewis et al. (2003) Cu–Cl-A in Lewis and Masin (2009) Five-step cycle (UOIT) in Wang et al. (2009)

NCLI - National Chemical Laboratory for Industry (Tokyo), ANL - Argonne National Laboratory, AECL - Atomic Energy Canada Limited, UOIT - University of Ontario Institute of Technology, IGT - Institute of Gas Technology

Perret et al. (2005). Other alternative identifications of the copper–chlorine cycles are Cu–Cl-A, Cu–Cl-B, Cu–Cl-C, UNLV-56, and H-5.

The full description of all cycles is presented in Table 6.5 which indicates the cycle identification (CID), the reactions for each step, their IDs, and their associated temperatures. In the table, the first step for each cycle represents the chemical reaction to which water is supplied. It can be observed that for cycles Cu–Cl-2, Cu–Cl-3A, Cu–Cl-3C, Cu–Cl-4B, and Cu–Cl-5, water is supplied as steam to the hydrolysis process. This implies that water is preheated, boiled, and superheated separately or in an integrated system prior to its supply to the reaction in the gaseous phase. The other two cycles, namely, Cu–Cl-3B and Cu–Cl-4A, do not require water boiling because water is supplied as a liquid to the electrochemical process where complexation occurs with cupric chloride and then it is heated up to the required temperature for oxychlorination.

The operating principle of each cycle is presented schematically in the diagrams shown in Fig. 6.1. These diagrams indicate the processes and main flows of chemicals among the processes. The diagrams in Fig. 6.1 present in a visual manner the same information as presented through the chemical equations in Table 6.5. The useful value of the diagram is to visually show the flow of chemicals between processes.

The conceptual flowcharts for the cycles, which are introduced next, describe the cycle in a more detailed manner than the schematic representations presented above. The conceptual flowcharts include chemical reactors, electrochemical

Table 6.5 Hybrid copper–chlorine thermochemical cycles for water splitting

CID	Reactions	ID	Chemical equation	<i>T</i> (K)
Cu–Cl-2	Hydrolysis	4	$T: \text{H}_2\text{O}(\text{g}) + 2\text{CuCl}_2 \cdot n\text{H}_2\text{O}(\text{s}) \rightarrow 0.5\text{O}_2(\text{g}) + 2\text{HCl}(\text{g}) + 2\text{CuCl}(\text{l}) + n\text{H}_2\text{O}(\text{g})$	823
	CuCl chlorination	7	$E: 2\text{CuCl}(\text{s}) + 2\text{HCl}(\text{aq}) + n\text{H}_2\text{O}(\text{l}) \rightarrow \text{H}_2(\text{g}) + 2\text{CuCl}_2 \cdot n\text{H}_2\text{O}(\text{aq})$	473
Cu–Cl-3A	Hydrolysis	4	$T: \text{H}_2\text{O}(\text{g}) + 2\text{CuCl}_2 \cdot n\text{H}_2\text{O}(\text{s}) \rightarrow 0.5\text{O}_2(\text{g}) + 2\text{HCl}(\text{g}) + 2\text{CuCl}(\text{l}) + n\text{H}_2\text{O}(\text{g})$	823
	Cu chlorination	6	$T: 2\text{Cu}(\text{s}) + 2\text{HCl}(\text{g}) \rightarrow \text{H}_2(\text{g}) + 2\text{CuCl}(\text{l})$	723
Cu–Cl-3B	Disproportionation	1	$E: n\text{H}_2\text{O}(\text{l}) + 4\text{CuCl}(\text{s}) \rightarrow 2\text{Cu}(\text{s}) + 2\text{CuCl}_2 \cdot n\text{H}_2\text{O}(\text{aq})$	350
	CuCl chlorination	7	$E: n\text{H}_2\text{O}(\text{l}) + 2\text{CuCl}(\text{s}) + 2\text{HCl}(\text{aq}) \rightarrow \text{H}_2(\text{g}) + 2\text{CuCl}_2 \cdot n\text{H}_2\text{O}(\text{aq})$	350
Cu–Cl-3C	Thermolysis	9	$T: \text{CuO} \cdot \text{CuCl}_2(\text{s}) \rightarrow 0.5\text{O}_2(\text{g}) + 2\text{CuCl}(\text{l})$	800
	Oxychlorination	8	$T: 2\text{CuCl}_2 \cdot n\text{H}_2\text{O}(\text{s}) \rightarrow \text{CuO} \cdot \text{CuCl}_2(\text{s}) + 2\text{HCl}(\text{g}) + (n-1)\text{H}_2\text{O}(\text{g})$	673
Cu–Cl-4A	Cl ₂ hydrolysis	5	$T: \text{H}_2\text{O}(\text{g}) + \text{Cl}_2(\text{g}) \rightarrow 0.5\text{O}_2(\text{g}) + 2\text{HCl}(\text{g})$	1,073
	CuCl chlorination	7	$E: 2\text{CuCl}(\text{s}) + 2\text{HCl}(\text{aq}) + n\text{H}_2\text{O}(\text{l}) \rightarrow \text{H}_2(\text{g}) + 2\text{CuCl}_2 \cdot n\text{H}_2\text{O}(\text{aq})$	473
Cu–Cl-4B	CuCl ₂ thermolysis	10	$T: 2\text{CuCl}_2 \cdot n\text{H}_2\text{O}(\text{s}) \rightarrow 2\text{CuCl}(\text{l}) + \text{Cl}_2(\text{g}) + n\text{H}_2\text{O}(\text{g})$	773
	Disproportionation	1	$E: n\text{H}_2\text{O}(\text{l}) + 4\text{CuCl}(\text{s}) \rightarrow 2\text{Cu}(\text{s}) + 2\text{CuCl}_2 \cdot n\text{H}_2\text{O}(\text{aq})$	350
Cu–Cl-5	Cu chlorination	6	$T: 2\text{Cu}(\text{s}) + 2\text{HCl}(\text{g}) \rightarrow \text{H}_2(\text{g}) + 2\text{CuCl}(\text{l})$	723
	Thermolysis	9	$T: \text{CuO} \cdot \text{CuCl}_2(\text{s}) \rightarrow 0.5\text{O}_2(\text{g}) + 2\text{CuCl}(\text{l})$	800
Cu–Cl-5A	Oxychlorination	8	$T: 2\text{CuCl}_2 \cdot n\text{H}_2\text{O}(\text{s}) \rightarrow \text{CuO} \cdot \text{CuCl}_2(\text{s}) + 2\text{HCl}(\text{g}) + (n-1)\text{H}_2\text{O}(\text{g})$	650
	Hydrolysis, dry	3	$T: \text{H}_2\text{O}(\text{g}) + 2\text{CuCl}_2(\text{s}) \rightarrow \text{CuO} \cdot \text{CuCl}_2(\text{s}) + 2\text{HCl}(\text{g})$	673
Cu–Cl-5B	CuCl chlorination	7	$E: 2\text{CuCl}(\text{s}) + 2\text{HCl}(\text{aq}) + n\text{H}_2\text{O}(\text{l}) \rightarrow \text{H}_2(\text{g}) + 2\text{CuCl}_2 \cdot n\text{H}_2\text{O}(\text{aq})$	350
	Thermolysis	9	$T: \text{CuO} \cdot \text{CuCl}_2(\text{s}) \rightarrow 0.5\text{O}_2(\text{g}) + 2\text{CuCl}(\text{l})$	800
Cu–Cl-5C	Crystallization	12	$T: 2\text{CuCl}_2 \cdot n\text{H}_2\text{O}(\text{aq}) \rightarrow 2\text{CuCl}_2(\text{s}) + n\text{H}_2\text{O}(\text{l})$	<373
	Hydrolysis	2	$T: \text{H}_2\text{O}(\text{g}) + 2\text{CuCl}_2 \cdot m\text{H}_2\text{O}(\text{s}) \rightarrow \text{CuO} \cdot \text{CuCl}_2(\text{s}) + 2\text{HCl}(\text{g}) + m\text{H}_2\text{O}(\text{g})$	650
Cu–Cl-5D	Cu chlorination	6	$T: 2\text{Cu}(\text{s}) + 2\text{HCl}(\text{g}) \rightarrow \text{H}_2(\text{g}) + 2\text{CuCl}(\text{l})$	723
	Thermolysis	9	$T: \text{CuO} \cdot \text{CuCl}_2(\text{s}) \rightarrow 0.5\text{O}_2(\text{g}) + 2\text{CuCl}(\text{l})$	800
Cu–Cl-5E	Disproportionation	1	$E: 4\text{CuCl}(\text{s}) + n\text{H}_2\text{O}(\text{l}) \rightarrow 2\text{Cu}(\text{s}) + 2\text{CuCl}_2 \cdot n\text{H}_2\text{O}(\text{aq})$	350
	Drying (spray)	11	$T: 2\text{CuCl}_2 \cdot n\text{H}_2\text{O}(\text{aq}) \rightarrow 2\text{CuCl}_2 \cdot m\text{H}_2\text{O}(\text{s}) + (n-m)\text{H}_2\text{O}(\text{g}), \quad n > m$	<530

CID cycle identifier format is Cu–Cl–Ns(–V), where Ns is the number of process steps and V is subversion identified with letters A, B, or C; g, gas; l, liquid (or molten), s, solid, · (bullet) indicates a chemical complex, E electrochemical reaction, T thermochemical reaction or physical process driven by heat

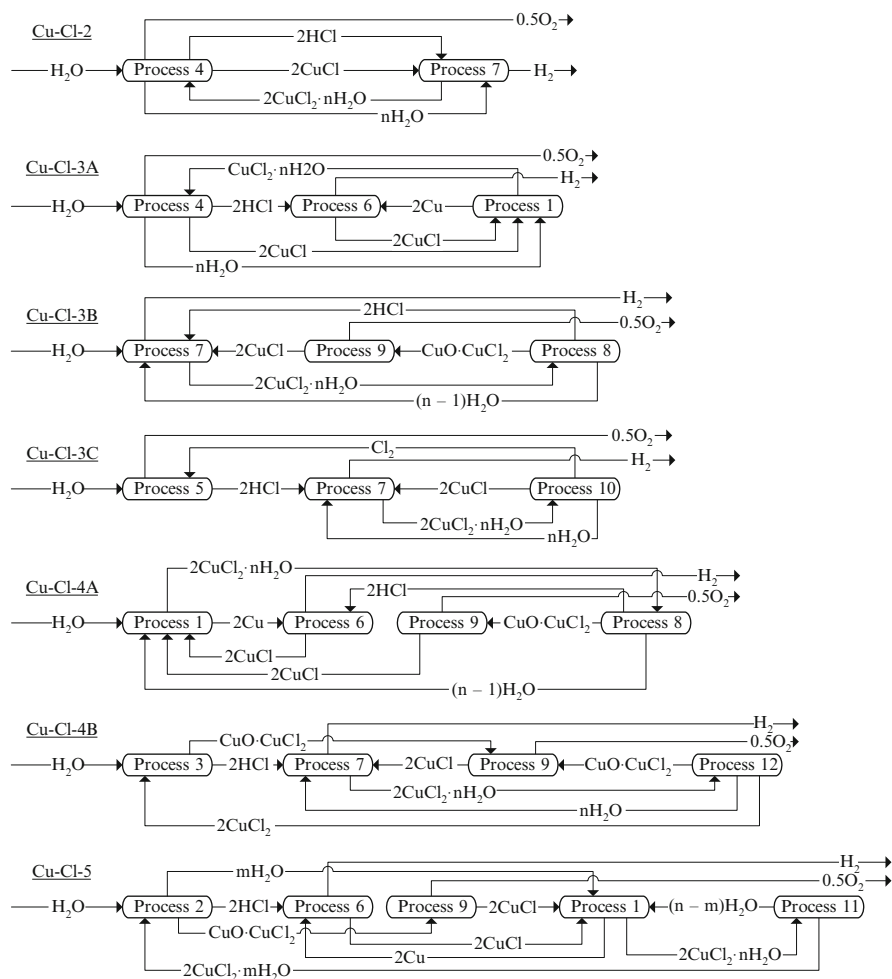


Fig. 6.1 Schematic representation of hybrid copper–chlorine cycles

reactors, dehydration reactors, heat exchangers, and separators. Various devices such as conveyors, pumps, compressors, and other auxiliary components are omitted. Also, the heat recovery and recycling systems are not shown. Full details regarding the cycles and their processes are given in subsequent sections of this chapter.

The conceptual flowchart for the two-step water splitting cycle Cu–Cl-2 is presented in Fig. 6.2. In this system, liquid water is supplied in #1, which is converted to superheated steam in #2 at a temperature that corresponds to the hydrolysis reaction. In the reactor R, the hydrolysis of CuCl_2 occurs at a high temperature according to process #4 (see Table 6.5). Hot gases, namely, oxygen, hydrochloric acid, and steam, are extracted at location #3. This mixture is cooled to a temperature close to the ambient in Hx2 and delivered as stream #4 to the liquid

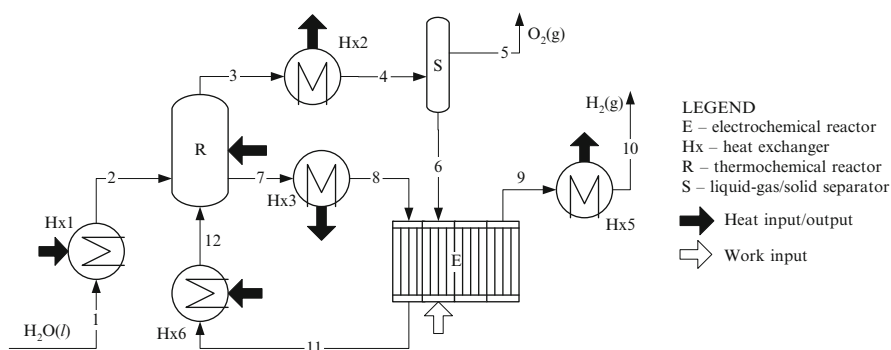


Fig. 6.2 Conceptual flowchart for Cu–Cl-2 cycle (two steps)

gas separator S. Then water is present as liquid and hydrochloric acid in the aqueous phase, while oxygen separates as a gas and it is extracted at #5. The liquid of the aqueous hydrochloric solution and water are transferred to the electrochemical cell, E. In the hydrolysis reactor R, molten cuprous chloride is generated at the outlet #7, which is thereafter cooled and solidified in the heat exchanger system Hx3, and then delivered as solid particles to the electrolytic cell E as stream #8. In the electrolytic cell, the solid CuCl particles dissolve and form an aqueous phase. The electrolytic cell E generates gaseous hydrogen in #9 at around 473 K, which is cooled in Hx5 and delivered as a product at a temperature close to the ambient in #10. The other product of the electrolytic step is aqueous cupric chloride which results at #11; this is heated in Hx6 to the reaction temperature of the hydrolysis process and supplied at point #12 of the hydrolysis reactor R.

The conceptual flowchart for the three-step cycle Cu–Cl-3A is presented in Fig. 6.3. This cycle comprises three reactors: R1 (hydrolysis reactor, process #4), R2 (chlorination reactor, process #6), and E (electrolytic disproportionation cell, process 1). Liquid water is fed at #1 of liquid–gas separator (LGS) S1 where it helps scrubbing of oxygen gas, which is delivered at #2 and mixes with aqueous hydrochloric acid and recycled water, which are then supplied to #2 of the separator. A liquid solution of water and aqueous HCl leaves the separator from the bottom location #4, and mixes in mixer M with a slurry formed of solid copper particles in liquid water, shown on the flowchart as stream #5. The resulting slurry in #5 comprises copper particles, water, and hydrochloric acid. This mixture is heated in heat exchanger Hx1 to a suitable temperature for chlorination (process #6 listed in Table 6.2).

The stream #7 consists of steam, gaseous hydrochloric acid, and copper particles. This is fed into chlorination reactor R1. At the top of the reactor, a gaseous product is generated, consisting of hydrogen and steam. This is extracted from topmost #8. The gaseous mixture is cooled in the heat exchanger system Hx2 where water condenses fully while hydrogen remains gaseous. This two-phase mixture is fed at #9 into the gas–liquid separator S2 where hydrogen separates at the top and it is extracted at port #10. Liquid water is extracted from the bottom #11

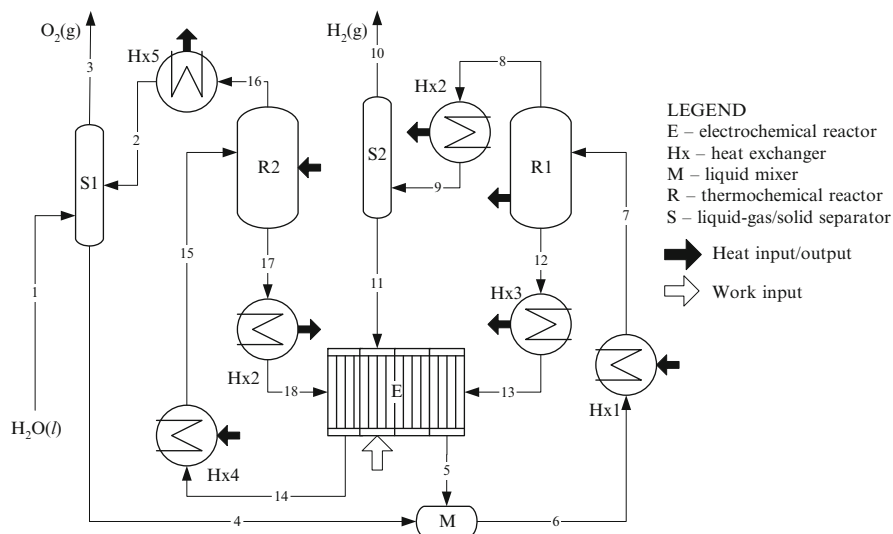


Fig. 6.3 Conceptual flowchart for Cu–Cl–3A cycle (three steps)

and fed to the electrolytic cell E. At the bottom of chlorination reactor R1, molten cuprous chloride is formed, then collected, and extracted at #12.

The molten CuCl is cooled in the heat exchanger system Hx3 such that cuprous chloride solidifies and moves as solid particles—stream #13—to the electrochemical cell E. The electrochemical cell generates solid copper in an aqueous slurry in #5. In addition, an aqueous mixture of wet cupric chloride, $\text{CuCl}_2 \cdot n\text{H}_2\text{O}(\text{aq})$, is formed, which is extracted at #14. This aqueous solution is heated in a heat exchanger system Hx4 such that all water boils and forms a mixture of solid $\text{CuCl}_2 \cdot n\text{H}_2\text{O}(\text{s})$ and steam, represented on the flowchart as stream #15. This stream is fed to the hydrolysis reactor R2 where process #4 occurs (see Table 6.2). In this process, oxygen is released together with other gaseous products which are steam and hydrochloric acid. This gas mixture is indicated in the diagram as stream #16, which after cooling in heat exchanger system Hx5 becomes a two-phase mixture in #2 which comprises liquid water, aqueous hydrochloric acid, and gaseous oxygen.

The three-step cycle Cu-Cl-3B is represented by the flowchart diagram indicated in Fig. 6.4. Liquid water is supplied as stream #1 directly to the electrochemical cell E where process 7 occurs. During this process, hydrogen is generated and delivered as product, stream #2. In addition, wet cupric chloride is generated in aqueous solution, namely, $\text{CuCl}_2 \cdot n\text{H}_2\text{O}(\text{aq})$, which is extracted as stream #3. The wet cupric chloride is heated in heat exchanger system Hx1 such that all free water boils and superheats while cupric chloride remains in hydrated form as solid, $\text{CuCl}_2 \cdot n\text{H}_2\text{O}(\text{s})$. This stream, namely, stream #4, is directed toward the oxychlorination reactor R1. In this reactor, process #8 occurs (Table 6.2), which forms solid copper oxychloride, gaseous hydrochloric acid, and steam. The gaseous phase is extracted from the top of the reactor as stream #5 and further directed

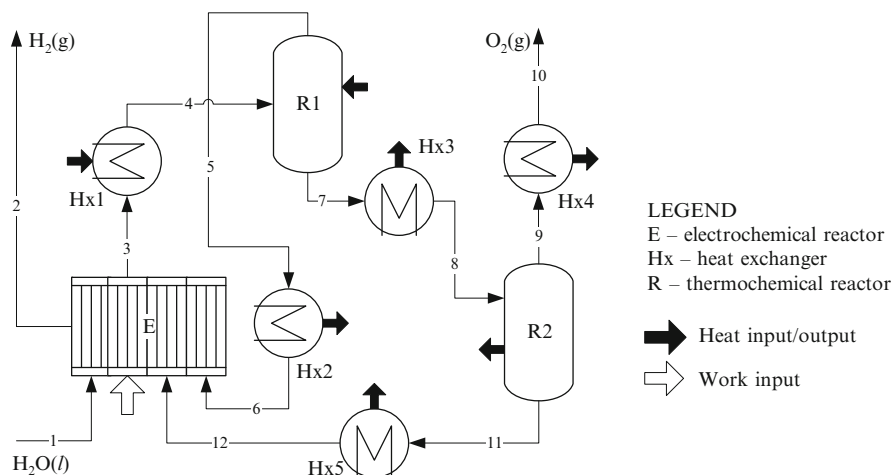


Fig. 6.4 Conceptual flowchart for Cu–Cl-3B cycle (three steps)

toward the heat exchanger system Hx2 where water condenses and hydrochloric acid completely dissolves in the aqueous solution. The resulting liquid solution is fed to the electrochemical cell E as stream #6. The solid particles of copper oxychloride, resulting from the oxychlorination reactor, are extracted as the bottom stream #7 and heated in heat exchanger system Hx3 to the temperature level compatible with the thermolysis reaction in reactor R2. The copper oxychloride is supplied to the thermolysis reactor R2 as stream #8. In the thermolysis reactor, process #9 occurs and releases gaseous oxygen and forms liquid cuprous chloride. The two phases—gas and liquid—separate inside the reactor. Oxygen is extracted as gas at the top of the reactor—stream #9—and further cooled to the ambient temperature in heat exchanger system Hx4 which delivers the oxygen product as stream #10. The molten cuprous chloride, collected from the bottom of the reactor as stream #11, is cooled and solidified in the heat exchanger system Hx5, and then supplied to the electrolytic cell E as stream #12.

The conceptual flowchart of Cu–Cl-3C cycle is presented in Fig. 6.5. In this cycle, water fed as liquid in #1 is heated and boiled in Hx1 to around 1,000 K to state #2 prior to entering into the hydrolysis reactor R1 that performs the reverse Deacon reaction, process #5. From this reactor, a stream #3 of gaseous products comprising oxygen and hydrochloric acid is generated. The gas mixture is cooled down in Hx2 to the ambient temperature and fed into a LGS S1 where liquid water is also supplied. The hydrochloric acid separates as an aqueous solution while gaseous oxygen is collected from the top of the separator as product stream #5. The aqueous hydrochloric acid solution—stream #6—is heated to around 473 K in Hx3 prior to feeding the electrochemical cell E at #7. The electrochemical cell generates pure hydrogen gas in #8 which is cooled to ambient temperature in Hx4 and delivered at #9. The other product of the electrochemical process is the hydrated cupric chloride—stream #10—which is heated in Hx5 prior to entering

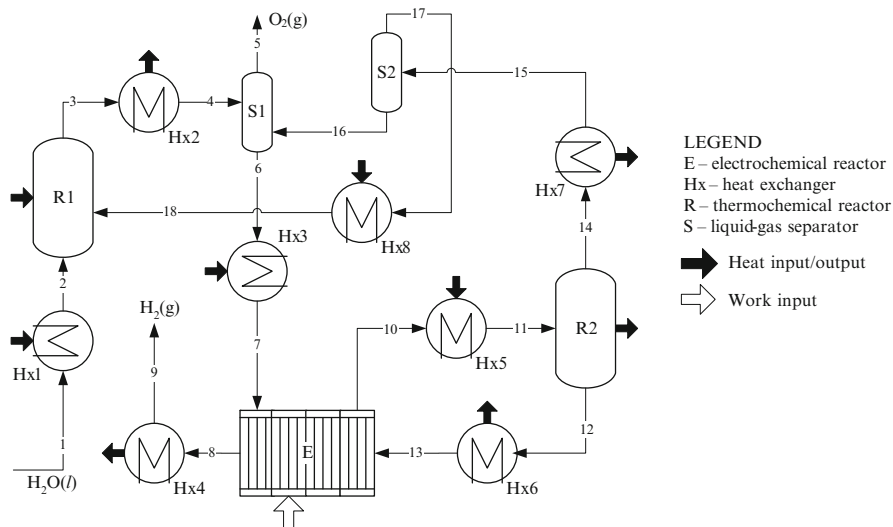


Fig. 6.5 Conceptual flowchart for Cu–Cl–3C cycle (three steps)

the thermolysis reactor R2 at #11. The reaction in the thermolysis reactor occurs according to process #10, Table 6.2. It generates molten cuprous chloride at #12 which is cooled and solidified in heat exchanger system Hx6 prior to flowing into the electrochemical cell as stream #13. The gaseous products of thermolysis consist of steam and chlorine collected from the top of the reactor as stream #14. This stream is cooled in Hx7 such that water condenses completely while chlorine remains as gas. The separation of chlorine from liquid water can be performed by distillation-based methods performed as successive boiling/condensation and gas-liquid separations, or other methods. In the flowchart, the separation process is shown in a simplified manner, such as stream #15 of water + gaseous chlorine fed to the LGS S2 where water separates at the bottom (stream #16) and chlorine at the top (stream #17). Water is fed to separator S1 where it dissolves the hydrochloric acid, while chlorine is heated to around 1,000 K and supplied to the reverse Deacon reaction reactor at #18.

The cycle Cu-Cl-4A with four steps has a conceptual flowchart presented in Fig. 6.6. Supply water in the liquid phase is fed to the electrochemical cell E (process #1, Table 6.2) as stream #1. The electrochemical cell produces hydrated cupric chloride in the aqueous phase represented by stream #2 in the flowchart. This is heated in the heat exchanger system Hx1 and fed into oxychlorination reactor R1 (process #8). In this reactor, a stream of gaseous products consisting of hydrochloric acid and steam is released as stream #4. This is cooled at lower temperature in heat exchanger system Hx2 and provided as stream #5 to a separator where hydrochloric acid is separated from water. This separator presents significant engineering challenges. Dehydrated hydrochloric acid results in #6 which is heated in Hx3 to a temperature level for the chlorination reactor R3 where it enters as

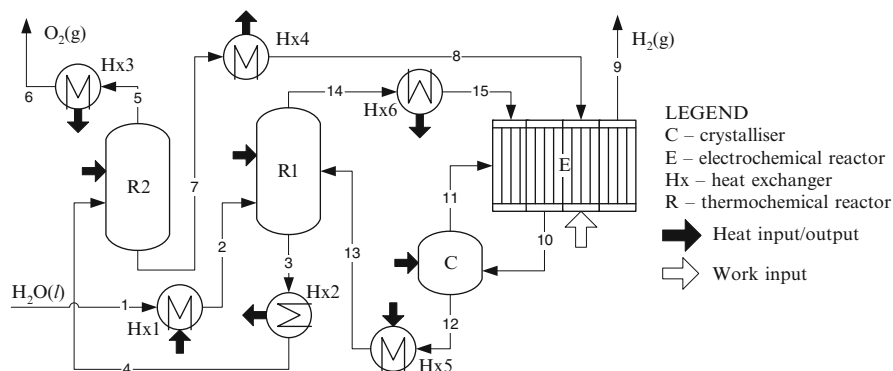


Fig. 6.7 Conceptual flowchart for Cu–Cl–4B cycle (four steps)

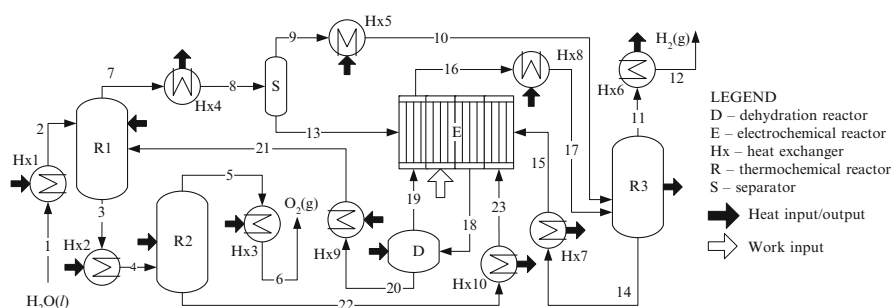


Fig. 6.8 Conceptual flowchart for Cu–Cl-5 cycle (five steps)

cuprous chloride which is collected at the bottom of R1—stream #7. Furthermore, the cuprous chloride is cooled in Hx4. It solidifies—stream #8—and it is fed to the electrochemical cell E. The electrochemical process (#7 in Table 6.2) generates a hydrogen product stream #9. In addition, the electrochemical process produces a hydrated cupric chloride output stream, namely, #10, which is directed toward a crystallization system C. The moisture is removed and dehydrated cupric chloride is obtained according to process #12 (Table 6.2). Water is returned to the electrochemical cell as stream #11. The dehydrated cupric chloride in stream #12 is heated in Hx5 and supplied as stream #13 to the hydrolysis reactor R1.

Figure 6.8 illustrates the conceptual flowchart of the copper–chlorine cycle with five steps, namely, Cu–Cl-5. This cycle comprises a hydrolysis reactor R1, a thermolysis reactor R2, a chlorination reactor R3, a dehydration reactor D, a separator S, and nine heat exchangers. Water is supplied as liquid in #1; then heated, boiled, and superheated in Hx1; and provided as gas—stream #2—to hydrolysis reactor R1. In the hydrolysis reactor, solid copper oxychloride is formed and collected at the reactor bottom as stream #3. Additional heating is supplied to the copper oxychloride stream in Hx2 prior to the supply of the thermolysis reactor

R3 as stream #4. Oxygen evolves from the thermolysis process—stream #5—which is cooled in heat exchanger system Hx3 and delivered in #6. The hydrolysis reaction also produces a gaseous mixture of hydrochloric acid and steam in #7 which is cooled in Hx4 in view of separation. It is assumed that stream #8 comprises liquid water and aqueous hydrochloric acid which are separated by a selected method (e.g., cascaded distillation) in separator S. Hydrochloric acid results as stream #9, further heated in Hx5 and supplied to the chlorination reactor R3 in a gas phase as stream #10. The chlorination process releases pure hydrogen which is extracted at #11, cooled in Hx6, and delivered as product in #12. Water from separator S—stream #13—is supplied to the electrochemical cell E. In the chlorination process, molten cuprous chloride is generated and collected at the bottom of the reactor in #14. It is further cooled and solidified in Hx7 and supplied as solid particles to the electrochemical cell in #15. The electrochemical cell disproportionates CuCl and generates particulate copper—stream #16—which is heated to the chlorination reaction temperature in Hx and supplied as stream #17 to R3. The electrochemical process also produces hydrated cupric chloride in #18 which is dehydrated in the spray drier D from which water is returned as stream #19 to the electrochemical cell E. The dehydrated cupric chloride—stream #20—is heated in Hx9 to the temperature level of the hydrolysis reaction and supplied as hot stream #21 of metallic particles to R1. The thermolysis reactor R2 produces molten cuprous chloride in #22 which is cooled and solidified in Hx10. A stream of solid CuCl particles is provided to the electrochemical cell.

Although the cycles are simplified in the figures, the actual flowcharts are more complicated as they involve additional heat exchange systems and separation systems. Heat recovery and recycling systems must be carefully designed. Also, the type and number of auxiliary devices for each chemical reactor depend on the reaction type, conversion factor, and the need for separation and chemical recycling. Physicochemical properties of chemicals—copper and chlorine compounds—must be well understood in order to effectively design the reactors, heat exchange systems, separators, and other devices. Moreover, all chemical reactions must be thoroughly analyzed based on thermodynamics and kinetics.

6.3 Physicochemical Properties of Copper and Chlorine Compounds in Cu–Cl Cycles

Four chemical elements are involved in copper–chlorine thermochemical cycles, namely, hydrogen, oxygen, chlorine, and copper. These elements form a number of chemical compounds which occur in different steps of the Cu–Cl cycle. The relevant compounds are water (H_2O), hydrochloric acid (HCl), copper oxychloride ($\text{CuO}\cdot\text{CuCl}_2$), cupric chloride (CuCl_2), and cuprous chloride (CuCl). In addition, cupric oxide (CuO) may be formed in reactions involving copper oxychloride. In this section, physicochemical properties of the main elements and compounds in the

hybrid copper–chlorine cycles are presented. Physicochemical properties relate to physical and chemical types of properties of substances. Thermophysical and thermochemical properties are included in the larger category of physicochemical properties. For example, valence and oxidation states of a chemical element are chemical properties; density is a physical property; formation enthalpy, entropy, or Gibbs free energy are physicochemical properties (also denoted as thermochemical); and specific heat, thermal conductivity, and expansion coefficient are thermophysical properties.

The main properties of chemical elements in the copper–chlorine cycle are summarized in Table 6.6. Hydrogen and its properties have been discussed extensively in Chap. 2. Oxygen and its compounds represent around 49 % by weight from the earth’s crust. It also represents nine-tenths part of water. Oxygen is very reactive; in the copper–chlorine cycle, it reacts with copper–chlorine compounds during the hydrolysis, chlorination, and oxychlorination reactions. The cost of oxygen is roughly \$1.7/N m³ (Haynes 2012). Copper is reddish in color, ductile, and malleable and it is mined from minerals such as azurite, bornite, chalcopyrite, cuprite, and malachite, and it also occurs naturally. One of the main methods of copper extraction from minerals is electrochemical. Commercial copper can be found in high purity, namely, higher than 99.999 % at a price of around \$1.5/kg (Haynes 2012). Copper has two oxidation states, namely, +1 and +2. Chlorine is largely available in nature as salt (NaCl), carnallite, or sylvite minerals. Chlorine is toxic in large quantities; it becomes fatal at 1,000 ppm but it can be detected by the human nose at as little as 3.5 ppm. Chlorine is highly soluble in water where it is used as a disinfectant. One volume of liquid water dissolves 3.1 volumes of chlorine gas at 10 °C (Haynes 2012). Chlorine is very reactive and it has four oxidation states.

Physicochemical properties of hydrogen and oxygen are well understood and predicted by advanced equations of state which are incorporated in process simulation software such as ASPEN Plus or general engineering software such as Engineering Equation Solver (EES). Some relevant properties of copper such as linear thermal expansion coefficient, density, specific heat, thermal conductivity, molar enthalpy, Gibbs free energy, and molar entropy are presented graphically as functions of temperature in Figs. 6.9 and 6.10, which are obtained by EES software. The Shomate equation is used for estimating C_p , H , S , and G as

$$\begin{cases} C_p = a_1 + a_2\theta + a_3\theta^2 + a_4\theta^3 + a_5/\theta^2 \\ H - H_0 = a_1\theta + 0.5a_2\theta^2 + 1/3a_3\theta^3 + 0.25a_4\theta^4 - a_5/\theta + a_6 - a_8 \\ S = a_1 \ln(\theta) + a_2\theta + 0.5a_3\theta^2 + 1/3a_4\theta^3 - 0.5a_5/\theta^2 + a_7 \\ G = H - T \times S \\ \theta = T/1,000. \end{cases} \quad (6.7)$$

In (6.7), a reduced temperature is used—denoted θ —which is defined based on the process temperature T in Kelvin. The molar specific quantities are expressed with (6.7) and the coefficients listed in Table 6.7. The table shows available

Table 6.6 Thermochemical properties of chemical elements in the Cu–Cl cycle

Chemical element	<i>Z</i>	Valence	Oxidation states	<i>M</i>	MP	NBP	<i>T_c</i>	ρ^0	c_p^0	S^0	ex^{ch}
Chlorine, Cl ₂	17	1, 3, 5, 7	+1, +5, +7, −1	35.4	171.7	239.1	417	3.214	33.9	2,23.1	124.0
Copper, Cu	29	1, 2	+1, +2	63.5	1,358	2,835	X	8,934	24.4	33.15	134.2
Hydrogen, H ₂	1	1	+1, −1	1	14.05	20.39	32.97	0.00898	28.8	130.7	236.1
Oxygen, O ₂	8	2	−2	16	54.36 ^a	90.2	154.6	1.31	29.4	205.1	3.97

Z atomic number, *M* molecular mass (kg/kmol), *MP* melting point, *NBP* normal boiling point (K), *T_c* critical temperature (K), ρ^0 standard density (kg/m³), c_p^0 standard specific heat (J/mol K), S^0 standard molar entropy (J/mol K), ex^{ch} molar specific chemical exergy (J/mol)

Source: Haynes (2012)

^aTriple point

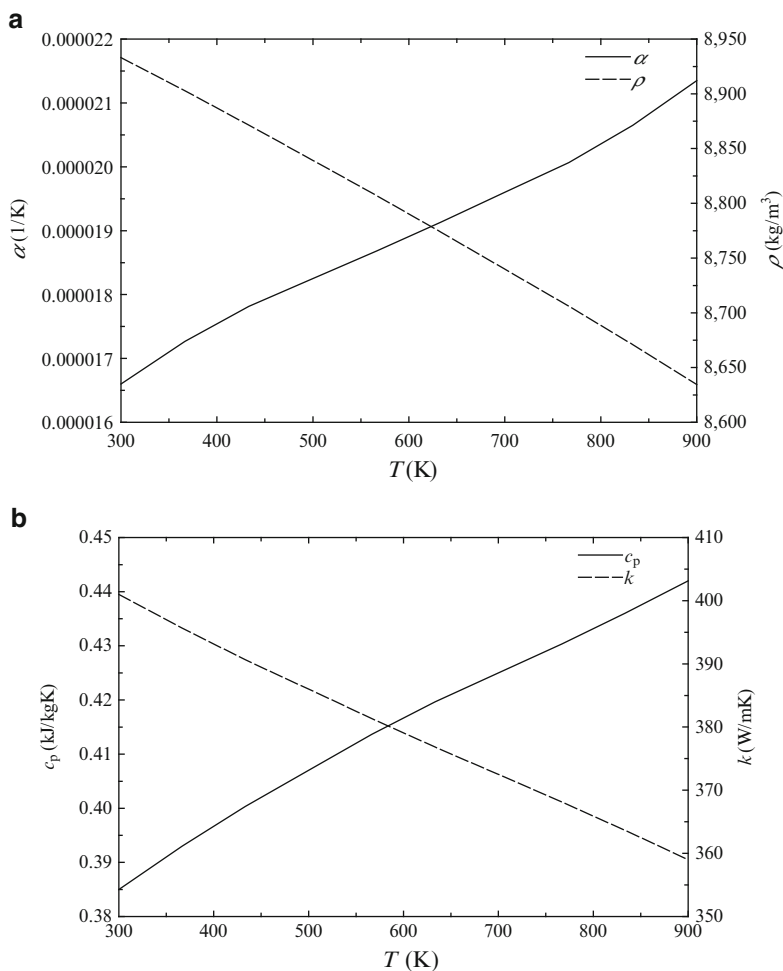


Fig. 6.9 Thermophysical properties of copper (a) thermal expansion coefficient and density, (b) specific heat and thermal conductivity

coefficients of other chemical compounds of interest. Figure 6.11 shows the variation of molar enthalpy, entropy, and Gibbs free energy of molecular chlorine (Cl_2) with temperature. Additional physicochemical properties of relevant compounds are summarized in Table 6.8.

The Shomate equation can be used for the determination of reaction enthalpies, entropies, and Gibbs free energy. However, in other cases, such as heat balance analyses of heat exchangers or other equipment when accurate estimation of specific heat is required, more rigorous models must be used. The importance of thermodynamic model selection for physicochemical properties of analyzed

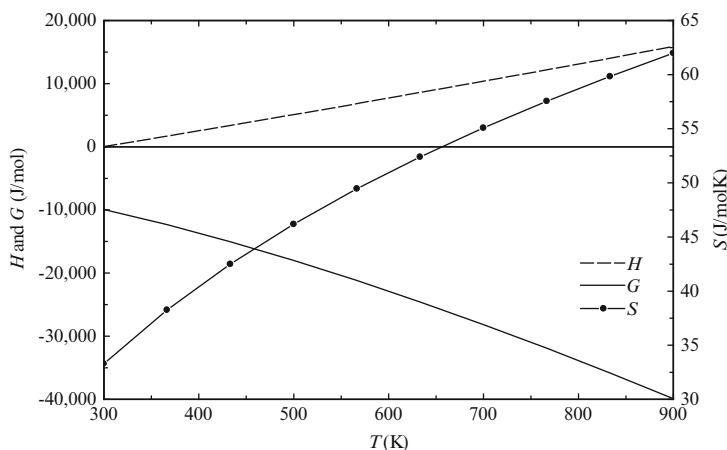


Fig. 6.10 Molar enthalpy, Gibbs energy, and entropy of metallic copper

compounds is discussed in Avsec et al. (2009) for the case of hydrochloric acid. The results predicted by the Shomate equation for the specific heat are compared with those generated by statistical thermodynamic simulations—which are considered more accurate. The results are shown in Fig. 6.12. A significant discrepancy has been observed among property data for copper oxychloride, copper oxide, and cupric and cuprous chloride from various sources. In Zamfirescu et al. (2009a), a careful selection of literature sources for thermochemical data of these compounds in modeling and design of the cycle is presented.

Two reaction processes of the Cu–Cl cycles have as a result the formation of cuprous chloride (CuCl , CAS 7758-89-6) in the form of a crystal (copper chlorination reactor), and in molten salt form (copper oxychloride thermolysis reactor). Cuprous chloride crystals occur naturally in the form of a mineral: nantokite (Stunz Class 3/A.01-10). Cuprous chloride in the solid phase has two crystalline forms: a γ cubic structure up to temperatures close to the melting point, and a β -hexagonal form up to the melting point. The properties of this chemical compound are summarized in Zamfirescu et al. (2009a).

Cuprous chloride is a salt, and molten salts are commonly assumed to be ionic liquids. However, there is little structural evidence that molten salts actually must consist of ions. As reported in Zamfirescu et al. (2009a), cuprous chloride is a molecular liquid above its melting point. Empirical equations for viscosity and thermal conductivity of low-temperature molecular liquids can be used in the absence of experimental data, whereby the low temperature of liquids is understood for temperatures between the melting point and about $T_r = T/T_c = 0.7$. For copper–chlorine cycle operation, CuCl occurs at reduced temperatures T_r of 0.1–0.4. The following equation is recommended for the dynamic viscosity (Zamfirescu et al. 2009a):

$$\mu = 0.365 \times \exp(-6.95 + 1,418/T), \quad (6.8)$$

Table 6.7 Shomate coefficients for chemical compounds in the Cu–Cl cycle

	T (K)	a_1	a_2	a_3	a_4	a_5	a_6	a_7	a_8
Cl ₂ (g)	298–1,000	33.0506	12.2294	–12.0651	4.38533	–0.159494	–10.8348	259.029	0.0
Cu(s)	298–1,358	17.72891	28.0987	–31.25289	13.97243	0.068611	–6.056591	47.89592	0.0
H ₂ (g)	298–1,000	33.066178	–11.363417	11.432816	–2.772874	–0.158558	–9.980797	172.70797	0.0
O ₂ (g)	100–700	31.32234	–20.23531	57.86644	–36.50624	–0.007374	–8.903471	246.7945	0.0
O ₂ (g)	700–2,000	31.32234	–20.23531	57.86644	–36.50624	–0.007374	–8.903471	246.7945	0.0
H ₂ O(l)	298–500	–203.606	1,523.29	–3,196.413	2,474.455	3.855326	–256.5478	–488.7163	–285.8304
H ₂ O(g)	500–1,700	30.092	6.832514	6.793435	–2.53448	0.082139	–250.881	223.3967	–241.8264
HCl(g)	298–1,200	32.12392	–13.45805	19.86852	–6.853936	–0.049672	–101.6206	228.6866	–92.31201
CuCl(s)	298–703	75.271	–26.83212	25.69156	–7.357982	–1.847747	–165.7299	174.6644	–138.072
CuCl(l)	703–3,000	66.944	–3.69 × 10 ^{–10}	2.16 × 10 ^{–10}	–3.9 × 10 ^{–11}	–9.8 × 10 ^{–12}	–151.1374	174.7653	–131.178
CuCl ₂ (s)	298–1,500	70.21882	23.36132	–14.86876	4.053899	–0.366203	–228.9405	184.6378	–205.8532
CuO(s)	298–2,000	48.56494	7.498607	–0.05598	0.013851	–0.760082	–173.4272	94.85128	–156.0632

Data from NIST (2012)

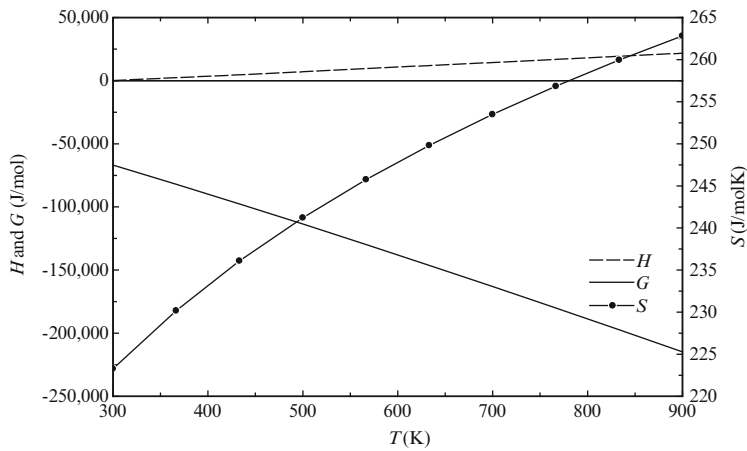


Fig. 6.11 Molar enthalpy, Gibbs energy, and entropy of molecular chlorine in the gas phase

Table 6.8 Properties of chemical compounds relevant to hybrid copper–chlorine cycles

Compound	<i>M</i>	MP	NBP	<i>T</i> _c (K)	<i>P</i> _c	ρ^0	ΔH^0	<i>S</i> ⁰	ΔG^0	ex ^{ch}
HCl(g)	36.46	158.98	188.15	324.61	8.31	1.49	−92.3 ^a	186.9	−95.3	84.73
H ₂ O(l)	18.015	0.0	99.97	647.10	22.06	997	−285.83	69.95	−237.1	0.77
CuCl(s)	98.99	703	1,485	2,435	2.65	4,139	−136.8	87.4	−119.4	75.0
CuCl ₂ (s)	134.45	871	1,266	2,010	N/A	3,400	−218.0	108.1	−173.8	82.4
CuO(s)	79.54	1,299 ^b	N/A	N/A	N/A	6,450	−156.06	42.59	−128.3	6.27
CuO–CuCl ₂	214	625 ^c	N/A	N/A	N/A	4,080	−384.65	154.3	−369.7	21.08

ex^{ch} molar specific chemical exergy (kJ/mol), *M* molecular mass (kg/kmol), *MP* melting point (K), *NBP* normal boiling point (K), *P*_c critical pressure (MPa), *T*_c critical temperature (K), ΔH^0 standard formation enthalpy (kJ/mol), *S*⁰ standard entropy (J/mol K), ΔG^0 standard Gibbs free energy (kJ/mol), ρ^0 standard density (kg/m³), *N/A* not available

Sources: Haynes (2012), Zamfirescu et al. (2010a), Parry (2008)

^aEnthalpy in solution electrolyte of HCl(aq) is −74.84 kJ/mol

^bDecomposition starts at slow rate at 1,000 K; it starts melting with simultaneous decomposition at 1,299 K

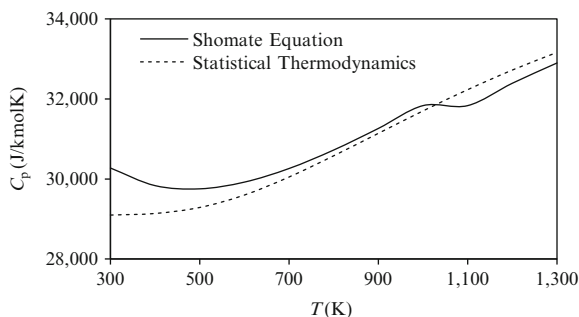
^cThere is no melting point for copper oxychloride; it starts a thermal decomposition at this temperature

where *T* is temperature in K and for the range of temperatures of interest (709–900 K), the dynamic viscosity varies from 2.6 to 1.7 mPa s. For the thermal conductivity of molten CuCl, the empirical equation presented by Zamfirescu et al. (2009a) is

$$k = 0.19 \times (1 - T_r)^{0.38} / T_r^{1/6}, \tag{6.9}$$

where *T_r* is the reduced temperature. At the melting point, the thermal conductivity of molten CuCl is estimated to be 0.21 W/mK while at 900 K, it is 0.19 W/mK.

Fig. 6.12 Comparison of specific heat estimation for HCl with Shomate equation and statistical thermodynamic-based models [data from Avsec et al. (2009)]



In Zamfirescu et al. (2009a), the vapor pressure data of CuCl are fitted by the following Riedel-like equation:

$$P_{\text{sat}} = \exp\left(273.8096 - 39,240.52/T + 0.27747 \times 10^{-5} \times T^2 - 33.261 \times \ln(T)\right), \quad (6.10)$$

where P_{sat} is in Pa and T is in K.

For a reduced temperature of 0.7 (i.e., 1,704 K), the vapor pressure calculated with (6.10) is 0.845 bar. Using this value and an estimation of the critical pressure, the acentric factor can be found. This factor is an important parameter that allows for establishing an equation of state for the fluid phase. A preliminary estimation of critical pressure, $P_c = 2.65$ MPa, can be obtained by setting $T = T_c$ in (6.10), where T_c is the critical temperature of CuCl listed in Table 6.8. The acentric factor can be calculated from its definition formula as follows:

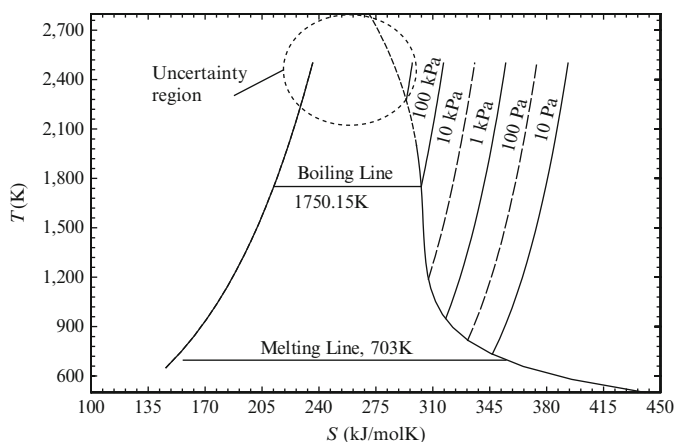
$$\begin{cases} \omega = -\log_{10}(P_{r,0.7}) - 1 \\ P_{r,0.7} = P_{\text{sat}}(T_{r,0.7})/P_c \\ T_{r,0.7} = T/T_c = 0.7. \end{cases} \quad (6.11)$$

With the estimated $P_{r,0.7} = 0.0323$, the calculated acentric factor is $\omega = 0.49$. There is a lack of data regarding the properties of the liquid phase, such as density and expansion coefficient. There is also a discrepancy in the melting point temperature, which was reported in various studies as 696, 703, and 709 K; the recommended value is 703 K (see Zamfirescu et al. 2009). High discrepancy also exists with past reported values for the boiling point: 1,763, 1,485, and 1,482 K; the recommended value is 1,485 K (Zamfirescu et al. 2009).

Development of a T – S diagram for cuprous chloride is important because this substance can have a role of a working fluid within the copper–chlorine thermochemical cycle. Cuprous chlorine has a relevant vapor pressure. Processes such as throttling, expansion with work generation, or compression of CuCl vapor may be considered within a Cu–Cl plant. The calculation of specific entropy and enthalpy at

Table 6.9 Thermodynamic functions for enthalpy and entropy as functions of pressure

Formula	Remarks
$\left(\frac{\partial H}{\partial P}\right)_T = v(1 - \alpha T)$	H —molar enthalpy, P —pressure, T —temperature, v —molar specific volume, $\alpha = \left(\frac{\partial v}{\partial T}\right)_P$ is the volumetric thermal expansion coefficient
$\left(\frac{\partial C_P}{\partial P}\right)_T = -T\left(\frac{\partial^2 v}{\partial T^2}\right)_P$	C_P —molar specific heat, defined by $C_P = \left(\frac{\partial H}{\partial T}\right)_P$
$\left(\frac{\partial S}{\partial P}\right)_T = -v\alpha$	S —molar entropy, defined by $\frac{C_P}{T} = \left(\frac{\partial S}{\partial T}\right)_P$

**Fig. 6.13** The T - S diagram of cuprous chloride (CuCl)

any given temperature and pressure can be made based on thermodynamic functions. Relevant thermodynamic functions are presented in Table 6.9.

The vapor and gas phases over the range of temperatures of interest exist at low pressures, mostly at vacuum, and high temperatures, which means that the gas and vapor can be treated as ideal gases. For an ideal gas ($Pv = RT$), one has $\alpha = 1/T$ and thus $(\partial H/\partial P)_T = 0$ and $(\partial S/\partial P)_T = -P/R$. Therefore, entropy in the vapor phase is $S(T, P) = S(T, P_0) + R \ln(P_0/P)$, and the enthalpy is $H(T, P) = H(T, P_0)$ for all phases, where P_0 is the reference pressure from thermodynamic tables. The estimated T - S diagram of CuCl is shown in Fig. 6.13. The Riedel equation (6.10) has been extrapolated outside of the range of pressures. However, at higher pressures, the uncertainty of the vapor pressure and the vapor line cannot be accurately quantified.

The recommended correlations for density of CuCl, CuO, and CuO·CuCl₂ are listed in Table 6.10. The density of solid CuCl₂ is listed in Table 6.8 for standard temperature.

The cupric chloride is produced in the electrolysis step of the Cu–Cl cycle, where copper is extracted electrochemically from solid cuprous chloride (CuCl). Cupric chloride is produced in its hydrated form (CuCl₂· n H₂O), which may be dried or crystallized (depending on the cycle version). Cupric chloride may result in one

Table 6.10 Recommended density correlations for CuCl, CuO, and CuO-CuCl₂

Compound	Density correlation	Validity range (K)
CuCl(s) (γ-crystal)	$\rho = \rho_0 \times \exp(0.000415281 - 0.0000311T + 1.082325 \times 10^{-7}T^2)$, $\rho_0 = 4,136 \text{ kg/m}^3$	273–687
CuCl(l)	$\rho = \rho_m + 0.000769 \times (T - 728)$, $\rho_m = 3,692 \text{ kg/m}^3$	728–883
CuO(s)	$\rho = \rho_0 \times (a + bT + cT^2)$; $\rho_0 = 6,450 \text{ kg/m}^3$	298–675
CuO-CuCl ₂ (s)	$a = 1.01143$, $b = 9.3396 \times 10^{-5}$, $c = 1.91537 \times 10^{-7}$	298–675
	$\rho = \rho_0 \times \exp(a\Delta T + b\Delta T^2)$; $\Delta T = T - 298.15$; $\rho_0 = 4,080 \text{ kg/m}^3$	
	$a = -2.660832 \times 10^{-24}$, $b = -1.221274397 \times 10^{-13}$	

Note: Density values are in kg/m³
Source: Zamfirescu et al. (2009a)

of the possible decomposition products (undesired) of copper oxychloride in the thermolysis reactor.

In hydrolysis or oxychlorination reactors, cupric chloride is used as a reactant. Cupric chloride has the Chemical Abstract Service (CAS) number CAS-7447-38-4 and occurs naturally in mineral form—known under the name tobachite—and called Strunz Class 3/A.07-30. Under atmospheric conditions, cupric chloride releases chlorine at 766 K, while at 1,266 K, it starts boiling and begins decomposition to form Cu_2Cl_2 .

Cupric chloride has a solid–solid transition at 675 K and a solid–liquid transition at 871 K. There is a γ -crystal which exists at 398–685 K. At 685 K, there is a phase transition between γ and β crystals accompanied by a latent heat release of 6 kJ/mol (see Avsec et al. 2009). The melting occurs at 696 K with a latent heat of melting of 7.08 kJ/mol (Avsec et al. 2009).

Cupric oxide (CuO) may be one of the decomposition by-products (undesired) of copper oxychloride. The knowledge of its properties is important in conjunction with the modeling of copper oxychloride decomposition and cupric chloride hydrolysis or oxychlorination processes. Cupric oxide is a recorded chemical (CAS 1317-38-0) and mineral (tenorite, Strunz Class IV/A.05-10). Solid cupric oxide is a gray-black monoclinic crystal having a density of 6,450 kg/m³ and Vickers hardness of 190–300 kg/mm². At high temperatures (over 1,000 K), cupric oxide decomposes into cuprous oxide (Cu_2O) and releases oxygen. This aspect is important for the study of thermal decomposition of copper oxychloride. Recent experiments showed that the heat capacity is highly influenced by the uncommon magnetic behavior of cupric oxide at high temperatures (see the literature review compiled by Zamfirescu et al. (2010a), Table 3). Due to magnetic components influencing the internal energy of a crystalline structure, the specific heat is almost constant between 600 and 700 K and it slightly decreases after 750 K.

One of the key substances in the hydrolysis reactor is copperoxychloride ($\text{CuO}\cdot\text{CuCl}_2$ or also denoted with Cu_2OCl_2). This is a classified mineral, melanothallite (Strunz Class III/D.01-60), which is part of the category of oxyhalogenides. It has an orthorhombic, dipyramidal crystalline structure with interlaced atoms of copper, chlorine, and oxygen. Limited experimental determinations of copper oxychloride have been published in the archival literature. There is no critical point of copper oxychloride because it decomposes thermally and releases oxygen. According to Parry (2008), the thermal decomposition of copper oxychloride starts at ~625 K. Copper oxychloride is a coordination complex with a Fddd *ortho*-rhombing cell. The determination of the standard enthalpy of formation of oxychloride has been performed in a reaction calorimeter, as reported by Parry (2008). Kinetic analyses of copper oxychloride synthesis and decomposition are presented in Lewis et al. (2003).

As it results from the analysis presented in Zamfirescu et al. (2009a), the specific heat of copper oxychloride at 298.15 K is 116.77 kJ/mol which agrees well with theoretical estimations and modeling. In Zamfirescu et al. (2009a), the estimation of specific heat at 298.15 K is made with the “element contribution method” by

$$C_p = \sum_{i=1}^N N_i \Delta E_i, \quad (6.12)$$

where N_i represents the number of atoms of species i , N is the total number of atomic species in the molecule, and ΔE_i is the contribution of each atomic species. According to the details given in Zamfirescu et al. (2009a), each copper atom has a contribution of $\Delta E_{\text{Cu}} = 26.92 \text{ kJ/kmol K}$. An oxygen atom contributes with $\Delta E_{\text{O}} = 13.42 \text{ kJ/kmol K}$ and the atom of chlorine with $\Delta E_{\text{Cl}} = 24.69 \text{ kJ/kmol K}$. The prediction accuracy of (6.12) is about $\pm 10 \%$.

Specific heat measurements at high temperatures are available only from Parry (2008). The value at 673 K is 114 kJ/kmol K . Using data from measurements, the following Debye–Einstein correlation for specific heat has been developed by Parry (2008) for a temperature range of 14–700 K:

$$C_p(T) = 3R \left[\frac{13.962}{\theta_D^3} \int_0^{\theta_D} \frac{x e^x}{(e^x - 1)^2} dx + 0.945 \theta_E^2 \times \frac{e^{\theta_E}}{(e^{\theta_E} - 1)^2} \right], \quad (6.13)$$

where R is the ideal gas constant, $\theta_D = T_D/T$ is the dimensionless temperature calculated with $T_D = 373.41 \text{ K}$ (Debye temperature), $\theta_E = T_E/T$ is calculated with the Einstein temperature, $T_E = 1,193 \text{ K}$, and T is temperature in K.

Since copper oxychloride is not commercially available, methods of synthesis are needed. The method adopted by Ikeda and Kaye (2008) involved the use of stoichiometric amounts of CuO and CuCl_2 . The process was carried out in a glove box under argon to avoid the presence of moisture. The reaction was performed in a sealed quartz ampoule with precursors (CuO and CuCl_2), dried overnight under $5 \times 10^{-8} \text{ mbar}$ vacuum at ambient temperature, and then inserted into a tubular oven. Crystal growth was achieved by holding the ampoule at 718 K for 2 days. The sample appeared as small black crystalline lumps that broke up easily when shaken with no visible CuCl spots. Characterization and synthesis of copper oxychloride are also reported in Nixon et al. (2011).

Trevani (2011) prepared copper oxychloride in a conventional horizontal tube furnace with a quartz tube and stainless-steel connections for gas injection. The copper precursor, CuCl or CuCl_2 , was loaded into an alumina crucible and exposed to a flow of high-purity dry air at 643 K for 48 h. Analysis with the XRD method confirmed that highly pure copper oxychloride samples were obtained. The method is easily scalable and it can be used to produce the amounts required for large-scale oxygen production experiments. Figure 6.14 illustrates the copper oxy- and hydroxyl-chloride samples obtained at UOIT and reported by Naterer et al. (2011b).

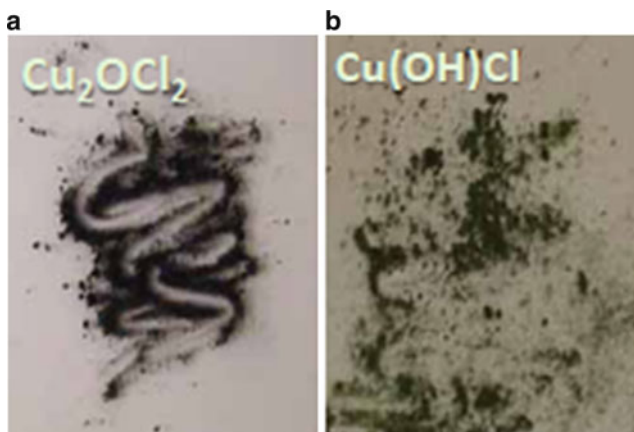


Fig. 6.14 Copper oxychloride powder (a) and side product Cu(OH)Cl obtained at UOIT (courtesy of Prof. L. Trevani)

6.4 Electrochemical Step in the Hybrid Copper–Chlorine Cycles

6.4.1 Classification of Electrochemical Cells

The electrochemical process within the Cu–Cl cycle has several variants depending on the cycle version and the type of membrane used within the cell. The cell can produce at the cathode either metallic copper or molecular hydrogen; also one can use a cation exchange membrane (CEM) that conducts protons or an anion exchange membrane (AEM) conductive to chlorine ions. Regardless of the cell variant, the anodic half-cell reaction is the same for all cases. Hydrochloric acid must be present in the anolyte and catholyte where it has multiple roles.

- It impedes precipitation of CuCl which otherwise is sparingly soluble in water.
- It facilitates complexation of copper ions with water molecules with an eventual formation of a hydrated cupric chloride within the catholyte.
- It contributes to an ionic balance in electrolyte, being either a source of protons or Cl^- .

Table 6.11 categorizes the electrochemical cell variants based on the half-cell reaction at the cathode and the type of membrane. A coded identification of the cell type is also proposed for presenting them in this chapter. The cell variants are illustrated schematically in Fig. 6.15. The cell variants are given as follows.

- Cu-Cl^- , see Fig. 6.15a which produces copper at the cathode and it has an AEM permeable to chlorine ions.
- Cu-H^+ , see Fig. 6.15b which produces copper at the cathode and it has a CEM permeable to protons.

Table 6.11 Electrochemical cell classifications based on cathodic reaction and membrane type

ID	Electrolyte/membrane processes	Anodic reaction	Cathodic reaction	Overall ^a
Cu-Cl ⁻	AEM (Cl ⁻)	2CuCl + 2Cl ⁻ → 2CuCl ₂ + 2e ⁻	2CuCl + 2e ⁻ → 2Cu + 2Cl ⁻	Process #1
Cu-H ⁺	Anolyte: 2HCl → 2H ⁺ + 2Cl ⁻ CEM (H ⁺) Catholyte: 2H ⁺ + 2Cl ⁻ → 2HCl			
H ₂ -Cl ⁻	AEM (Cl ⁻)	2H ⁺ + 2e ⁻ → H ₂	2H ⁺ + 2e ⁻ → H ₂	Process #7
H ₂ -H ⁺	Catholyte: 2HCl → 2H ⁺ + 2Cl ⁻ Anolyte: 2HCl → 2H ⁺ + 2Cl ⁻ CEM (H ⁺)			

ID cell identification, the cell is identified by the product obtained at the cathode, namely, Cu or H₂, and by ionic species transferred between the anode and cathode, namely, Cl⁻ or H⁺

AEM anion exchange membrane, *CEM* cation exchange membrane

^aOverall process as described in Table 6.2

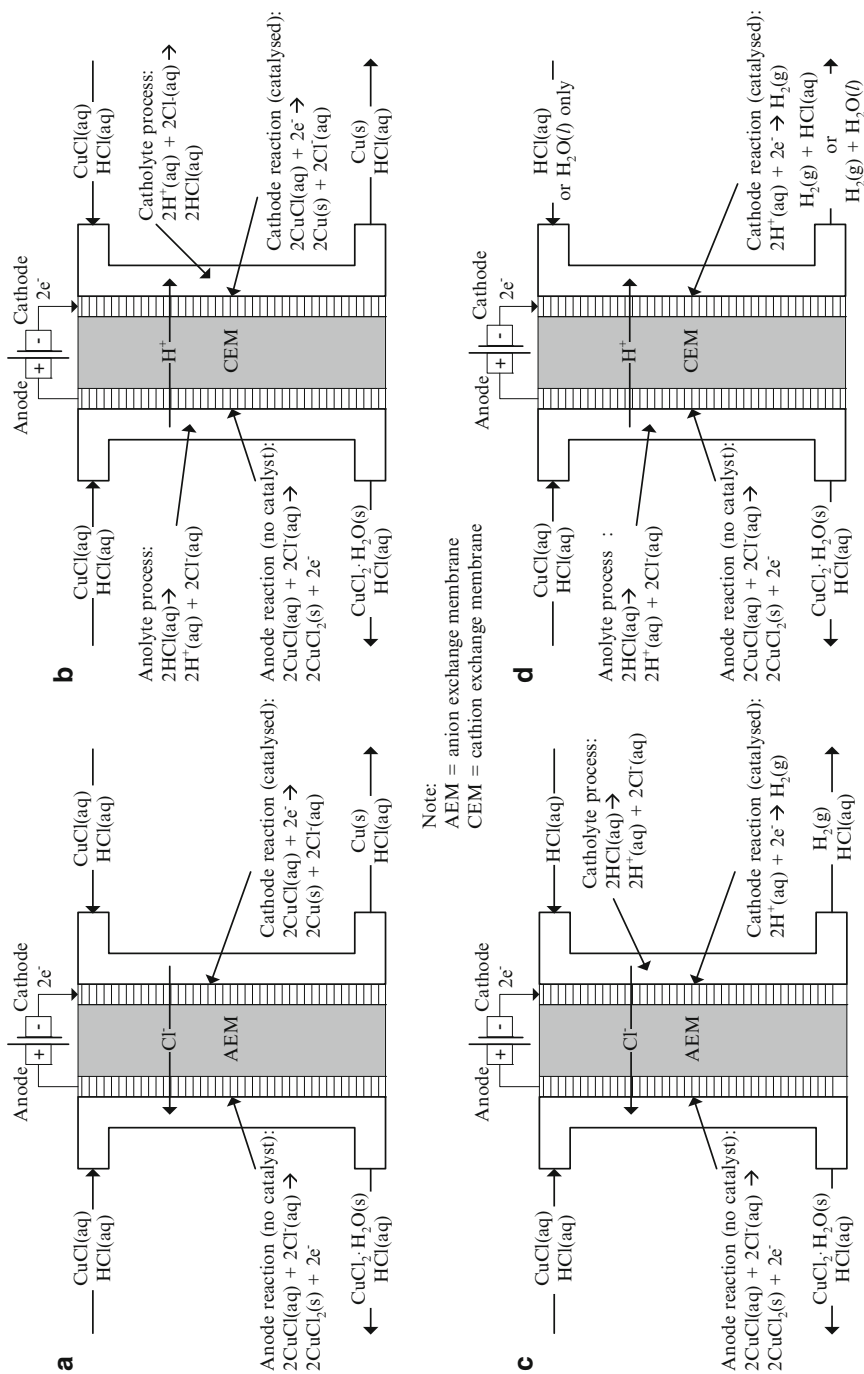


Fig. 6.15 Electrochemical cell variants encountered in copper–chlorine cycles. (a) Cell ID: Cu-Cl^- , (b) Cell ID: $\text{H}_2\text{-H}^+$, (c) Cell ID: Cu-Cl^- , (d) Cell ID: $\text{H}_2\text{-Cl}^-$

- $\text{H}_2\text{-Cl}^-$, see Fig. 6.15c which produces hydrogen gas at the cathode and it has an AEM permeable to chlorine ions.
- $\text{H}_2\text{-H}^+$, see Fig. 6.15d which produces hydrogen gas at the cathode and it has a CEM permeable to protons.

Note that the cells Cu-Cl^- and Cu-H^+ conduct the disproportionation process #1 while the $\text{H}_2\text{-Cl}^-$ and $\text{H}_2\text{-H}^+$ cells conduct the HCl/CuCl electrolysis process #7 (see Table 6.2). It was found that the anodic reaction does not require a catalyst but rather an electrode with a large exposed surface. The cathodic side however requires catalysts, in general platinum based. The membrane poses important technical challenges; the main problem is the undesired crossover of ionic species.

The anodic reaction—common for all cells—is a non-catalytic electrochemical process in which aqueous cuprous chlorine combines at the electrode surface with a chlorine ion, forms cupric chloride, and releases two electrons to the anode. The cupric chloride forms the complexation product $\text{CuCl}_2 \cdot n\text{H}_2\text{O(s)}$ which is retrieved from the anolyte exit stream.

The cathodic reaction for the Cu-Cl^- cell consumes aqueous cuprous chloride and electrons (provided at the cathode surface) and generates metallic copper particles (with a dendritic structure) and chlorine ions. Chlorine ions cross the membrane and become consumed in the anodic reaction. The cell Cu-H^+ requires two additional processes which occur spontaneously in the anolyte and catholyte, respectively. Due to the high hydrochloric acid concentration, both the anolyte and catholyte are used as a source of protons and chlorine ions. In the anode side, the anolyte gives the chlorine ions that are required for the cathodic reaction, while the protons cross through the membrane to the cathodic side where they combine spontaneously in the catholyte to form aqueous hydrochloric acid. Overall, in the Cu-H^+ cell, hydrochloric acid is consumed at the anode side and produced at the cathode side.

For both copper-producing electrochemical cells— Cu-Cl^- and Cu-H^+ —there is a substantial challenge with the handling of metallic Cu generated at the cathode. As discussed in Ranganathan and Easton (2010a), electrowinning of copper from a solution of chloride is plagued by the copper growth as dendritic structures can physically tear the membrane leading to catastrophic cell failure. It is also complicated to remove the precipitated metallic copper from the cathode side.

The process in cell $\text{H}_2\text{-Cl}^-$ uses the catholyte as a source of chlorine and protons which result from a spontaneous dissociation of HCl molecules. Chlorine ions cross from the cathode side to the anode side where they are consumed in the reaction of cupric chloride formation, while the protons are reduced at the cathode surface. In cell $\text{H}_2\text{-H}^+$, the process of proton generation takes place in the anolyte—sourced from HCl . Protons cross the membrane and reach the cathode side where they are reduced at the electrode surface. At the same time, chlorine ions from anolyte enter into the anodic reaction. Thus, hydrochloric acid is consumed at the anodic side of $\text{H}_2\text{-H}^+$ cell, while for the $\text{H}_2\text{-Cl}^-$ cell, it is consumed at the cathode side.

Although with cells $\text{H}_2\text{-Cl}^-$ and $\text{H}_2\text{-H}^+$ the problems caused by copper electro-winning are eliminated, these cells pose a major technological challenge due to occurrence of a copper crossover process. Copper crosses through membranes

whether as ions (if a CEM is used) or as a complex in the aqueous solution. Due to the copper complexation process at the anode side, copper complexes in the aqueous phase exist. Such complexes can cross the AEM. The occurrence of ionic copper or copper complexes to the cathode side leads to the unavoidable formation of metallic copper, which greatly reduces the activity of catalysts and leads to a significant decrease of cell performance. This is therefore a topic of intense research to find a suitable membrane that impedes copper crossover in the hydrogen-producing electrochemical cell (see Naterer et al. 2011a).

6.4.2 *Electrode Development for Anodic and Cathodic Reactions*

The anodic side half-reaction is essentially the same for all possible cell configurations. It has been extensively studied by Easton et al. at UOIT (see Ranganathan and Easton 2010a, b) and at AECL (Stolberg et al. 2008). Half-cell experiments with various electrodes were performed at UOIT using a standard three-electrode cell arrangement comprising a saturated calomel reference electrode (SCE), a platinum wire counter electrode, and the anode. The aim of the experiment was to determine a better structure for the anode electrode characterized by high current densities and reduced over-potentials. Electro-catalysts are not required; this has been confirmed by Suppiah et al. (2009) at AECL. Data for stirred and quiescent electrolytes were obtained at 298 K. The anodic half-reaction occurs as



AECL measured the equilibrium potential for reaction (6.14) which was reported in Stolberg et al. (2008) to be 0.237 V. The most promising results obtained at UOIT were with ceramic carbon electrodes (CCE) based on poly-aminopropyl siloxane (PAPS), as described in Ranganathan and Easton (2010b) by using a base-catalyzed sol-gel method. A precursor 3-aminopropyl trimethoxy silane (APTMS) was combined with carbon black (type Vulcan XC72) in a methanol–water solution with ammonium hydroxide addition, which catalyzed the polymerization process of APTMS. A gel was obtained and coated on a strip of 1 cm² of carbon fiber paper (CFP) type TPGH-090 (from BASF), which was subsequently dried at room temperature for 6 h, followed by drying in an oven at 80 °C for 12 h. Two types of electrodes were prepared in this way: single-face coated and double-face coated. The coating deposition was of 2.7 mg/cm². The weight percent of PAPS in CCE was determined by thermogravimetric analysis and 36 %. Figure 6.16 shows a photo and microscopy photo of the electrode and its coated surface. The surface is visualized through scanning electron microscopy (SEM). The figure shows that the CCE layer is a uniform three-dimensional structure with high porosity and large surface area.

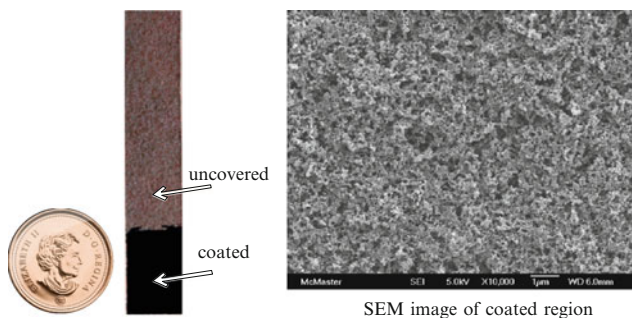
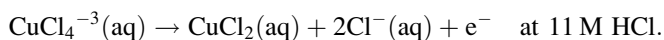
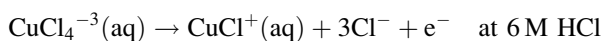


Fig. 6.16 CCE-PAPS anodes obtained at UOIT (courtesy of Prof. B. Easton)

Ranganathan and Easton (2010a) determined the current density vs. voltage diagrams for the half-cell reaction with respect to SCE. Three types of experiments were performed: with uncovered CFP electrode, with single-side coated CFP and double-side coated CFP. The measurements were performed in solutions of 3 and 6 mol/L HCl concentration and 1, 10, and 100 mmol/L CuCl concentration. At 100 mmol/L CuCl, the current saturation has been observed, which indicates mass transport limitation. It was also observed that the cell performance decreased at higher concentrations of HCl (the current density at saturation decreased by ~20 %). The impact of HCl concentration on reaction kinetics is explained by the influence of dissolved CuCl species. The following main species are generated when cuprous chloride is dissolved in an aqueous solution of hydrochloric acid: $\text{CuCl}(\text{aq})$, $\text{CuCl}_2^{-1}(\text{aq})$, $\text{CuCl}_3^{-2}(\text{aq})$, and $\text{CuCl}_4^{-3}(\text{aq})$. In addition, at higher HCl concentrations, the following species may be present: $\text{Cu}_2\text{Cl}^{-}(\text{aq})$, $\text{Cu}_2\text{Cl}_2(\text{aq})$, and $\text{Cu}_2\text{Cl}_3^{-1}(\text{aq})$. Therefore, in addition to the oxidation reaction (6.14), the following concurrent reaction may occur (see Naterer et al. 2011a):



Since Cu(II) occurs at higher concentrations of HCl, the ionic species have a larger size, they are less mobile, and the convection limitation of kinetic current occurs faster than for the case when HCl concentration is reduced. From experimental data, for similar experimental conditions, the catholyte copper species concentration decreases with increasing HCl concentration. In 6 mol/L HCl, the CuCl^{+} that is formed can be transported across the membrane by diffusion and migration. In 11 mol/L HCl solution, the CuCl_2 and HCl are transported across the membrane by diffusion only. Nonetheless, in highly concentrated solutions of HCl, the neutral and cationic species of copper mono and bivalent are lower, thereby facilitating a reduced crossover rate.

Polarization curves for the anodic reaction were obtained by Ranganathan and Easton (2010a, b) with CCE electrodes as well as bare CFP electrodes. The results

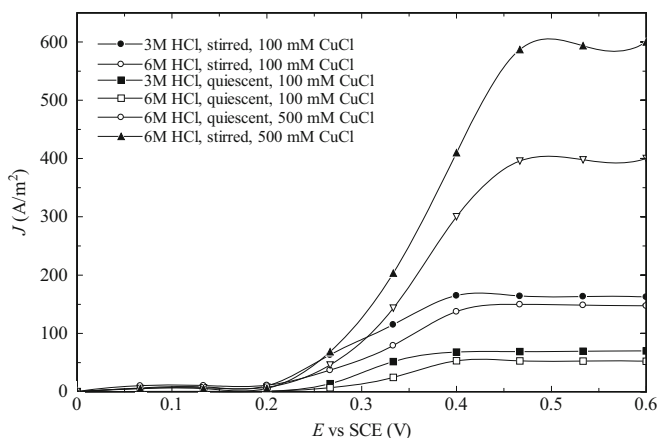


Fig. 6.17 Polarization curve for anodic reaction with a solution of 100 mmol/L CuCl using CCE electrodes prepared at UOIT [data from Ranganathan and Easton (2010a); cubic spline data smoothing is applied]

show the net improvement of CCE electrodes. Figure 6.17 presents the polarization curves for double-side coated electrodes (CCE) having a total exposed area (two sides) of 2 cm². The experiments were performed in a solution of 100 mmol/L CuCl. Data was obtained for 3 mol/L HCl and 6 mol/L HCl in stirred and quiescent solution. The results show that the half-cell potential corresponding to the current saturation is around 0.4–0.5 V. The maximum current density is around 600 A/m² with the corresponding over-potential for the half-cell reaction at the anode ~0.2 V.

At around 6 mol/L HCl, the electric conductivity of the aqueous HCl solution reaches a maximum. Under quiescent conditions for 6 mol/L HCl solution, the following saturation current is obtained experimentally by Ranganathan and Easton (2010a): 0.15, 0.8, 11.2, and 80 mA for CuCl concentrations of 1, 10, 100, and 500 mmol/L, respectively. If the electrolyte is stirred, the following saturation currents are reported: 0.34, 2.7, 30, and 120 mA for the mentioned CuCl concentrations, respectively. The analysis presented graphically in Fig. 6.18 demonstrates that the saturation current density increases quasi-linearly with molarity of cuprous chloride. If experimental data is extrapolated to 1 mol/L CuCl, it appears that the current density with a stirred anolyte surpasses 1,000 A/m², which is promising.

According to Stolberg et al. (2008), AECL performed full-cell experiments which confirm that a current density higher than 1,000 A/m² is achievable when 6 mol/L HCL anolyte is used with 1 mol/L CuCl molarity. The half-cell tests at AECL were performed with a catalyst-free graphite separator plate (GSP), coated GSP with Pt/XC-72R catalyst mixture, catalyst-free CFP type EC-TP1-060, and platinized CFP and coated CFP with Pt/XC-72R catalyst. The analyte was stirred and a solution of 1 mol/L CuCl/6 mol/L HCl has been used. The results show that a catalyst-free GSP performs the best with a saturation current density of 1,200 A/m² at 0.5 V polarization, which is a 0.263 V anodic over-potential.

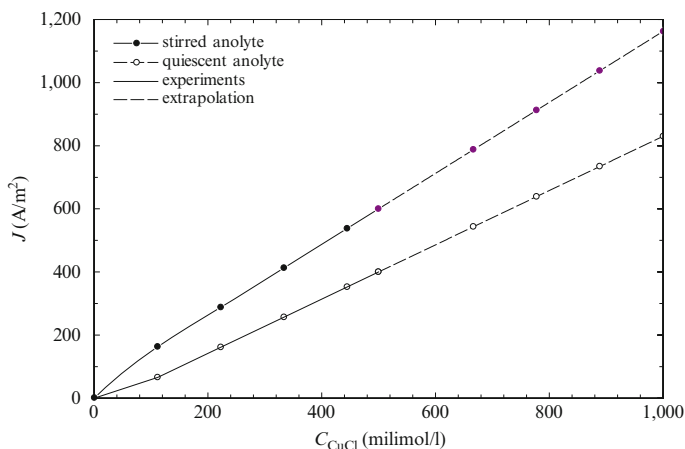


Fig. 6.18 Dependence of anodic saturation current density on CuCl molarity in a 6 mol/L HCl electrolyte based on experiments by Ranganathan and Easton (2010a) and extrapolation

AECL focused mainly on the development of the electrochemical cell for CuCl/HCl electrolysis to generate hydrogen and hydrated cupric chloride (Suppiah et al. 2009). An essential part of the research involves development of advanced electrodes for the cathode. The cathodic half-cell reactions were studied in a three-electrode electrochemical cell. The reference electrode of the half-cell was the SCE while the counter electrode was a graphite rod.

The tested electrodes for the cathode were fabricated by deposition of various platinized catalysts on a CFP type EC-TP1-060 Toray. The application of platinized catalysts was done by painting or direct spraying. The cathodic reaction was carried out in HCl (20 % by weight). The following coatings were applied:

- Electrode #1: Pt/XC-72R catalyst mixture with Pt loading of 19 % painted on graphite
- Electrode #2: Pt deposited on CFP type TGP-H-060 (Toray)
- Electrode #3: Pt/CV-72R catalyst mixture deposited on CFP type EC-TP1-060
- Electrode #4: Catalyst-free graphite
- Electrode #5: Catalyst-free CFP type EC-TP1-060

The polarization curves obtained at AECL with these electrodes #1 to #5 as cathodes are presented in Fig. 6.19. The best cathode is electrode #1 which shows 1,000 A/m² at 0.33 V polarization vs. SCE. Catalyst-free electrodes cannot be used for the cathode side reaction. Copper deposits on the cathode surface. AECL observed visually the copper deposits on the cathode after dismantling their single cell which had a cathode with 25 cm² area.

The metallic copper deposits can be observed in Fig. 6.20. A proprietary cell (described subsequently) was developed at AECL. This cell showed no (or very limited) copper crossover. A specimen has been extracted from the electrode of the cell after experimental tests. The Pt-based electro-catalyst structure was analyzed

Fig. 6.19 Polarization curves for cathode obtained at AECL with various electrodes [data from Suppiah et al. (2009)]

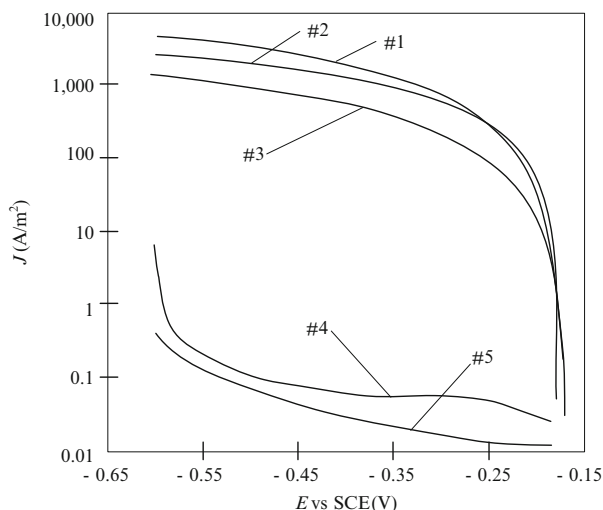
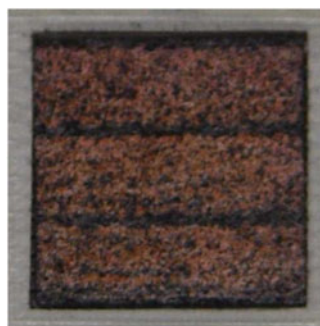


Fig. 6.20 Copper deposits on a 25 cm² cathode (courtesy of AECL)



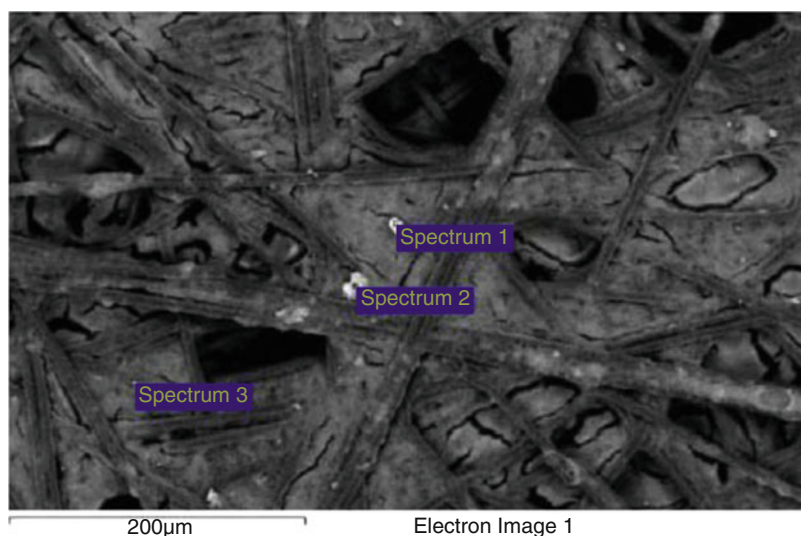
with the help of a SEM and energy-dispersive X-ray spectroscopy (EDX). The technique of EDX characterizes the atomic composition of interactions between electromagnetic radiation and matter, by analyzing X-rays emitted by the sample in response to impact by charged particles. The results regarding the spectrum of atomic percentages are presented in Table 6.12, while the image obtained by the SEM is shown in Fig. 6.21. The figure shows the locations for each of the spectra listed in Table 6.12. Copper was not found in the crystal-free regions of the electro-catalyst.

Balashov et al. (2011) showed that it is not necessary that the cathodic reaction is conducted with a high concentration of hydrochloric acid. It can be conducted simply in water which can maintain the proton transport. These researchers reported encouraging experimental results obtained with water as the catholyte. The results were obtained in a full-cell water electrolysis system which used a proprietary membrane–electrode assembly (MEA) of which cathode materials were undisclosed. The MEA used by Balashov et al. (2011) was a commercial type HYDRion 115 and HYDRion 117 produced by Electrochem Inc. Another conceptual system

Table 6.12 Spectrum of atomic percentages at three locations (see Fig. 6.21)

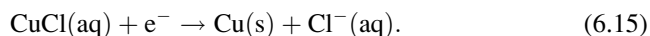
Element	Spectrum number (atomic %)		
	#1	#2	#3
C	88.93	90.99	90.65
O	3.11	1.62	N/A
F	7.09	5.20	8.89
Al	N/A	0.09	N/A
Si	0.03	N/A	N/A
S	0.30	0.70	0.22
Cl	0.19	0.66	N/A
Cu	0.05	0.10	N/A
Pt	0.30	0.64	0.15

Source: Naterer et al. (2011a)

**Fig. 6.21** SEM/EDX image of the Pt electro-catalyst for cathode used by AECL (courtesy of AECL)

which uses a nonaqueous catholyte made of acetonitrile or dimethylformamide solvents was proposed by Zamfirescu et al. (2012).

The cathode process in electrochemical cells with Cu-Cl^- and Cu-H_2 generates metallic copper at the cathode according to the half-reaction as



Electrowinning technology recommends the use of carbon electrodes at the cathode because copper precipitates as dendritic powder. The anolyte with aqueous cuprous chloride is fed at the bottom of the cathode compartment and the product stream is extracted from the top side. This type of process has been studied in past

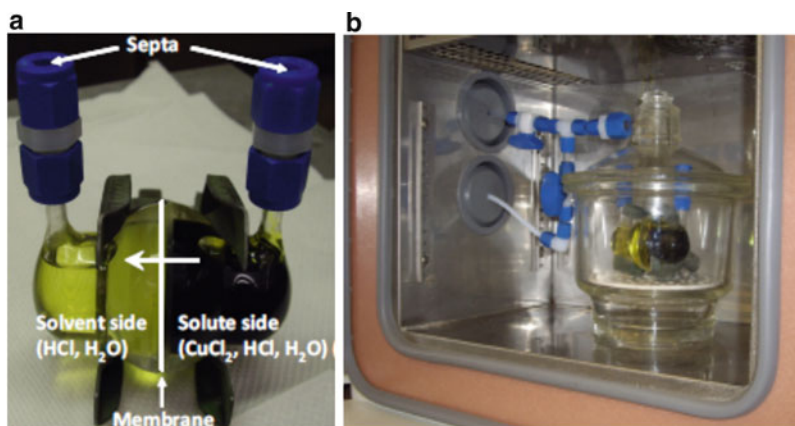


Fig. 6.22 Permeability experimental apparatus at Argonne National Laboratory: (a) permeability cell and (b) arrangement of the cell in a thermostated furnace (courtesy of ANL)

seminal work by Lewis et al. (2003) which reported the formation of dendritic copper powder at the cathode with sizes from 3 to 100 μm . It appears that the development of copper-producing electrochemical cells for the copper–chlorine cycle has been set aside by most of the researchers because the alternative hydrogen-producing electrochemical process appears to be more competitive.

6.4.3 Membrane Development

As depicted in Fig. 6.15, two types of membranes have been studied for electrochemical cell development, namely, an AEM and CEM. Although CEMs appear attractive because they can impede cationic copper species to migrate to the cathode side, there has been no research reported for their use within the Cu–Cl cycle. The focus of researchers has been toward the development of AEMs which are resistant to copper crossover (Naterer et al. 2011a).

The ANL, GTI (De Plaines, IL), Pennsylvania State University (PSU), and AECL collaborated in finding and testing proton-selective membranes with lower rate of diffusion/migration for copper species. ANL developed a diffusion cell system for testing membrane permeability. The cells comprise a solute-rich compartment and a solvent-rich compartment between which the membrane is interposed. The cell used by ANL is shown in Fig. 6.22a. During the tests, the cell was placed in a thermostated furnace where the temperature was kept constant at an imposed value. Because the cell emits gaseous hydrochloric acid during the experiments, it must be safely vented. Therefore, the cell was placed in a secondary enclosure with argon purge and venting lines. The arrangement of a cell in the furnace is shown in Fig. 6.22b.

Table 6.13 Membranes tested at various institutions

Investigator	Membrane	Remarks
ANL/AECL	NAFION 117	This is a reference membrane trademark of Du Pont Du Nemours.
PSU/ANL/AECL	S-Radel	Polysulfonate membrane based on the commercially available polymer from Solvay Advanced Polymers Radel NT 5500.
	CEM IEC 2.0	Cross-linked polysulfone membrane. IEC = 2.5 was also tested.
GTI/ANL	CM2-base	Consists of a double layer of Nafion. The membranes were treated to improve wettability and remove skin effects by an etching process.
	GC2hydromod	Based on commercially available membranes. No heat treatment before testing.

Table 6.14 Measured permeability to CuCl_2 and proton conductivity of selected membranes

Membrane	δ (cm)	σ (S/cm)	K (cm^2/s)	σ/K ($\text{S s}/\text{cm}^3$)
Nafion 117	0.020	0.0840	4.6×10^{-7}	1.8×10^5
CG2	0.003	0.0054	9.4×10^{-10}	57×10^5
CEM (IEC = 2.0)	0.01	0.038	2.1×10^{-8}	18×10^5
CM2-base	0.035	0.083	5.8×10^{-9}	143×10^5

Note: δ membrane thickness, σ membrane proton conductivity, K membrane permeability to CuCl_2 , σ/K is called membrane selectivity, namely, the ratio of conductivity and permeability Data from Naterer et al. (2011a)

A buffer solution comprising 1 mol/L CuCl_2 dissolved in 10 mol/L $\text{HCl}(\text{aq})$ was placed in the solute side compartment of the permeability cell (see Fig. 6.22a). In the other cell—solvent side—a solution of 10 mol/L $\text{HCl}(\text{aq})$ exists. The diffusion process allows various species to pass through the membrane and consequently the solvent side concentrates in CuCl_2 . ANL determined the CuCl_2 concentration at the solvent side by UV/visible light spectroscopy analyses. The CuCl_2 concentration in the buffer solution at the solute side has been assumed constant in time. The CuCl_2 concentration measurements were performed at several time instances such that the permeability could be determined as a function of time. Two sets of measurements were performed at ANL, namely, one at ambient temperature and the other at 353 K. It was observed that the permeability at 353 K is higher than at ambient temperature in all tests. The measurements at ambient temperature included a test of a commercial NAFION 117 membrane for which the permeability has been found to be $K = 1.3 \times 10^{-8} \text{ cm}^2/\text{s}$. The permeability of NAFION 117 to CuCl_2 has been proposed by ANL as a reference value and a target was set to develop proton-selective membranes with a permeability to CuCl_2 reduced to one-tenth of NAFION 117; thus the permeability target is $K = 1.3 \times 10^{-9} \text{ cm}^2/\text{s}$ (Naterer et al. 2011a).

Table 6.13 shows membranes tested at ANL, AECL, PSU, and GTI for CuCl_2 permeability. The main results regarding the permeability are listed in Table 6.14.

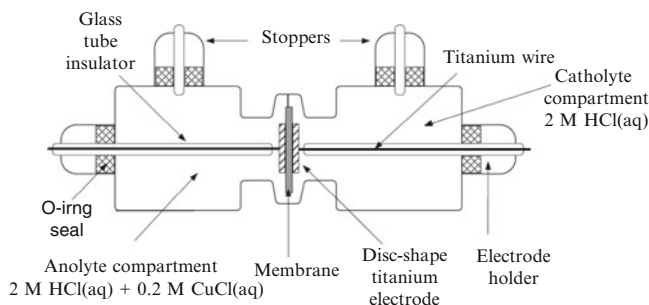


Fig. 6.23 Schematic of the custom-made “clip”-type two-probe conductivity cell used in proton conductivity tests of membranes performed at PSU (modified from Balashov et al. 2011)

Some of the membranes were tested separately in a custom-made electrochemical cell at AECL. As reported by Naterer et al. (2011a), Radel membranes from PSU showed higher copper diffusion than Nafion when tested in an electrochemical cell of AECL, although the test made with an ANL permeability cell showed that these membranes have about a ten times lower diffusivity of CuCl_2 than NAFION 117.

The conductivity to protons of various membranes was characterized at PSU with the aid of a custom-made through-plane conductivity cell of which a schematic is presented in Fig. 6.23. The cell comprises two compartments separated by a membrane which is sandwiched between two titanium disks that serve the role of electrodes. The compartments were filled with solutions that simulate the anolyte and catholyte of an actual electrochemical cell. An electrochemical impedance spectroscopy (EIS) method was applied to eventually determine the membrane conductivity in chloride media. The method is described in detail in Balashov et al. (2011), which performed tests with a NAFION 115 membrane. Additional results of the same group were reported by Naterer et al. (2011a) and summarized in Table 6.14. All conductivity measurements were made at ambient temperature. In the same table, the ratio between conductivity and permeability is also presented for each membrane. This ratio is a measure of the membrane selectivity to protons. The membrane with the highest selectivity should be the best choice. The data from Table 6.14 indicates that the membrane CM2-base developed at PSU has the best selectivity.

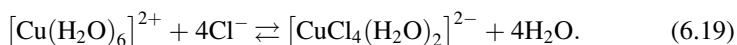
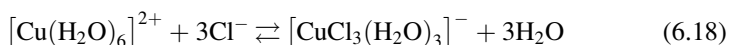
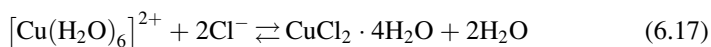
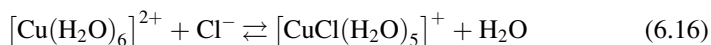
Experimental observations made at AECL with their custom-made electrochemical cell revealed that copper(II) diffusion through Nafion membranes shows a strong dependence on membrane pretreatment conditions. This may explain why modified Nafion membranes do not perform as well as non-treated membranes.

6.4.4 Copper-Chloride Complexation Studies

The presence of copper-chlorides (CuCl , CuCl_2) in anolyte solution leads to the occurrence of various complexation reactions of Cu(I) and Cu(II) . It is indicated in

Table 6.6 that copper has two oxidation states (+1 or +2), while chlorine has four oxidation states (−1, +1, +5, +7). Therefore, copper and chlorine may form several molecular and ionic species. The copper (II) cation forms a pale-blue octahedral complex with six water molecules $[\text{Cu}(\text{H}_2\text{O})_6]^{2+}$.

In chloride media, Cu(I) can exist as several different anionic species (for example, CuCl_2^- , CuCl_3^{2-}). The abundance of each species is dependent on the concentration of chlorine ions. The copper complex reacts with chlorine ions in aqueous solutions according to the following reactions at equilibrium that describe the complexation process (see Trevani et al. 2010):



It can be observed that both copper(I) species and copper(II) species can be formed in the electrolyte of the electrochemical cell. Furthermore, molecular cupric chloride is formed according to (6.17) as a hydrated complex. Chemical equilibrium data of copper complexation processes is essential for modeling speciation in both the anolyte and catholyte of the electrochemical cell and copper transport processes. Moreover, it is essential to determine equilibrium constant data and chemical activities at high temperatures and pressures, because it is expected that in an actual process, the electrochemical cell for hydrogen generation will operate at ~15 MPa and temperatures up to 423 K (see Trevani et al. 2010).

Aiming to determine equilibrium constants and other relevant parameters related to copper-chloride complexation within the electrochemical cell, Trevani et al. (2010) performed a series of experiments at high pressure and temperature. The experimental data was further processed by various modeling methods. The testing pressure was 9 MPa for two operating temperatures, namely, 373 and 423 K. An experimental arrangement comprising a high-pressure titanium cell of 0.34 cm³, having a sapphire window (1.72 cm optical path length), was coupled to a custom-made automatized dosing system for chemicals (e.g., copper-chloride). The concentration measurements were performed with a UV-visible spectrometer which was used to collect spectral data in the range 200–1,100 nm with a browsing step of 1 nm.

The experimental data at high pressure and previously published data at low pressure have been further used to calculate the association constants for the Helgeson–Kirkham–Flowers (HKF) equation of state, which models the behavior of any species in water. The HKF is specifically used to predict the equilibrium constants of various reactions in aqueous solutions. Based on their experiments and modeling, Trevani et al. (2010) predicted the equilibrium constant for equilibrium

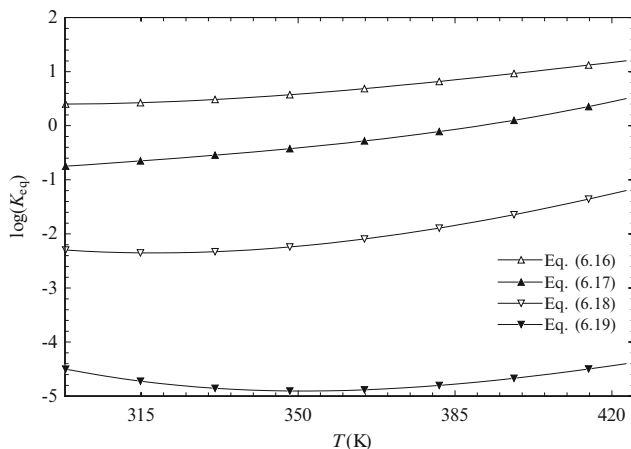


Fig. 6.24 Equilibrium constant of complexation reactions of the copper(II) cation with chlorine anion in aqueous solutions [data from Trevani et al. (2010)]

reactions in (6.16)–(6.19). The results are shown graphically in Fig. 6.24. It is interesting to note that thermodynamics favors reaction (6.17) at high temperature and intermediate chlorine concentrations, which means that the dominant species in these conditions will be the hydrated cupric chloride, $\text{CuCl}_2 \cdot 4\text{H}_2\text{O}$, with over 90 % species abundance (see Trevani et al. 2010).

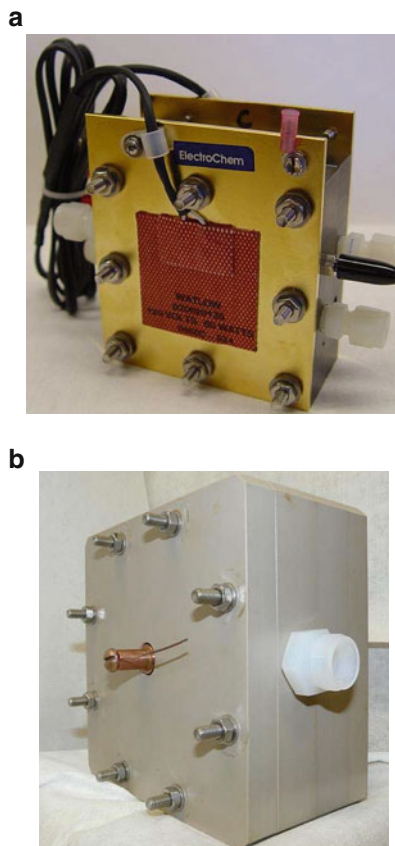
6.4.5 Full-Cell Experiments

Full-cell experiments for process #7 (Table 6.2), namely, CuCl/HCl electrolysis (or electrochemical chlorination), were performed at AECL and PSU in a cell configuration that corresponds to the $\text{Cu}-\text{H}^+$ system described in Fig. 6.15. The essential difference between AECL and PSU cells is that the first uses an aqueous hydrochloric acid solution at the cathode while the other uses water as a proton transport medium through the membrane.

AECL has successfully demonstrated the production of hydrogen over a period of several days with a CuCl/HCl electrolysis cell. The initial experiments were performed with a commercial water electrolysis cell from Electrochem Inc. under low-flow test conditions. The cathode and anode were custom-made, produced from CFP (type Toray EC-TP1-060) painted on one side with a Pt/XC-72R catalyst mixture. Subsequent experiments were performed at higher flow rates using a custom-made electrolysis cell with a catalyst-free anode (graphite separator plate). At the cathode, a catalytic layer was applied by direct spraying of Pt/XC-72R catalyst mixture on the GSP. Figure 6.25 shows photos of the two electrolysis cells at AECL.

The cells were installed into a test loop of which a diagram is shown in Fig. 6.26a and a photograph in Fig. 6.26b. As described by Suppiah et al. (2009), the catholyte

Fig. 6.25 Single cells for electrochemical step of copper–chlorine hybrid cycle for experimental investigations at AECL (courtesy of AECL).
(a) Commercial cell with custom electrodes,
(b) Custom-made cell



is kept in a 4 L catholyte reservoir #1 which is circulated with a peristaltic pump and directed to a column comprising anion exchange resin (AER) (see figure) containing a DOWEXTM 21 K XLT AER. This removes complexes of copper-II/chloride. Further, the catholyte is directed into a column containing a chelating ion exchange resin CR (see figure) of type DOWEXTM M4195 which removes uncomplexed copper (II) cations. After the electrochemical process at the cathode, the hydrogen-rich catholyte is returned to catholyte reservoir #1.

The anolyte is kept in the anolyte reservoir #2 which is circulated with a peristaltic pump through the anode compartment where Cu(I) oxidizes to Cu(II). Further, the catholyte passes through vessels #3 where copper coils are inserted. A reverse reaction occurs to recycle the anolyte, namely, Cu(II) ions from the anolyte react with metallic copper and form two moles of Cu(I) for each mole of Cu(II). Therefore the concentration of Cu(I) ions tends to increase in the anolyte reservoir. In order to compensate, an HCl vessel is installed (see figure) from which concentrated HCl is injected into the anolyte reservoir with a pump. This maintains the concentration of Cu(I) ions relatively constant for the experiment. The anolyte

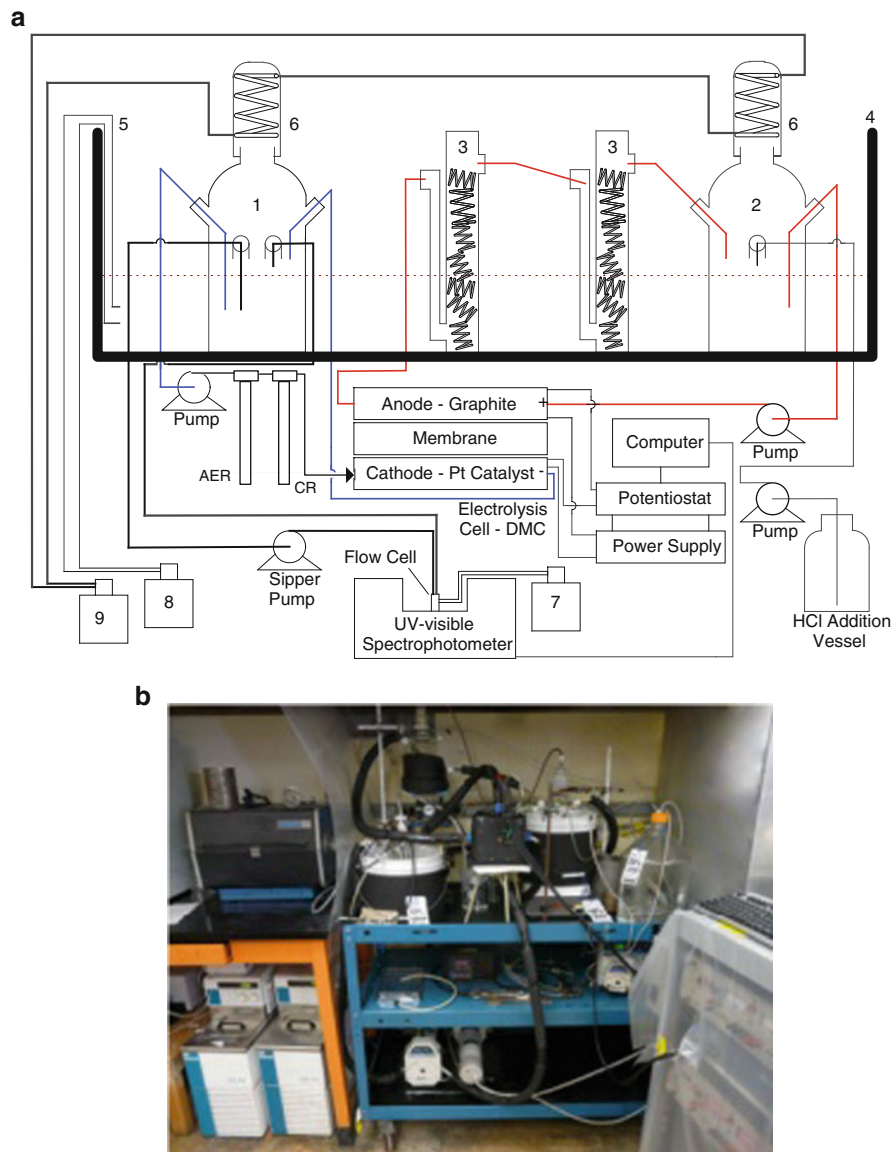


Fig. 6.26 Experimental facility at AECL for testing a single-cell electrolyzer for the CuCl/HCl solution: (a) system diagram (modified from Naterer et al. 2011a), (b) photograph (courtesy of S. Suppiah)

and catholyte solutions are maintained at constant temperature by immersion of the anolyte and catholyte reservoir as well as a copper coil vessel in a thermostated water bath #4, which is coupled through lines #5 to a temperature-controlling unit #8. In addition, condenser coils #6 are used at the top of the anolyte and catholyte

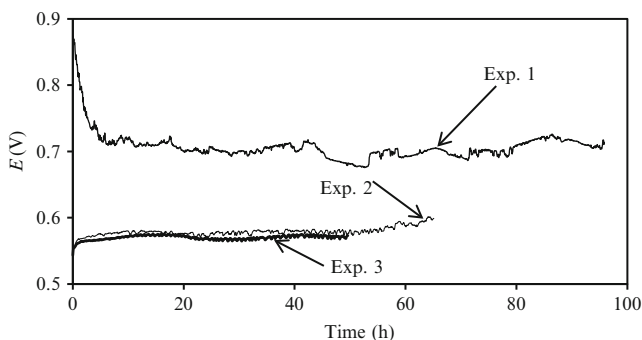


Fig. 6.27 AECL results of cell voltage for CuCl/HCl electrolysis process (courtesy of AECL)

reservoirs which are coupled to a chilled water bath #9. The condensers are used to condense gaseous species (e.g., HCl) in the anolyte and catholyte reservoirs.

An UV/visible spectrophotometer is coupled to the catholyte reservoir through a circuit including a pump. The spectrometer requires cooling via the bath #7; it is used to monitor the species concentration in the catholyte reservoir. The electrochemical cell is coupled to a power supply and a computer-controlled potentiostat.

The experiments were performed over a range of HCl concentrations in the anolyte and catholyte solutions for a domain of CuCl(aq) concentrations in the anolyte. The copper (I) oxidation reaction is presently conducted in a 0.5 mol/L CuCl(aq)/11 mol/L HCl(aq) anolyte and 11 mol/L HCl(aq) catholyte. The experiments confirmed that copper deposition is absent at such a high catholyte concentration in hydrochloric acid, even at 1,000 A/m².

The catholyte flow rate was 1.5 L/min and the anolyte flow rate was 1.25 L/min. A zero-gap configuration was used. The operating temperature was ~325 K. The temporal records of cell voltage (E) are presented in Fig. 6.27 for three experimental tests. The experimental data (Exp. 1) was obtained during preliminary experiments with a cell with conventional design; the anolyte was 0.5 mol/L CuCl(aq) in 10 mol/L HCl(aq) and the catholyte was 10 mol/L HCl(aq). The cell voltage was quasi-stable at 0.7 V. As mentioned by Naterer et al. (2011a), stable cell performance at voltages down to 0.477 V has been observed for 10 h using an electrolysis cell of conventional design.

The data sets (Exp. 2) and (Exp. 3) were obtained using an electrolysis cell having a proprietary (nonconventional) design that is capable of suppressing copper species crossover into the catholyte. The proprietary cell of AECL uses a Pt-based electrocatalyst at the cathode and a CEM. No catholyte copper was observed when the electrolysis was conducted using the new electrolysis cell. The results—produced for 0.5 mol/L CuCl(aq) in 11 mol/L HCl(aq) at the cathode and 11 mol/L HCl(aq) at the anode—show very promising stable performance at a cell voltage of about 0.57 V over a period of about 50 h.

A polarization curve with the modified cell of AECL is presented by Suppiah et al. (2009) for 1 mol/L CuCl(aq)/6 mol/L HCl(aq) anolyte and 6 mol/L HCl(aq)

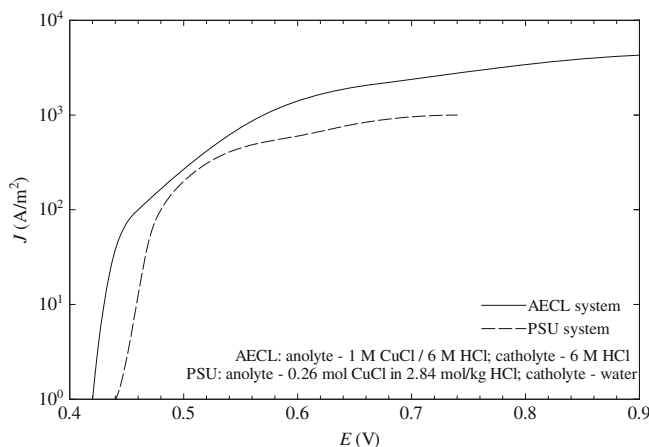


Fig. 6.28 Polarization curves obtained with full-cell systems [data from Suppiah et al. (2009) for AECL, and Balashov et al. (2011) for PSU]

catholyte. It shows that the current density is 1,000, 2,380, 3,420, and 4,290 A/m^2 for 0.57, 0.7, 0.8, and 0.9 V, respectively. Figure 6.28 shows the polarization curve for these experiments. These results show that it is possible to obtain high current densities with the cell at reasonably low cell voltages.

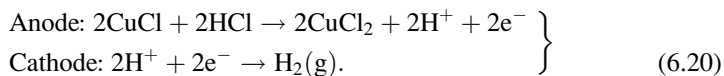
Researchers at PSU reported an experimental investigation of a CuCl/HCl electrochemical process performed with a commercial cell for water electrolysis. The cell is supplied by Electrochem Inc. and has a proton exchange membrane of 5 cm^2 , which is the same as the effective area of the electrodes. NAFION membranes were used with two thicknesses, namely, 127 and 178 μm . Two carbon paper diffusion layers (AA10, Ion Power Inc.) were applied to each side of the membrane after which graphite bipolar plates were attached. There is proprietary undisclosed information about the electro-catalysts. The experimental setup at PSU is different than developed at AECL mainly because it does not recycle the spent anolyte after its passage through the cell. There is a large reservoir of anolyte which supplies a solution with CuCl(aq) concentrations in the range of 0.1–0.3 mol/kg in 1.5–4 mol/kg HCl(aq). The catholyte was deionized water. The anolyte flow rate was varied in a range of 30–68 mL/min.

The polarization results for PSU obtained with an anolyte consisting of 0.26 mol CuCl in 2.84 mol/kg HCl at 26 °C are superimposed in Fig. 6.28 for comparison purposes. The current density is 100 and 1,000 A/m^2 for 0.48 and 0.74 V, respectively.

6.4.6 Electrochemical Cell Modeling

Predictive formulations can be obtained by thermodynamic and kinetic modeling of the electrochemical cell. The cell model can be used for parametric analysis purposes

aimed to provide new insight for the effective design and improvement of the electrolysis process. Electrochemical chlorination processes of CuCl (process #7, Table 6.2) have been modeled thermodynamically and kinetically at UOIT by Odukoya and Naterer (2011). The reversible cell is derived from thermodynamics, based on the Gibbs free energy of the reaction, assuming the following half-reactions:



Because two electrons are transferred for one molecule of hydrogen, the reversible open-circuit voltage is $\text{ROCV} = -\Delta G/2F$, where F is Faraday constant, and ΔG represents the Gibbs free energy for the overall cell reaction: $2\text{CuCl} + 2\text{HCl} \rightarrow 2\text{CuCl}_2 + \text{H}_2(\text{g})$. The actual cell potential is given by the sum of ohmic, activation, and concentration potentials according to

$$\mathbb{E} = \text{ROCV} + V_{\text{ohm}} + V_{\text{act}} + V_{\text{conc}}. \quad (6.21)$$

The concentration over-potential is calculated based on the Butler–Volmer and Tafel equations for a given current density (j) and under the assumption that the charge transfer coefficient a at the anode and cathode are similar. Therefore,

$$V_{\text{conc}} = \frac{RT}{2(1-a)F} \ln\left(\frac{j}{j_0}\right) \quad (6.22)$$

where j_0 is the exchange current density. The ohmic over-potential is a summation of over-potentials due to effective electric charge transport through the electrolyte (r_e), and the electrical resistances of the anode (r_a) and cathode (r_c). These electrical resistances can be written per unit of surface area of the electrode; using area-specific resistances, the total ohmic over-potential is

$$V_{\text{ohm}} = j \times (r_e + r_a + r_c). \quad (6.23)$$

In the particular case of the CuCl/HCl electrolysis cell, one assumes that the electrolyte is a proton exchange membrane. Therefore the apparent electrical resistance of the electrolyte is obtained from the local electrical conductivity (σ_e) through a membrane via integration as follows:

$$r_e = \int_0^\delta \frac{dx}{\sigma_e(x)}, \quad \text{where } \sigma_e(x) = \sigma_{e0} \times \frac{C_{\text{CuCl}}(x)}{C_{\text{H}^+}}. \quad (6.24)$$

Equation (6.24) was proposed by Odukoya and Naterer (2011) and assumes that σ_{e0} is the membrane conductivity for a molar concentration of cuprous chloride of unity. Moreover, the molar concentration of CuCl varies across the membrane as $C_{\text{CuCl}}(x)$ and the proton concentration $C_{\text{H}^+}(x)$ is assumed constant. Determination

of the concentration profile $C_{\text{CuCl}}(x)$ can be made based on Fick's law of diffusion which can be integrated over the membrane thickness, namely:

$$C_{\text{CuCl},a} = C_{\text{CuCl},c} - \frac{n_d \times j}{D \times F} \times \delta, \quad (6.25)$$

where subscripts a and c refer to the anode and cathode, respectively, D is the diffusion coefficient, δ is the membrane thickness, and n_d is the electro-osmotic drag coefficient. Since the diffusive flux is proportional to the molar concentration, Ohm's law requires that the molar concentration increases linearly across the membrane. Therefore, from (6.25) one can obtain the following:

$$C_{\text{CuCl}}(x) = C_{\text{CuCl},c} \times \left[1 + \left(\frac{x}{\delta} - 1 \right) \times \frac{j}{j_L} \right], \quad \text{where } j_L = \frac{FDC_{\text{CuCl},c}}{n_d\delta} \quad (6.26)$$

where the limiting current density is introduced as j_L , because when $j = j_L$, there is no presence of CuCl at the cathode–electrolyte interface $C_{\text{CuCl}}(x = 0) = C_{\text{CuCl},c} = 0$. Substituting (6.26) into (6.24), one obtains

$$r_e = \int_0^\delta \left[\left(\frac{C_{\text{H}^+}}{C_{\text{CuCl},c}} \right) / \left(1 + \left(\frac{x}{\delta} - 1 \right) \times \frac{j}{j_L} \right) \right] dx. \quad (6.27)$$

Assuming that the electrical resistance of the membrane is the dominant term in (6.23), then consequently V_{ohmic} can be approximated with $V_{\text{ohmic}} = j \times r_e$. Regarding the activation over-potential, this is made based on the Nernst equation; the activation over-potential is

$$V_{\text{act}} = \frac{RT}{2aF} \times \ln \left(\frac{j}{j_0} \right). \quad (6.28)$$

Entropy generation in the electrolytic cell is a measure of irreversibility and voltage loss within the cell. In other words, voltage losses are a direct result of entropy production within the cell. Hence, entropy generation is a robust way to analyze the irreversibilities within the cell. There are other sources of irreversibility within the system, which could impede the overall performance of the cell. These include frictional losses and losses within other devices connected to the cell. The over-potential is a measure of irreversibility. According to (6.21), the total potential that must be applied to the electrodes is a summation of the reversible open-circuit voltage and various over-potentials. Each over-potential has an irreversibility. The sum of all over-potentials, $\text{OVP} = V_{\text{ohm}} + V_{\text{act}} + V_{\text{conc}}$, quantifies the total irreversibilities. Therefore, the generated entropy is $S_{\text{gen}} = 2F \times \text{OVP}/T$, where T is the operating temperature in K. Based on the above equations, one obtains the following expression for generated entropy:

$$S_{\text{gen}} = \frac{2F}{T} \times \left[j \times r_e + \frac{RT}{2aF} \times \ln \left(\frac{j}{j_0} \right) \right]. \quad (6.29)$$

Table 6.15 Operating parameters for electrochemical cell modeling

Operating parameters	Value
Temperature of the cell, T (K)	373.15
Exchange current density, j_o (A/m^2)	0.7
Activation potential, η (mV)	0.515
Electrons transferred in the reaction, Z	2
Charge transfer coefficient, a	0.5
Molar weight of mixture, M (kg/kmol)	0.17048
Universal gas constant, R ($\text{J}/\text{mol K}$)	8.314
Faraday constant, F (C/mol)	96,500
Concentration of CuCl (mol)	1.5
Concentration of HCl (mol)	6
Over-potential, E_0 (mV)	0.515
Reversible open circuit voltage, ROCV (mV)	−1.009

Source: Odukoya and Naterer (2011)

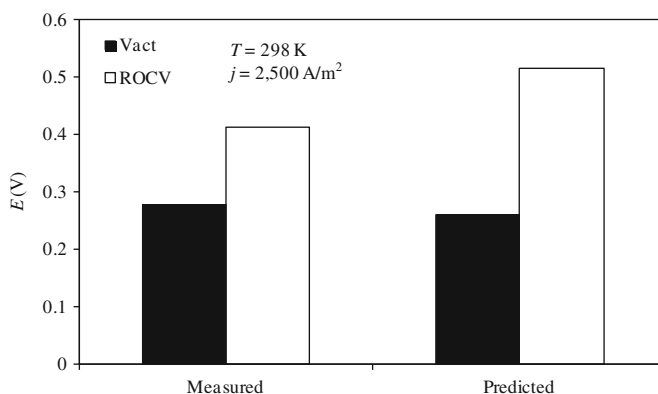


Fig. 6.29 Comparison between predicted and measured data. Predictions are based on modeling by Odukoya and Naterer (2011). Measured data is taken from Stolberg et al. (2008)

Unlike other parameters such as over-potential or polarization, entropy production can provide a more robust metric, from which all irreversible losses within an electrochemical system can be characterized. For example, entropy production encompasses both irreversible voltage losses of concentration polarization within the electrode, as well as viscous losses induced by frictional irreversibilities of fluid motion within the electrochemical cell. The operating parameters in the modeling are listed in Table 6.15; they are intended to replicate conditions of experimental studies conducted by AECL for the CuCl/HCl electrolysis cell.

Figure 6.29 shows a comparison between measured current densities and the predictions. The comparison shows that the magnitudes of the predicted over-potential in the new formulation show close agreement with experimental half-cell data reported previously by Stolberg et al. (2008) for cuprous chloride electrolysis. It can be observed that the activation potential shows only about a 6 % difference between the experimental activation potential and the predicted results. Note that

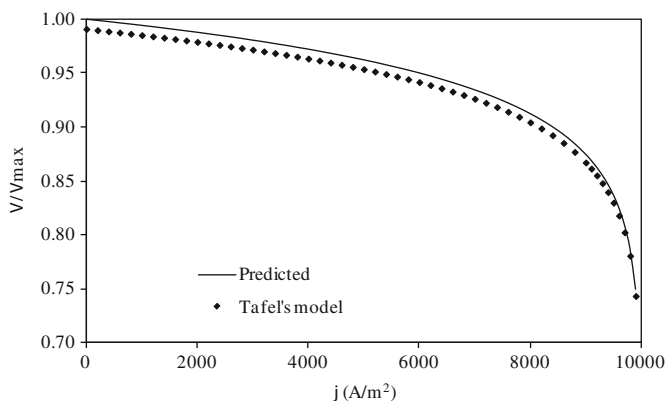


Fig. 6.30 Model validation through comparison with Tafel's reference model [data from Odukoya and Naterer (2011)]

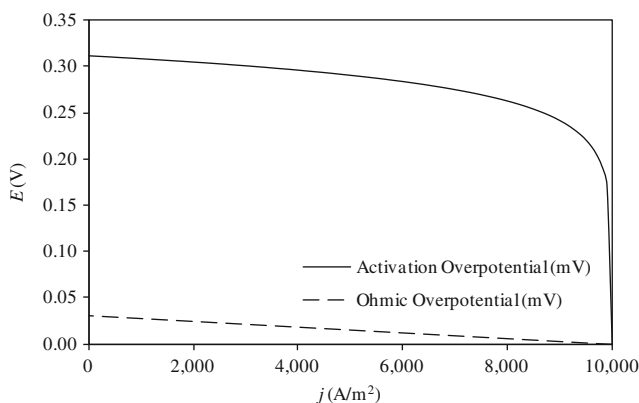


Fig. 6.31 Variation of ohmic and activation over-potentials with current density [data from Odukoya and Naterer (2011)]

the comparison is made for a single operating condition of 298 K and current density is $2,500 \text{ A/m}^2$. Additional model validation is presented in Fig. 6.30 where the Tafel model for over-potential prediction (see Chap. 4) is used as a comparison base. The predictions of the new formulation by Odukoya and Naterer (2011) were compared to the Tafel model. Close agreement between the results provides a useful validation of the current formulation, as the maximum difference between both methods is only about 0.08 %. This comparison serves as a useful verification of the model for predicting entropy production during the oxidation of cuprous chloride.

Based on the parametric analyses with the validated model, it shows that the activation over-potential is much greater than the ohmic over-potential. This is indicated in Fig. 6.31. The change in current density significantly affects the

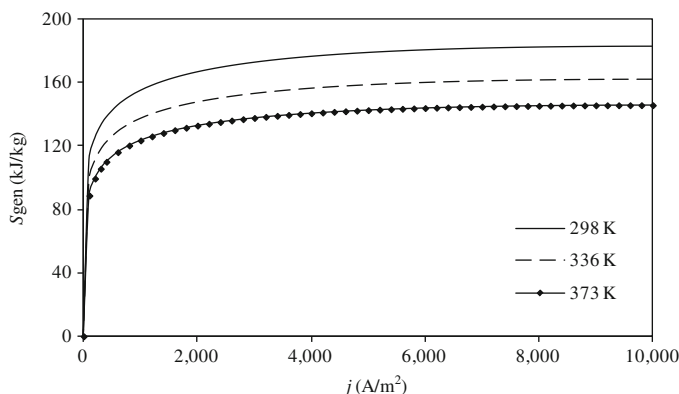


Fig. 6.32 Variation of generated entropy with current density and operating temperature [data from Odukoya and Naterer (2011)]

activation over-potential. This increase in over-potential is about 81 %, when compared with its value at the lowest current density. The ohmic over-potential can be neglected at very high current densities, but it has a significant effect at low and intermediate current densities (0–7,000 A/m²). The ohmic resistance increases linearly with current density, as expected by the relationship of Ohm's law.

The operating temperature of the electrochemical cell has a significant effect on the entropy generation in Fig. 6.32. The entropy generation for the three temperatures is nearly equal until about 100 J/kg K. Beyond a current density of 2,000 A/m², the rate of change of entropy production is not significant for each temperature under consideration. It can be inferred that some level of equilibrium has been obtained for the electrochemical reaction. When the temperature of the cell varies from 298 to 373 K, the entropy generation decreases by about 25 %. Thus, increasing the cell temperature reduces the energy required by the electrochemical cell. For a cell temperature of 298 K, a percentage increase of 58 % was observed between a current density of 100 and 4,000 A/m², while the increase beyond this range is only about 3.6 %.

The new model developed by Odukoya and Naterer (2011) predicts the entropy production in the electrochemical cell, particularly diffusive irreversibilities of cuprous chloride electrolysis. The ohmic resistance appears to have minimal effect on the electrolytic cell performance at high current densities. A significant effect of current density on over-potential was observed at low current densities (0–250 mA/cm²). From the entropy production results, it is preferable to operate the electrochemical cell at higher temperatures to reduce the irreversible losses. However, there are other limitations at high temperatures due to the corrosive nature of hydrochloric acid. The current density has a significant effect on entropy production between 0 and 400 mA/cm². The exchange current density has been shown to have little effect on the cell over-potential. The activation over-potential has the most significant effect on the cell performance. Although the ohmic resistance has little effect at high current densities, the effects become significant

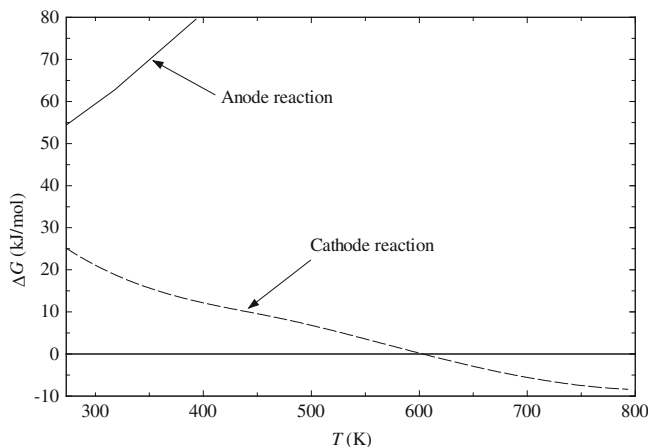
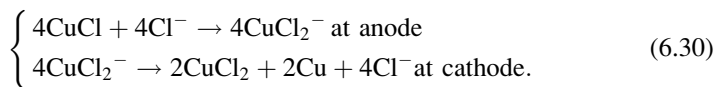


Fig. 6.33 Gibbs free energy for half-reactions of Cu–Cl copper disproportionation process [data from Lewis et al. (2003)]

at lower current densities. Also, high charge transfer coefficients are undesirable, as they increase the entropy production in the system. At a high charge transfer coefficient, the energy required for cell operation nearly doubles, which makes the system less commercially viable.

Other modeling results obtained at UOIT relate to thermodynamic analyses through energy and exergy balance equations for the electrolytic copper production step via disproportionation process #1 (see Table 6.2). Based on Table 6.11, the half-reactions for the disproportionation process can be written as (see Lewis et al. 2003)



Using the process representation in (6.31), the Gibbs free energy of the electrochemical process can be calculated as a function of temperature for anodic and cathodic reactions. This data can be further used in thermodynamic analyses through energy and exergy. Figure 6.33 shows the variation of Gibbs free energy. This data reveals that the cathode half-reaction is facilitated by higher temperature. In other words, the reversible cell potential at the cathode can be very low, or reversed if the cathode is maintained at high temperature.

A thermodynamic modeling study of the CuCl disproportionation process has been reported in Orhan et al. (2008a). Several factors affect the energy balances for systems involving chemical reactions. Some of these apply generally, without regard for whether a reaction occurs. For example, it is necessary to determine work and heat transfer, as well as the importance of kinetic and potential energy. Other considerations relate to the occurrence of combustion or other reactions.

For example, it is important to have the states and conditions of the reactants before a reaction occurs, and if fluids are premixed. The state of the products also must be assessed, e.g., if water formed in the reaction has condensed.

The exergy efficiency can be formulated for the reacting system. At steady state, the rate at which exergy enters the reacting system equals the rate at which exergy exits plus the rate at which exergy is destroyed within the system. It is assumed that the reactor is well insulated, so there is no heat transfer and thus no accompanying exergy transfer. The exergy efficiency is defined usually with $\psi = ex_{out}/ex_{in}$. In the analysis, a preliminary analysis assumes that the reaction is complete. Under this assumption, one can obtain the upper bound of exergy efficiency and its correlation with reaction temperature and the temperature of the environment. The results reported in Orhan et al. (2008a) show that the exergy efficiency is higher at lower reaction temperatures. The relationship of exergy efficiency with reference-environment temperature is obtained for a constant reaction temperature of 353 K and with a reaction temperature evaluated at a constant reference-environment temperature of 298 K.

6.5 Hydrolysis Reaction Step

6.5.1 Thermodynamics of Hydrolysis Reaction

Thermodynamic analysis is a key step in the study of any thermochemical reaction. The aim is to determine the equilibrium yields and identify possible side reactions. Processes #2 to #5 listed in Table 6.2 are hydrolysis processes encountered in various versions of the copper–chlorine hybrid cycle. Processes #2 and #3 which form copper oxychloride have been actively studied. Process #8, oxychlorination, is a reaction between cupric chloride and steam. The reaction is endothermic and non-catalytic and operates between 625 and 675 K as described in Table 6.2.

The Gibbs free energy and enthalpy of the reaction at 673 K was estimated by Lewis et al. (2003) as ~40 kJ/mol H₂O and ~117 kJ/mol H₂O, respectively, based on the assumption that the molar enthalpy and entropy of copper oxychloride (CuO·CuCl₂) can be represented as a summation of enthalpies of cupric oxide (CuO) and cupric chloride (CuCl₂). Although small, the Gibbs free energy of the reaction is positive. Therefore the reaction is not spontaneous and one may expect relatively low yields.

Besides the main reaction—(6.2), the desired reaction—several side reactions may occur. Thus, hydrolysis is considered by researchers the most challenging reaction of the cycle—see Ferrandon et al. (2008). Table 6.16 shows some of the main reactions that may occur when cupric chloride is in the presence of steam at high temperature. The main products in the hydrolysis reactor are copper oxychloride and hydrochloric acid. However, the temperature in the hydrolysis reactor is sufficiently high for copper oxychloride to decompose partially (reaction #2) and

Table 6.16 List of desired and possible side reactions in a CuCl_2 hydrolysis reactor

ID	Reaction	Remarks
1	$\text{CuCl}_2(\text{s}) + \text{H}_2\text{O}(\text{g}) \rightarrow \text{CuO} \cdot \text{CuCl}_2(\text{s}) + \text{HCl}(\text{g})$	Desired reaction, hydrolysis, (6.2)
2	$\text{CuO} \cdot \text{CuCl}_2(\text{s}) \rightarrow 0.5\text{O}_2(\text{g}) + 2\text{CuCl}(\text{s}, \text{l}, \text{g})$	Thermolysis of copper oxychloride, (6.5)
3	$\text{CuCl}_2(\text{s}) \rightarrow \text{CuCl}(\text{s}, \text{l}, \text{g}) + 0.5\text{Cl}_2(\text{g})$	Thermolysis of CuCl_2 with CuCl formation
4	$3\text{CuCl}(\text{g}) \rightarrow \text{Cu}_3\text{Cl}_3(\text{g})$	Formation of tricopper trichloride
5	$\text{Cl}_2(\text{g}) + \text{H}_2\text{O}(\text{g}) \rightleftharpoons 0.5\text{O}_2(\text{g}) + \text{HCl}(\text{g})$	Reverse Deacon and Deacon reactions

possibly release gaseous oxygen and cuprous chloride. The CuCl may be present as solid, liquid, and/or gas. If the temperature is lower, below the normal boiling point of CuCl , sublimation of solid CuCl may occur—see Ferrandon et al. (2008). For a temperature over the melting point, liquid and vapor CuCl are produced. The most important side reaction is the cupric chloride decomposition (process #3 in the table) which generates cuprous chloride and chlorine.

It is also possible that tricopper trichloride (a gaseous compound, Cu_3Cl_3) is formed from gaseous cuprous chloride directly. Cuprous chloride formed in the hydrolysis reactor is not necessarily problematic because this is the desired product of copper oxychloride decomposition within the cycle. The main problem is the formation of molecular chlorine which must be recycled in the system. Formation of significant quantities of chlorine negatively impacts the cycle of chemical reactions within the thermochemical cycle. Therefore, the process parameters and reactor must be selected and designed such that the chlorine yield is minimized or avoided. In addition, there may be traces of tricopper trichloride generated as side reactions; this must be avoided too, because Cu_3Cl_3 is stable since it has a circular molecule.

Preliminary experimental results from ANL—published by Lewis et al. (2003)—show that the maximum conversion of cupric chloride occurs when steam is supplied by about 20 times more than the stoichiometric quantity. Ferrandon et al. (2010a, b) show that in a spray atomizer operated under vacuum, the conversion of CuCl_2 is facilitated better than a reactor operating at a pressure higher or equal than atmospheric. Because the conversion of CuCl_2 is not complete, it becomes possible that CuCl_2 enters the next reactor—the thermal decomposition reactor for copper oxychloride. In this case, due to a higher operating temperature, thermolysis of cupric chloride occurs and releases chlorine gas. This changes the partial pressure of gases in the reactor and affects the purity of produced oxygen, while at the same time disturbs the balance of chemicals within the plant.

The variation of Gibbs free energy for each of the reactions from Table 6.16 is presented in Fig. 6.34 which has been obtained with EES software. At temperatures over 500 K, the reaction of copper oxychloride decomposition (reaction #2) becomes a spontaneous endothermic reaction. On the contrary, the reaction of interest (#1 in the table) has a positive Gibbs free energy (although small) at the temperatures of interest. This is an indication that the reaction produces lower yields. Yields can be improved if excess steam is supplied; this implies further separation of steam from other products. The cupric chloride direct

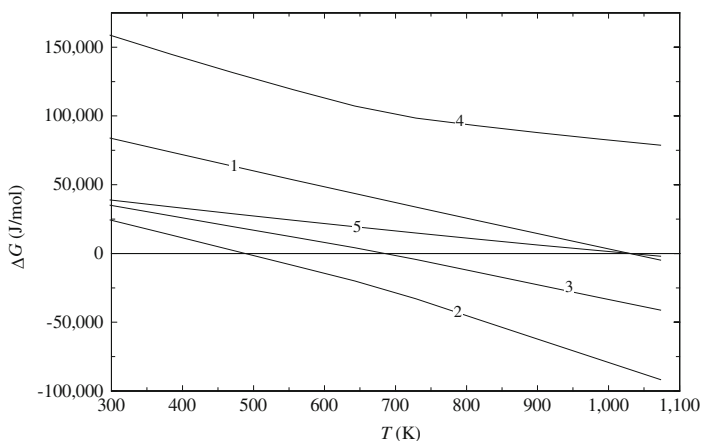


Fig. 6.34 Variation of Gibbs free energy with reaction temperature (reaction numbers correspond to ID from Table 6.16)

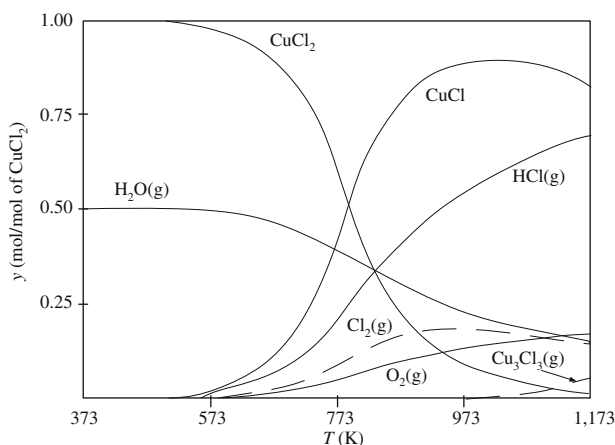
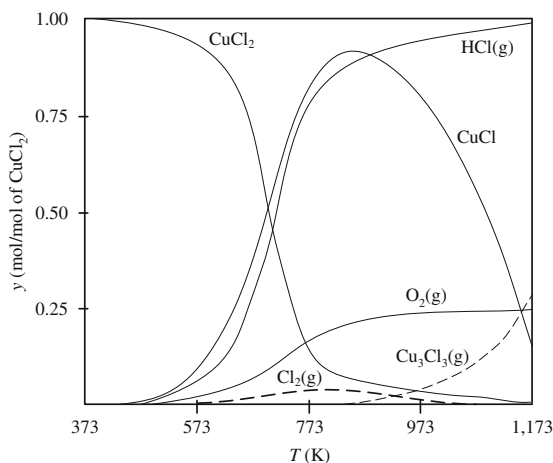


Fig. 6.35 Equilibrium yields of a $2\text{CuCl}_2 + \text{H}_2\text{O}$ reaction (*dashed lines* refer to the undesired side products) [data from Lewis et al. (2009a)]

thermolysis—reaction #3—becomes spontaneous at temperatures over 700 K. Therefore its yield may be high. In order to reduce chlorine formation, the temperature in the hydrolysis reactor must be kept below 700 K. Reaction #4 also has a positive Gibbs free energy, which is high, so therefore this side reaction may generate relatively small yields.

The forward reaction #5 is the reverse Deacon reaction that occurs in the gas phase. This reaction consumes the side product $\text{Cl}_2(\text{g})$ and generates hydrochloric acid and oxygen. However, it has a positive Gibbs energy and thus is not favored thermodynamically. The backward reaction #5 is the Deacon reaction. This is favored thermodynamically as it will tend to generate chlorine once hydrochloric

Fig. 6.36 Equilibrium yields of a $2\text{CuCl}_2 + 10\text{H}_2\text{O}$ reaction (*dashed lines* refer to the undesired side products) [data from Lewis et al. (2009a)]



acid has reacted with oxygen. Oxygen is not desired in the hydrolysis reactor in order to minimize/avoid chlorine release.

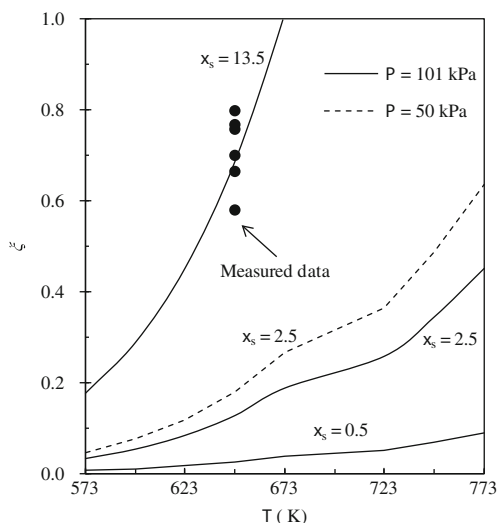
Figure 6.35 shows the calculated equilibrium yields as a function of temperature in a reaction vessel where 2 mol of cupric chloride and 1 mol of steam are supplied. It can be observed that at 573 K, there is no chlorine generation; however, CuCl_2 conversion is very low (below 5 %). At around 773 K, the conversion reaches around 50 %, but the chlorine yield is too high (around 0.5 moles per mole of CuCl_2). At 973 K, the chlorine production reaches an apparent maximum of 20 %. Over 973 K, gaseous tricupric trichloride starts to be produced.

This analysis demonstrates that molecular chlorine is the only relevant side product that occurs at temperatures of interest (623–723 K). If excess steam is used then the chlorine generation decreases. Figure 6.36 presents the equilibrium yields of cupric chloride conversion at ten times more steam than required stoichiometrically. The conversion becomes higher than 80 % at temperatures over 773 K when the generated yield of chlorine is ~ 0.05 moles per mole of CuCl_2 . If the reaction is conducted at 973 K, the conversion is higher than 95 % while the molar percent of generated chlorine is near or below 1 %. However, around 0.05 mol of undesired side product, Cu_3Cl_3 , may be generated per mole of cupric chloride. In the study by Lewis et al. (2009a) it is mentioned that the appropriate engineering design should maintain the temperature in the hydrolysis reactor in the range of about 600–700 K and separate the solids, liquids, and gases to eventually extract steam and hydrochloric acid before the remaining products are fed to the next reactor where thermal decomposition of copper oxychloride occurs predominantly at a slightly higher temperature.

Four hydrolysis processes are listed in Table 6.2. Process #4 has been studied in the past by Dokyia and Kotera (1976). Hydrolysis without the formation of copper oxychloride occurs according to the following simplified reaction:



Fig. 6.37 Variation of the extent of reaction (ξ) for the hydrolysis reaction (6.2) at various steam to CuCl_2 molar ratios (x_s) [data from Daggupati et al. (2009)]



As mentioned by Wang et al. (2008), the reactor for process #4 must perform simultaneously a spray drying process for CuCl_2 dehydration and the thermochemical reaction of hydrolysis, (6.31). As indicated by Wang et al. (2008), around 27.2 mol of steam are necessary for hydrolysis of 2 mol of cupric chloride when the process is conducted according to (6.31). For this estimate, it was assumed that superheated steam is supplied at 873 K and 1 bar and its sensible heat is used until the steam temperature drops to 773 K. It is also assumed that the heat delivered by the steam is used to provide the necessary reaction heat and preheat the reactants at the required temperature.

Process #2 (Table 6.2) is hydrolysis performed with cupric chloride in hydrated form. Wang et al. (2008) reported for this case that 26.7 mol of steam are needed for hydrolysis of two moles of cupric chloride. The process #3 (see Table 6.2) assumes an additional dehydrating step within the cycle to obtain a dehydrated copper oxychloride solid. In this case, the quantity of required steam is substantially reduced, namely, one requires about 8.2 mol of steam for 2 mol of cupric chloride fed to the reactor. An exergy analysis of this reaction step was performed by Orhan et al. (2009a). It shows that the exergy efficiency of hydrolysis step—assuming that the reaction is complete—is around 75 %.

The extent of the hydrolysis reaction—(6.2) and #1 in Table 6.16—has been analyzed by Daggupati et al. (2009), as indicated in Fig. 6.37. The predicted results compare well to the measurements from Ferrandon et al. (2008) at 650 K. As derived by Daggupati et al. (2009), the extent of reaction for (6.2) can be expressed as

$$\xi = \sqrt{0.25K_{\text{eq}}x_s^2/(K_{\text{eq}} + 4P)},$$

where P is the operating pressure and x_s is the molar ratio of steam vs. cupric chloride supplied to the reaction. If the reaction is stoichiometric, then $x_s = 0.5$.

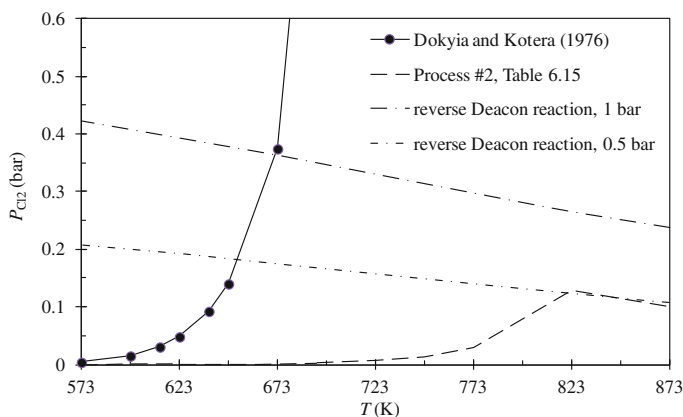


Fig. 6.38 Partial pressure of chlorine in equilibrium with the CuCl_2 decomposition reaction and reverse Deacon reaction (for Cl_2 consumption) [data from Daggupati et al. (2009)]

The equilibrium constant is calculated from the Gibbs energy of the reaction at the specified temperature:

$$K_{\text{eq}} = -\Delta G^0(T)/(RT).$$

From Fig. 6.37, with excess steam of 13.5 more than stoichiometric (27 mol of steam per 2 mol of cupric chloride), the reaction goes to completion at 673 K; it has reasonable equilibrium yield at 650 K. Figure 6.38 shows the variation of equilibrium partial pressure of chlorine with temperature. The criterion used to identify the operating conditions for complete consumption of chlorine is such that the equilibrium partial pressure of chlorine in the decomposition reaction should be lower than the equilibrium partial pressure of the chlorine reverse reaction for stable operation. Based on this criterion, it yields—according to Fig. 6.38—that the reactor operation can be stable for temperatures in the range of approximately 573–800 K.

6.5.2 Overview of Experimental Reactor Developments

A number of experiments and reactor developments for hydrolysis within the Cu–Cl cycle can be observed in the literature back to 2003. Various reactors were tested such as packed bed, fluidized bed, and spray reactors. The reactor sizes range from a small bench, operating with CuCl_2 samples of tens of grams, to larger engineering-scale reactors at UOIT. Most of the experimental reactors were a batch type; some semi-batch (in which only the fluids are supplied and extracted continuously and the reacting solids remain in the reactor until the experiment ends); or flow reactors. In this section, the experimental research on reactor development is examined.

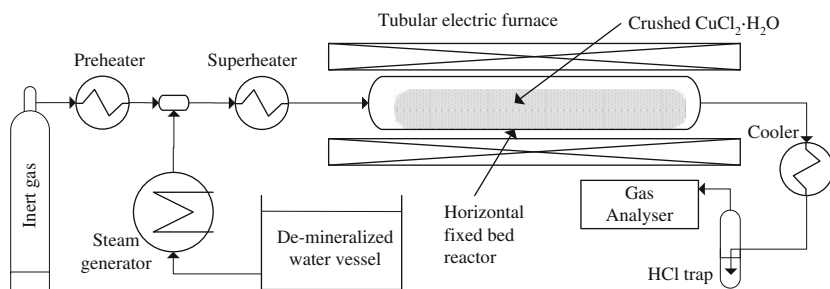


Fig. 6.39 Configuration of hydrolysis experiments in a fixed bed horizontal reactor

Basic thermochemistry experiments aimed to characterize the hydrolysis reaction were performed in a fixed bed reactor in an arrangement illustrated in Fig. 6.39. The reactor typically consists of a quartz tube in which crushed reactant $\text{CuCl}_2 \cdot \text{H}_2\text{O}(\text{s})$ is deposited in a fixed bed. The reactor is placed in a tubular horizontal furnace. The probe weight is measured before and after hydrolysis. During the experiments, a flow of steam is injected from one side of the reactor. The steam is prepared in an auxiliary unit comprising a demineralized water vessel and steam generator. During the experiment, inert gas is used to adjust various parameters or other procedures. For example, the partial pressure of steam may be reduced by adding an inert gas. In addition, inert gas may be used for preheating purposes, or during the shutoff period. On the opposite side of the reactor, gaseous products are collected. These cases normally comprise HCl , H_2O , and Cl_2 . Hot gases may be characterized by various techniques including UV/visible spectroscopy (see Croizé et al. 2010). After cooling the product gases, HCl can be trapped in an alkaline solution (typically NaOH). The pH measurements on the HCl trap may be used to determine the hydrochloric acid concentration. Other gas analyzers may be used such as the chromatograph. Before and after each experiment, the solid sample may be characterized by X-ray diffraction (XRD). The scale of the hydrolysis process at the lab-scale experiments is characterized by the mass of the solid CuCl_2 sample.

There have been reported experiments in large vertical fluidized bed reactors. Such reactors consist of a quartz tube placed vertically in an electrical furnace. The sample, consisting of granular matter, is placed on a porous media distributor inside the reactor. Steam and inert gas are injected from the bottom and the bed is fluidized. Typically the steam/copper ratio is much larger than the stoichiometric amount. Figure 6.40 presents a typical configuration of a vertical fluidized bed reactor and auxiliary devices. Vertical fluidized bed reactors were tested with 1.35 g CuCl_2 samples at ANL and 2,250 g at UOIT.

Fluidized bed reactors provide the opportunity for better contact between the reactants—steam and particles of CuCl_2 . However, there are disadvantages: large quantities of steam must be (re)circulated in order to be able to fluidize the bed, to transfer the necessary reaction heat, and to supply the required steam flow rate to the reaction. Large steam requirements may result in an energy penalty to the cycle.

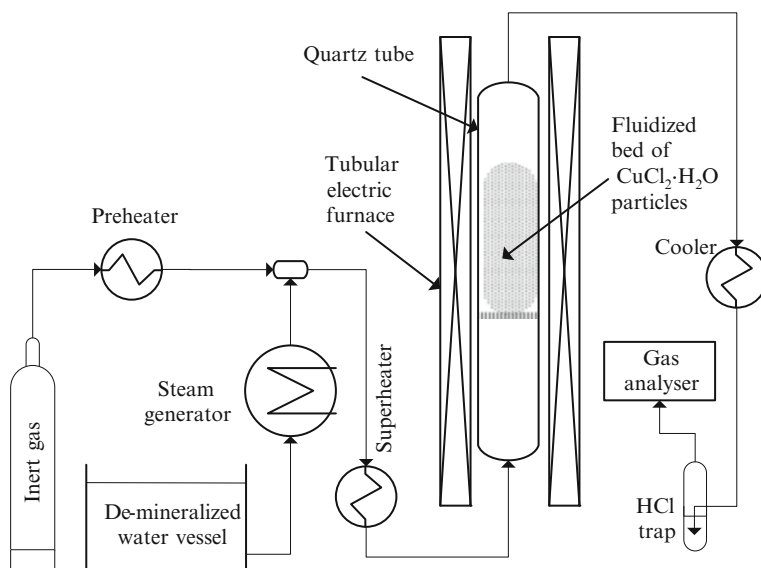


Fig. 6.40 Vertical fluidized bed reactor for hydrolysis experiments and auxiliary systems

An alternative option is a spray reactor. As opposed to a fluidized bed reactor, in a spray reactor, atomized particles formed from an aqueous solution of hydrated CuCl_2 are sprayed in a large vessel filled with steam at the reaction temperature. The residence time of droplets is designed to be sufficient to allow particles to reach the reaction temperature and react. The pressure in the reaction vessel can be at vacuum, which facilitates the reaction thermodynamically. This type of design was tested at ANL (Ferrandon et al. 2010a, b).

The solubility limit of CuCl_2 in water is about 750 g/l; therefore a solution with dissolved CuCl_2 can be pumped at high pressure and injected from the top of a spray reactor. The general configuration of the experimental setup with a spray reactor is presented in Fig. 6.41. The diagram shows that steam together or without a carrier gas (argon or nitrogen) is introduced into the spray reactor at the top, in a co-current configuration with sprayed particles. It is also possible to introduce steam in a countercurrent configuration. An injection nozzle is placed at the topmost position of the reaction vessel. While falling down, the atomized particles react with steam. At the bottom of the reactor, the reacted particles are collected and extracted.

The main experimental reactors developed at various institutions are listed in Table 6.17. Most of the experimental studies were performed at lab and benchtop scales. ANL developed a bench-scale spray reactor which can operate with ca. 300 g cupric chloride di-hydrate $\text{CuCl}_2 \cdot 2\text{H}_2\text{O}$ in a continuous flow system with solid products accumulated at the bottom of the reactor. As mentioned previously, UOIT developed a semi-batch fluidized bed reactor with a load of 2,250 g of solids which is the largest scale reactor developed up to this time.

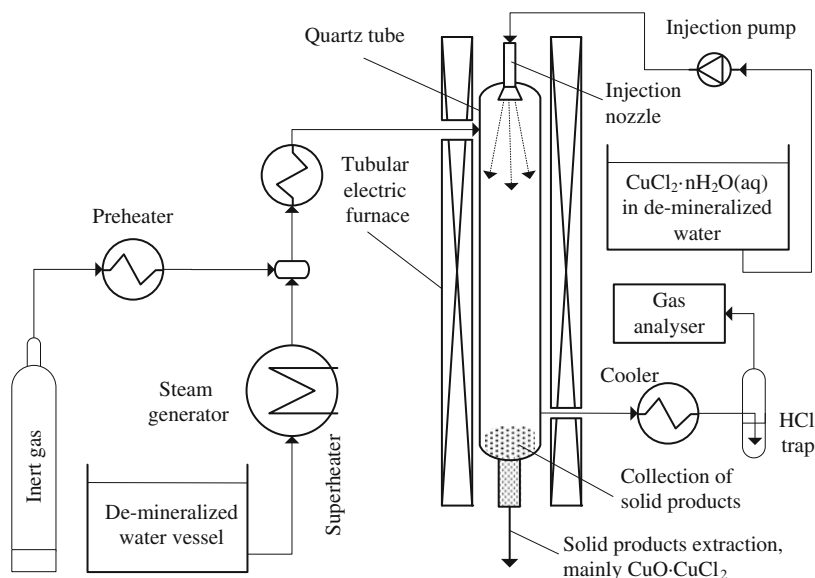


Fig. 6.41 Principle of a spray reactor system for CuCl_2 hydrolysis

Table 6.17 Reactor characteristics of main hydrolysis experiments

Research group	Reactor type	Reactor details	References
CEA	Fixed bed horizontal reactor	Horizontal glass reactor, 10 mm i.d. Sample of 860 mg of crushed $\text{CuCl}_2 \cdot 2\text{H}_2\text{O}$. Tubular furnace. $\text{H}_2\text{O}/\text{Cu}$ ratio of 15. Analysis of gaseous HCl and Cl_2 at 663 K.	Ferrandon et al. (2010a)
ANL	Fixed bed horizontal reactor	70 cm long glass tube, 12.7 mm o.d. Placed in a tubular electric furnace; 40 mg of CuCl_2 sample; experiments performed in a temperature range of 573–623 K.	Lewis et al. (2005a, b)
	Fluidized bed vertical reactor	25.4 mm i.d., 35.6 cm height quartz tube with quartz frit in the middle. Reaction sample of 1.35 g; molar ratio of steam to CuCl_2 of 16:1.	Lewis et al. (2005a, b)
	Fixed bed vertical reactor	12.7 mm o.d. quartz tube with a basket and quartz frit at the bottom. Sample was ~300 mg.	Lewis et al. (2009a, b)
	Continuous spray reactor	Borosilicate glass, 1.3 m height, 11.4 cm i.d., 14 L volume; central port atomizer at top; two ports for gas injection/extraction with co-current configuration; vertical furnace with three independent heating zones. Injection of $\text{CuCl}_2 \cdot 2\text{H}_2\text{O}$ at 1–5 mL/h in hot steam at 673 K under vacuum, 0.25 bar. Argon sweep gas at 300 mL/min.	Ferrandon et al. (2010a)
UOIT	Vertical fluidized bed reactor	15 cm i.d., 1.1 m height; 2.25 kg bed weight. Flow distributor for steam injection made in ceramic porous media. Split tubular electric furnace of 15 kW with three heating zones.	Naterer et al. (2011a)

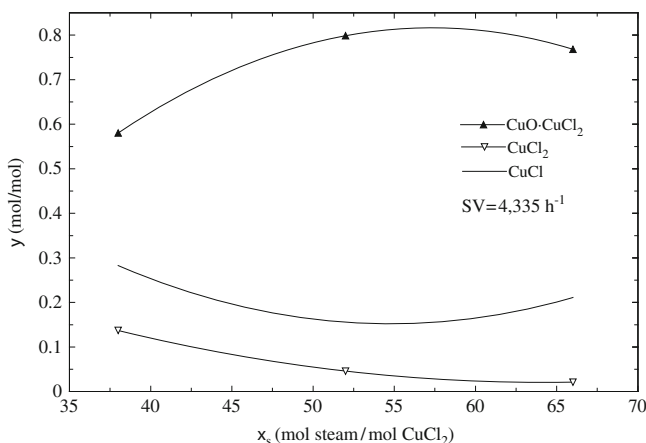


Fig. 6.42 Molar fraction of products of CuCl_2 hydrolysis in fixed bed horizontal micro-reactor [data from Ferrandon et al. (2008)]

6.5.3 Benchtop Experiments and Results

The first set of comprehensive experiments for hydrolysis was reported by Lewis et al. (2005b). Two types of experiments were performed: (1) a fixed bed horizontal reactor (40 mg sample) and (2) a vertical fluidized bed reactor (1,350 mg sample). It was found that the reaction has reasonable kinetics above 573 K, although as shown in Fig. 6.34, the Gibbs free energy of the reaction is positive. The experiments confirmed that the major product of the reaction is copper oxychloride, although some amounts of cuprous chloride are also formed. Excess steam and a lower reaction temperature disfavor the formation of CuCl . However, the observed rate of reaction at lower temperatures is reduced; according to Lewis et al. (2005b) it is about ~2 times slower at 573 K vs. 623 K. In the fluidized bed reactor, the reaction temperature was kept at ~650 K with a molar steam vs. CuCl_2 ratio of 16:1.

A subsequent series of hydrolysis experiments was reported by ANL in a fixed bed horizontal reactor of 70 cm length and 12.5 mm o.d. placed in a tubular electric furnace. The results were presented in Ferrandon et al. (2008) for a test temperature of 650 K. The yield of copper oxychloride depends on the steam vs. cupric chloride molar ratio. The trend in Fig. 6.42 was recorded. A maximum yield of 80 % occurs at an ~57.5:1 steam vs. cupric chloride molar ratio. The CuCl by-product yield is minimized for a 55:1 steam-to- CuCl_2 molar ratio. No chlorine production was observed.

In addition, it was observed that the CuCl yield is lower at lower reaction temperatures; also, the yield decreases with the size of CuCl_2 particles. Another test performed in the same reactor at a fixed steam-to- CuCl_2 molar ratio of 17:1 was reported by Lewis et al. (2009b). It was observed—see Fig. 6.43—that the copper oxychloride yield increases at higher gas hourly space velocities (GHSV). Moreover, the influence of GHSV on the desired product yield is more important than the influence of the steam-to- CuCl_2 ratio.

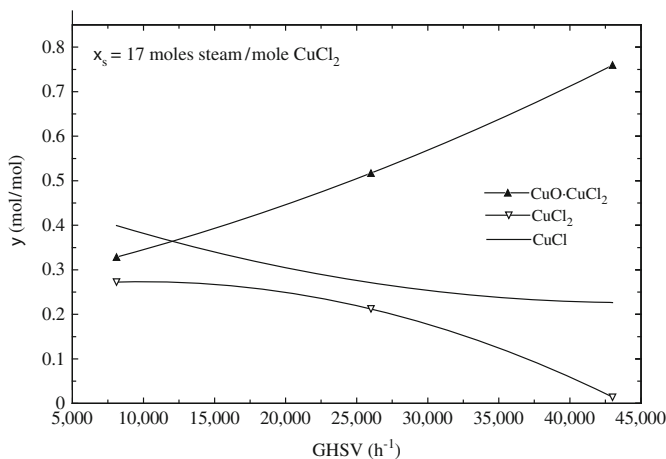


Fig. 6.43 The influence of gas hourly space velocity (GHSV) on yields of the hydrolysis reaction for a fixed molar steam-to- CuCl_2 molar fraction [data from Lewis et al. (2009b)]

A horizontal fixed bed reactor has been used at CEA to study hydrolysis reactions during collaborative research with ANL (Ferrandon et al. 2010a). The concentration of gaseous products was determined by Fourier transform infrared (FTIR) spectroscopy in conjunction with the use of a conductivity probe for HCl(g) and $\text{Cl}_2(\text{g})$ detection. During hydrolysis at 663 K, no chlorine evolution has been observed. However, when the furnace temperature was increased over 673 K, chlorine presence was detected. The chlorine concentration increases with temperature. It is determined that at 733 K, the chlorine concentration reached a maximum of 1.34 mmol/L; when the temperature was increased to 773 K, chlorine gas was not detected, which indicated that it was “consumed” in the chemical reactions.

Studies on thermochemical decomposition of cupric chloride have been reported by various researchers including Serban et al. (2004), and Ferrandon et al. (2010a). These studies are important for understanding the occurrence of chlorine as a possible side product during hydrolysis. Most studies were performed using thermogravimetric analyzers. As indicated by Serban et al. (2004), the reaction kinetics for CuCl_2 thermal decomposition is represented by a zero-order rate law with a pre-exponential factor $\mathcal{A} = 2.9 \times 10^7 \text{ min}^{-1}$ and an activation energy of $E = 102.2 \text{ kJ/mol}$. Therefore, based on the Arrhenius equation, the rate constant is $k = \mathcal{A} \times \exp(-E/RT)$.

6.5.4 Spray-Type Mini-Reactor for Hydrolysis (ANL)

A spray reactor has been developed at ANL as reported in several publications by Ferrandon et al. (2010a, b). The principle of the spray reactor system is illustrated in Fig. 6.41 and the main reactor characteristics are listed in Table 6.17. Because flow rates were relatively small, e.g., cupric chloride injection of 1–5 mL/h and liquid water at 0.5 mL/h, syringe pumps were used within the experimental setup.

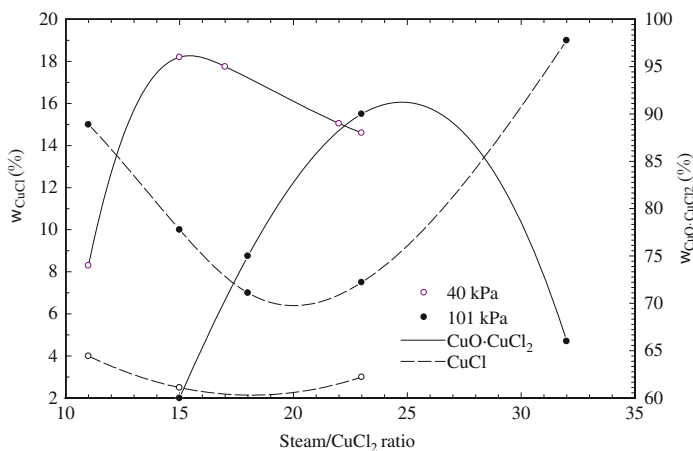


Fig. 6.44 Characterization of solid products of the hydrolysis reaction in terms of $\text{CuO} \cdot \text{CuCl}_2$ and CuCl concentrations by weight (w) [data from Ferrandon et al. (2010b)]

The temperature regulation system is capable of maintaining a constant temperature at the outer wall of the reactor. During the operation, due to continuous flow, the temperature varies axially from about 623 K at the upper heated side to 713 K at the lower side. The resulting solid products are collected at the reactor bottom and maintained at 423 K with electrical heating tape. After the experiments end, the solids are weighted and analyzed with specific methods (e.g., XRD). Two types of particle atomizers were used to spray the CuCl_2 from the top of the reaction vessel: a pneumatic nebulizer (which requires the use of a sweep gas) and an ultrasonic nozzle (which consumes electrical energy).

It was reported that an ultrasonic nozzle performs better than the nebulizer. The droplets formed by atomization with the ultrasonic nozzle have around a 25 μm average diameter. As observed in the experiments (by the use of SEM), during the reaction, the particles were broken down to 2–3 μm . The formation of a CuCl side product is mainly influenced by the steam-to- CuCl_2 ratio in the input stream; lower ratios are not good as they facilitate formation of CuCl . A ratio of 20:1 minimizes the CuCl formation to about 4 % by weight in the output stream. Furthermore, reduction of the operating pressure leads to an increased yield of copper oxychloride while it reduces the yield of the CuCl side product. This result—reported by Ferrandon et al. (2010b)—is illustrated graphically in the plot in Fig. 6.44.

At a reduced pressure, the maximum yield of copper oxychloride is obtained at a much lower steam/copper ratio (around 40 % steam reduction if one operates at 40 kPa with respect to 101 kPa). Ferrandon et al. (2010b) showed that the residence time of the particle in the reactor decreases when reducing the pressure. With a reduction of residence time, thermolysis of cupric chloride has a lower rate; therefore, less cuprous chloride is observed. The residence time decreases with a lower pressure because natural convection effects due to heat transfer within the reactor are diminished at lower pressure (Grash of number is lower at lower pressures).

6.5.5 Scaled-Up Hydrolysis Reactor and Test Loop (UOIT)

A hydrolysis step testing loop with a production capacity of about 1,000 times larger than lab tests performed for proof-of-concept studies has been built and tested at UOIT (see schematic diagram in Fig. 6.45). The test loop comprises a hydrolysis reactor, nitrogen flow line with a heater, high and low flow superheated steam lines, condensers for cooling the exit gas stream, gas–liquid separator, and a scrubber for noncondensable gases in the downstream region of the hydrolysis reactor. Nitrogen gas from cylinders is needed to preheat the cupric chloride during the experiment startup. Dehydrated cupric chloride particles are enclosed in the hydrolysis reactor (HR). The hydrolysis lines are heated electrically with an electric heater (EH) equipped with temperature controllers.

During the startup operation, nitrogen from the cylinder N_2 is supplied through line #1 and valve V_1 with a flow rate measured and regulated precisely with the flow-meter battery formed by the fine flow meter F_1 for low flow and the flow meter for a high flow rate F_2 . A pressure and temperature station is placed in order to determine the density of nitrogen just after the flow rate measurement point. Nitrogen is heated in the electric heater up to the reaction temperature which is reached by stream #4. A valve V_2 is used to close or open the hot nitrogen supply to the reactor. The main flow of steam is generated in electric steam generator ESG_1 and superheated in the electric superheater (ESH). Fresh water is supplied at #6 and saturated vapor is delivered in #7. If needed, for flow regulation or various procedures (e.g., start-up, shutdown), a part of the saturated steam is expelled via valve V_3 . A safety valve SV_1 is installed on the steam generator. The steam flow rate can be regulated via valve V_4 and measured by flow meter F_3 . Superheated steam is obtained at #13 at a temperature corresponding to the hydrolysis reaction. A secondary generator of saturated steam is also used for the purpose of tuning the experimental parameters. The steam is produced in electric steam generator ESG_2 which is supplied from the deionized water vessel DSV using the water pump (WP).

The flow rate of saturated steam in #17 is regulated by the valve V_6 . The hydrolysis reactor is supplied with nitrogen, steam, or superheated steam through line #19, valve V_8 , and line #20. This reactor is equipped with a safety valve SV_3 and a line for hot gas exhaust #21 on which the valve V_9 is placed. The product gases of the reaction are collected in #23 and directed toward a condensation battery formed from water-cooled condensers C_1 , C_2 , and C_3 . The booster condenser is C_1 , which lowers the reaction gas mixture temperature from 673 to 523 K. The booster condenser is followed by C_2 and C_3 coupled in parallel; they are used to condense the reaction gas mixture at maximum steam flow conditions. In line #29, the condensate comprises water, hydrochloric acid in the aqueous phase, and noncondensable gases. The gases are separated in the LGS at line #33 and passed to the scrubber SCRB. In the scrubber, the remaining traces of hydrochloric acid are absorbed in water and the remaining noncondensable gases are expelled out in #34. The liquid collected at the bottom of LGS in #30 accumulates in the liquid collection vessel (LCV) where the acid is neutralized by an alkaline solution. A sample port #32 is operated with the valve V_{12} installed in order to determine the concentration of hydrochloric acid during the experiments. A chiller is used to cool the

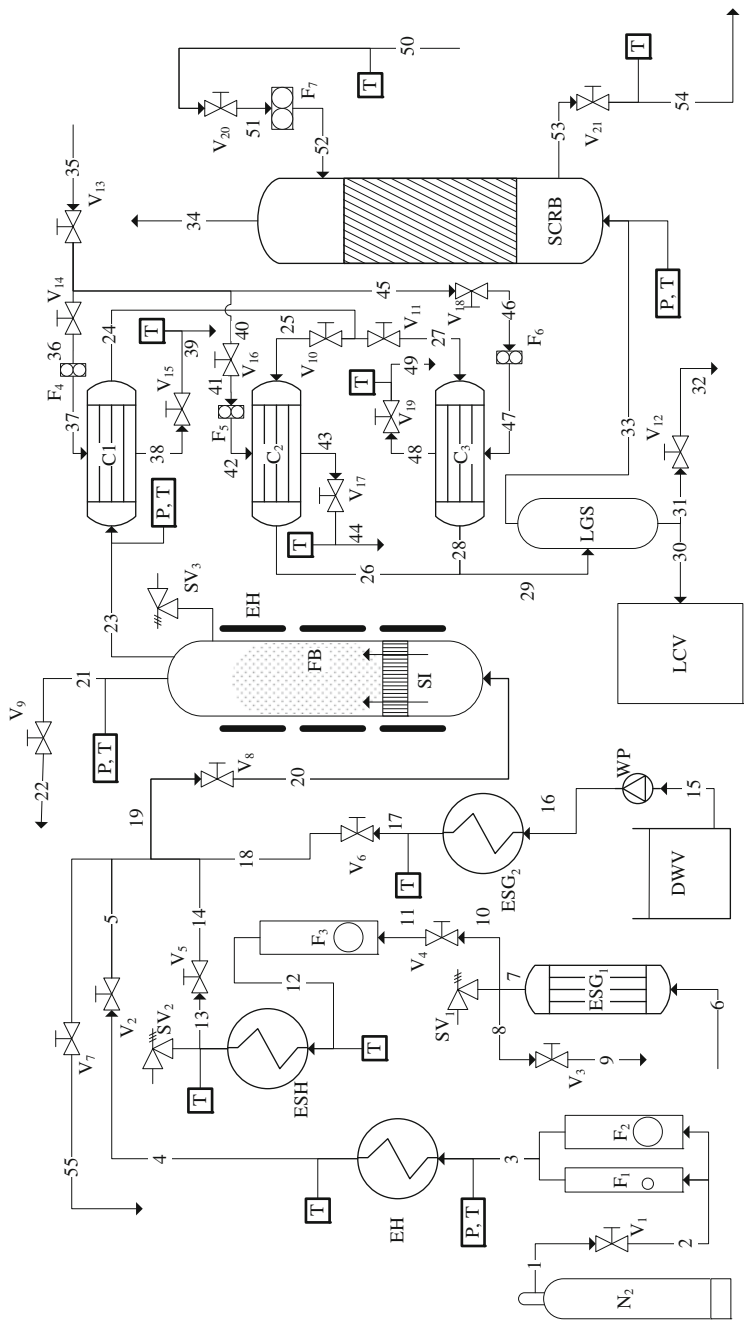


Fig. 6.45 Schematic of the hydrolysis test loop at UOIT



Fig. 6.46 Photograph of the hydrolysis test loop at UOIT

condenser with glycol–water coolant. Cold coolant is provided at #35 and divided in three streams, namely, #36, #40, and #46 toward each of the condensers. For each condenser, the flow rate of coolant and the temperature of coolant before and after the condenser are measured. Valves are installed to regulate the coolant flow. Cold water is supplied in #50 to the scrubber. The water flow rate and temperature are measured. There is also a valve V_7 which allows the exhaust of hot steam and/or nitrogen before its supply to the reactor. This maneuver may be necessary during experiments.

The photograph of the hydrolysis testing loop is presented in Fig. 6.46. Its general characteristics are given as follows.

- The main steam generator consisting of ESG_1 and ESH (see schematics from Fig. 6.45) has a capacity of 45 kW and produces superheated steam at above 773 K with a maximum mass flow rate capacity of 30 kg/h.
- The supplementary saturated steam generator ESG_2 produces 3 kg/h.
- Condenser C_1 is a high-temperature heat exchanger made of quartz glass.
- Condensers C_2 and C_3 —made in pyrex glass—have a heat transfer area of 1.2 m².

Two types of scaled-up reactors were developed at UOIT: a vertical fluidized bed reactor and a horizontal packed bed reactor. The photograph of the fluidized bed reactor for hydrolysis is presented in Fig. 6.47.

The vertical hydrolysis reactor is made of quartz glass with an internal diameter of 150 mm and height of 1.1 m. The solid cupric chloride reactant is contacted with superheated steam injected from the bottom of the reactor. A steam injection (SI) system (in Fig. 6.45) is placed at the lower side of the reactor. This is made in ceramic porous media with the role of flow distribution. Steam injected from below creates and maintains the fluidized bed at the upper side of the reactor. A tubular electrical furnace encloses the reactor. The furnace is made of ceramic fibers containing three electrical heating elements regulated independently. The power rating is 15 kW.

Fig. 6.47 Scaled-up fluidized bed reactor for CuCl_2 hydrolysis at UOIT



An additional test loop was devised for the study of fluidized bed hydrodynamics with the purpose of predicting the optimum fluidization parameters as well as to improve the reactor reliability and safety. The loop has a fluidized bed reactor of 65 cm height which is filled with cupric chloride powder and fluidized with a nitrogen–helium mixture with a density ratio equivalent to steam at high temperatures inside an actual reactor. Pressure probes were installed above the distributor plate and around 10,000 measured data points were collected during the tests. A photograph of the fluidized bed test facility for cold experiments is shown in Fig. 6.48.

Figure 6.49a shows the minimum fluidization velocity using a standard deviation of pressure fluctuations with Puncochar's method. The bed height between the pressure probes was $L = 0.065$ m and around 10,000 data points were collected. Figure 6.49a presents the mean values of pressure drop variation with gas velocity in the bed. The pressure drop values increase with gas velocity in the fixed bed range, after reaching the minimum fluidization velocity. The pressure drop does not increase for a higher gas velocity in the fluidized bed range.

The reaction tests performed with the scaled-up hydrolysis test loop require a start-up sequence. The boiler is cleared by flowing steam through a bypass line to the atmosphere before starting the experiment. Cupric chloride solids are fed into the hydrolysis reactor from the top. The solids are preheated with nitrogen which also fluidizes the bed. After heating the solids to the predetermined test temperature of the reaction, steam is fed into the reactor from the bottom. The reactant superheated steam is generated with the steam boiler and superheater to a required temperature before it is introduced into the reactor. The steam flow can be regulated



Fig. 6.48 Photograph of low-temperature fluidized bed apparatus for the hydrolysis reaction at UOIT

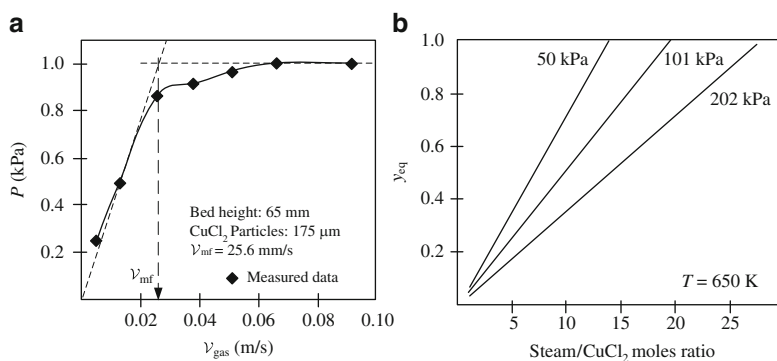


Fig. 6.49 Test results with the fluidized bed reactor at UOIT: minimum fluidization velocity (V_{mf}) of cupric chloride during cold experiments (a) and equilibrium conversion (y_{eq}) of cupric chloride (b) [data from Naterer et al. (2011a)]

in the measurement range of 3–30 kg/h. Nitrogen gas may be used during the tests to control the reaction.

The major products in the reaction step are copper oxychloride (solid) and HCl (gas). After the reaction, the HCl gas and unreacted steam are condensed using quartz and pyrex condensers for condensation. The noncondensable gases pass through a sodium hydroxide solution in the scrubber to completely remove traces of HCl gas, if any. The liquid separated from the gas–liquid separator is taken into a neutralization tank and neutralized with alkali solution. Reaction gas mixture samples are collected after the quartz condenser C_1 to monitor progress of the reaction. The formation of HCl gas is used to estimate the cupric chloride conversion in the reaction.

Before the tests, the anhydrous CuCl_2 powder size distribution and volume mean diameter were quantified with a particle analyzer. The reactant was analyzed for its purity using XRD analysis which determined that the purity is over 98 %.

The tests confirmed the steady production of copper oxychloride from solid/dehydrated cupric chloride. It was found that the cupric chloride conversion increases with a higher steam–copper ratio, temperature, and reduced pressure. This recorded trend is illustrated in Fig. 6.49b. The presence of hydrochloric acid in the input steam limits the conversion of solid. From the experimental studies, a key objective is to further reduce the excess steam requirement. Also, operating parameters need to be optimized to achieve the maximum copper oxychloride yield.

6.5.6 Hydrolysis Process Modeling and Simulations

Although there has been significant experimental research reported in the literature, the hydrolysis process of cupric chloride is not fully understood. From an engineering point of view, it is important to devise a hydrolysis reactor with low steam consumption, high conversion, and no side products. Thus, modeling studies of the process were conducted and additional numerical simulations aimed to help process understanding and design of a more efficient reactor. The research at ANL led to the formulation of a model for a hydrolysis spray reactor which was reported by Ferrandon et al. (2008). The model uses ASPEN Plus simulation software. The related research at UOIT was reported in a series of papers addressing various aspects such as:

- Hydrolysis reaction kinetics (Daggupati et al. 2010b)
- Diffusion of gaseous products through CuCl_2 particle surface layer (Daggupati et al. 2010a)
- Conversion of solid cupric chloride reacting particles during hydrolysis (Daggupati et al. 2011a)
- Fluid-particle mass transport modeling in the fluidized bed hydrolysis reactor (Haseli et al. 2009)
- Hydrodynamics of fluidized bed in the hydrolysis reactor (Haseli et al. 2008)

In the modeling results at ANL for the spray reactor, the APEN Plus simulations extended the understanding of spray operation and to better set the operating parameters. Figure 6.50 shows these results which indicate the cupric chloride conversion with temperature for three steam vs. CuCl_2 molar ratios. According to these results, the conversion of cupric chloride is very high (near 100 %) at 673 K for a steam-to- CuCl_2 ratio of 17. The simulation predicted at the same condition that CuCl side product is generated in amounts as low as 2 % (molar) with respect to the cupric chloride. At temperatures higher than 673 K, the molar fraction of CuCl in the product stream increases fast and reaches ~17 % at 723 K. If the steam-to- CuCl_2 ratio (x_s) is set at higher values than 17, then the maximum conversion occurs at lower temperatures, e.g., for $x_s = 30$, the maximum occurs at around 623 K.

Mechanistic models that account for transport phenomena and reaction kinetics are needed for improving the performance of the reactors. Two main reactions must

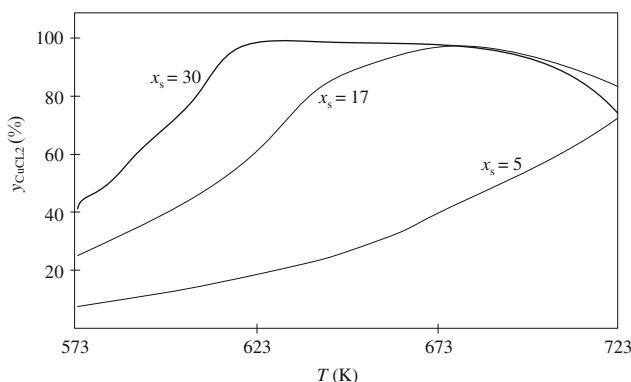


Fig. 6.50 ASPEN Plus simulation results with spray reactor developed at ANL [data from Ferrandon et al. (2008)]

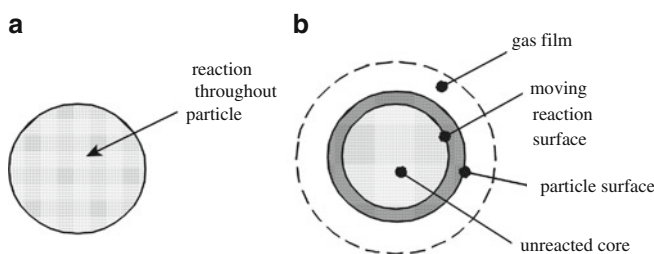


Fig. 6.51 Gas–solid reaction models: (a) uniform conversion model (UCM) and (b) shrinking core model (SCM)

be considered simultaneously in a model that accounts for gas-to-solid diffusion phenomena and gas–solid chemical reactions for hydrolysis process.

1. The hydrolysis reaction itself—with steam diffusion toward the core of a solid cupric chloride particle, steam consumption in the reaction, hydrochloric acid release, and diffusion toward particle surface.
2. The thermolysis of cupric chloride—with chlorine production and diffusion toward the particle surface; in addition, cuprous chloride is generated; depending on the reaction conditions, this can be solid or liquid (molten salt) or it can sublime.

Any gas–solid reaction can be modeled based on two well-known models: the uniform conversion model or the shrinking core model. These mechanistic models are explained with the help of Fig. 6.51 where it is shown for gas reactant diffusion of a uniform-reaction model (Fig. 6.51a) and the solid-layer configuration of a reacting particle for a shrinking core model (Fig. 6.51b). A uniform-reaction model is used when the diffusion of gaseous reactant into a particle is much faster than the chemical reaction.

The solid reactant is consumed nearly uniformly throughout the particle. On the other hand, a shrinking core model is used if the diffusion of gaseous reactant is

much slower and it restricts the reaction zone to a thin layer that advances from the outer surface into the particle. Diffusion of gaseous reactant occurs through a film surrounding the particle, after which the reactant penetrates and diffuses through a layer of ash to the surface of the unreacted core. The shrinking core model for spherical particles predicts the reaction of gaseous reactant with solid at the particle surface, and diffusion of gaseous products through the ash, back to the exterior surface of the solid. The reaction conditions are assumed isothermal, with a constant pellet size, and pseudo-steady-state conditions that are valid for gas–solid reactions.

The conversion of a particle of CuCl_2 in the hydrolysis reactor can be expressed geometrically based on the shrinking core reaction model as the ratio between the outer shell, consisting of copper oxychloride product, and the particle volume:

$$X = 1 - (d_c/d_o)^3, \quad (6.32)$$

where d_c is the diameter of the unreacted core and d_o is the particle radius. As reported by Daggupati et al. (2009), the maximum equilibrium conversion is given by

$$X_{\text{eq}} = \left(\frac{K_{\text{eq}} x_s^2}{4P + K_{\text{eq}}} \right)^{0.5},$$

where K_{eq} is the equilibrium constant calculated based on the Gibbs free energy at the reaction temperature, P is the operating pressure, and x_s is the steam-to- CuCl_2 ratio. The reaction rate for water consumption can be expressed in four different ways as indicated by Daggupati et al. (2010b), namely,

$$r_{\text{H}_2\text{O}} = \begin{cases} k_1 \left(P_{\text{H}_2\text{O}} - \frac{P_{\text{HCl}}^2}{K_{\text{eq}}} \right) \\ k_2 C_{\text{H}_2\text{O}} \\ D_{\text{e,H}_2\text{O}} \left(\frac{d^2 C_{\text{H}_2\text{O}}}{d\tau^2} + \frac{2}{\tau} \frac{dC_{\text{H}_2\text{O}}}{d\tau} \right) \\ D_{\text{e,HCl}} \left(\frac{d^2 C_{\text{HCl}}}{d\tau^2} + \frac{2}{\tau} \frac{dC_{\text{HCl}}}{d\tau} \right), \end{cases} \quad (6.33)$$

where $k_{1,2}$ are the reaction rate constants, which are assumed to follow the Arrhenius law for temperature dependence; C are molar concentrations (moles per volume); D_e is the effective diffusivity; τ is the radial coordinate; and $P_{\text{H}_2\text{O}}$ is the partial pressure of steam. Based on (6.33), the following compact expression for CuCl_2 conversion for the kinetic-controlled regime during hydrolysis was reported by Daggupati et al. (2010b):

$$\frac{dX}{dt} = \frac{3(1-X)^{2/3}}{d_o \times \rho_{\text{CuCl}_2}} \times k_1 \left[\frac{x_s - X}{x_s + X} P - \frac{1}{K_{\text{eq}}} \left(\frac{2X}{x_s + X} P \right)^2 \right]. \quad (6.34)$$

Table 6.18 Parameters for kinetic modeling of hydrolysis process

Parameter	Symbol	Value	Units
Rate constant for kinetically controlled regime	k_1	2.2	mmol/m ² s
Rate constant for first rate reaction	k_2	0.1	mmol/s
Effective diffusivity of chloride at CuCl ₂ decomposition	D_e	2.4×10^{-9}	m ² /s

Source: Daggupati et al. (2010b)

If one assumes diffusion control for kinetics of the hydrolysis process, then a first-order reaction rate applies. In this case, the CuCl₂ conversion is given by

$$\frac{dX}{dt} = \frac{3(1-X)^{2/3}}{d_o \times \rho_{\text{CuCl}_2}} k_2 C_{\text{H}_2\text{O}}. \quad (6.35)$$

The decomposition is analyzed by diffusion through the product layer to control the reaction. The total gas pressure is assumed to be constant and the pellet is assumed spherical. For the cupric chloride decomposition reaction, the rate of diffusion of chlorine through the product layer, based on the assumption of equimolar counter diffusion, is

$$r_{\text{Cl}_2} = \frac{2\pi d_o d_c D_e}{d_o - d_c} (C_{\text{Cl}_2,i} - C_{\text{Cl}_2,b}), \quad (6.36)$$

where $C_{\text{Cl}_2,i}$ is the chlorine concentration at the interface and $C_{\text{Cl}_2,b}$ is the chlorine concentration in the bulk phase. The equilibrium constant of the CuCl₂ decomposition reaction is related to the partial pressure of chlorine, according to $K_{\text{eq}} = P_{\text{Cl}_2}$. The CuCl₂ dissociates until the partial pressure of Cl₂ reaches the equilibrium constant, K_{eq} , at a given temperature. Since the rate of chlorine production is equated to the rate of particle shrinking during decomposition, the following equation can be obtained (Daggupati et al. 2010b):

$$3D_e t \left(\frac{K_{\text{eq}}}{RT_b} - C_{\text{CuCl}_{2b}} \right) = \rho_{\text{CuCl}_2} d_o^2 \left(1 - 3(1 - X_d)^{2/3} + 2(1 - X_d) \right), \quad (6.37)$$

where R is the universal gas constant, T_b is the temperature in bulk phase (Kelvin), t is time, and X_d is the conversion during the decomposition reaction.

In the above equations for conversion, (6.34), (6.35), and (6.37), the rate constants k_1 and k_2 and the diffusion coefficient D_e must be specified. Daggupati et al. (2010b) fitted the models to the experimental data of Ferrandon et al. (2008) of cupric chloride hydrolysis at 650 K, for particle sizes of 150–250 μm . The results are summarized in Table 6.18. The comparison between predicted and measured data can be observed in Fig. 6.52.

Fig. 6.52 Comparison between predicted and measured conversion rates of CuCl_2 hydrolysis and CuCl_2 thermolysis [measured data from Ferrandon et al. (2008), predicted data from Daggupati et al. (2010b)]

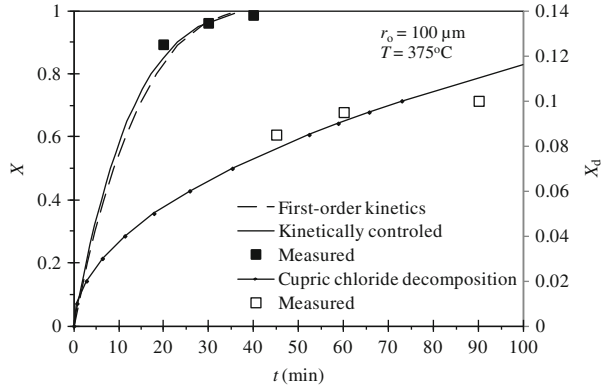
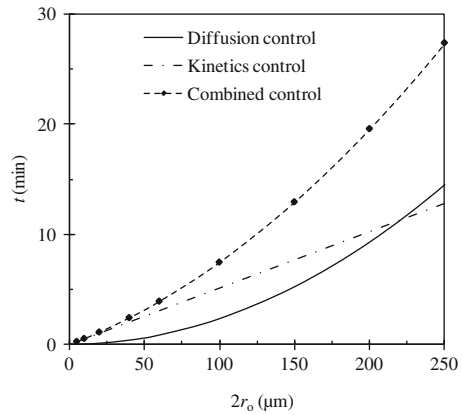


Fig. 6.53 Variation of hydrolysis reaction time with particle size as predicted by a shrinking core model [data from Daggupati et al. (2010a)]



The reaction times for the cases of (1) diffusion control of reaction, (2) reaction kinetics control, and (3) combined control, are presented in Daggupati et al. (2010a). The reaction time is expressed by

$$\begin{cases} \tau_d = \frac{\rho d_o^2}{3D_e C_{\text{H}_2\text{O}}}, & \text{for diffusion controlled reaction} \\ \tau_r = \frac{\rho d_o}{k C_{\text{H}_2\text{O}}}, & \text{for kinetics controlled reaction} \\ \tau_c = \frac{\rho d_o}{C_{\text{H}_2\text{O}}} \times \left(\frac{1}{k} + \frac{d_o}{3D_e} \right), & \text{for combined control,} \end{cases} \quad (6.38)$$

where k is the intrinsic rate of reaction.

Figure 6.53 illustrates the influence of CuCl_2 particle diameter on the reaction time for the three control cases of chemical reaction. The time required for the complete conversion of solids increases with particle size. The diffusion time is smaller than the reaction control time at a smaller particle size, with an increase in

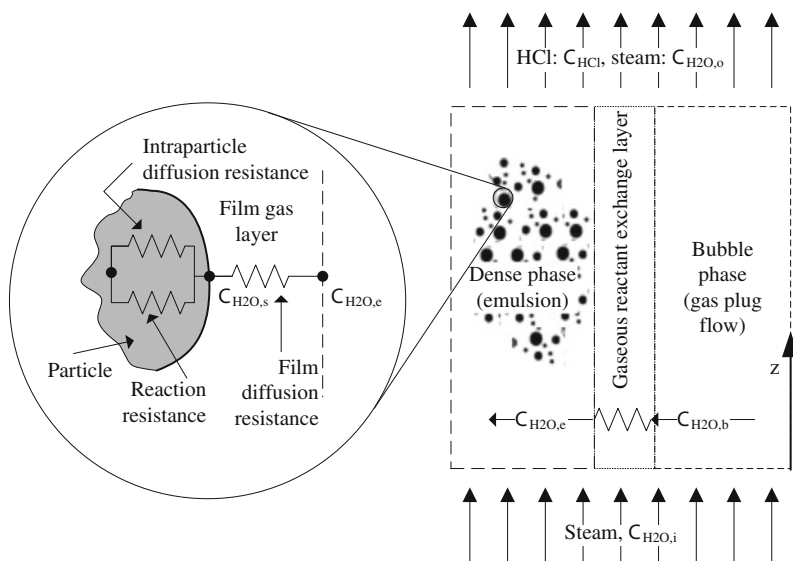


Fig. 6.54 Schematic model of transport processes in a reacting fluidized bed for hydrolysis

particle size, as the diffusion time dominates over the reaction time. With a combined resistance, the required time for complete conversion of solid is much higher than the other two resistances, and it increases with particle size.

A hydrodynamic model of reacting cupric chloride particles in a fluidized bed reactor has been developed by Haseli et al. (2008, 2009). Consider that steam at a concentration $C_{H_2O,i}$ is fed into a fluidized bed reactor, which consists of bubble and emulsion phases. The steam reactant is transferred from the bubble phase (with a concentration bulk concentration $C_{H_2O,b}$) to the emulsion phase (with a lower emulsion-phase concentration $C_{H_2O,e}$) to react with particles of $CuCl_2$ which are fluidized in the bed. The schematic of the process is presented in Fig. 6.54. It was assumed that a solid particle S is made of an active reactant solid particle C , and nonreactive material D . The transport resistances are the bubble to emulsion resistance, external film resistance around the solid particle, and interparticle resistance. The reactor contains particles that have spent different periods inside the bed, and hence they have a distribution of conversion.

The predicted steam and $CuCl_2$ particle conversions at various superficial gas velocities and three typical bed inventories predicted by Haseli et al. (2009) are shown in Fig. 6.55. The solid conversion increases with the fluidizing gas velocity, since the solid particles are more immersed with steam. On the other hand, however, the steam conversion decreases as its superficial velocity increases. For a certain quantity of bed inventory and constant particle feed rate, a higher superficial velocity means a higher gas flow rate, which consequently results in less conversion of steam. Furthermore, from Fig. 6.55, a higher bed inventory improves the conversion of both reactants. At given feed rates of reactants, the mean

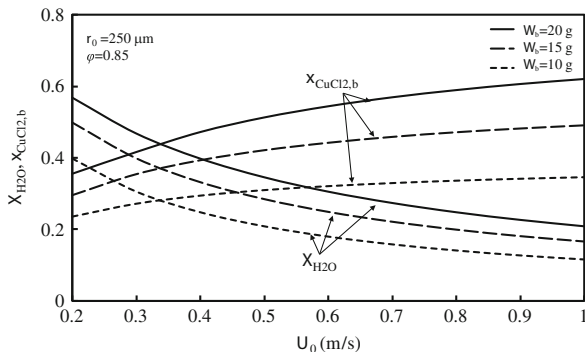


Fig. 6.55 Prediction of conversion rates of gaseous and solid reactants with UCM for three bed inventories W_b in a benchtop fluidized bed reactor of 2.66 cm/16.5 cm bed diameter/height, $d_0 = 250 \mu\text{m}$ particle average diameter with $\phi = 0.85$ sphericity, and particle mass flow rate at the inlet of $\dot{m}_i = 0.9 \text{ g/s}$ [data from Haseli et al. (2009)]

residence time, τ , increases as the bed inventory rises. Thus, the contact opportunity for both reactants increases. In Fig. 6.55, a uniform conversion model (UCM) has been used for the predictions. The steam conversion X_g is defined by

$$X_{\text{H}_2\text{O}} = 1 - \frac{C_{\text{H}_2\text{O},o}}{C_{\text{H}_2\text{O},i}}. \quad (6.39)$$

The average conversion of solid particles in the bed $x_{\text{CuCl}_2,b}$ depends on the conversion at the inlet conditions $x_{\text{CuCl}_2,0}$ and mass fraction of solid reactant in the fed stream $Y_{\text{CuCl}_2,0}$ according to

$$x_{\text{CuCl}_2,b} = x_{\text{CuCl}_2,0} + X_{\text{H}_2\text{O}} \times a \times (1/Y_{\text{CuCl}_2,0} - x_{\text{CuCl}_2,0}), \quad (6.40)$$

where a is a dimensionless parameter characterizing the fluidized bed, defined by Haseli et al. (2008), through the following relationship:

$$a \times \dot{m}_i = 2 \times \mathcal{V}_0 \times A \times M \times C_{\text{H}_2\text{O},i}, \quad (6.41)$$

where M is molecular mass of CuCl_2 , A is the cross-sectional area of the bed, \mathcal{V}_0 is the superficial gas velocity, and \dot{m}_i is the inlet flow rate of solids.

The mechanism of heat transfer between the gas and a particle, and/or bed of particles, was analyzed by Daggupati et al. (2011a, b). The heat transfer in a gas–solid two-phase flow undergoing a chemical reaction within a fluidized bed is determined by simultaneously solving the mass and energy balance equations for the bed. The important process parameters are the steam-to-cupric chloride mole ratio, superficial velocity of steam through the fluidized bed at a given mass flow rate of solid, and the reaction/bed temperature. In order to maintain the hydrolysis reaction at a required temperature, the amount of heat required for the endothermic

reaction at a given operating condition should be supplied externally to maintain isothermal conditions. In practice, removal/input of reaction heat to/from a fluidized bed is usually accomplished by an immersion surface, such as heat transfer tubes that carry cooling/heating fluids.

An alternative approach is to provide the required heat of reaction into the fluidized bed reactor by supplying hot fluidizing gas with an inlet temperature higher than the bed temperature. Due to direct contact of steam with solid particles, this method of heat transfer can be more efficient than utilizing a submerged surface. The steam temperature must be maintained below 423 °C to avoid melting of small quantities of cuprous chloride (CuCl) formed due to the decomposition of cupric chloride during the hydrolysis process. At temperatures above the melting point of cuprous chloride, the solids agglomerate and reduce the bed performance.

Relevant modeling parameters for the hydrolysis reactor of the fluidized bed configuration are listed and defined in Table 6.19. A modeling case study is considered by Daggupati et al. (2011a, b) which refers to the operating conditions of the scaled-up hydrolysis reactor at UOIT. The parameters and operating conditions for the hydrolysis reaction for the case study are listed in Table 6.20.

Based on the predicted results, the required steam inlet temperature to maintain the reactor at a desired temperature under the conditions of maintaining an endothermic reaction is indicated in Fig. 6.56. The steam inlet temperature depends on the melting or the decomposition temperature of solid components of the reaction mixture in the bed. The melting point of the solid reactant, CuCl₂, is ~771 K. The solid hydrolysis reaction product, namely, the copper oxychloride Cu₂OCl₂, decomposes to CuO and CuCl₂ at ~673 K. If the steam inlet temperature is higher than the melting point of its decomposition product, CuCl (696 K), the solid reactant may agglomerate or coalesce into a larger combined mass, thereby resulting in poor fluidization behavior. The inlet temperature is very important to maintain the required superficial velocities inside the reactor for good fluidization.

Figure 6.57 shows the time required to raise the temperature of a single cupric chloride particle from room temperature to the fluidized bed temperature, T_b . This is determined based on an energy balance equation that leads to the following equation:

$$t = \frac{mc_p}{hA} \ln((T_b - T_p)/(T_b - T_{pb})), \quad (6.42)$$

where T_p is the temperature of the cold particle and T_{pb} is the temperature of the particle in the bed. As observed in the figure, the time required to raise the solid temperature decreases with fluidization velocity. It is much lower than the time estimated based on the overall bed heat transfer coefficient.

Figure 6.58 shows the variation of conversion of cupric chloride solid and steam with superficial velocity, solid flow rate, and temperature. From this figure, it appears that a higher temperature and steam flow rate increase the solid conversion, and they decrease at a higher solid rate. The conversion of steam is constant for a given temperature, irrespective of the mole ratio of steam, and it only increases with reaction temperature. As shown in Daggupati et al. (2011a, b) the cupric chloride

Table 6.19 Modeling parameters for fluidized bed reactor for CuCl_2 hydrolysis

Parameter	Correlation	Units
Minimum fluidization velocity	$\mathcal{V}_{\text{mf}} = \left[33.7^2 + 0.0408 \frac{d_p^3 \rho_g s (\rho_p - \rho_g)}{\mu_g^2} \right] \frac{\mu_g}{d_p \rho_g}$	m/s
Bubble relative velocity	$\mathcal{V}_{\text{br}} = 0.711 \times (g d_b)^{1/2}$	m/s
Bubble velocity	$\mathcal{V}_b = 1.6 [(\mathcal{V}_o - \mathcal{V}_{\text{mf}}) + 1.13 d_t^{1.35}] d_t^{1.35} + 0.711 (g d_b)^{0.5}$	m/s
Bubble diameter	$d_b = d_{\text{bm}} - (d_{\text{bm}} - d_{\text{bo}}) e^{-0.3 L_t / D_t}$ $d_{\text{bm}} = \min \left\{ 0.0065 \left[\frac{\pi}{4} d_t^2 (\mathcal{V}_o - \mathcal{V}_{\text{mf}}) \right]^{0.4}, d_t \right\}$ $d_{\text{bo}} = \frac{0.0278}{g} (\mathcal{V}_o - \mathcal{V}_{\text{mf}})^2$ for $d_{\text{bo}} > l_{\text{or}}$ $d_{\text{bo}} = \frac{0.082}{g^{0.2}} \left[\frac{\mathcal{V}_o - \mathcal{V}_{\text{mf}}}{N_{\text{or}}} \right]^{0.4}$ for $d_{\text{bo}} \leq l_{\text{or}}$ $d_{b,\text{av}} = \frac{1}{L_t} \int_0^{L_t} d_b dz$	m
Bubble fraction in the bed	$\epsilon_b = \frac{\mathcal{V}_o - \mathcal{V}_{\text{mf}}}{\mathcal{V}_b - \mathcal{V}_{\text{mf}}}$, for fast bubbles	—
Interchange coefficient between bubble and emulsion	$\mathcal{K}_{\text{be}} = \frac{2 \mathcal{V}_{\text{mf}}}{d_b} + 5.7 (D_g \epsilon_{\text{mf}})^{0.5} g^{0.25} / d_b^{1.25}$, freely bubbling beds	s^{-1}
Bed height	$L_t = \frac{L_{\text{mf}}}{(1 - \epsilon_b)}$	m
Number of transfer units	$\text{NTU} = \frac{K_{\text{be}} \epsilon_{\text{b}, L_t}}{\mathcal{V}_o}$	—
Excess gas flow ratio	$\beta = \frac{\mathcal{V}_o - \mathcal{V}_{\text{mf}}}{\mathcal{V}_o}$	—
Concentration efficiency	$N_a = \frac{C_i - C_o}{C_i - C_e} = 1 - \beta \exp \left(-\frac{\text{NTU}}{\beta} \right)$	—
Dimensionless parameter, reactor level	$\alpha = 2 U_o A_{\text{c,bed}} C_i M_p / \dot{m}_i$	—
Gas concentration, emulsion phase	$C_e = C_i (1 - X_g / N_a)$	mol/m^3
Kinetic coefficient	$K_{\text{re}} = b \frac{M_p}{\rho_p} k_o C_e^n$	s^{-1}
Damkohler number at reactor scale	$D_{\text{as}} = \frac{K_{\text{re}} W_b}{\dot{m}_o} = K_{\text{re}} \bar{t}$	—
Dimensionless factor	$\lambda = \frac{D_{\text{as}}}{1 - D_{\text{as}}}$ or $\frac{K_{\text{re}} W_b}{F_o - r_{\text{c,b}}}$	—
Overall rate of reaction in the bed	$r_{\text{c,b}} = \dot{m}_o \lambda \left[\left(1 - \frac{\lambda}{3} \right)^2 + \left(\frac{\lambda}{3} \right)^2 - 2 \left(\frac{\lambda}{3} \right)^2 \exp \left(-\frac{3}{\lambda} \right) \right]$	kg/s
Equilibrium conversion of gas	$X_{\text{e,g}} = 3 \times 10^{-7} e^{0.0175 T}$, $T = 573 - 673 \text{ K}$, at 101 kPa	—
Gas conversion	$X_g = \min \left\{ \frac{1}{\alpha} \left(1 - \frac{D_{\text{as}}}{\lambda} \right), X_{\text{e,g}} \right\}$, $X_g \leq X_{\text{e,g}}$	—
Solid conversion	$X_c = \alpha X_g$	—

Source: Daggupati et al. (2011a).

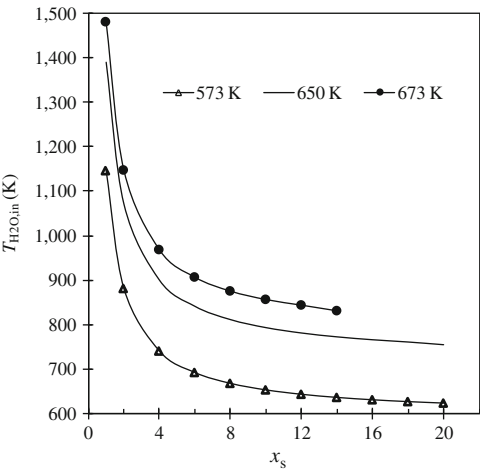
solid conversion is limited to 26 % at a 20 mole ratio of steam at 573 K. However, at 673 K, the required mole ratio is 13.5. A three-step calculation procedure is followed for the conversion of steam and cupric chloride solid. The procedure involves (1) calculation of the gas conversion, (2) calculation of the solid conversion, and (3) equating the gas conversion with the solid conversion, taking fluid flow factors of the fluidized bed into consideration.

Table 6.20 Parameters and operating conditions for a case study with the UOIT fluidized bed reactor for cupric chloride hydrolysis

Parameter	Symbol	Range	Units
Particle diameter	d_p	200	μm
Reactor diameter	d_t	0.15	M
Weight of bed material	W_b	2.24	Kg
Mass flow rate of solid	\dot{m}	1.5–5.0	kg/s
Minimum fluidization velocity	V_{mf}	0.0343	m/s
Gas velocity	V_0	0.0343–0.4	m/s
Steam initial concentration	C_i	0.0178	kmol/m^3
Order of reaction for steam	n	1	–
Density of cupric chloride solid	ρ_p	3,386	kg/m^3
Reaction temperature	T	573–673	K
Reaction pressure	P	101	kPa

Source: Daggupati et al. (2011a, b, c)

Fig. 6.56 Variation of steam inlet temperature with mole ratio of steam and mass flow rate [data from Daggupati et al. (2011a)]



6.6 Thermolysis Reaction Step

6.6.1 Reaction Kinetics Thermodynamics

The thermolysis process—thermal decomposition of copper oxychloride—is an endothermic solid conversion process which generates oxygen gas and molten cuprous chloride. Consequently, in a thermolysis reactor for copper oxychloride, three phases coexist: solid, liquid, and gas. Copper oxychloride particles decompose into oxygen gas bubbles and molten CuCl. The reactant particles absorb heat from the surrounding molten CuCl salt. Gaseous products leaving the oxygen reactor include oxygen gas and CuCl vapor, and potentially products from side reactions, such as Cl₂ gas, HCl gas, and H₂O vapor (in trace amounts). The other

Fig. 6.57 Time required to raise the solid particle temperature from 298 K to the bed temperature of 673 K [data from Daggupati et al. (2011a)]

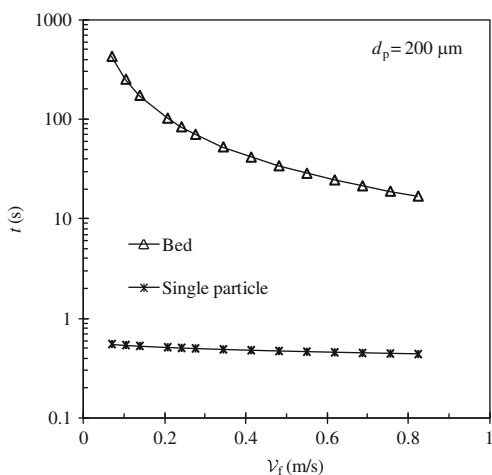
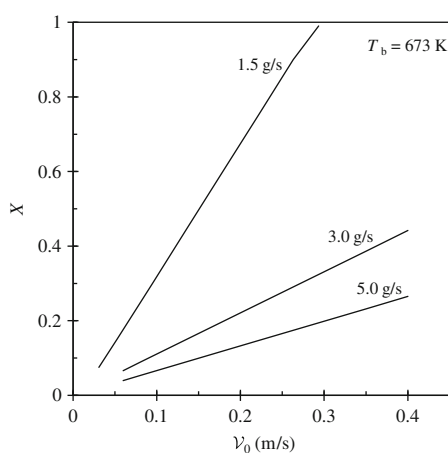


Fig. 6.58 Conversion of solid cupric chloride particles vs. superficial velocity [data from Daggupati et al. (2011a, b, c)]

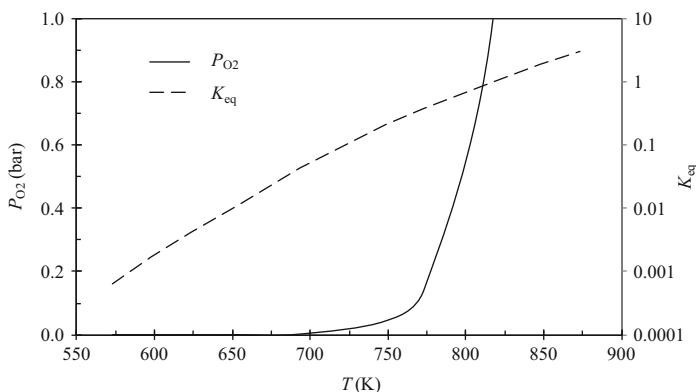


liquid/solid products leaving the reactor are molten CuCl , unreacted solid CuCl_2 from the upstream hydrolysis reaction, as well as reactant particles entrained by the flow of molten CuCl .

The decomposition mechanism is due to a number of elementary reactions as indicated in Table 6.21. Copper oxychloride decomposes thermally after 673 K and one of the released products is cupric oxide. One first pattern of decomposition occurs according to reaction #1 listed in the table: 2 mol of copper oxychloride generate 2 mol of cupric oxide solid and 1 mole of cupric chloride plus 1 mol of cuprous chloride (solid or molten, depending on the temperature), plus 1/2 mol of chlorine gas. This process is identified in Nixon et al. (2011) to occur immediately above 673 K and it may be observed up to 753 K. At higher temperatures, two other competing reactions occur in the range of 753–823 K: one desired reaction of cupric oxide chlorination (#3 or #4) and an undesired reaction of cupric chloride thermolysis (#2).

Table 6.21 Elementary reactions of copper oxychloride thermal decomposition

ID	Process	Elementary reaction	Temperature range (K)
1	Decomposition	$2\text{CuO} \cdot \text{CuCl}_2(\text{s}) \rightarrow 2\text{CuO}(\text{s}) + \text{CuCl}_2(\text{s}) + \text{CuCl}(\text{s}, \text{l}) + 0.5\text{Cl}_2(\text{g})$	673–753
2	Thermolysis	$\text{CuCl}_2(\text{s}) \rightarrow \text{CuCl}(\text{l}) + 0.5\text{Cl}_2(\text{g})$	753–823
3	Chlorination	$\text{CuO}(\text{s}) + 0.5\text{Cl}_2(\text{g}) \rightarrow \text{CuCl}(\text{l}) + 0.5\text{O}_2(\text{g})$	753–823
4	Chlorination	$\text{CuO}(\text{s}) + \text{Cl}_2(\text{g}) \rightarrow \text{CuCl}_2(\text{l}) + 0.5\text{O}_2(\text{g})$	>753
5	Oxidation	$\text{CuCl}(\text{l}) + 0.5\text{O}_2(\text{g}) \rightarrow \text{CuO}(\text{s}) + 0.5\text{Cl}_2(\text{g})$	>823
6	Decomposition	$\text{CuO} \cdot \text{CuCl}_2(\text{s}) \rightarrow \text{CuO}(\text{s}) + \text{CuCl}_2(\text{s})$	673–753
7	Oxidation	$2\text{CuCl}(\text{l}) + 0.5\text{O}_2(\text{g}) \rightarrow \text{CuO} \cdot \text{CuCl}_2(\text{s})$	>823
8	Decomposition	$\text{CuO} \cdot \text{CuCl}_2(\text{s}) \rightarrow \text{CuO}(\text{s}) + \text{CuCl}(\text{s}, \text{l}) + 0.5\text{Cl}_2(\text{g})$	>673

**Fig. 6.59** Equilibrium constant and partial pressure of oxygen released by the reaction of copper oxychloride thermolysis

Chlorination consumes chlorine and releases the oxygen product. However, the competing reaction of thermolysis generates additional chlorine as an undesired side product. Over 823 K, the kinetics of the oxidation reaction (#5) of cuprous chloride becomes favorable which consumes oxygen and generates chlorine. Another possible reaction of thermal decomposition is mentioned by Serban et al. (2004); it consists of reaction #6 which generates cupric oxide and cupric chloride at temperatures above 673 K. The generated cupric chloride decomposes thermally according to process #2 and produces chlorine, which in a stoichiometric amount with cupric oxides is consumed in chlorination process #3. Marin et al. (2011a, b) studied also the reverse reaction which can occur in the thermolysis reactor according to process #7. This process is a chemical reaction with a negative Gibbs free energy over the range of operating temperatures of interest. Therefore, it must be disfavored by appropriately setting the reaction parameters. Marin et al. (2011a) mentioned another decomposition pathway, process #8.

The variation of equilibrium constant, $K_{\text{eq}}(T) = -\Delta G^0(T)/RT$, of the thermal decomposition reaction, $\text{CuO} \cdot \text{CuCl}_2(\text{s}) \rightarrow 2\text{CuCl}(\text{s}, \text{l}) + 0.5\text{O}_2(\text{g})$, is presented in Fig. 6.59. Based on reaction stoichiometry, $K_{\text{eq}} \times P = P_{\text{O}_2}$, where P is the operating pressure and P_{O_2} is the partial pressure of oxygen. If the operating pressure is 1 bar,

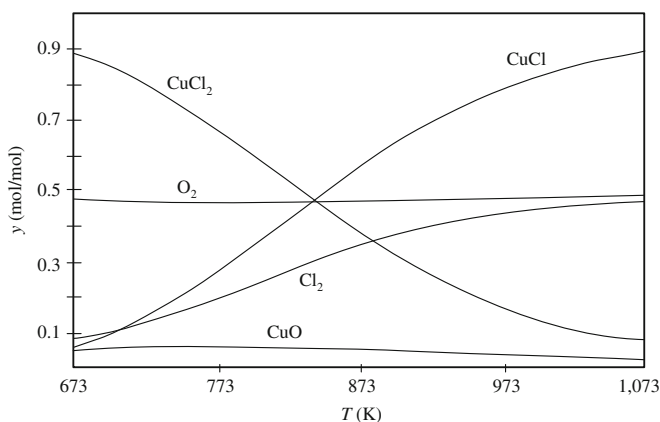


Fig. 6.60 Equilibrium molar fractions of the equimolar CuO/Cl₂ system [data from Nixon et al. (2011)]

it yields the partial pressure of oxygen and its variation with temperature as indicated on the graph in Fig. 6.59. It can be observed that the release of oxygen at equilibrium becomes significant only after 700 K.

Thermogravimetric experiments reported by Nixon et al. (2011) revealed that the decomposition of copper oxychloride becomes important at temperatures higher than 753 K, which is relatively close to the temperature at which cupric chloride starts to decompose. It can be concluded that cupric oxide and cupric chloride must be formed in the first phase of copper oxychloride decomposition. This confirms the assumption made by Serban et al. (2004) that the decomposition starts with processes #6 and #2 (Table 6.21) simultaneously. Chlorine is rapidly consumed in a subsequent reaction via processes #3 and #4 as mentioned above. Chlorine is consumed as per the experiments of Serban et al. (2004) and Nixon et al. (2011). In addition, equilibrium calculations of equimolar CuO and Cl₂ system were performed. As indicated in Fig. 6.60, at lower temperatures, formation of CuCl₂ with oxygen release is favored thermodynamically with respect to the formation of CuCl.

Consumption of chlorine in the $\text{CuO(s)} + \text{Cl}_2\text{(g)} \rightarrow \text{CuCl}_2\text{(l)} + 0.5\text{O}_2\text{(g)}$ reaction has been studied by Serban et al. (2004). The rate of this reaction is expressed by

$$r = k \times \left(P_{\text{Cl}_2}^{0.25} - P_{\text{O}_2}/K_{\text{eq}} \right), \quad (6.43)$$

where the rate of reaction k is determined by Serban et al. (2004) as $\sim 10 \text{ mmol/g}_{\text{CuO}} \text{ h bar}^{0.25}$.

6.6.2 Scaled-Up Thermolysis Reactor (UOIT)

A large reactor and experimental test loop have been developed at UOIT to conduct thermolysis experiments of copper oxychloride at a scale 1,000 times larger than

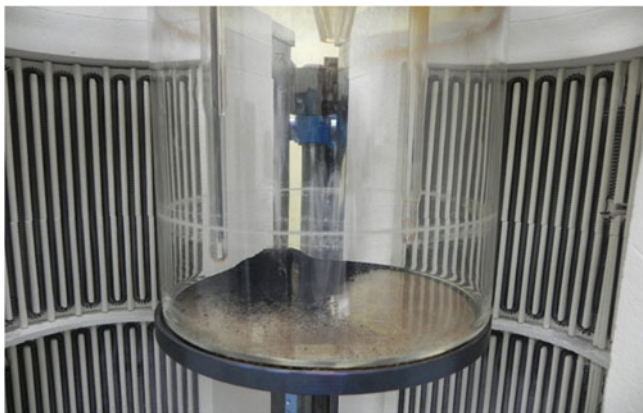


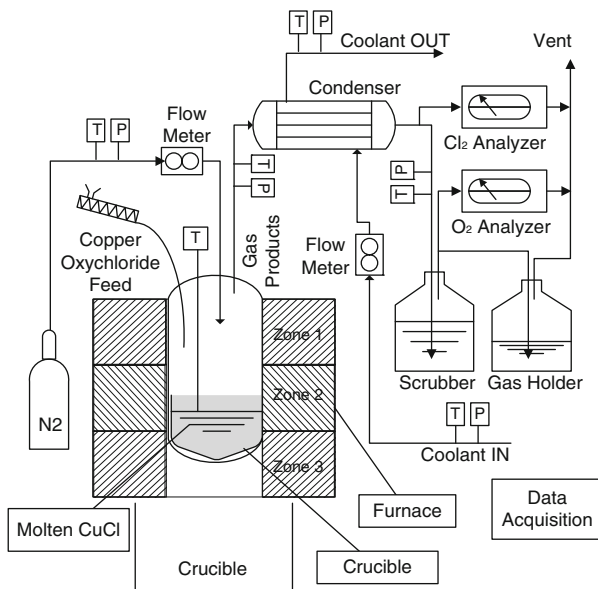
Fig. 6.61 Scaled-up thermolysis reactor at UOIT, charged with copper oxychloride

prior proof-of-principle experiments (Serban et al. 2004, Lewis et al. 2005a, b, Nixon et al. 2011). The reactor consists of a vertical cylindrical vessel made of stainless steel 316 and hastelloy C. It contains a crucible fabricated in ceramic where the sample of copper oxychloride is placed. There is also a secondary containment to the sample that allows for channeling of the gases outside via a liquid seal that maintains a backpressure within the chamber slightly above atmospheric pressure. This method is used to prevent gases from outside to enter the reactor during tests. A photograph of the reactor is shown in Fig. 6.61. It is placed in an electrical furnace with three heating zones able to control the temperature in the range of 300–1,273 K. The furnace can operate within 1 °C of the target temperature. The schematic of the thermolysis test loop in which the reactor is installed is shown in Fig. 6.62 and a photograph in Fig. 6.63.

Copper oxychloride powder is placed in a cleaned crucible prior to the experiments. Nitrogen is injected into the reactor at a desired flow rate which is continuously measured with a mass flow meter with ± 0.8 % accuracy and ± 0.2 % repeatability. Thermolysis reaction produces gases which are directed to an ABB-AO202 chlorine gas analyzer that provides readings in a continuous manner, with accuracy to within 1 %, and repeatability of 0.5 %. A separate stream of gas products is directed via the continuous oxygen analyzer AMI-201RSP with five selected ranges of operation, a minimum detection of 0.01 % and repeatability of 0.2 %. Cuprous chloride vapor escapes with the gaseous products of decomposition during the tests. Therefore, a condenser installed on the discharge of the reactor prevents condensate and retains the CuCl. Temperatures of streams in/out of the reactor are monitored via type K thermocouples with an accuracy of ± 0.2 %. Solid reactants and products are measured via a Mettler Toledo ML3002E weight scale with a repeatability of 0.01 g and linearity at 0.02 g.

Prior to the start of experiments, the solid reactants are placed in the furnace for a minimum of 24 h at 423 K. The sample is placed inside the reactor, then the reactor is closed, and nitrogen is used to purge and eliminate any traces of oxygen. When the oxygen content is below detectable levels, the furnace begins to heat the sample.

Fig. 6.62 Schematic of copper oxychloride reactor and its test loop at UOIT



At the sample temperature of 723 K, further addition of reactants is initiated depending on the goal of the experiments (see Marin et al. 2011b).

- For experiments focused on the decomposition of CuCl_2 , a sample of 200 mmol is used and decomposed at various temperatures.
- For experiments focused on the decomposition of the mixture of CuO and CuCl_2 , solids have been added at a continuous rate to the reactor.

The addition of solids is performed through a special opening of the reactor. The test temperature is maintained after the addition of solids has finished and until no oxygen evolution is detected. Experiments with continuous addition into molten CuCl resulted in an approximately linear release of oxygen with respect to the addition of solids. The total mass of oxygen is then determined from numerical integration of the oxygen generation curve. The solid products of reaction were analyzed by XRD with a Philips PW1830HT PANalytical X'pert diffractometer where the diffraction angle 2-Theta varied between 5° and 60° . Subsequent quantification used X'pert PANalytical software.

The experimental equipment was first tested with a salt that dissociates at temperatures similar to those required by copper oxychloride, in order to provide a pattern of reference and obtain a reactor performance characterization. Potassium chlorate was used in the process of reactor performance characterization. Potassium chlorate is a solid at normal ambient temperatures and it melts at 629 K. It boils and separates into potassium chloride (KCl) and oxygen when exposed to temperatures beyond 673 K.

The average oxygen production rate is approximately 0.04 mol/min from a sample of 0.082 mol of KClO_3 , when extrapolated to the capacity of the reactor.



Fig. 6.63 Photograph of copper oxychloride decomposition test loop at UOIT

This suggests an oxygen generation capacity beyond $1.13 \text{ N m}^3/\text{h}$ that corresponds to an H_2 production rate above 4 kg/day , which is 10,000 times larger than past proof-of-principle experimental tests.

In the oxygen reactor, copper oxychloride particles decompose into molten salt and oxygen. The reactant particles absorb heat from the surrounding molten bath. Once the temperature of 773 K is reached, the sample decomposes quickly with oxygen released at the peak rate of 0.006 mol/min . A total of 0.107 mol of oxygen were released with a yield of 89% . The yield was calculated by comparing the actual oxygen generated with the amount of oxygen that could have been generated if the reaction was completed to 100% . According to the results presented in Fig. 6.64, the entire decomposition of 0.236 mol of $\text{CuO} + \text{CuCl}_2$ occurred within 35 min of the initial 10 min, showing a marked oxygen evolution while the balance of time shows the reaction rate slowly decaying to negligible oxygen release.

The solid products of oxygen production from copper oxychloride appear as a black hard sintered material, as shown in Fig. 6.65. The solids are mildly hygroscopic, and they can be pulverized with some mechanical effort. This means that an

Fig. 6.64 Oxygen production from the reactant copper oxychloride [data from Marin et al. (2010)]

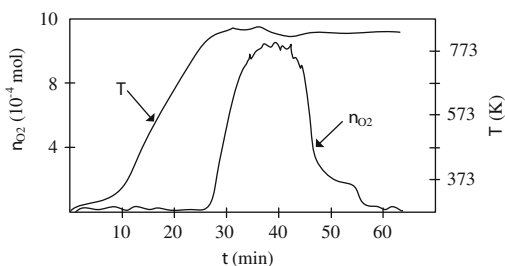


Fig. 6.65 Sample of products of $CuO-CuCl_2$ decomposition

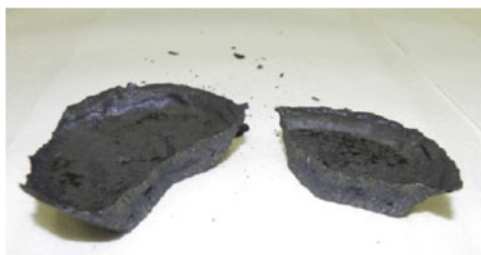
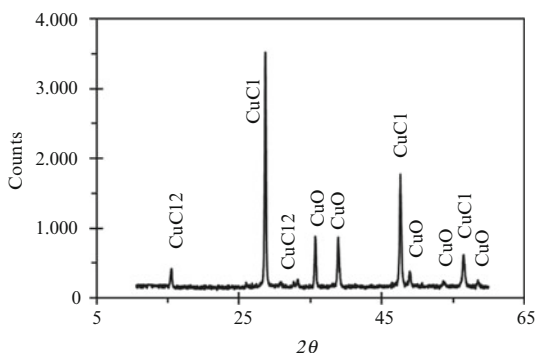


Fig. 6.66 Measured XRD results of copper oxychloride decomposition product [data from Naterer et al. (2011a)]



additional process must be introduced for the cycle integration before the downstream electrolysis reaction. The chunks of solid $CuCl$ must be mechanically removed from the oxygen production reactor and then pulverized. In this condition, the solids are dissolved in water for the preparation of the aqueous solution needed by the downstream electrolytic hydrogen production cell. Since the $CuCl$ must be first solidified, thermal energy recuperated from the phase change of molten salts from the decomposition reactor can be used elsewhere in the $Cu-Cl$ cycle for thermal energy integration.

The analysis based on XRD powder techniques of the composition of the solid product of the oxygen production resulted in patterns shown in Fig. 6.66. The spectrum revealed a mixture of solids where copper oxide, cupric chloride, and cuprous chloride were present. The major product component is $CuCl$ with mixed

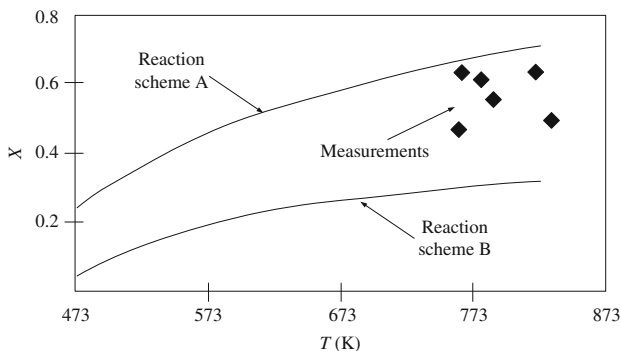


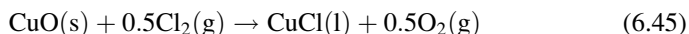
Fig. 6.67 Predicted vs. measured conversion of copper oxychloride at various temperatures and atmospheric pressure [data from Marin et al. (2011b)]

quantities of CuCl_2 and CuO . The analysis of the relative amounts of XRD peaks with reference to standard samples indicated the composition of solids.

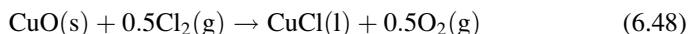
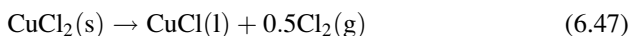
Figure 6.66 shows that the unreacted CuCl_2 in the hydrolysis may not be fully decomposed in the downstream oxygen production reaction. Therefore, CuCl_2 may be further carried by CuCl to the downstream cell for the electrolytic hydrogen production. This same situation occurs with CuO present in the output stream from the oxygen reactor. The figure also indicates the presence of unreacted CuCl_2 and cupric oxide in addition to cuprous chloride with the solid products of decomposition. A longer residence time will lead to a full decomposition of cupric chloride into cuprous chloride and chlorine.

The theoretical and measured yields of copper oxychloride decomposition were compared in Marin et al. (2011b), as shown in Fig. 6.67, where the predictions represent the predicted equilibrium yield. At equilibrium, the predictions show that the conversion of the mixture of $\text{CuO} \cdot \text{CuCl}_2$ is between 50 and 80 % at 800 K. The experimental decomposition of copper oxychloride resulted in conversions between 60 and 80 % when operated at atmospheric pressure. Two reaction schemes are considered in the models developed by Marin et al. (2011b):

- Scheme A, defined by the reaction sequence:



- Scheme B, defined by the reaction sequence:



The decomposition rate falls close to the predictions of the reaction scheme A and B. In the analysis, the partial pressures of chlorine in the reactor rise up to four orders of magnitude larger than the partial pressure of CuCl vapor at temperatures between 723 and 833 K. Ongoing research is being conducted to improve the yields of oxygen gas and reduce side reactions and by-products, among which chlorine side product is the most significant, although some traces of cuprous chloride vapor were also encountered.

6.7 Dehydration Step of Cupric Chloride

6.7.1 *Spray Drying Experiments (UOIT)*

Adjusting the molar fraction of H_2O and CuCl_2 is important for optimization of the hydrolysis reaction which eventually generates HCl and $\text{CuO}\cdot\text{CuCl}_2$. The electrolytic step produces a stream of hydrated cupric chloride diluted in aqueous solution of hydrochloric acid: 1 mol of CuCl_2 is dissolved in about 8 mol of water. In view of conducting the hydrolysis process, the molar ratio of steam and cupric chloride must be adjusted to about 2:1, namely, $\text{CuCl}_2\cdot 2\text{H}_2\text{O}$ is the desired reactant for hydrolysis. Alternatively, anhydrous cupric chloride $\text{CuCl}_2(\text{s})$ may be used as a reactant for the hydrolysis process—see Naterer et al. (2008b). The hydrated halide complex $\text{CuCl}_2\cdot 2\text{H}_2\text{O}$ forms crystals with copper atoms surrounded by two chlorine atoms and two water molecules placed approximately in the corners of a square; therefore the crystals appear as an agglomeration of planar square cells.

The solubility limit of CuCl_2 in water—which influences the concentration limit of cupric chloride molecules in aqueous solutions—ranges from 0.1075 mol CuCl_2 per mole of water at 303 K to 0.1333 mol CuCl_2 per mole of water at 353 K. If the solution is concentrated over the solubility limit, a slurry containing solid particles of hydrated cupric chloride in water is formed. Further water removal—obtained by various methods of drying (evaporation)—leads to generation of solid powder of CuCl_2 in its hydrated form. If more heating is applied, water is fully eliminated and anhydrous cupric chlorine is formed. The following drying methods were analyzed for cupric dehydration:

- Spray drying of aqueous solution—An evaporative heat and mass transfer process to remove water molecules when spraying the droplets of aqueous $\text{CuCl}_2(\text{aq})$ in hot air maintained in a large vessel at 353 K.
- Spray drying of cupric chloride slurry—An evaporative heat and mass transfer process to remove water molecules when spraying a slurry containing about 55 % solids per volume with a ratio of 3.5 mol of water per mole of cupric chloride.
- Flash drying—Evaporation of moisture takes place when the surrounding liquid conditions suddenly change and become lower than the saturation point,

such as conditions leading to a large pressure drop that converts an initial subcooled liquid to superheated liquid.

- Combined flashing and spray drying—An aqueous solution or slurry is sprayed into a chamber where hot air is circulated.
- Crystallization—Formation of solid crystals precipitating from an aqueous solution by cooling and/or concentration changes that bring the solution below the solidification point.

Within the Cu–Cl cycle, approximately 116 kJ of heat is released internally within the thermochemical cycle (by exothermic reactions, solidification, and cooling) and 277 kJ of heat is required (for endothermic reactions, drying, and heating) for each gram of hydrogen produced with the precipitate slurry drying method. If internal heat is ideally recycled, then a net heat input of about 161 kJ/g H₂ would be needed, of which ~82 kJ/g H₂ represents the low-grade heat for spray drying, vaporizing water, and heating of low-temperature solid particles and gas in the Cu–Cl cycle.

Two experimental facilities were used at UOIT for dehydration tests of cupric chloride: (1) low-temperature spray drying unit, and (2) high-temperature spray drying unit. The low-temperature spray drying test unit has been designed and built at Clean Energy Research Laboratory (CERL) at UOIT. This unit—called dryer 1 unit—is based on a Yamato dryer model D-41 which was modified to avoid corrosion caused by the corrosive cupric chloride solution. A titanium two-fluid nozzle was used and stainless steel parts downstream of the nozzle were coated with a thin layer of Viton. The test system comprises the following elements:

- Cylindrical glass drying chamber of 0.45 m diameter with 1.0 m cylindrical height.
- Glass-made cyclone and particle collection vessel.
- One two-fluid atomization nozzle of 0.7 mm diameter made of titanium.
- Air is cleaned via a scrubber.
- Peristaltic pump for solution to spray.
- Flow meter for measurement of the flow rate of air for atomization.
- Evaporation capacity of 3 L/h.
- Temperature sensors mounted in the drying air at the inlet and outlet.
- Digital instruments for barometric pressure and ambient air temperature and humidity.

A schematic diagram of the experimental setup for low-grade heat utilization—called dryer 2—is shown in Fig. 6.68 and a photograph is shown in Fig. 6.69. The high-temperature spray drying unit is based on a Niro mobile minor dryer and has the following characteristics:

- Cylindrical drying chamber: 0.8 m diameter, 0.6 m height, and a 60° conical bottom.
- Two-fluid nozzle of 0.8 mm diameter.
- Drying gas is introduced from the top.
- Cyclone separator used to separate air and powder.
- Comprises an air cleaning unit.

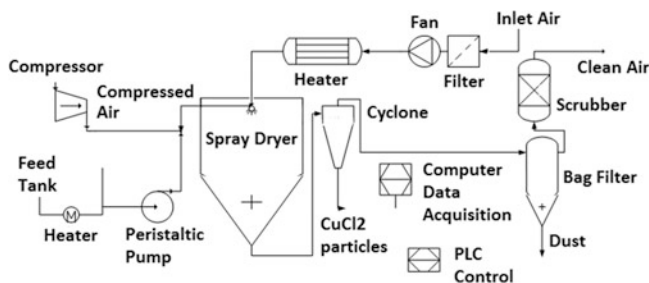


Fig. 6.68 Experimental facility for low-temperature spray drying of hydrated cupric chloride at UOIT



Fig. 6.69 Photograph of the experimental spray drying unit for $\text{CuCl}_2 \cdot n\text{H}_2\text{O}$ dehydration at UOIT

Aqueous solutions of sodium bicarbonate, sodium carbonate, and cupric chloride were used for the study. Experimental data has been collected and analyzed to identify the main effects of operating variables on powder quality, and utilization of low-grade heat input. The main operating variables are the inlet air temperature, atomization liquid feed rate, and atomization air pressure. The dependent variables are the outlet air temperature, moisture content in the product, and powder quality. A larger atomization air pressure increases the atomization airflow rate. The change in atomization airflow with the type of solution and its solid concentration is negligible.

The test parameters for low- and high-temperature experiments are listed in Table 6.22. The experimental data was used to determine the values of the Hausner ratio which indicates the flow behavior of powders from cohesive non-flowing to free-flowing regimes. The Hausner ratio is defined as the ratio of tapped density (ρ_{tap}) to aerated bulk density (ρ_{bulk}) of a powder, as follows:

$$\text{HR} = \rho_{\text{tap}} / \rho_{\text{bulk}}. \quad (6.49)$$

Bulk density of a powder is measured by allowing powder to settle in a measuring vessel under the influence of gravity, whereas tapped density of a powder is measured by tapping the measuring vessel. An Electrolab's microcontroller-based tap density tester (Model ETD-1020) was used for the measurement of tap density and Hausner ratio. In this method, the cylinder is raised and dropped under its own weight by a fixed drop height of $3 \text{ mm} \pm 10 \%$ at a nominal rate of 250 drops per minute. The cylinder is initially tapped for 500 times, and then the measured volume to the nearest graduated unit is obtained.

After the measurement, it continued tapping for 750 times and then again it measured the volume to the nearest graduated unit. If the difference between the two volumes is less than 2 %, the final tapped volume is considered. If not, it continues further until the difference between the measurements is less than 2 %. A Microtrac S3500 unit was used for particle size analysis. It works on light scattering technology. The particle range for this model is $0.024\text{--}2,800 \text{ }\mu\text{m}$. Each sample was taken more than two times for accuracy and repeatability. The particle analyzer gives the particle volume mean diameter, number mean diameter, and area mean diameter, and also the particle size distribution. The Sauter mean diameter of the solid particle is estimated in this study as

$$d_p = \left(\frac{\sum d^3}{\sum d^2} \right). \quad (6.50)$$

For a distribution analysis of particle size, the span is calculated using the following diameters: $d_{10\%}$ —the diameter for which 10 % of the sample is smaller; $d_{50\%}$ —the diameter for which 50 % of the sample is smaller; and $d_{90\%}$ —the diameter for which 90 % of the sample is smaller. The span is calculated as follows:

$$\text{SP} = (d_{90\%} - d_{10\%}) / d_{50\%}. \quad (6.51)$$

Product moisture content is represented either on a dry or a wet basis. A drying method for determination of moisture content depends on the nature of the tested material. Sodium bicarbonate decomposes at 373 K. This must be dried under vacuum for moisture removal. Sodium carbonate powder and cupric chloride powders were dried by taking 4–5 g of a sample and heating at 375–378 K. Samples were checked at every hour until there was no change in the subsequent values. The experimental results are summarized in Table 6.23. The data has been compared with reference results published in past literature. As indicated in Fig. 6.70, the

Table 6.22 Experimental parameters for drying tests of CuCl₂ at UOIT

Dryer	Experiment ID	Atomization liquid			Atomization air			Drying air	
		\dot{m} (kg/h)	Solid fraction	T (K)	\dot{m} (kg/h)	P (bar)		\dot{m} (kg/h)	T_{in} (K) T_{out} (K)
1	1	0.58–1.33	4–8 % NaHCO ₃	293–303	2.36–4.68	2–4		57.6–86.4	323–373 303–318
	2	0.58	8 % NaCO ₃	293	4.68	4		82	323 303
	3	0.58	10 % CuCl ₂	293	3.84	4		72	333–393 303–328
	4	0.464	44.83 % CuCl ₂	293	10.4	2		82	473 383
2	5	0.864	44.83 % CuCl ₂	293	7.3	1.5		82	443 373

Source: Daggupati et al. (2011c)

Table 6.23 Experimental results of drying tests at UOIT

Experiment ID	Moisture (wt. %)	ρ_{tap} (kg/m ³)	ρ_{bulk} (kg/m ³)	d_p (μm)	SP	HR
1	21.3	547	325	29.67	1.01	1.68
2	20.89	605	385	24.6	1.36	1.57
3	20.88	652	411	21.56	1.58	1.58
4	5.29	752	631	23.97	3.26	1.19
5	2.7	701	590	21.31	3.21	1.19

Source: Daggupati et al. (2011c)

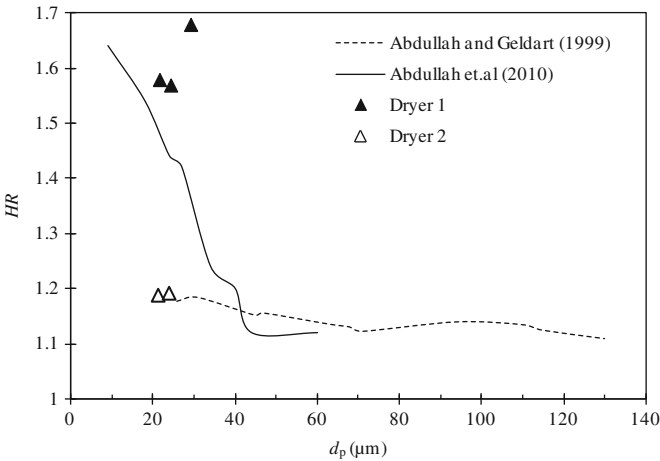


Fig. 6.70 Drying experiment validation against published reference results [data from Daggupati et al. (2011c)]

measured data agrees well with other published works, in terms of Hausner number correlated to the particle size. The Hausner ratio for the cupric chloride powder in high-temperature drying (dryer 2) is 1.18, which is less than 1.25. This indicates a free-flowing character of the powder, whereas the Hausner ratio in low-temperature drying (dryer 1) is above 1.4, which indicates a non-flowing and cohesive nature of powder. This occurs because the powder cohesiveness increased due to an increase in moisture content for low-temperature drying, compared to high-temperature drying. At high-temperature drying (dryer 2), a lower moisture content in the powder allows free flowing behavior, even though there is not much change in the Sauter mean diameter of the particles.

The product recovery rate for these runs was above 80 %. The overall recovery rate for these runs was calculated by taking the powder collected in the cyclone separator, conical section, in the drying chamber, as well as trapped powder in the connecting hose pipe between the drying chamber and cyclone separator. The difference in recovery rate may be due to low feed sampling rates and loss of powder in the conical section and inside the hose connector. There was no coating

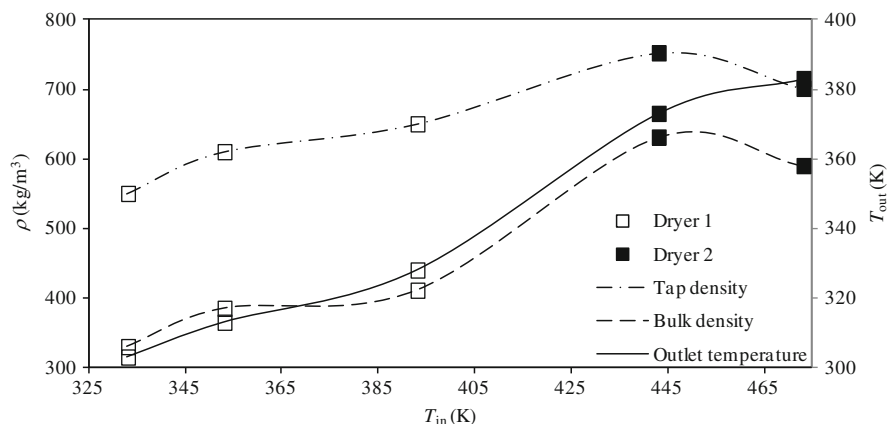


Fig. 6.71 Variation of tapped and bulk densities of the particles obtained by drying with the inlet temperature of the drying air [data from Daggupati et al. (2011c)]

of powders observed on the drying chamber. The experimental tests were stable without fluctuations in the atomization airflow and pressure for cupric chloride solution drying.

The variation of tapped and bulk densities with inlet temperature of drying air is presented in Fig. 6.71. Note that the tapped density is a measure of the flow ability of powders. The figure shows that the tapped and bulk density of the powder produced by drying shows maxima at an air inlet temperature of around 450 K when the temperature at outlet (air) is ~ 375 K. The tapped bulk density also decreases with increasing moisture content, and in turn reduces the flow ability of solids.

The outlet air temperature depends on the inlet air temperature, drying airflow rate, and atomization liquid flow rate. An increase in inlet air temperature and airflow rate increases the outlet air temperature and it decreases with an increase of atomization liquid rate. The inlet air temperature for cupric chloride solid varied from 333 to 393 K for low-temperature drying using the Yamato spray dryer. The corresponding air outlet temperatures varied from 303 to 328 K. Similar phenomena were also observed with sodium carbonate, and bicarbonate solutions. It shows that low-grade heat can be used for drying of cupric chloride solution to solid. The moisture content in the product depends on the air outlet temperature. The spray-dried product at low temperatures below 373 K contains moisture, which is removed in a downstream fluidized bed in two stages: one for removal of moisture, and the other for the hydrolysis reaction.

Figure 6.72 shows the particle size and size distribution for cupric chloride and sodium bicarbonate powders. The mean particle size for cupric chloride solid was around 31 μm in dryer 1, and 18.5 μm in dryer 2, with a broad size distribution. As indicated in Table 6.23, the span for particles varied from 1.1 to 1.4 for low-temperature drying and it was ~ 3.2 at high-temperature drying. These results may be attributed to the size of the two-fluid nozzle used in dryer 1. Moreover, the

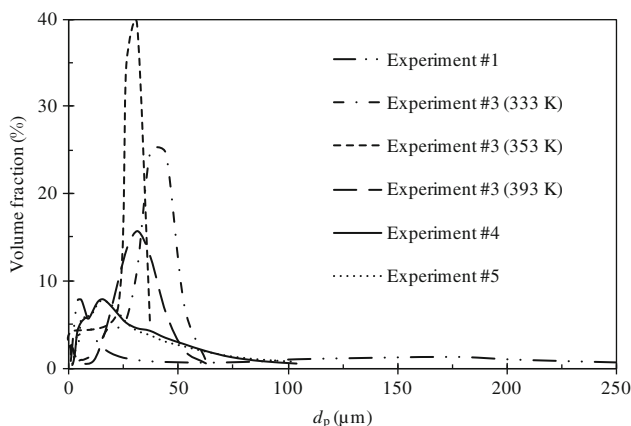


Fig. 6.72 Volumetric distribution of particle mean size [data from Daggupati et al. (2011c)]

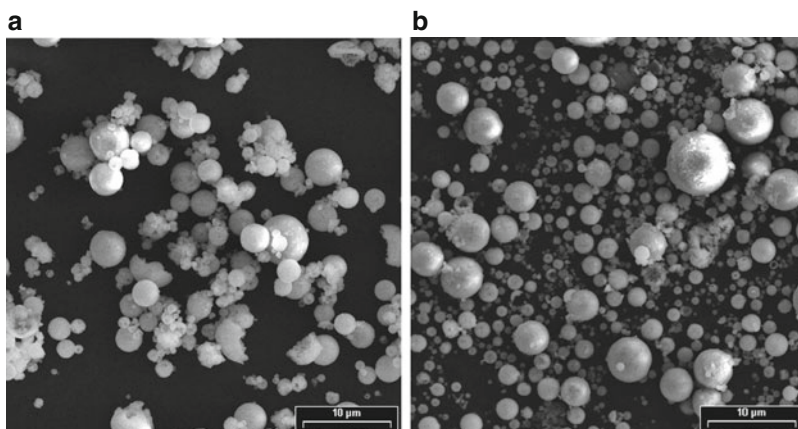


Fig. 6.73 SEM images of CuCl_2 particles formed by spray drying at UOIT. (a) High-temperature experiments, (b) low-temperature experiments

moisture content in the particle might have caused agglomeration of solids for a large particle size and distribution.

Powder characteristics and properties can be controlled and maintained uniformly throughout a drying operation. A sample SEM image of CuCl_2 particles obtained by spray drying is shown in Fig. 6.73. The particle morphology was investigated with a JEOL JSM-6400 scanning electron microscope. Since the SEM requires a vacuum, the procedure required the complete dehydration of the sample before placing it into the SEM vacuum chamber. Therefore, the crystal structure observed under the SEM was the anhydrous cupric chloride.

Cubic crystals were obtained by vacuum drying at room temperature, whereas long prisms were formed under normal drying conditions.

As the drying temperature increases, the solid becomes amorphous, because there was less time for crystals to grow before contacting another crystal growing in the droplet. Many nucleation points give rise to many small crystals—see Fig. 6.73a. Because of the increased number of crystals, there is less precipitate per crystal, and the crystals are much smaller in size. As the temperature is reduced, the number of nucleations is more orderly. It was also observed that part of the spheroid is thicker on one side than the other, particularly at lower temperatures, due to the remaining liquid inside the center of the droplet drifting away from the direction of flow causing the wall to be thicker on the side opposite to the direction of flow. At low drying temperatures (333 K), the particles did not form hollow spheroids, indicating that there was sufficient time for only one crystal to form for each droplet—see Fig. 6.73b.

In the process of spray drying the aqueous cupric chloride, volatile compounds (water and hydrochloric acid) evaporate from the droplets generated by the atomization nozzle. Because they are evaporated at the surface of the droplet, nucleation points occur first on the surface. This causes crystals to form and grow internally into the droplet. Based on the SEM images, it was observed that a higher temperature increases the number of nucleation points.

At temperatures of 393 K, the color of the dried solids was light green, indicating that the hydrate was forming first, and then later shrinking to form the anhydrous form. The formation of the hydrate has significant implications on the drying rate, since the first drying rate is determined by the hydrate, and later the drying rate is affected by the anhydrous form.

Ongoing research is examining the crystal structure of the CuCl_2 product, particularly to determine if there are interstitial water molecules inside a crystal lattice of CuCl_2 . Other issues under investigation include whether there are water molecules bonded to the edges of the CuCl_2 crystal, whether there are interstitial Cu and Cl atoms inside a lattice of the di-hydrate, and gaining a deeper understanding of the precise mechanism of drying. The molecular structures of both the di-hydrate and anhydrous forms are planar. Bonds are formed between adjacent planes at specific angles. In the hydrate form, removal of water leads to collapse of the crystals.

The low-temperature experiments (dryer 1) showed that the produced powder shows cohesive and non-flowing behavior due to high moisture content. The moisture content in the powder also depends on the drying air inlet, as well as outlet temperatures. However, drying of cupric chloride and sodium bicarbonate solutions at low temperature demonstrates the potential for low-temperature spray drying of cupric chloride solution, for utilizing low-grade heat from nuclear, solar, and other industrial sources. Additional studies are recommended to identify the critical particle size for low- and high-temperature drying to improve the flow ability of cupric chloride powder. Experimental spray drying studies for cupric chloride solid at high temperature (dryer 2) gave acceptable particle size and flow ability of powder for high-temperature drying.

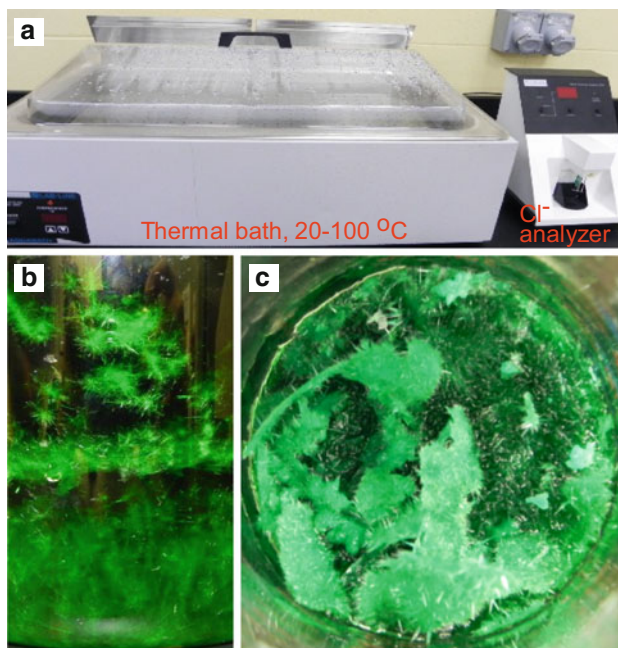


Fig. 6.74 Images of CuCl_2 particles formed by crystallization at UOIT

6.7.2 Crystallization Experiments (UOIT)

Due to the large-size equipment required for industrial scale drying of aqueous CuCl_2 in a future commercial hydrogen plant, alternative methods of water removal from the CuCl_2 were also investigated to improve the economic viability of the processes. In particular, methods of crystallization were examined by cooling the aqueous solution of cupric chloride. Crystallization is a process of formation of solid crystals precipitating from the aqueous solution. It is a physicochemical solid–liquid separation technique, whereby mass transfer of a solute occurs from the liquid to solid crystalline phase. The crystallization occurs by precipitation, through a variation of the solubility conditions of the solute in the solvent, rather than precipitation due to chemical reaction.

Crystallization experiments for the binary system of $\text{CuCl}_2 + \text{H}_2\text{O}$ were performed at saturation conditions using a thermal bath and a chlorine ion analyzer (Fig. 6.74a). It was found that 20 % of the CuCl_2 can be crystallized upon cooling from 80 to 20 °C. Figure 6.74b shows a sample of grown crystals during an experiment. The dimensions of the dendritic crystals were in the range of 0.1–0.6 cm. After the clear solution is removed, the crystals appear in Fig. 6.74c. Ongoing research is being performed to increase the portion of solids formed and reduce the temperature requirements of drying. This would enable the Cu–Cl cycle to utilize waste heat from thermal power plants or other industrial sources for the spray drying heat input requirements.

6.7.3 Modeling of Spray Drying Process

Additional numerical studies—reported in Naterer et al. (2008b)—have been conducted to analyze the process of spray drying of aqueous cupric chloride droplets. The analysis assumed that evaporation results in a continuous shrinkage of the droplet with no solid core formation, but rather a continuous growth of CuCl_2 crystals, with the average thermal conductivity of the droplet remaining constant. Additional assumptions for modeling of spray drying process are listed as follows:

- Mass and momentum changes of dispersed droplets do not contribute to corresponding changes of the drying medium (air).
- Kinetic energy changes in the drying air stream due to droplet movement are negligible.
- Drying air remains at constant temperature and humidity conditions.
- Evaporation produces a continuous shrinkage of the droplet with no solid core formation.
- Evaporation produces a continuous growth of CuCl_2 crystals.
- The average thermal conductivity of the droplet remains constant.

The main correlations used for modeling of the mass transport in spray drying are listed in Table 6.24. If one denotes with α the droplet thermal diffusivity, r the radial coordinate of droplet assumed spherical, and h the convective heat transfer coefficient at the droplet surface, and consider symmetry of heat transfer throughout the droplet ($\partial T/\partial r = 0, r = 0$), heat flux continuity at the droplet surface $-k_d(\partial T/\partial r) = h_g(T_s - T_\infty), r = d_d/2$, and that at the initial moment the droplet temperature is $T(t = 0) = T_i$, then the transient heat conduction equation $r^2(\partial T/\partial t) = \alpha \partial[r^2(\partial T/\partial r)]/\partial r$ can be integrated. In addition, the differential mass transfer equation can be formulated—as indicated by Naterer et al. (2008b)—in the following way:

$$\frac{d(d_d)}{dt} = \frac{2DM_w}{\rho_w d_d} (1 + 0.6Re^{0.5}Sc^{0.33}) \times (C_s - C_g), \quad (6.52)$$

where M_w is the molecular weight of the water, ρ_w is the density of saturated water in thermodynamic equilibrium with the droplet surface, D is the diffusion coefficient, and C_s and C_g are the vapor concentrations at the droplet surface and bulk flow, respectively. The variation of droplet diameter in time, due to the evaporation process, can be eventually expressed with

$$\frac{d(d_d)}{dt} = \frac{2k_d(1+B)^{-0.7}}{\rho_w d_d \lambda} (2 + 0.6Re^{0.5}Pr^{0.33})(T_g - T_d), \quad (6.53)$$

where T_d is the droplet temperature and B and λ are defined in Table 6.24. In order to find the droplet shrinkage rate, it can be assumed that the droplet mass decrease is

Table 6.24 Correlations used for spray drying modeling

Equation	Remarks
$d_s = \sum_d^3 / \sum_d^2$	It expresses the Sauter mean diameter of the droplets; each droplet has a diameter d_d .
$\ln(1 - v) = -0.3 \times (d_d/d_s)^{1.6}$	Rosin–Rammler correlation of droplet size distribution in sprays. Here v is the fraction of total volume of spray contained in droplets smaller than d_d .
$Bi = Nu \times k_g / (2k_d)$	Biot number characterizing heat transfer within a droplet as a function of Nusselt number (Nu) and thermal conductivity of gas phase (k_g) and of droplet (k_d).
$Nu = 2 + 0.6Re^{0.5} Pr^{0.33}$	Ranz–Marshall correlation for Nusselt number, where Pr is Prandtl number and Re is Reynolds number.
$Re = (\mathcal{V}_g - \mathcal{V}_d) \times d_d \rho_g / \mu_g$	Definition for Reynolds number, where subscript g represents gas phase, \mathcal{V} is velocity, μ is dynamic viscosity, and ρ is density.
$Sh = 2 + 0.6Re^{0.5} Sc^{0.33}$	Mass transfer in the convection process is defined by the Sherwood number (Sh), Reynolds number (Re), and Schmidt number (Sc).
$k_c \times d_d = Sh \times d_g$	Definition of (Sh) number based on mass transfer coefficient (k_c).
$C_d = \frac{24}{Re} (1 + 0.17Re^{0.632} + 10^{-6}Re^{2.25})$	Correlation for drag coefficient of the droplet as a function of Reynolds number.
$\lambda = h_{lg}(T_s) + \pi d_d^2 h (T_g - T_s) / \dot{m}$	Definition of dimensionless droplet evaporation constant where \dot{m} is the mass rate of droplet shrinkage, T is temperature at the gas bulk (g) and droplet surface.
$B = \frac{c_p(T_g - T_s)}{\lambda}$	Definition of Spalding number where c_p is the specific heat of water vapor, T is temperature at the gas bulk (g) and droplet surface.

Source: Naterer et al. (2008b)

proportional to the droplet diameter shrinkage; thereby the following energy balance can be written for the droplet:

$$mc_p \frac{dT_d}{dt} = h\pi d_d (T_g - T_d) + \lambda \dot{m}. \quad (6.54)$$

Furthermore, the aerodynamic momentum balance results in the following expression for the velocity of the droplet—see Naterer et al. (2008b) for the detailed derivation:

$$m_0 \mathcal{V}_0 = m(t) \times \mathcal{V}_d(t) + \int_0^t [0.5\pi \rho_g C_d \mathcal{V}_d^2(t) d_d^2] dt, \quad (6.55)$$

where C_d is the drag coefficient defined in Table 6.24.

Model validation was performed by comparing the model predictions with relevant published experimental data from past literature. Figure 6.75 shows a validation example where predictions of the particle diameter distribution are compared to experimental results from Cleary et al. (2007). For the results shown

Fig. 6.75 Validation of spray drying model against published experimental data—fraction of the total volume of spray contained in the droplets smaller than d_d vs. droplet diameter [data from Naterer et al. (2008b)]

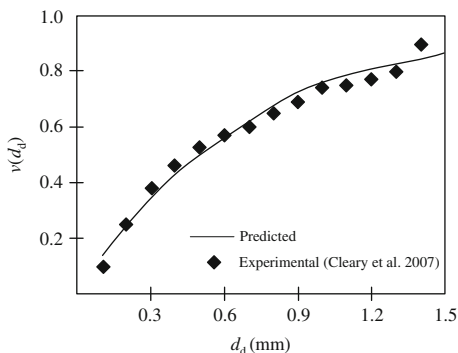
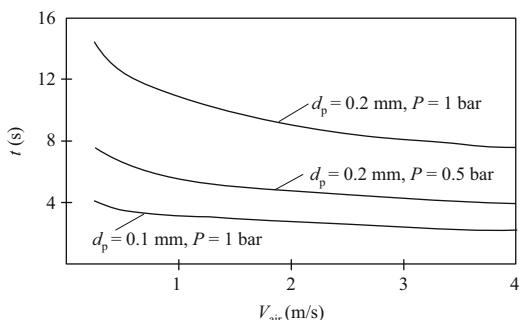


Fig. 6.76 Predicted drying time for inlet air at 303 K with 0.01 kg moisture per kg dry air for various droplet diameters and pressures [data from Naterer et al. (2008b)]



in the figure, it is assumed that the release pressure of the droplets is 24 bar and the Sauter diameter is 0.344 mm. The model results compare well against the experiments. Moreover, it can be observed that the amount of liquid evaporated as a consequence of flashing is relatively small, compared to the amount of rained-out liquid with droplet diameter. Furthermore, the Sauter mean diameter strongly depends on the nozzle characteristics and also the downward movement of spray flow, as this may increase the potential for coalescence and droplet size. This result makes the flashing effect minor in spray/flash drying, in comparison to the spray drying process of evaporation.

Figure 6.76 illustrates the variation of drying time with air velocity, temperature, and operating pressure. It was observed that the drying time depends strongly on the inlet air humidity, temperature, particle size, and operating pressure. At a low humidity of 0.0025 kg water/kg dry air, the drying time is less than 6 s for droplet sizes less than 200 μm , at 308 K. At a humidity of 0.01 kg water/kg dry air, the drying time is less than 6 s for droplet sizes less than 100 μm , at 308 K, and droplet sizes less than 150 μm , at 343 K and 1 bar operating pressure. At low operating pressures of 0.5 bar, the drying time is less than 8 s for droplet sizes less than 200 μm , at 308 K. The results predict that evaporative drying is possible down to temperatures as low as 308 K, although such low-temperature drying may limit the product quality and throughput.

6.8 Thermochemical Chlorination Step of Copper Particles

6.8.1 Reaction Kinetics and Thermodynamics

The reaction of copper chlorination with HCl which evolves hydrogen within some versions of Cu–Cl cycle has been intensively studied experimentally at ANL in 2003–2005; see Lewis et al. (2003), Lewis et al. (2004), Serban et al. (2004), and Lewis et al. (2005b). A numerical model for kinetics of this reaction was presented by Zamfirescu et al. (2010b). The reaction equilibrium and reaction extent were analyzed by Daggupati et al. (2009). This reaction is listed as process #6 in Table 6.2 and it is exothermic.

The equilibrium constant of the hydrogen production reaction can be expressed either in terms of Gibbs free energy or in terms of fugacities of reacting species, according to

$$K_{\text{eq}}(T) = -\frac{\Delta G(T)}{RT} = f_{\text{H}_2} f_{\text{HCl}}^2 \left(\frac{f_{\text{CuCl}}}{f_{\text{CuCl}}^0} \right)^2 \left(\frac{f_{\text{Cu}}}{f_{\text{Cu}}^0} \right)^{-2}, \quad (6.56)$$

where f^0 are the fugacities at 1 bar. Assuming that the pressure is low enough for ideal gas conditions at equilibrium, the equilibrium constant from (6.56) can be rewritten as

$$K_{\text{eq}} = \frac{1}{P} \times \frac{y_{\text{H}_2}}{y_{\text{HCl}}^2}, \quad (6.57)$$

where y_{H_2} and y_{HCl} are the mole fractions of hydrogen and hydrochloric acid in the gas phase.

The mole fraction of gaseous components can be expressed in terms of the extent of reaction, ξ . In stoichiometric conditions, 2 mol of copper are reacted with 2 mol of HCl. In order to decrease the equilibrium constant—for higher conversion—hydrochloric acid must be supplied in excess; one denotes $N \geq 2$ the number of moles of HCl supplied for each two moles of copper. As detailed by Daggupati et al. (2009), one can then express (6.56) and (6.57) in the following form:

$$-\frac{\Delta G(T)}{RT} = \frac{1}{P} \left(\frac{\xi}{N - \xi} \right) \bigg/ \left(\frac{N - 2\xi}{N - \xi} \right)^2. \quad (6.58)$$

The second degree equation (6.58) gives a direct solution for ξ , with two roots. The positive root, less than unity, can be used for predicting the extent of the reaction. Figure 6.77 illustrates the effects of operating pressure, temperature, and excess reactant on the extent of the reaction for the hydrogen production

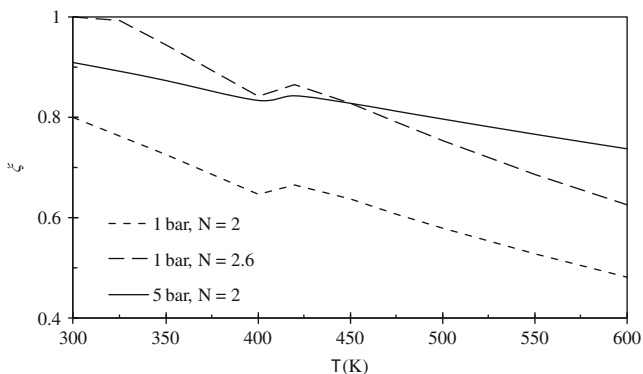


Fig. 6.77 Variation of reaction extent of copper chlorination reaction with reaction temperature, pressure, and excess HCl reactant [data from Daggupati et al. (2009)]

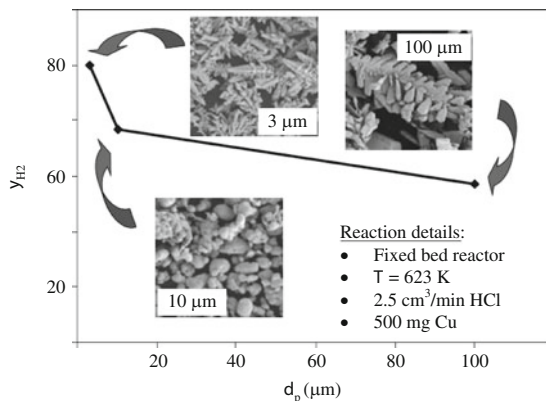
reaction. An increase in temperature reduces the equilibrium conversion. The increase in the operating pressure and excess reactant hydrogen chloride raises the equilibrium conversion values. At the operating pressure of 1 bar, the equilibrium conversion values are above 90 %, with 40 % excess reactant (hydrogen chloride) and 55 % excess reactant for complete conversion of the copper solid. The gas–solid reaction may be conducted either by increasing the operating pressure or excess reactant below 400°C. Above 800 K, the reaction system becomes three phase, with gas–liquid–solid phases, because of the melting of cuprous chloride at about 703 K.

Serban et al. (2004) determined the reaction rate in a fixed bed reactor made of a quartz tube of 12.7 mm i.d., 35.6 cm height placed in a vertical electric furnace, and connected to a mass spectrometer calibrated to detect HCl, H₂, and Cl₂ gases. At a temperature where cuprous chloride starts melting (703 K), the reaction accelerates considerably. The gas–solid mass transfer is controlled by chemical reactions at the interface. The forward reaction is order 0.5 and the backward reaction is order one. The reaction is reversible and the reaction constant varies in the range 0.85–2.5 atm^{0.5} when the temperature falls from 745 to 673 K. Serban et al. (2004) fit the experimental results on a “ln *K* vs. 1/*T*” curve and determined the Arrhenius equation for the reaction rate constant. The kinetic experiments were performed with commercially available Cu particles of 3 μm. The reaction rate is expressed by

$$r = k_f P_{\text{HCl}}^{0.5} - k_b P_{\text{H}_2} = k_f (P_{\text{HCl}}^{0.5} - P_{\text{H}_2} / K_{\text{eq}}), \quad (6.59)$$

where *k* is the reaction constant and the index “f” stands for forward and the index “b” refers to backward reactions, and $K_{\text{eq}} = k_f / k_b$. Based on the data published by Serban et al. (2004) and Zamfirescu et al. (2010a, b, c), the rate

Fig. 6.78 Hydrogen yields with a fixed bed reactor [data from Serban et al. (2004)]



constant of the forward reaction can be estimated with the following Arrhenius-type equation:

$$k_f = 1,737,573 \exp(-7,515.5/T), \quad (6.60)$$

where k_f is given for 1 atm, 1 g of copper, and 1 μmol of HCl and it has units of h^{-1} .

The size and shape of electrolytic copper particles were affected by the operating parameters of the cell. To directly measure the kinetics of the reaction between HCl and Cu, the reaction rates were measured at four different temperatures (673, 700, 723, and 750 K). The hydrogen yields were determined by comparing the measured amount of hydrogen produced vs. the stoichiometric amount of hydrogen that would be formed if all Cu was oxidized to CuCl. Hydrogen yields decreased with larger Cu particle sizes, indicating that high surface areas of contact between HCl and Cu are necessary for high hydrogen yields. Figure 6.78 shows SEM images of the spheroidal and dendritic Cu particles used in the hydrogen generation reaction. No gaseous products other than hydrogen and HCl were observed in the effluent stream. XRD examination of the solid product resulting from the reaction showed patterns only for CuCl and Cu. No secondary reactions were favored in the temperature range studied.

6.8.2 Hydrodynamic Cold Tests with a Scaled-Up Packed Bed Reactor (UOIT)

Scale-up studies were performed on the process to generate larger capacities of hydrogen production (about 3 kg/day in a larger reactor, see Naterer et al. 2009). A packed bed reactor was developed and tested at UOIT for this purpose. The packed bed has been tested at cold operation conditions with the aim to study the flow hydrodynamics of various particle sizes and fillings. Also, the purpose of the tests

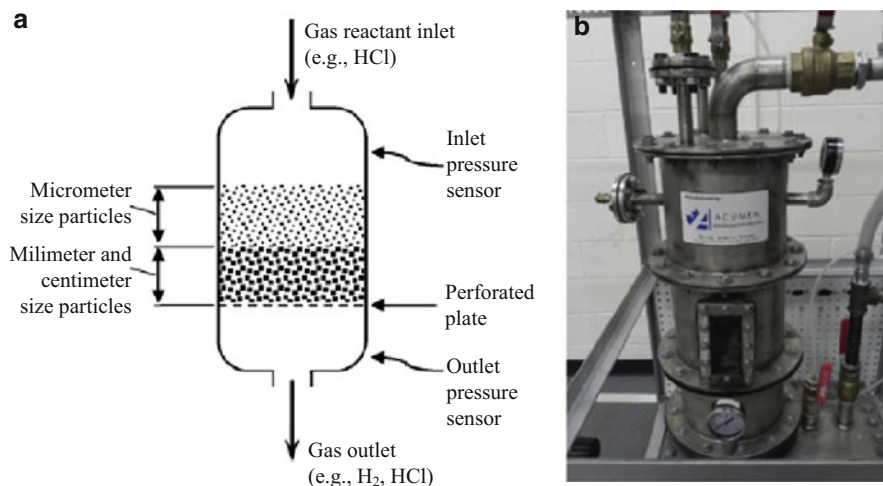


Fig. 6.79 (a) Schematic and (b) photograph of the packed bed reactor for thermochemical chlorination step

was to obtain hydrodynamic data for designing two of the reactors needed for the copper–chlorine cycle: the chlorination reactor (namely, the reaction step discussed in this section) and hydrolysis reactions (the process presented in Sect. 6.5). This section summarizes the past research results obtained during cold tests with the scaled-up packed bed reactor for conducting the thermochemical chlorination of copper particles.

The test reactor consists of a vertical pressure vessel 21 cm in diameter with a support mesh installed inside to hold the packed solids. A schematic and a photograph of the reactor are illustrated in Fig. 6.79. The system is connected to a compressed air station which is adjusted to provide pressurized air at 2 atm (gauge) at the reactor inlet (top side in the figure). The gas pressure is measured at the inlet and outlet (bottom) with pressure transducers (PX142-001D5V, 22 Pa uncertainty). The assembly photograph of the test loop is presented in Fig. 6.80. On the air line, a Chemline FT0025 flow meter is installed (uncertainty 0.27 N m³/h).

The system calibration has been made with an empty reactor to determine a reference pressure drop. The reference pressure drop has been subtracted from pressure drop measurements of a filled reactor to determine the dynamic effects of the packing.

Figure 6.81 shows photographs of packing materials used for three sets of experiments. Table 6.25 lists the characteristics of the packing material and the associated experimental conditions. A Microtrac particle was analyzed to determine the particle characteristics. The 4 mm diameter particles are used as a support bed for the 450-mm diameter particles. The pressure drop measurements from the 4 mm particles are subtracted from the combined 4 and 450 mm experiments, to obtain data for the 450-mm particles.



Fig. 6.80 Scaled-up reactor for thermochemical chlorination step (UOIT)

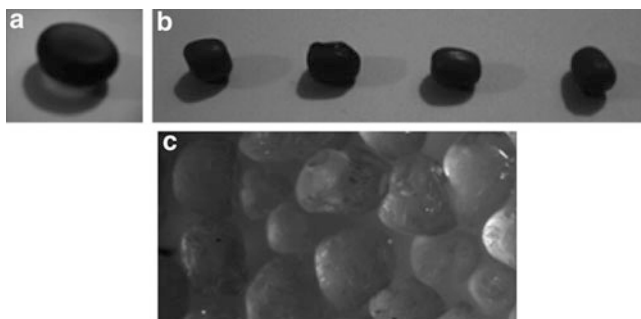


Fig. 6.81 Packing materials used in hydrodynamic tests with the scaled-up chlorination reactor: (a) 1 cm, (b) 4 mm, (c) 450 μm

The calibration data for the experimental tests is presented in Fig. 6.82 in terms of the pressure drop over the reactor against the airflow rate. Two measurements were performed: one with the reactor empty, and one with the perforated plate installed. A net pressure drop increase of around 10 Pa is due to the perforated plate.

Table 6.25 Packed bed parameters used in the hydrodynamic experiments

Material	d_p (mm)	Φ	ε	L (cm)	Re_p
Glass beads	10	0.88	0.38	10, 20, 30	15–150
Peas	4.0	0.98	0.33	10, 15	5.4–54
Sand	0.436	0.75	0.17	10, 15, 20	0.47–4.7

Note: d_p particle diameter, Φ sphericity, ε void fraction, L bed height, Re_p bed Reynolds number
Airflow rate range of 490–4,900 cm³/s

Source: Pope et al. (2011)

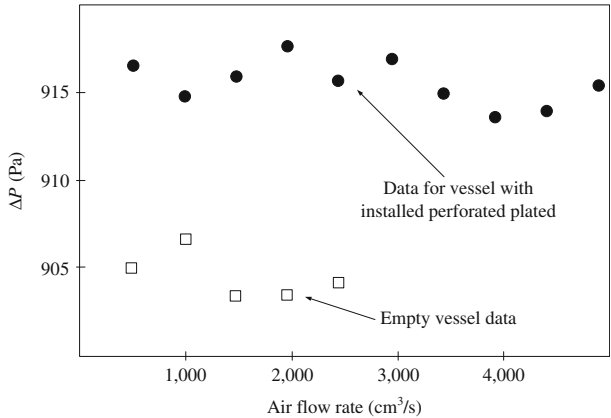


Fig. 6.82 Experiment calibration data for packed bed chlorination reactor [data from Pope et al. (2011)]

Table 6.26 Experimental correlation of f_p with Re_p for packed bed reactor

d_p (mm)	0.45	Re_p	1	1.25	1.5	2.	2.5	3	4	5	N/A	N/A
		f_p	11	6	4.5	4	3	2.8	2.5	2	N/A	N/A
	4	Re_p	5	10	16	22	26	34	38	43	48	54
		f_p	3.7	4	7.5	8.2	6	5.5	5.3	5.2	5.3	5.1
	10	Re_p	14.5	30	44	58	74	87	104	118	132	147
		f_p	50	33	10	1	6.5	4	3.9	5.8	4.5	3

Source: Pope et al. (2011)

The collected experimental data are shown graphically in Table 6.26 where the packed friction factor (f_p) is correlated with the particle Reynolds number (Re_p). Here the Reynolds number for the bed is defined by the following equation:

$$Re_p = \frac{\rho \times \mathcal{V} \times d}{\mu \times (1 - \varepsilon)}, \tag{6.61}$$

where ρ is gas density, \mathcal{V} is the superficial velocity of the gas phase, d is diameter, μ is dynamic viscosity of the gas, and ε is the void fraction. The friction factor of the bed can be estimated—as detailed in Pope et al. (2011)—by

$$f_p = \frac{150}{\Phi \times Re_p} + 1.75. \quad (6.62)$$

6.8.3 Modeling of Chlorination Reactor

Thermodynamic, kinetic, and hydrodynamic modeling of the chlorination reactor which conducts the solid–gas reaction of copper with hydrochloric acid, $2\text{Cu(s)} + 2\text{HCl(g)} \rightarrow \text{H}_2\text{(g)} + 2\text{CuCl(l)}$, which is exothermal, is a key step for reactor analysis and design. Orhan et al. (2008b) reported a thermodynamic analysis of the chlorination reaction step, based on energy and exergy methods. Zamfirescu et al. (2010b) reported a reactor modeling study based on reaction kinetic analysis. Pope et al. (2011) modeled the flow hydrodynamics through a scaled-up packed bed reactor for chlorination. Subsequently, the main analysis and modeling results for system kinetics and hydrodynamics were summarized.

The modeling of the chlorination reactor is also complicated because three phases are involved: gaseous, liquid (molten salt), and solid. Some multiphase reactor concepts and their auxiliary systems were reported by Wang et al. (2008). Using packed bed reactors is one of the options. In a multiphase packed bed reactor for copper chlorination, the solid and gaseous reactants are fed and a molten salt product is produced together with hydrogen gas. Heat is released by the reaction which must be removed via specific means of heat transfer. One of the key challenges is that three phases are present in the chemical reactor—molten (liquid) CuCl; gaseous HCl, H₂, and possibly CuCl vapor; and solid copper.

Packed bed reactors expose a large total surface area of solid particles to a fluid. The efficiency of the packed bed is an important factor in the operating and product costs. Investigating the pressure drop through the packed bed is important for maximizing the efficiency of the hydrolysis reaction for a variety of reasons. The use of auxiliary pumps and other parasitic losses are affected by a large pressure drop, since they need to supply capacity and input power.

The flow paths taken by the fluid through a packed bed are very complex and irregular. This makes it difficult to obtain exact solutions and precise representations of the fluid flow. The radial fluid velocity is significant because the irregularity of the packing material causes highly variable flow paths and large differences in local and average velocities. As specified in Pope et al. (2011), numerical predictions of fluid flow through a variety of structured packing arrangements showed good agreement with the Ergun equation, when the flow conditions were represented by Reynolds numbers (Re_p) less than 130.

This equation correlates the friction factor of the packed bed to the pressure drop and relevant geometric characteristics of the bed, according to the following mathematical expression:

$$f_p = \frac{\Phi d}{L \rho V^2} \left(\frac{\varepsilon^2}{1 - \varepsilon} \right) \Delta P, \quad (6.63)$$

where ΔP is the pressure drop across the bed and all other quantities are specified in Table 6.25.

When the flow conditions are represented by a very low Reynolds number, the Stokes law can be applied. Low Reynolds flow ($Re_p < 5$) represents conditions where conduits through the packing material are extremely small (due to the microscale particles), so viscous effects between the fluid and packing material become important. A friction factor for the bed based on the Stokes law has been derived in Pope et al. (2011) as follows:

$$f_p = \frac{24\mu\varepsilon}{\rho\Phi dV}. \quad (6.64)$$

For the hydrodynamic modeling of the packed bed, (6.64) is applied when $Re_p < 5$ and (6.63) is applied when $Re_p > 22$. A composite solution that predicts the friction factor in the transition, creeping flow, and Ergun regions was proposed in Pope et al. (2011). The equation, valid for $5 \leq Re_p \leq 22$, is expressed by

$$f_{p,c} = f_{p,s} + \left[f_{p,T}^{-n} + f_{p,E}^{-n} \right]^{-1/n}. \quad (6.65)$$

In (6.65) $f_{p,s}$ represents the packed bed friction factor in the Stokes flow regime, defined by (6.64); $f_{p,E}$ represents the friction factor for Ergun flow regime, predicted with (6.63); n is an empirical coefficient of correction; and $f_{p,T}$ represents a transitional friction coefficient defined by

$$f_{p,T} = f_{p,E} \times (Re_p/20)^m, \quad (6.66)$$

where m is a correction coefficient determined as 1.3, based on experimental data.

The composite solution, (6.66), exhibits close agreement throughout the entire range of Re_p , for which experimental measurements were obtained. Four different values of the coefficient n for (6.65) are tested: 0.5, 1, 5, and 50. There is a low sensitivity exhibited between the predicted friction factor and the parameter n . However, when n is between 1 and 5, this provides the best agreement. A comparison of modeling results and experimental determinations is shown in Fig. 6.83.

The results of the hydrodynamic modeling suggest that predictions of friction factor through a packed bed, for micrometer-sized packing material, exhibit altered

Fig. 6.83 Modeling versus experimental results for packed bed reactor [data from Pope et al. (2011)]

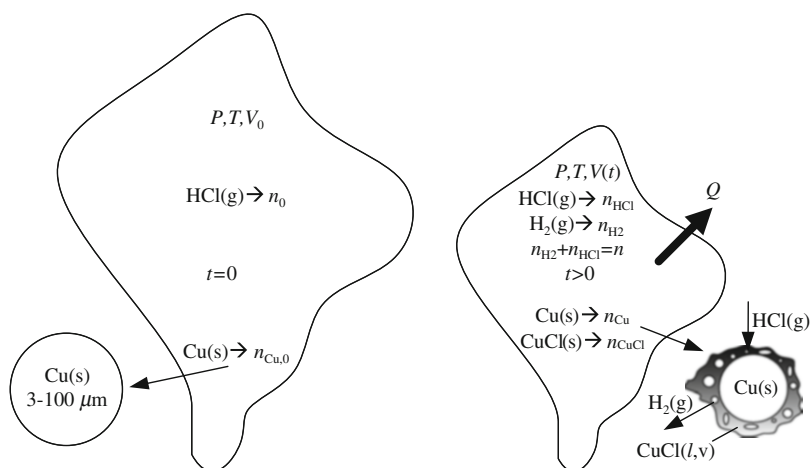
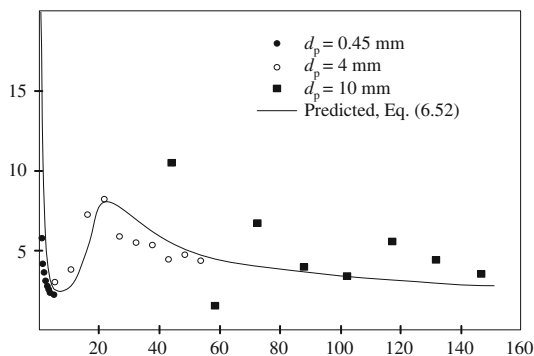


Fig. 6.84 Model of chlorination reaction process at constant pressure [modified from Zamfirescu et al. (2010b)]

flow phenomena than when the particles have larger diameters. These provide useful information and measured data to improve packed bed designs by limiting the adverse impact of undesirable pressure drops during operation.

The chemical reaction is modeled kinetically, and a parametric study is performed to determine the influences of particle size, temperature, and molar ratios on the hydrogen conversion aspects. For modeling purposes, it is assumed that chemical reactions and heat transfer are decoupled. Since the reaction is exothermic, it transfers reaction heat in the amount of about ~ 46 kJ/mol H_2 at 723 K.

The relevant transport phenomena at the gas/solid interface are heat and mass transfer and the chemical reaction. Figure 6.84 shows a model of the reactor. The reactor is a constant-pressure, isothermal batch type and it can be viewed as a thermodynamic system of variable volume $V(t)$, where $t \geq 0$ is time. At the initial moment, $t = 0$, in the reactor, one finds only n_{Cu} moles of copper and $n_{HCl} = n_0$

moles of gaseous hydrochloric gas. At any later moment, in addition to the two reactants in the reactor, there are n_{H_2} moles of hydrogen and n_{CuCl} moles of cupric chloride (assumed here in the solid state). The figure suggests that the gas volume around a reacted particle shrinks, because 1 mol of hydrochloric acid gas converts to a half mole of hydrogen. The fractional conversion X of hydrochloric acid gas is the ratio of converted reactant to the initial molar content, n_0 . Since the converted HCl at the current time t is $n_0 - n_{\text{HCl}}$, the fractional conversion is

$$X = \frac{n_0 - n_{\text{HCl}}}{n_0}. \quad (6.67)$$

Based on stoichiometry and fractional conversion of HCl, the number of moles of gases participating to the chemical reaction (hydrogen and hydrochloric acid) within the reactor is $n = n_0 \times (1 - 0.5X)$. Initially, copper particles present a bare surface exposed to HCl reactant. During the reaction, at the surface of the particle, the CuCl product is formed (see Fig. 6.84). The reaction heat will increase the particle temperature up to the melting point of CuCl. As saturated liquid, cuprous chloride partially evaporates. Its vapor pressure is about 10 Pa close to the normal melting point. Through the two-phase CuCl shell, gaseous HCl diffuses toward the copper surface and generated gaseous hydrogen diffuses toward the exterior.

This depicted situation suggests that the outer shell that embeds the copper core is unstable and thus facilitates good mass transfer. For gas–solid non-catalytic reactions, the mass transfer mechanism may be controlled by diffusion through the gas film, diffusion through the outer layer, or the chemical reaction. In the last case, which is assumed to represent the present situation, the mass transfer depends on the concentrations in the bulk flow (HCl) and at the copper surface (H_2). At the same time, the molar consumption rate of copper is the same as the rate of production of hydrochloric gas:

$$\dot{n}_{\text{Cu}} = \dot{n}_{\text{HCl}} = r_{\text{HCl}}. \quad (6.68)$$

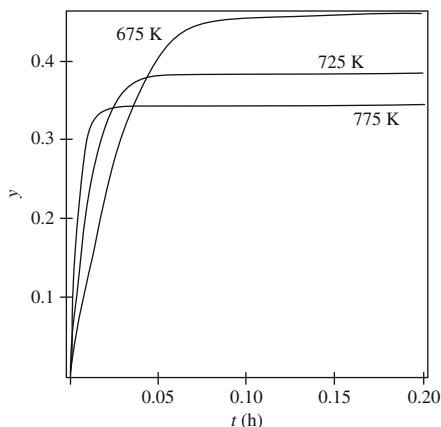
In (6.68), the rate of HCl consumption (r_{HCl}) depends on partial pressures of HCl and H_2 gases in the reactor space. The reaction rate is defined by (6.59) and (6.60). Therefore, one has

$$d^3 - d_0^3 = \frac{6M_{\text{Cu}}}{\pi\rho_{\text{Cu}}} \int_0^t \dot{n}_{\text{HCl}} dt. \quad (6.69)$$

The right side of (6.69) is negative (HCl is consumed) and the radius of the copper particle diminishes until it vanishes. On the right side, by setting $R = 0$, one may determine the time to complete the reaction, t_c . As detailed in Zamfirescu et al. (2010b), the conversion rate may be expressed by

$$\frac{dX}{dt} = k_f \left[\left(\frac{1-X}{1-0.5X} \right)^{0.5} - \frac{1}{K_{\text{eq}}} \left(\frac{0.5X}{1-0.5X} \right) \right]. \quad (6.70)$$

Fig. 6.85 Hydrogen yield variation with time for three reaction temperatures [data from Zamfirescu et al. (2010b)]



Equation (6.70) can be integrated numerically for a given operating temperature at which the constants are known. The fractional HCl conversion at equilibrium can also be computed by setting $dX/dt = 0$ and solving for X . It results in the time to reach chemical equilibrium in the batch reactor. The solution $X(t)$ of (6.70) is essential in the reactor design because it allows for calculation of other quantities, e.g., \dot{n}_{HCl} as a function of time. This leads to a particle diameter variation $d(t)$ with (6.69), but also allows for the calculation of heat generation at the particle surface based on the heat of reaction, $\Delta H_r(T)$:

$$q''(t) = -\frac{\Delta H_r(T)}{\pi d(t)^2} \dot{n}(t). \quad (6.71)$$

The hydrogen yield (y) represents the number of moles of hydrogen generated per mole of HCl reactant. Hydrogen yield can thus be calculated based on fractional HCl conversion, by $y = 0.5X$. In Fig. 6.85, the hydrogen yield variation against the time is shown, whereas the time origin is the moment when copper particles enter the reaction. The hydrogen yield is obtained by integration of (6.55); this integration has been made for three reaction temperatures. It is observed from the figure that the magnitude of the hydrogen production is faster at higher temperatures, although the equilibrium yield is lower. The time to equilibrium t_{eq} varies from 0.06 to 0.14 h.

Figure 6.86 presents the variation with reaction temperature of the hydrogen yield at equilibrium (y_{eq}), hydrochloric acid conversion at equilibrium (X), and equilibrium hydrogen concentration (molar fraction) in the gas phase (C_{eq}). Obtaining good conversions (over 80 %) is possible at the lowest temperatures in the range of interest, but this leads to larger equilibrium times, or in other words, larger residence times of particles in the reactor.

Denote n as the excess number of moles of hydrochloric acid, defined as the moles of HCl supplied to the reactor per mole of copper. In mathematical terms, this can be written as $n_{\text{Cu}} \times n = n_0$, where n_0 is the number of moles in HCl in the feed

Fig. 6.86 Variation with reaction temperature of the H_2 yield at equilibrium (y_{eq}), HCl conversion at equilibrium (X), and equilibrium hydrogen concentration in the gas phase (C_{eq}) [data from Zamfirescu et al. (2010b)]

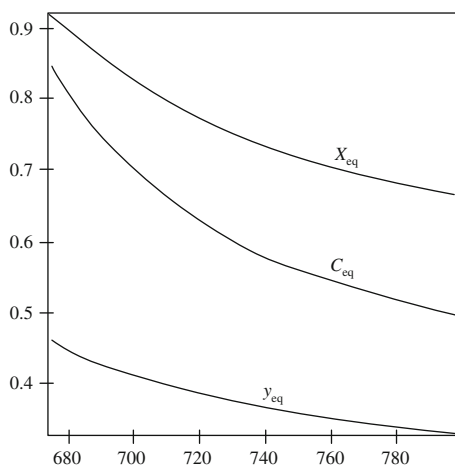
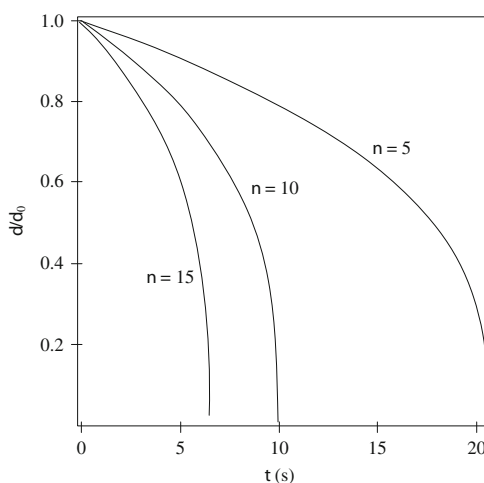


Fig. 6.87 Copper particle shrinkage during the reaction for various excess numbers (n) of hydrochloric acid in the feed stream [data from Zamfirescu et al. (2010b)]



stream. Then, as detailed in Zamfirescu et al. (2010b), the copper particle shrinkage with time is governed by the equation

$$d(t) = d_0 \times \left[1 - n \int_0^t \left(\frac{dX}{dT} \right) dt \right]^{1/3}. \quad (6.72)$$

Equation (6.72) can be integrated numerically to observe the particle shrinkage in time, during the reaction process. For stoichiometry, $n = 1$, so for 1 mol of copper there is 1 mol of HCl. In a reactor, the HCl must be supplied in excess in order to shift the reaction equilibrium to the forward direction. Figure 6.87 shows the decrease during the reaction time of the particle diameter relative to its initial diameter for excess hydrochloric acid, $n = 5, 10$, and 15 . The particle shrinks in

an accelerated manner especially after the diameter decreases below 20 % of the initial value. The solid copper particle completely disappears after a few tens of seconds. It is found that the residence time of copper particles varies between 10 and 100 s, depending on the operating conditions. The hydrogen conversion at equilibrium varies between 55 and 85 %, depending on the reaction temperature.

6.9 Heat Recovery and Reuse Within a Cu–Cl Plant

6.9.1 Pinch Analysis

The Cu–Cl cycle is expected to be driven in an environmentally benign manner using nuclear energy. Since each step occurs at a different temperature, the product of a step needs to be cooled or heated to the next step's temperature. Thus, there are many heat recovery opportunities within the cycle. The recovered energy as well as the energy released from the exothermic reactions could be reused in the cycle. Heat is transferred between various endothermic and exothermic reactions in the Cu–Cl cycle through heat exchangers that supply or recover heat from individual processes. There is also opportunity to integrate heat pumps and heat engines with the cycle.

Effective thermal management within the Cu–Cl cycle is crucial for achieving high efficiency. The cycle's efficiency is improved drastically when all heat released by the products of reactions is recycled internally. Therefore, the energy matching and hence heat exchangers within the cycle have a significant role in terms of overall effectiveness of the cycle.

As a first step of the pinch analysis of the cycle, the heat fluxes crossing the thermodynamic boundary of the water-splitting cycle are identified and listed in terms of their temperature level and enthalpy. In order to have uniform energy units, the enthalpy is expressed in kJ/mol of hydrogen produced.

The five-step cycle Cu–Cl-5 has the most opportunities of heat recovery and reuse because it comprises four thermal reactors. Other heat fluxes are required to preheat the reactants at the desired level of temperature. Some other fluxes are associated with heat recovery from the hot products. The inventory of heat transfer for the five-step Cu–Cl cycle is presented in Table 6.27. One observes that copper particles must be heated from 333 to 723 K, which is the temperature of the hydrogen production reactor. For the purpose of the thermodynamic analysis, the Cu particle heating is divided into three processes, namely: process 1 → 2 discussed above, where the enthalpy required to heat Cu and CuCl₂ and water between 333 and 373 K is 14 kJ/mol H₂; process 3 → 4 along which three different substance streams are heated from 373 to 673 K, i.e., 2 mol of Cu, 1 mol of steam, and 2 mol of dry CuCl₂ with an enthalpy input of 75 kJ/mol H₂; and lastly the 2 mol of Cu particles are heated from 673 to 723 K within process 5 → 6 that consumes

Table 6.27 Energy inputs and outputs for Cu–Cl-5 cycle

Process	ΔH (kJ/mol H ₂)	T (K)	Remarks
1 → 2	+14	333	Electrolytic Cu(s) production step: $4\text{CuCl(s)} \rightarrow 2\text{CuCl}_2\text{(aq)} + 2\text{Cu(s)}$
2 → 3	+75	333 → 373	Heating: $2\text{Cu(s)} + 2\text{CuCl}_2\text{(aq)} + 1.248\text{H}_2\text{O(l)}$
3 → 4	+87	373 → 673	Heating: $\text{H}_2\text{O(g)} + 2\text{Cu(s)}$; $2\text{CuCl}_2\text{(s)}$
4 → 5	+132	673	Hydrolysis reactor: $2\text{CuCl}_2\text{(s)} + \text{H}_2\text{O(g)} \rightarrow \text{CuO}^*\text{CuCl}_2\text{(s)} + 2\text{HCl(g)}$
5 → 6	+3	673 → 723	Copper particles heating: 2 mol Cu(s) per mol H ₂
7 → 8	+146	823	Oxygen production reactor: $\text{CuO}^*\text{CuCl}_2\text{(s)} \rightarrow 2\text{CuCl(l)} + 0.5\text{O}_2\text{(g)}$
9 → 10	−10	823 → 723	Cooling: $0.5\text{O}_2\text{(g)} + 2\text{CuCl(l)}$
10 → 11	−47	723	Hydrogen production reactor: $2\text{Cu(s)} + 2\text{HCl(g)} \rightarrow 2\text{CuCl(l)} + \text{H}_2\text{(g)}$
11 → 12	−162	723 → 373	Cooling: $\text{H}_2\text{(g)} + 0.5\text{O}_2\text{(g)} + 4\text{CuCl(l)} \rightarrow \text{s}$
12 → 13	−75	373 → 333	Cooling: $\text{H}_2\text{(g)} + 0.5\text{O}_2\text{(g)} + 4\text{CuCl(s)} + 1.248\text{H}_2\text{O(g)} \rightarrow \text{l}$
W_{EL}	+110	−	Electrical power needed to drive Cu(s) production step (1 → 2)
Q_{H}	+458	−	Total heat input into the cycle
Q_{C}	−294	−	Total heat rejected by the cycle
Q_{Loss}	−21	−	Assumed heat losses, amounting to 5 %

Sign convention: (+) = heat or work input, (−) = heat output

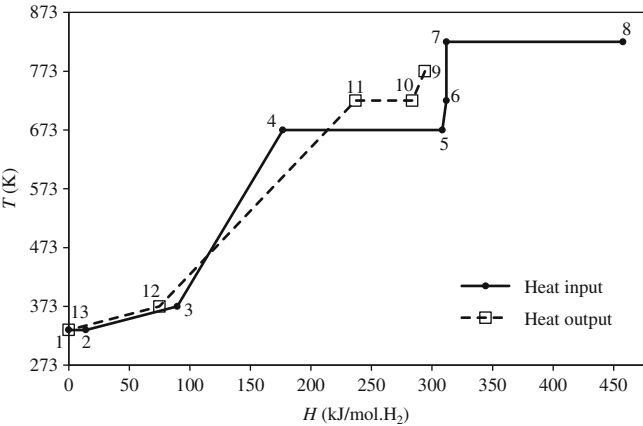


Fig. 6.88 Pinch diagram for the five-step copper–chlorine cycle

3 kJ/mol H₂. A similar approach is pursued to identify all processes listed in Table 6.1, where the energy efficiency of the cycle is also indicated.

Starting from the process data in Table 6.27, it is possible to construct a temperature–enthalpy diagram (pinch diagram) as shown in Fig. 6.88. This indicates the required heat inputs and outputs and their associated temperature levels. In the diagram, the continuous line refers to heat input streams, while the

dashed line refers to heat outputs. The processes illustrated in the figure have labels corresponding to those indicated in the table. Thus the streams requiring heat are identified with the line 1–2–3–4–5–6–7–8, and those releasing heat are 9–10–11–12–13. The construction of the pinch diagram imposes a convention for “zero” enthalpy. The enthalpy of the state at the lowest temperature is set to zero. This is state 1—the isothermal process in the electrolytic bath that produces copper from cuprous chloride at 333 K.

Note that the value of 333 K is adopted here from the perspective of coupling the process to the moderator of a nuclear power plant. However, in general, the temperature associated with the Cu production step can be closer to the ambient. For the heat releasing process, zero enthalpy is assumed for the cooled product streams of H_2 , O_2 , $CuCl(s)$, and $H_2O(l)$ —the last two chemicals are recycled. This temperature is 333 K, the lowest in the cycle, even though in an actual implementation, the streams of hydrogen and oxygen should be cooled more, i.e., to the ambient temperature or below, to facilitate compression and storage.

Considering the temperature–enthalpy profiles from Fig. 6.88, one observes that for $T < 373$ K, the temperature of streams releasing and absorbing heat are almost superimposed. This suggests that relatively straightforward flow arrangements can be devised for heat recovery. Orhan et al. (2011) report an exergy and energy analysis of heat exchangers within the copper–chlorine cycle aimed to enhance the heat recovery and reuse options for improved efficiency.

The analysis of heat exchangers involves calculations of the number of heat transfer units (NTU) and heat exchanger effectiveness (ϵ). These parameters are defined by known relationships, depending on the specific heat (c_h, c_c) of the hot and cold streams, respectively, overall heat transfer coefficient (U), heat exchanger area (A), and mass flow rate \dot{m} ; the definition relationships are given below:

$$\epsilon = \frac{c_c \times (T_{c,out} - T_{c,in})}{c_{min} \times (T_{h,in} - T_{h,out})}, \quad NTU = UA/(\dot{m} \times c)_{min}, \quad (6.73)$$

where $c_{min} = \min\{c_c, c_h\}$ and $(\dot{m} \times c)_{min}$ is the minimum of the products of the mass flow rate and specific heat for hot and cold fluids.

The effect of the heat exchanger effectiveness on thermal management in the Cu–Cl cycle is illustrated in Fig. 6.89. The amount of recovered heat within the cycle can be increased by using heat exchangers with higher effectiveness. Then, the total heat requirement and consequently the net heat requirement for the cycle are decreased. At $\epsilon = 0.85$, the total heat demand is equal to the recovered heat and thus the net heat requirement is zero. Beyond that point ($\epsilon = 0.85$), the net heat requirement is negative since the recovered heat is more than the total heat demand in the cycle. However, the heat requirement for chemical reactions and the electrical energy needed for electrolysis, pumping, and compression are not included, as the analysis is only considering the heat exchangers.

The variation of the overall efficiencies of the Cu–Cl cycle with heat exchanger effectiveness is—as shown in Orhan et al. (2011)—approximately linear. Both energy and exergy efficiencies of the cycle increase with more effective heat

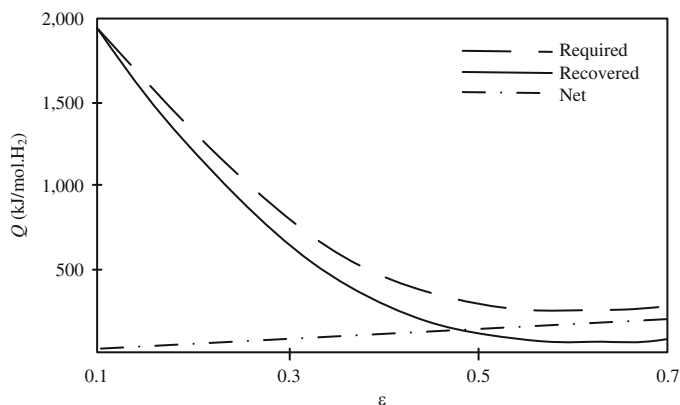


Fig. 6.89 Effect of heat exchanger effectiveness on heat recovery in the Cu–Cl cycle [data from Orhan et al. (2011)]

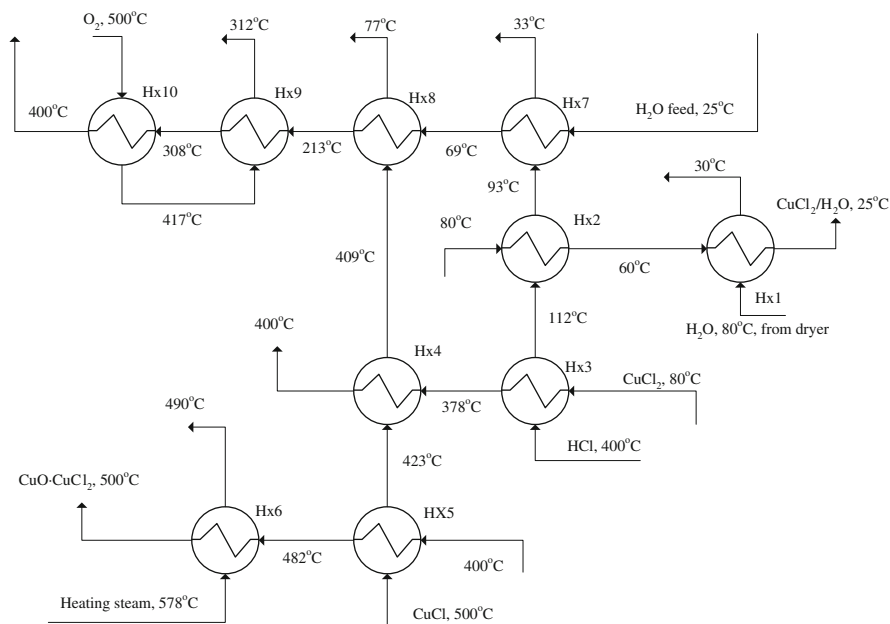


Fig. 6.90 Heat exchanger network of heat recovery and reuse within the Cu–Cl cycle [modified from Orhan (2011)]

exchangers in the cycle. This is because heat exchangers with a higher effectiveness result in more heat recovery within the cycle and thus decrease the external heat requirements for the cycle. Based on a pinch analysis, integrated heat exchanger networks of enhanced heat recovery and reuse can be used. A heat exchanger network was presented by Orhan et al. (2011) as indicated in Fig. 6.90.

6.9.2 Heat Recovery from Molten CuCl

The most challenging heat recovery process within the copper–chlorine cycle is from molten cuprous chloride droplets that solidify and must be cooled to a temperature corresponding to the electrochemical step (about 353 K). Recovering heat during the solidification of molten CuCl and efficient utilization of this recovered heat are crucial to the efficient performance of the copper–chlorine cycle. Several studies reported theoretical results of heat recovery process and modeling—Jaber et al. (2010a, b) and Ghandehariun et al. (2011)—and some yet unreported experimental work is under way at UOIT.

The process of cuprous chloride droplet cooling is a type of multiphase flow, similar to droplet/particle flows in spray columns, packed beds, and other devices involving the interaction between particles or droplets with gas streams. Heat recovery from molten CuCl droplets has similarities with the dynamics of droplets with high viscosity ratios like solid particles, as with liquid metal droplets. Heat transfer from the continuous phase to the droplet involves convective heat transfer, and complex interactions of velocity, droplet breakup, elongation, and so forth.

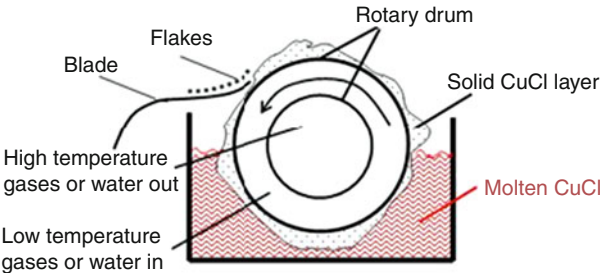
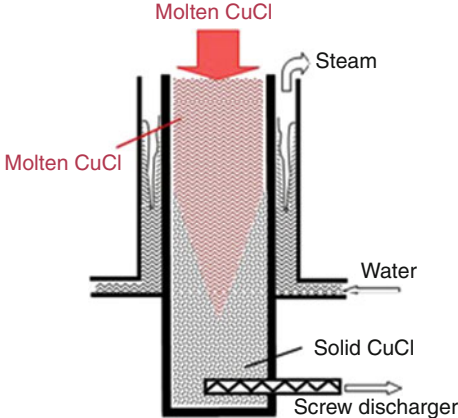
Various methods for recovering heat from molten CuCl—suggested by Ghandehariun et al. (2011)—are presented in this section. Table 6.28 presents various heat recovery options that were considered in cooling of cuprous chloride droplets. Several lab experiments for cuprous chloride solidification were performed at UOIT. Figure 6.91 presents two experimental units used for heat recovery experiments from molten CuCl. Figure 6.92 illustrates some samples obtained during the solidification experiments. A scaled up tilt furnace apparatus is used at UOIT for large-scale heat recovery from molten cuprous chloride. A photograph is shown in Fig. 6.93.

Direct heat and mass transfer from sprayed droplets of CuCl to a gaseous coolant has been modeled by Jaber et al. (2010a, b). Fluid flow around droplets can be categorized into low Reynolds number flows, and high Reynolds (Re) number flows. Low Reynolds number flows can be creeping flow if $Re \ll 1$ for which the inertia of the fluid can be neglected. The flow around the droplets is asymmetric only for small Reynolds numbers. For flows with $Re > 1$, the pattern becomes distorted, and a wake is generated at the back of a droplet. At very high Reynolds numbers, the wake becomes unsteady and very strong, with shedding of vortices.

The following flow regimes are encountered for high Reynolds numbers of solid spheres.

- *Attached flow* ($1 < Re < 20$): The flow remains attached to the droplet surface and separation does not occur in this flow regime. The generated wake behind the droplet is weak and steady.
- *Steady-state wake* ($20 < Re < 130$): At the beginning of this flow regime, a weak circulation region is attached to the back of the droplet. As Re increases, the wake becomes stronger, its width and length increase, and its point of attachment moves forward on the surface of the droplet.

Table 6.28 Heat recovery options from molten cuprous chloride within the Cu–Cl cycle

Type and description	Diagram
<p><i>Drum flaker</i></p> <ul style="list-style-type: none"> • Solidification onto the outer surface of a rotating cylinder • Inner surface is cooled by a coolant • Knife or blade removes the solids • 80 % of the circumference in contact with material • Drum surface temperature lower than the melting point • Molten CuCl solidifies at the outside wall forming a solid layer 	 <p>Labels in diagram: Rotary drum, Flakes, Blade, Solid CuCl layer, Molten CuCl, High temperature gases or water out, Low temperature gases or water in.</p>
<p><i>Casting extruder</i></p> <ul style="list-style-type: none"> • Tube in a tube heat exchanger configuration is used • Water supplied to the bottom at the outer shell is the coolant • Steam is generated via heat recovery • Molten CuCl enters at ~800 K • Solids exit at ~323 K • Extruder removes solids to prevent plugging of channel • Method involves thorough selection of materials 	 <p>Labels in diagram: Molten CuCl, Steam, Water, Solid CuCl, Screw discharger.</p>
<p><i>Spinning atomizer</i></p> <ul style="list-style-type: none"> • Nozzle introduces the molten CuCl • Spinning disk or rotary cup generates centrifugal force • Droplets disperse around and fall as a spray • Air or inert gas is distributed through a perforated plate • Heat from CuCl is transferred to the coolant • Care must be taken to retain all droplets inside the system • Solid particles are removed at the bottom 	

(continued)

Table 6.28 (continued)

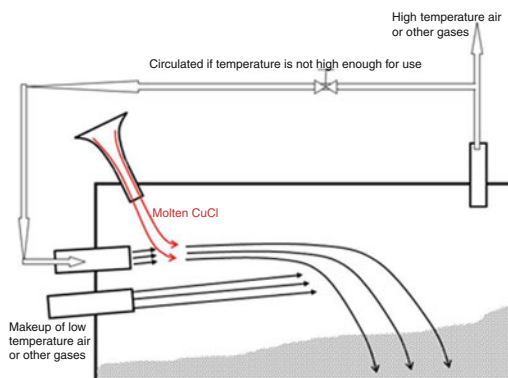
Type and description	Diagram
<ul style="list-style-type: none"> The vessel must be relatively large care in selecting materials for rotary cup must be taken 	

Inert gas atomizer

- CuCl is granulated by atomization with inert gas or air
- Possible to atomize a slurry of water and CuCl
- System is largely extended horizontally
- Second air/gas gun is needed to extent particle jet
- Design must avoid the buildup of particles on walls
- Particles must solidify before colliding with walls
- cyclone may be placed to separate the entrained solids

Falling-through atomizer

- Molten CuCl sprayed by a sieve shaker
- Spraying may be difficult due to corrosive effects of molten salt
- If upstream process is carried out at high temperature, it facilitates



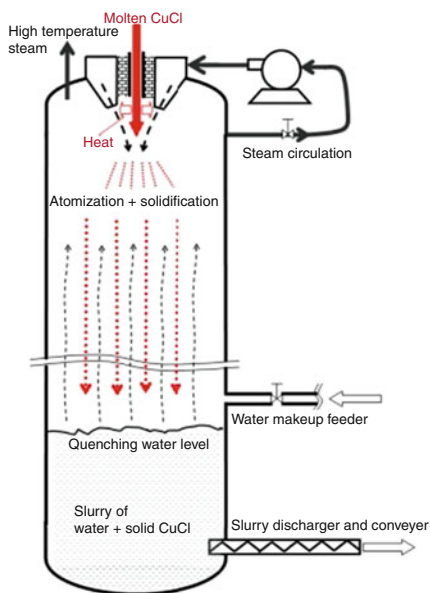
(continued)

Table 6.28 (continued)

Type and description	Diagram
spraying <ul style="list-style-type: none"> • Droplets solidify before reaching the bottom of the vessel • Countercurrent airflow used to recover heat • A fluidized bed can be also used at the column base to remove additional heat • Resulting hot air from recovery is at ~ 473 K 	

Quenching atomizer

- Molten salt must be pumped through a spray nozzle at the top of the vessel
- Injection temperature must be ~ 800 K for good atomization
- Atomized salt then falls into a quenching water bath
- CuCl further transfers its residual heat to the upward flowing steam
- Not all droplets are solidified during descent; some solidify in the quenching bath
- Heat received from quenching bath generates steam
- Steam is superheated in the region above the bath
- No atomization gases are required
- CuCl can be easily separated from water and directed toward the next process



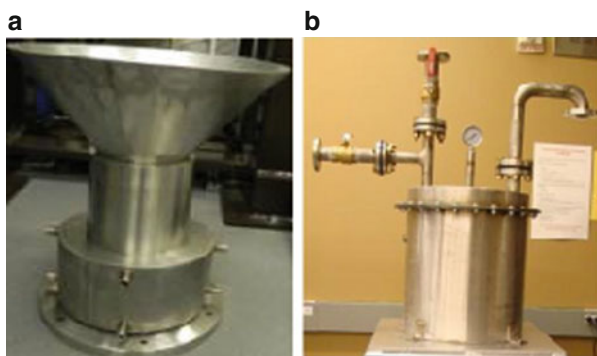
(continued)

Table 6.28 (continued)

Type and description	Diagram
<p><i>Quenching atomizer with slurry vessel</i></p> <ul style="list-style-type: none"> • No quench bath is used, rather all droplets are solidified in the column • Solid particles agglomerate at the bottom of the main (granulation) vessel • Particles are conveyed to a water bath where they release their sensible heat • Saturated steam flows in the granulation vessel • Steam is superheated in the granulation vessel by heat transfer from droplets • Control of droplet dimensions is not essential because the risk of steam explosion is eliminated • Corrosion protective coatings are needed inside the vessel 	

Source: Ghandehariun et al. (2011)

Fig. 6.91 Heat exchanger (a) and buffer tank for steam (b) used for heat recovery experiments from molten CuCl at UOIT



- *Unsteady wake in laminar flow* ($130 < Re < 270$): at the beginning of this flow regime, a weak, long-period oscillation at the tip of the wake occurs. Oscillations increase with increasing Re , but the wake remains attached to the droplet. In this flow regime, the viscous effects have a small role on the value of the drag coefficient. Most of the generated drag is due to the pressure difference between two sides of the droplet. The flow outside of the wake remains laminar throughout this flow regime.

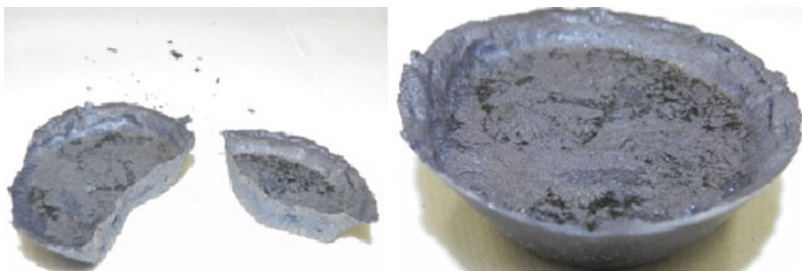


Fig. 6.92 Samples with solidified cuprous chloride

Fig. 6.93 Tilt furnace apparatus for large-scale molten salt heat recovery at UOIT



- *Vortex shedding* ($270 < Re < 6,000$): Pockets of vorticity are shed away from the tip of the droplet in this flow regime. This influences the flow velocity and its fluctuations at far fields. The separation point of the flow moves forward on the droplet's surface, reaching a point on the droplet that corresponds to an angle measured from the forward axis of the sphere of 83° .
- *Unsteady boundary layer separation* ($6,000 < Re < 300,000$): At the beginning of this flow regime, which is usually called the “lower critical Reynolds number,” the separation point at the droplet surface starts rotating around the droplet in a frequency equal to the vortex shedding frequency. The wake behind the droplet does not reach a turbulent stage, and the value of the drag coefficient reaches an almost constant value throughout this flow regime.
- *Transition and supercritical flow* ($Re > 300,000$): The wake becomes turbulent in this flow regime. The transition to a turbulent wake starts at $Re = 2 \times 10^5$ and it is completed at $Re = 3.7 \times 10^5$. However, the critical point of transition is usually at around $Re = 3 \times 10^5$. The point of separation moves downstream of the droplet, from an angle of 83° – 120° , and it remains constant thereafter. The free shear layer in the flow becomes turbulent and attached to the surface of the droplet, which causes a sharp reduction in the value of the drag coefficient.

Flow around liquid droplets has the same characteristics as solid particles. However, at high Reynolds numbers, the shear stresses acting on the droplet's surface lead to a significant shape distortion that might lead to breakup of the droplet. There are several differences between flow around liquid droplets and solid particles. Firstly, internal circulations within liquid droplets delay the formation of the wakes by delaying the boundary layer separation. They also cause the length of the wake to be slightly shorter. Secondly, two symmetric internal weak wakes appear at the back of liquid droplets at high Reynolds numbers. These cause a flow reversal at the rear of the droplet, so the velocity vector points in the positive direction for a short distance. Liquid droplets exhibit a lower drag coefficient than that of solid droplets. A high Reynolds number causes the shear stresses to deform liquid droplets and change their shape from perfect spheres to spheroids. Internal flow fields within liquid droplets also affect the external flow field, which can significantly lower the vorticity compared to solid particles. These characteristics and features of fluid flow past droplets and spheres will be used for physical development and understanding of the droplet flow modeling and results. In the next section, predictive formulations will be developed for the fluid flow and heat transfer from the molten CuCl droplets.

In a falling-through heat recovery system configuration as indicated in Table 6.28, the droplets fall under gravity, and transfer heat to the upward flowing surrounding gas stream. The flow is assumed to be one-dimensional countercurrent symmetrical flow. Droplets enter the heat exchanger from the top, initially at a near-zero velocity, and then increase as they fall down the heat exchanger under the action of different forces.

The heat transfer phenomena between the droplets and air is assumed as one-dimensional transient heat transfer, with heat transfer at the surface of the droplet to the air by forced convection. The temperature distribution within a droplet is assumed to be spatially uniform. The lumped capacitance assumption is made for the droplet so that internal temperature gradients within a droplet can be neglected. To determine the temperature distribution, the convective heat transfer rate can be found as

$$\dot{Q}_c = 0.5\bar{h}A_d(T_{d,i} + T_{d,e} - T_{f,i} - T_{f,e}), \quad (6.74)$$

where A_d is the surface area of the droplet corresponding to the droplet mass flow rate; $T_{d,i}$ and $T_{d,e}$ are the temperatures of the droplet at the inlet and exit of each element, respectively; and $T_{f,i}$ and $T_{f,e}$ are the temperatures of the fluid at the inlet and exit of each element, respectively; and \bar{h} is the average heat transfer coefficient. The heat transfer rate from the droplet during sensible cooling can be written as

$$\dot{Q}_d = \dot{m}_d c_{p,d}(T_{d,i} - T_{d,e}), \quad (6.75)$$

where \dot{m}_d is the droplet mass flow rate, and $c_{p,d}$ is the specific heat of the droplet at constant pressure. The heat transfer rate to the fluid may be expressed as

$$\dot{Q}_f = \dot{m}_f c_{p,f}(T_{f,e} - T_{f,i}). \quad (6.76)$$

The heat transfer rates are then equated for the sensible heating/cooling portions of the heat exchange trajectory of the droplets, namely, $\dot{Q}_c = \dot{Q}_d = \dot{Q}_f$. Therefore, from (6.74), (6.75), and (6.76), one obtains the exit temperature of the fluid as reported by Jaber et al. (2010a):

$$T_{f,e} = \left[\frac{\bar{h}A_d}{2\dot{m}_f c_{p,f}} \times T_{d,i} + \frac{\bar{h}A_d}{2\dot{m}_f c_{p,f}} \times T_{d,e} + \left(1 - \frac{\bar{h}A_d}{2\dot{m}_f c_{p,f}} \right) \times T_{f,i} \right] / \left(1 + \frac{\bar{h}A_d}{2\dot{m}_f c_{p,f}} \right). \quad (6.77)$$

Equation (6.77) does not depend on the CuCl properties; it only requires the droplet temperature at the inlet and exit. There exist two cases of heat transfer due to phase change of the droplet. In the first case, the temperature of the droplet is constant during the phase change process, so $T_{d,i}$ and $T_{d,e}$ are equal in (6.77). In the second case, the temperature of the droplet changes between the inlet and exit due to sensible heat loss.

The increase in heat transfer does not take long because the first-phase transformation process differs with the second-phase transformation process by 11 °C. In the first-phase transformation process, the heat transfer rate decreases again and reaches close to zero, because the temperature difference reaches a value of 1 °C. Finally, the heat transfer rate increases again in the final sensible heat transfer process.

Because there is no available experimental data on spraying of molten CuCl, the validation of the model by Jaber et al. (2010a) is performed against reference data of a problem of heat transfer from a droplet to a stream of air. It is found that predictions from Jaber et al. (2010a) have a 0.4 % relative error for the Nusselt number, 1.7 % for convective heat transfer coefficient, and 1.7 % for the heat transfer rate.

With a validated model, two case studies were considered by Jaber et al. (2010a, b) with the parameters indicated in Table 6.29. The variation of the heat transfer rate throughout the height of the heat exchanger is presented in Fig. 6.94. It is evident from the results that the larger droplet diameter has a higher heat transfer rate. This occurs because of the area ratio between two droplets. A droplet with a diameter of 1 mm has four times the surface area of a droplet with a 0.5 mm diameter. The heat transfer rate increases initially at the bottom of the heat exchanger because of the increasing temperature difference between both streams in this region, which yields a higher potential for heat transfer.

The heat transfer rate reaches a maximum value when the second-phase transformation ends. After this point, it starts decreasing due to the decreasing temperature difference between both fluids in the phase transformation process. When the second sensible heat transfer process is reached, the heat transfer rate starts increasing again.

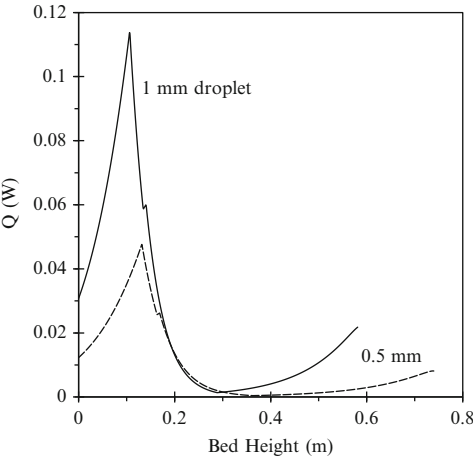
Figure 6.95 illustrates a case with a CuCl flow rate of 3.4 g/s, which is equivalent to the flow from an oxygen production reactor for a Cu–Cl plant that generates 3 kg of hydrogen per day. The airflow rate is 3 g/s, which is slightly higher than the

Table 6.29 Simulation parameters of CuCl spray heat exchanger for two case studies

Parameter	d_d	
	1 mm	0.5 mm
CuCl mass flow rate (g/s)	3.4	3.4
Air mass flow rate (g/s)	3	3
CuCl inlet temperature (°C)	530	530
CuCl exit temperature (°C)	70	70
Air inlet temperature (°C)	25	25
Air exit temperature (°C)	493	493
Number of CuCl droplets	1,779	14,226
CuCl droplet inlet velocity (m/s)	0.02	0.07
Air inlet velocity (m/s)	0.2	0.2
Droplet travel time (s)	0.36	0.40
Number of droplet injectors	100	100
Heat exchanger height (m)	0.6	0.8
Heat exchanger diameter (m)	0.13	0.13

d_d droplet diameter
Source: Jaber et al. (2010a, b)

Fig. 6.94 Heat transfer rate variation with bed height [data from Jaber et al. (2010a)]



minimum airflow required to recover all heat from a stream of CuCl droplets at a temperature of 800 K. Because of the high average temperature difference between the CuCl droplets and airstreams, the heat transfer rate is high. The heat transferred to the airstream is more than three times the amount of heat transferred in the latent heat transfer process. This implies that the average required length to transfer one unit of thermal sensible energy was about 0.02 m, compared to 0.03 m to transfer the same amount of heat in a latent heat transfer process, with the same inlet temperature difference. Once the CuCl droplet stream reaches a temperature of 695 K, a second-phase transformation process occurs. Here CuCl droplets have a constant temperature solid–solid phase change. The air temperature still increases, but with a decreasing rate of increase. When the air temperature increases, the temperature difference between both streams decreases and causes the heat transfer

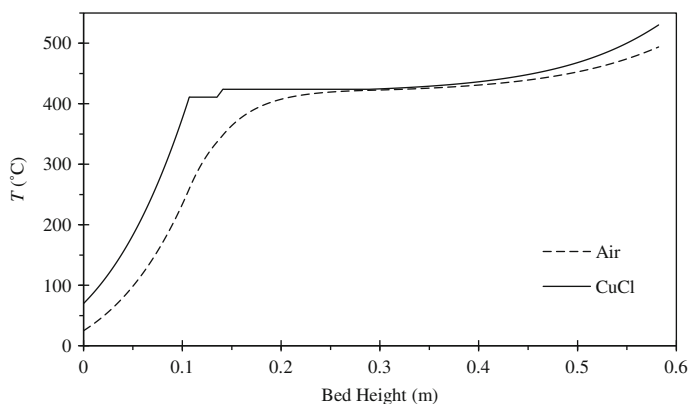


Fig. 6.95 Temperature distribution in air and CuCl for sprayed droplets of 1 mm [data from Jaber et al. (2010a)]

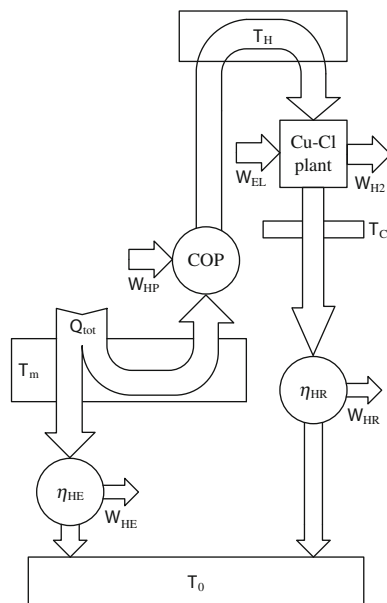
rate to decrease. This causes the required length of interaction between both streams to recover one unit of thermal energy to increase. The rate at which the air temperature increases keeps decreasing until it nearly reaches a value of zero. This occurs at the end of the process, where the air temperature reaches a value of 675 K. This point has the lowest heat transfer rate throughout the heat exchanger.

The final sensible heat transfer process starts when all latent heat energy is absorbed by the airstream from the first-phase change process. In this final process, the CuCl droplets and air temperatures start increasing at a higher rate, similar to the temperature increase in the first sensible heat transfer process. The temperature difference between both streams also increases. The process ends when the CuCl droplets reach a temperature equal to 803 K and the air reaches a temperature of about 766 K. The required dimensions of the heat exchanger for this example case study to complete all of the heat transfer processes are a height of 0.6 m and a diameter of 0.13 m.

6.9.3 Heat Pump Integration in a Copper–Chlorine Plant

As discussed previously, heat from hotter streams can be recovered and used to heat other streams within the Cu–Cl cycle. With respect to the pinch diagram in Fig. 6.88, for $T < 373$ K, the temperature of streams releasing and absorbing heat are almost superimposed. This suggests that straightforward flow arrangements can be devised for heat recovery between them. For the other streams, it is desirable to use heat recovery as much as possible and upgrade the temperature of the rejected heat such that it reaches the level needed for heat input. The heat released by stream 9–10–11–12 should be received by a heat pump, which at the expense of additional power input upgrades the temperature and enthalpy content and delivers a hot stream to the Cu–Cl cycle that matches the profile 3–4–5–6–7–8.

Fig. 6.96 General layout of an integrated copper–chlorine cycle and heat pump system



The work required to operate such a heat pump can come from a sustainable heat source available at an intermediate temperature T_m , which drives a heat engine operating between T_m and the ambient at T_0 . This heat engine also delivers power to the Cu–Cl cycle. However, because the ambient temperature is lower than 333 K (assumed to be the minimum temperature within the system), it is better from a thermodynamic point of view to use the heat rejected to drive a heat engine that discharges heat to the environment while producing useful work output. For example, if the ambient is a lake at 288 K and the average temperature rejected by the Cu–Cl cycle is 573 K, then the Carnot efficiency of the heat engine is $\sim 50\%$.

A thermodynamic model for coupling the Cu–Cl cycle to a sustainable heat source is proposed in Fig. 6.96. This model comprises four components, namely, the Cu–Cl plant, a heat pump “COP,” and two heat engines, η_{HE} and η_{HR} . The model assumes four temperature reservoirs as follows:

- Ambient temperature reservoir at T_0
- Sustainable heat source reservoir at $T_m > T_0$
- High-temperature reservoir that delivers useful heat to the Cu–Cl cycle at $T_H > T_m$
- Cold-temperature reservoir at which the Cu–Cl cycle rejects heat at T_C , with $T_H > T_C > T_0$

The plot from Fig. 6.97 shows the variation of hydrogen production efficiency of the Cu–Cl cycle, with idealized constant-temperature heat reservoirs, as a function of the abatement of heat engines/pumps from the Carnot efficiency. For 50 % abatement, one can expect a hydrogen production efficiency range from 4 to 39 % if the temperature of the sustainable energy source T_m varies from 333 to 623 K. The

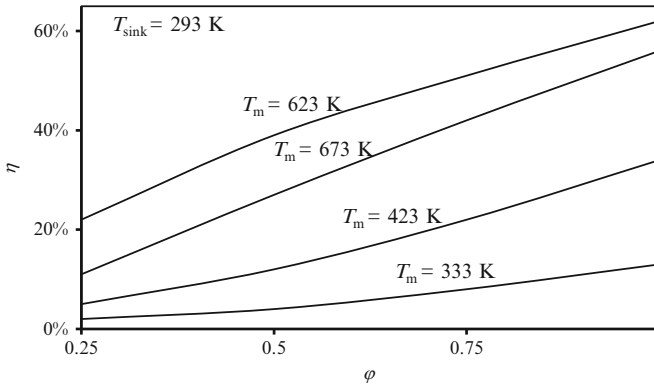


Fig. 6.97 Upper bound energy efficiency variation with abatement ϕ from the Carnot efficiency for water-splitting system integrated with a heat pump

Carnot abatement factor—denoted with ϕ —is a parameter ranging from 0 to 1 that expresses the abatement of the COP of a heat pump or efficiency of a heat engine from the Carnot value. For $\phi = 0$, the COP takes its minimal value of 1, while for $\phi = 1$, the COP and the efficiency are maximum and equal to the Carnot limit.

Using the Carnot abatement efficiency, the following set of relationships express the energy efficiency and COP of heat engines and heat pumps of the system in Fig. 6.96:

$$\left. \begin{aligned} \text{COP} &= 1 + \phi[Q_H/(W_{\text{HP}} - W_{\text{HR}}) - 1] \\ \eta_{\text{HE}} &= \phi(1 - T_0/T_m) \\ \eta_{\text{HR}} &= \phi W_{\text{HR}}/Q_C \end{aligned} \right\} \quad (6.78)$$

The pinch diagram of the process (see Fig. 6.88) can be transposed in T – S coordinates, where S is the stream entropy expressed in kJ/kmol H_2 . The streams are thermodynamic systems that interact with the surroundings by heat transfer only. Consequently, for any stream, $\delta Q = dH$; thus, $dS = \int (1/T)dH$.

For processes evolving at constant temperature (like $4 \rightarrow 5$, $7 \rightarrow 8$, $10 \rightarrow 11$), one obtains $\Delta S = \Delta H/T$. If the temperature is not constant, assume a linear variation of the enthalpy with temperature; then

$$S - S_a = \frac{H_b - H_a}{T_b - T_a} \times \ln\left(\frac{T}{T_a}\right), \quad (6.79)$$

where a is the initial state, b is the final state, and T and S correspond to any intermediate state of the process.

The area embraced by the lines 1–2–3–4–5–6–7–8 and that indicated by “Heat Source” in Fig. 6.98 represent the ideal/minimum work needed by the heat pump to

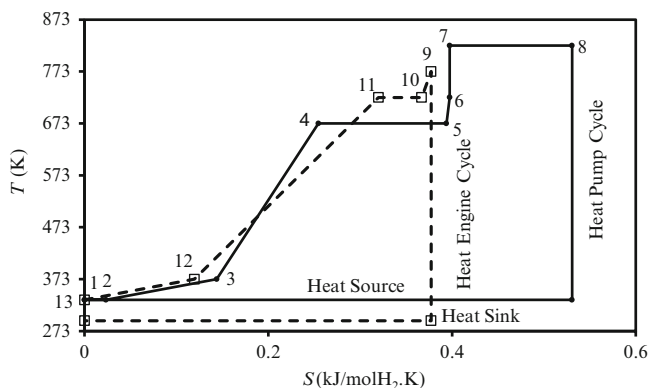


Fig. 6.98 Ideal power and heat pump cycles integrated to a Cu–Cl plant, represented in a T – S diagram

upgrade the temperature of the heat source and deliver useful heat to the Cu–Cl cycle. The area encompassed by lines 9–10–11–12–13 and that indicated with “Heat Sink” in Fig. 6.98 represents the ideal/maximum work that can be obtained from the heat recovered from the Cu–Cl cycle. The temperature of the “Heat Source” shown in Fig. 6.98 is taken as 333 K; however, it can be any value in the range above for T_m . The temperature of the “Heat Sink” represented in the figure is taken as 293 K. The engineering challenge regarding the integration of the Cu–Cl plant with the thermal energy source T_m consists of finding suitable working fluids and processes that allow for the construction of a heat pump and heat engine cycle operating according to that presented in Fig. 6.98.

The upper bound efficiency of hydrogen production with the ideal system varies between 6 and 23 % for heat source temperatures in the range of 353–523 K if the Carnot abatement of the integrated heat engines and heat pump is taken as 0.5. Various options of heat pumps—chemical processes based on salt/ammonia- and magnesium-oxide reactions—for upgrading the temperature of thermal energy are presented by Naterer (2008); these systems can be integrated with the copper–chlorine cycle. Integration of a chemical heat pump based on the reversible steam–methane reaction with a copper–chlorine plant linked to a nuclear reactor is presented by Granovskii et al. (2008). Zamfirescu et al. (2009, 2010c, 2011) presented a number of vapor compression heat pumps applicable to a copper–chlorine plant.

Figure 6.99 shows a scheme of cascaded heat pump systems integrated with a copper–chlorine cycle and a cascaded heat engine system. In this concept, the main power plant (e.g., nuclear power plant) generates net power with an efficiency η_1 (the heat source is assumed at a level of ~ 623 K, while the sink is at 373 K). Further heat recovery (e.g., from the moderator of the nuclear reactor) allows for the operation of a low-temperature heat engine as a sink at the environment at 298 K. This heat engine generates sustainable power ($W_{\text{sustainable}}$), which is used to drive cascaded heat pumps that upgrade the temperature of recovered heat up to the level

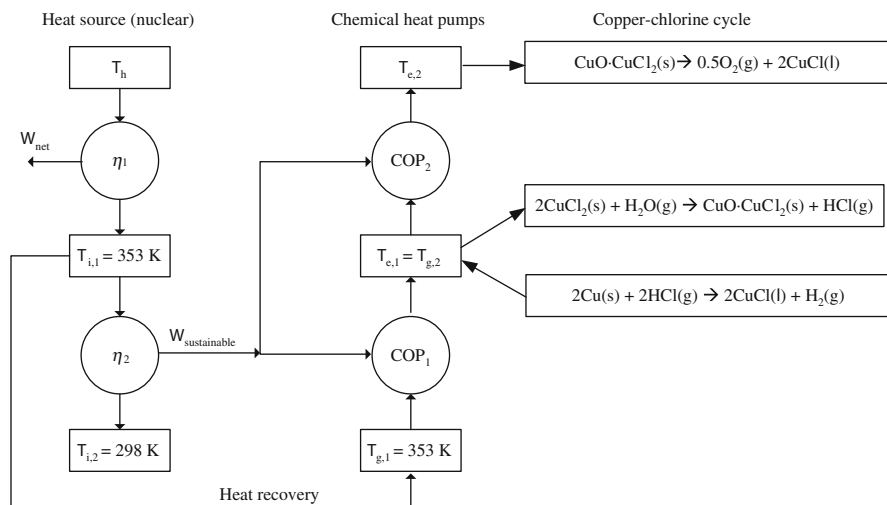


Fig. 6.99 Layout of a copper–chlorine plant integrated with two heat engines and two heat pumps [modified from Naterer (2008)]

required for driving chemical reactions within the Cu–Cl cycle. The exothermic reaction within the cycle is also used at a heat source for further upgrading of the temperature to the level required by the thermolysis reaction (~ 800 K). Two chemical heat pumps are proposed by Naterer (2008) for the integrated system shown in Fig. 6.99. These are salt/ammonia and magnesium oxide based heat pumps. The chemical reactions with these pumps are presented in Table 6.30.

The lower temperature heat pump is the salt ammonia pump which requires a heat source at 353 K and delivers heat at an upgraded temperature level of 532 K. For the operation, an intermediary heat source is needed at 413 K and intermediary temperature level at 393 K. The magnesium oxide heat pump operates at higher temperatures. It requires 532 K at the source and delivers heat at 783 K at the sink. There is a need for an intermediate heat source and sink of temperature levels of 573 and 583 K for the heat storage mode of operation. The results presented in Naterer (2008) show that the cascaded heat pump system can reach an overall COP in the range of 2–3 which appears promising for linkage with the Cu–Cl cycle.

Granovskii et al. (2008) have shown that it is possible to integrate a steam Rankine power plant—coupled to a supercritical water reactor—with a chemical heat pump based on the following reactions:

- Endothermic, steam methane reaction: $\text{CH}_4 + \text{H}_2\text{O} + Q_{\text{inp}} \rightarrow \text{CO} + 3\text{H}_2$
- Endothermic, reverse water gas shift reaction: $\text{CO}_2 + \text{H}_2 + Q_{\text{inp}} \rightarrow \text{CO} + \text{H}_2\text{O}$
- Exothermic, water gas shift reaction: $\text{CO} + \text{H}_2\text{O} \rightarrow \text{CO}_2 + \text{H}_2 + Q_{\text{out}}$
- Exothermic, methane synthesis reaction: $\text{CO} + 3\text{H}_2 \rightarrow \text{CH}_4 + \text{H}_2\text{O} + Q_{\text{out}}$

It has been shown that the integrated system allows for improved energy utilization efficiency by at least 2 % without jeopardizing the reactor safety.

Table 6.30 Chemical reactions and temperatures of two chemical heat pumps

	Operation mode	T (K)	Reactions
A	Heat storage mode	413	$\text{NiCl}_2 \cdot 6\text{NH}_3 + Q_{\text{in}} \rightarrow \text{NiCl}_2 \cdot 2\text{NH}_3 + 4\text{NH}_3$
		393	$\text{MnSO}_4 \cdot 2\text{NH}_3 + 4\text{NH}_3 \rightarrow \text{MnSO}_4 \cdot 6\text{NH}_3 + Q_{\text{rej}}$
	Heat supply mode	353	$\text{MnSO}_4 \cdot 6\text{NH}_3 + Q_{\text{waste}} \rightarrow \text{MnSO}_4 \cdot 2\text{NH}_3 + 4\text{NH}_3, \quad Q_{\text{waste}} = +57.6 \text{ kJ/mol } \text{NH}_3$
		532	$\text{NiCl}_2 \cdot 2\text{NH}_3 + 4\text{NH}_3 \rightarrow \text{NiCl}_2 \cdot 6\text{NH}_3 + Q_{\text{out}}, \quad Q_{\text{out}} = -55.3 \text{ kJ/mol } \text{NH}_3$
B	Heat storage mode	583	$\text{Mg}(\text{OH})_2 + Q_{\text{in}} \rightarrow \text{MgO}(\text{s}) + \text{H}_2\text{O}(\text{g}), \quad Q_{\text{in}} = 81.02 \text{ kJ/mol}$
		573	$\text{H}_2\text{O}(\text{g}) \rightarrow \text{H}_2\text{O}(\text{l}) + Q_{\text{rej}}$
	Heat supply mode	783	$\text{MgO}(\text{s}) + \text{H}_2\text{O}(\text{g}) \rightarrow \text{Mg}(\text{OH})_2, \quad Q_{\text{out}} = 81.02 \text{ kJ/mol}$
		532	$\text{H}_2\text{O}(\text{l}) + Q_{\text{waste}} \rightarrow \text{H}_2\text{O}(\text{g})$

Note: A salt ammonia heat pump, B magnesium oxide heat pump
Source: Naterer (2008)

The manner in which the heat pump is integrated with a nuclear steam cycle and copper–chlorine cycle is presented in the next chapter of the book.

Regarding the use of vapor compression heat pumps in connection with the copper–chlorine cycle, there are at least two major technical constraints: finding a suitable working fluid, and obtaining a coefficient of performance (COP) high enough to justify the use of a heat pump. If the COP is close to 1, then one can use electric heating instead of a heat pump. Zamfirescu et al. (2009) analyzed six organic and titanium-based working fluids for mechanical heat pumps such as biphenyl, biphenyl-methane, naphthalene, isoquinoline, titanium tetrabromide, and titanium tetraiodide. The organic fluids allow heat pump operation using a heat sink with a temperature in the range of 483–533 K, while the heat sink temperature is in the range of 573–753 K. Titanium-based working fluids can operate in heat pumps with a source between 500 and 630 K and heat sink temperature in the range of 573–823 K. Another option is TiI_4 with a COP higher than 2. A cascaded heat pump with vapor compression operating with cyclohexane as a bottoming cycle and biphenyl as a topping cycle was reported in Zamfirescu et al. (2010c). The topping cycle is supercritical and delivers heat at variable temperatures (sensible heat). During the cooling process of the working fluid at the sink side heat exchanger of the heat pump, the temperature varies between 873 and 523 K. Under the assumption that both compressors have an isentropic efficiency of 0.75 and the heat source temperature is 333 K, the COP of the cascaded heat pump becomes higher than 5.

A new method of internal heat recovery and reuse with the five-step copper–chlorine cycle was reported by Zamfirescu et al. (2011). A vapor compression heat pump which uses cuprous chloride as a working fluid is used to couple thermally the exothermic hydrogen production reactor to the thermolysis reactor. The heat and temperature level is upgraded through compressors that raise the enthalpy of cuprous chloride vapors. Cuprous chloride is one of the products of the oxy-decomposer (thermolysis reactor) and the working fluid of the heat pump creates an opportunity of better thermal coupling through direct contact heat exchangers for reduced temperature gaps.

Figure 6.100 shows a system where copper oxychloride is fed at #1 into the thermolysis reactor at 675 K where the particulate $\text{CuO}\cdot\text{CuCl}_2$ is heated by direct contact with molten cuprous chloride injected at state point # 15 at 950 K. The molten salt transfers its sensible heat and cools down to the average reactor temperature which is assumed to be 850 K for the reference case in this study.

The heat delivered by the hot stream #15 at 950 K makes copper oxychloride decompose thermally and release oxygen (expelled in #2) while forming molten cuprous chloride (drained out in #3). One part (#4) of the CuCl stream is sent for further processing within the plant while the remaining (streams #5 and #6) are further processed thermo-mechanically within the heat pump. The stream (#5) is throttled to 0.2 mbar and reaches a two-phase state at #7 at a saturation temperature of 755 K. This stream is further heated to saturation with heat recovered from the chlorination reactor of the copper–chlorine cycle.

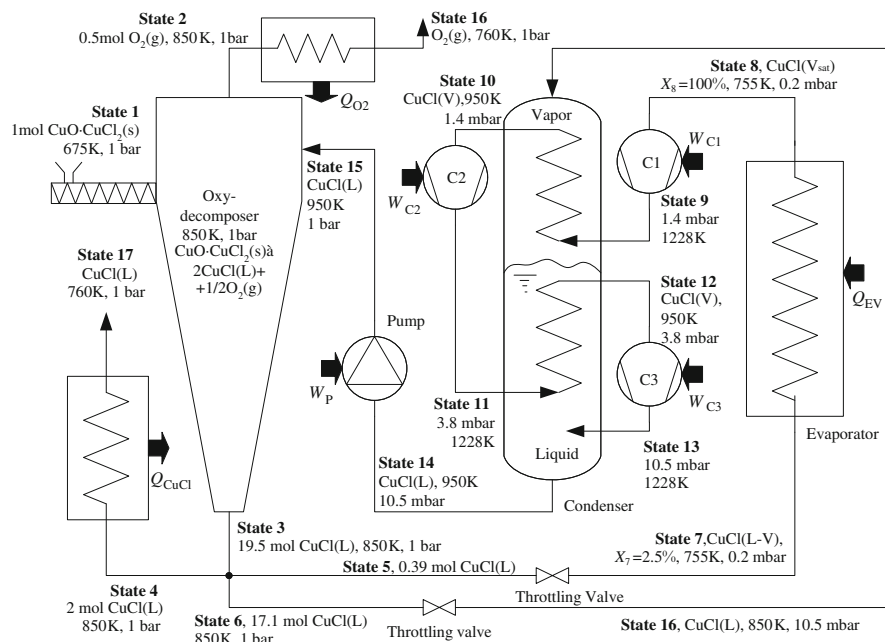


Fig. 6.100 Vapor compression heat pump system with CuCl working fluid, integrated with the five-step copper–chlorine cycle [modified from Zamfirescu et al. (2011)]

The vapor is then compressed in three stages with intercooling. The final pressure is 10.5 mbar, for which the corresponding saturation temperature is 950 K. The condenser in the figure consists of a vessel that incorporates two coils where superheated vapors are cooled after stage 1 and 2 of compression. During the operation, at the bottom of the condenser, saturated CuCl collects. The superheated vapor at the final stage of compression (#13) is injected into this liquid, cooled by direct contact, and condensed. The condensation heat is transferred to molten CuCl which originates from stream #6. The liquid collected in #14 is pumped to atmospheric pressure and injected into the oxy-decomposer.

The thermodynamic cycle in the T – S diagram is presented in Fig. 6.101. The reported COP of the heat pump is remarkably high, namely, 6.6 with an assumed isentropic efficiency of 0.85 for all compressors and the pump. The work needed to drive the heat pump associated with production of 1 mol of hydrogen by the Cu–Cl cycle is studied in Fig. 6.102. This work is calculated for a fixed temperature of 850 K in the oxy-decomposer and a range of temperatures at the heat pump sink, T_{15} . Three values were considered for the isentropic efficiency, which is taken to be the same for all compressors and the pump. At a reasonable isentropic efficiency of 0.7, 5 the specific work needed to drive the pump is around 15 kJ/mol of produced hydrogen. Moreover, one observes that further increases in isentropic efficiency do not lead to significant reduction of the specific work.

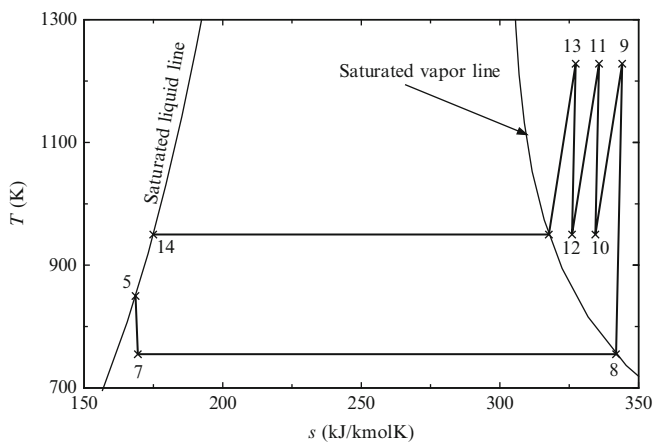


Fig. 6.101 Thermodynamic cycle of CuCl vapor compression heat pump [data from Zamfirescu et al. (2011)]

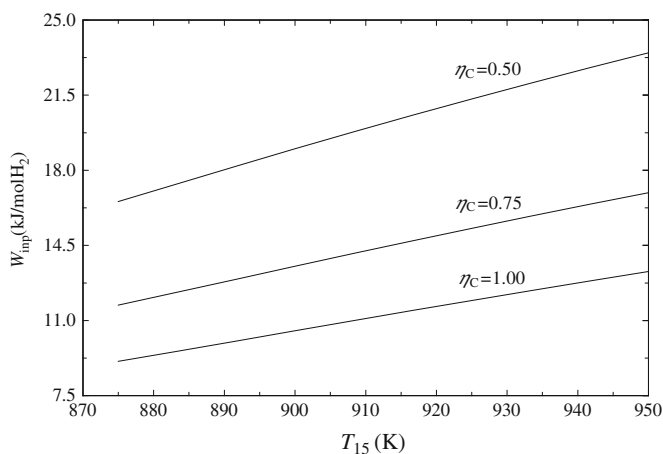


Fig. 6.102 Specific molar work required to drive the CuCl heat pump [data from Zamfirescu et al. (2011)]

6.10 Material Selection and Research

Development of advanced materials for the copper-chlorine thermochemical cycle has major importance. Many components of the cycle work in highly corrosive conditions and high temperatures. One major focus is to develop thermal spray coating technology for thermochemical reactors and other components of the cycle.

A collaborative research program between UOIT and the University of Toronto (UT) has characterized the necessary coatings, as well as test their surface integrity in molten CuCl. Some of the tested materials and procedures are given as follows:

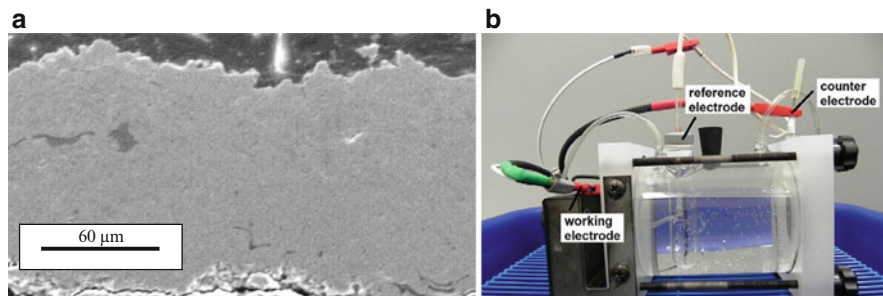


Fig. 6.103 Micrograph of coating cross section deposited from Metco 143 (a) (courtesy of Prof. J. Mostaghimi) and electrochemical cell for corrosion testing (b)

- Inconel 625 (a nickel-based superalloy) thermally sprayed.
- Austenitic stainless steel AL-6XN with 24 % Ni, 6.3 % Mo thermally sprayed.
- Metal coating with Diamalloy 4006 from Sulzer-Metco ($\text{Ni}_{20}\text{Cr}_{10}\text{W}_9\text{Mo}_4\text{Cu}_1\text{C}_1\text{B}_1\text{Fe}$).
- Spraying of additional ceramic top layer on metal coatings for various samples. Two ceramic powders were used: zirconia-based Metco 143 ($\text{ZrO}_2\cdot 18\text{TiO}_2\cdot 10\text{Y}_2\text{O}_3$) of 70 μm thickness, and 170 μm thick alumina-based coating Metco 101NS ($\text{Al}_2\text{O}_3\cdot 3\text{TiO}_2$).

In the process of coating, a high-pressure mixture of fuel and oxygen ignites in the combustion chamber and the combustion products are accelerated through a converging–diverging nozzle. Particle temperatures are over 2,000 K. As a result, the injected particles attain high velocity at relatively low temperatures. The high kinetic energy of the particles upon impact leads to the formation of a dense and well-adhered coating. The relatively low temperature prevents the particles from excessive oxidation.

Figure 6.103a shows a micrograph of coating cross section deposited from Metco 143 material which was measured by an image analysis technique. The porosity of the coatings was in the order of 1–2 %. The ceramic top coat provides additional protection because of its low thermal conductivity. This insulates the underlying materials, thereby reducing the temperature of the amorphous metallic coating. For example, a 100 μm thick ceramic layer acting as a thermal barrier coating can decrease the temperature of the amorphous coating by about 50 K. Yttria-stabilized zirconia (8 % $\text{Y}_2\text{O}_3\text{-ZrO}_2$) and Al_2O_3 are two common compositions used for this purpose. They were deposited on amorphous metallic coatings. The metal and ceramic coatings have a dense, low-porosity microstructure that enhances the temperature and corrosion resistance of the multilayer coating.

Selected specimens were tested for corrosion and showed fractured ceramic coatings due to high cooling rates after spraying. The results indicated that the coating integrity can be identified using the electrochemical cell (UOIT) shown in Fig. 6.103b. Electrochemical characterization has been performed on Inconel 625 and AL6XN Stainless Steel samples coated with Diamalloy 4006 metallic layer, and Diamalloy 4006 specimens top coated with either zirconia or alumina.

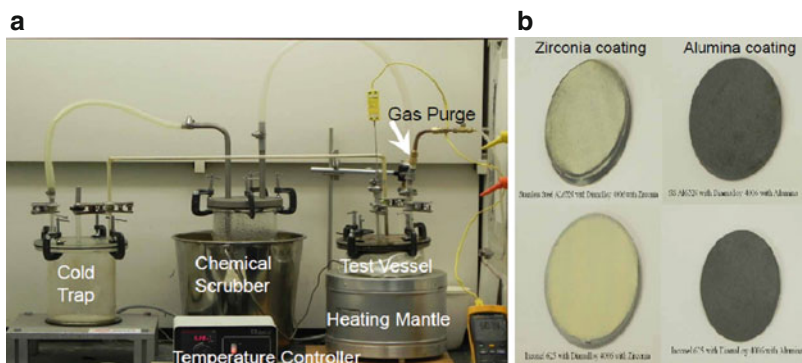


Fig. 6.104 Immersion apparatus for CuCl corrosion tests (a) and coating test specimens (b)

Salt solutions up to 5 mol/L NaCl were used for characterization at room temperature of the corrosion behavior of coated surfaces with two methods: SEM of the surface and EIS/AC impedance. SEM imaging of the surface was used to identify any physical breakdown, loss of integrity, or restructuring of the surface. Using EIS/AC impedance, the chemical integrity of the film, chemical breakdown, interfacial breakdown, and solution penetration of the specimen were examined. The results of the experiments were consistent with the presence of a passive film.

A CuCl immersion test apparatus was developed for corrosion testing in Fig. 6.104a. Several test immersion were performed with a test duration limited to 8 h for safety concerns. The corrosion specimens remained immersed in the salt as it froze each night. Difficulties in extricating the specimen from the frozen salt have been identified and methods were developed that will enable the removal of solid CuCl from the specimen without damaging or corroding the specimen. Selected surface coating specimens are shown in Fig. 6.104b.

6.11 Scaled-Up Test Loop at UOIT

A scaled-up test loop of the copper–chlorine cycle is under development at UOIT for a projected production of 3 kg hydrogen per day, when all unit operations are connected and integrated together. The test loop consists in four separate main units which are the CuCl/HCl electrolyzer, dehydration reactor, hydrolysis reactor, and oxy-decomposer. In addition, several auxiliary units necessary for system integration are under development. These include the heat recovery system for molten cuprous chloride, apparatus for hydrochloric acid/water separation, among others. A general layout of the scaled-up system is depicted in Fig. 6.105. Each major unit of the test bench is operational. Research studies have been conducted at UOIT on system integration of experimental unit operations of the Cu–Cl cycle, including integration of electrolysis, water separation, and hydrolysis processes, as well as the integration of hydrolysis, oxygen, and hydrogen generation processes.

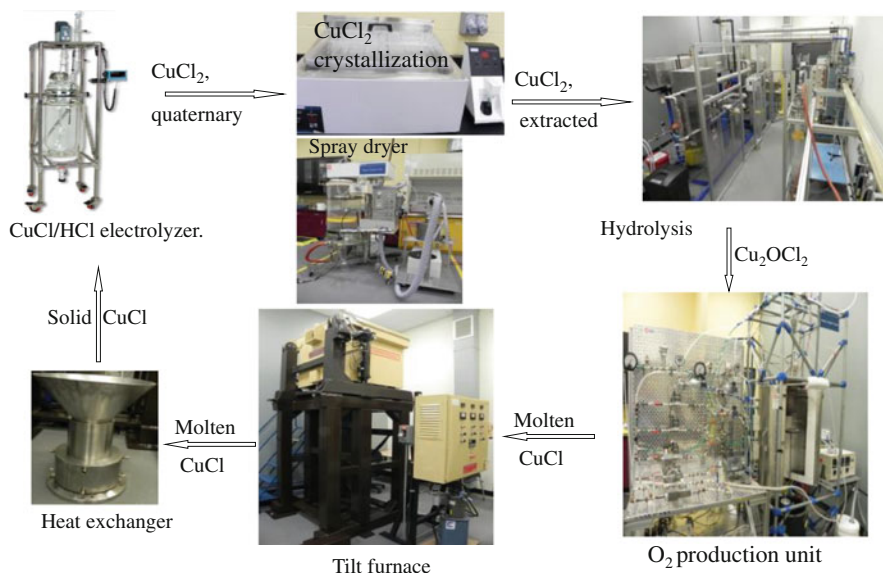


Fig. 6.105 System integration for scaled-up and integrated Cu-Cl cycle at UOIT

The dominant parameter that influences the integration of the electrolysis and hydrolysis processes is the steam quantity required by hydrolysis step. Another parameter that affects the processes of integration is the concentration of cupric chloride exiting the electrolytic cell. The output stream from the electrolytic cell has been simulated using the quaternary system of H_2O , CuCl_2 , CuCl , and HCl in the experiments with varied concentration of each constituent. Crystallization and spray drying experiments have been performed to concentrate the CuCl_2 solution so as to accommodate the variations of electrolysis outputs and deliver CuCl_2 of different water contents to the hydrolysis reactor. Crystallization experiments of cupric chloride were also performed by varying the HCl concentration and temperature of the quaternary system. The CuCl_2 output from the crystallization and spray drying is delivered separately to the hydrolysis reactor to produce HCl liquid.

With respect to system integration of hydrolysis and oxygen and hydrogen generation processes, studies have also been conducted on the interactions between the Cu_2OCl_2 decomposition and CuCl_2 hydrolysis steps. The effects of completion of the hydrolysis reaction on the Cu_2OCl_2 decomposition were studied by varying the fraction of CuCl_2 in a mixture of CuCl_2 and Cu_2OCl_2 that are fed into the Cu_2OCl_2 decomposition reactor. The primary influences include the conversion of by-products such as Cl_2 , partial evaporation of molten CuCl , and heat requirements. The composition of the gaseous products and molten product are analyzed by XRD. The heat input to the oxygen production reactor was characterized by the enthalpy change of the Cu_2OCl_2 and CuCl_2 decomposition processes. A mixture of CuCl_2 and CuO was also used in the experiments to study the oxygen production reaction so as to accommodate different hydrolysis technologies that may reduce the excess steam and temperature requirements.

Fig. 6.106 Experimental apparatus for HCl/H₂O separation (UOIT)



For separation of HCl and steam downstream of the hydrolysis reactor, the mixture of H₂O and HCl can be concentrated (individually or a combination) by distillation and extractive rectification performed near or below the azeotrope temperature (381 K, at 1 bar; 0.4 HCl mass fraction). An experimental apparatus, shown in Fig. 6.106, was set up at UOIT for investigating water/hydrochloric acid separation. Significant quantities of heat flow are required to condense the high-temperature products, which then must be reheated for other processes. Thus, the downstream design of the hydrolysis reactor can have significant impact on the thermodynamic efficiency of the Cu–Cl cycle. Several techniques to condense the HCl/H₂O mixture are being analyzed and studied experimentally to determine and compare the effectiveness of each system.

Experimental work is also under way on the processing of solidified CuCl and entrained by-products produced from the oxygen production reactor. The processed CuCl will provide the feedstock to the downstream HCl/CuCl electrolyzer. The preparation of the ternary system of CuCl, HCl, and water at various concentrations was for the integration of oxygen and hydrogen production steps. It has been shown that the high conversion of CuCl₂ to Cu₂OCuCl₂ in the hydrolysis step has vital importance to reduce the challenges of the integration of hydrolysis and oxygen and hydrogen production steps.

6.12 Conceptual Designs of Full-Size Plant and Reactors

Experiments have confirmed the feasibility of the copper–chlorine cycle and offer the promise of economic competitiveness of the process to produce hydrogen efficiently in an environmentally benign manner from an inexhaustible resource, water. As discussed in the previous section of this chapter, most experiments related to chemistry were conducted in standard test tube reactors. Larger engineering-scale test reactors were developed at UOIT for a hydrogen production of about 3 kg/day which is 1,000 times higher than initial benchtop proof-of-concept experiments. Reactors of fluidized bed, packed bed, or spray reactors were successfully demonstrated. Much knowledge has been acquired for the process to be scaled up to an industrial plant of much larger capacity and eventually linked to next-generation nuclear reactors.

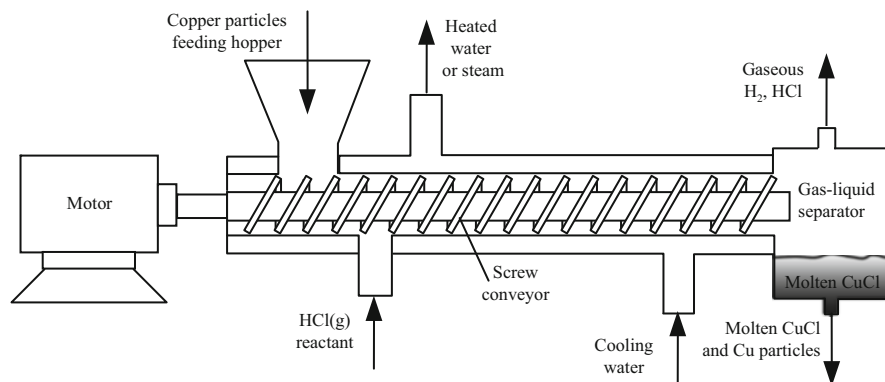


Fig. 6.107 Conceptual design of full-scale chlorination reactor for five-step copper-chlorine cycle [modified from Wang et al. (2008)]

This section presents some design concepts published in past literature for a full-scale copper-chlorine hydrogen plant for nuclear-driven water splitting. Apart from reactors, major equipment such as a sedimentation cell for copper separation in the five-step version of the cycle or a hydrochloric acid gas absorption tower (applicable for all cycle variants) are discussed. Scale-up design issues were examined by Wang et al. (2008) for handling three phases within the molten salt reactor, i.e., solid copper oxychloride particles, liquid (melting salt), and exiting gas (oxygen). It is also important to specify required capacities of feed materials for the multiphase reactors, steam, and heat requirements, as well as other key design parameters for reactor scale-up to a pilot-scale, up to full-plant-scale capacity.

Large-scale implementation of the cycle implies challenges with equipment design especially due to solid handling because solid injection and removal can block equipment operation and generate undesirable side reactions in downstream processes. Corrosion problems are other issues to consider for full plant design because expensive materials may be required. Surfaces exposed to molten CuCl , spray drying of aqueous CuCl_2 , and high-temperature HCl and O_2 gases can be corroded or damaged during the plant operation unless special measures are taken to impede corrosive attack. Separation of chemicals requires design of special equipment, customized to specific requirements of the cycle. Mechanical equipment such as pumps, blowers, compressors, mixing devices, heat exchangers, and conveyors require special design and thorough material selection.

A possible configuration of the chlorination reactor and its subsystem—for a full-scale plant—was proposed by Wang et al. (2008). The reactor itself is in the form of a kiln with an axial screw conveyor for solid particles. Recall that in the chlorination reaction, 2 mol of copper are reacted to 2 mol of gaseous hydrochloric acid to release hydrogen and form a molten cuprous chloride. As outlined in Sect. 6.8, three phases must be handled in a chlorination reactor for the copper-chlorine cycle: solid, liquid, and gas phases. The design in Fig. 6.107 is one of the possible reactor configurations. During the start-up period, this reactor must be heated up together with the initial

Table 6.31 Flow rates in chlorination reactor for various scales of production

H ₂ production				Mass flows (t/h)			Volume flows (m ³ /h)			
				HCl	Cu	CuCl	Cu	CuCl		V _{sed}
Scale	Nm ³ /day	t/day	MW _{th}	(g)	(s)	(l)	(s) ^a	(l)	HCl(g)	(m ³)
Test-bench	36	0.003	>0.01	0.005	0.008	0.0124	0.002	0.003	7.42	0.025
Pilot plant	36,000	3	>10	4.5	7.94	12.4	1.77	3.351	7,420	25.6
Full scale	3,000,000	250	~600	375	662	1,034	148	279	620,000	2,133

^aAssumed 50 % void fraction; V_{sed} volume of sedimentation vessel

Source: Wang et al. (2008)

charge of copper particles to around 623 K after which the reaction is initiated. It is important to keep the reaction temperature constant. Based on thermodynamic calculations, it is estimated that without external cooling, the adiabatic reaction temperature is ~877 K (Wang et al. 2008).

Another major technical issue is to avoid generation of cuprous chloride vapors in the reactor. At temperatures over 823 K, the saturation pressure of CuCl vapor becomes high. Based on energy balance calculation, at a 723 K reaction temperature, with copper particles fed at 353 K, and eight times HCl excess feed at 673 K, one generates 2 mol of molten copper cuprous chloride and 1 mol of hydrogen per 2 mol of copper. Some unreacted copper remains in the molten CuCl output stream and must be separated and recycled. A sedimentation vessel is needed for this process. To provide enough contact area between HCl reactant gas and solid Cu in the hydrogen reactor, enough volume of copper is accumulated in the sedimentation cell for copper particles. The sedimentation time of copper particles may be several hours, so the sedimentation cell would have about 5-h quantities of solid Cu particles and molten CuCl. Based on this assumption, the volume of the sedimentation vessel can be calculated based on the volume flow rates. The estimated flow parameters and the volume of sedimentation vessel are indicated in Table 6.31 as a function of production scale. Two configurations are proposed for the sedimentation vessel as shown in Fig. 6.108. There is a vertical configuration (Fig. 6.108a) and a horizontal configuration (Fig. 6.108b).

Gaseous hydrochloric acid in the exit stream must be separated from the hydrogen product. The HCl gas can be absorbed by an alkali solution, preferably sodium hydroxide. To absorb efficiently, a bubbling packed tower would be advantageous over a shower hollow tower. In a bubbling packed tower, a gas mixture of HCl and H₂ flows through the NaOH solution. The gas flow path is detoured by packing materials like small plastic rings or cylinders. In a shower hollow tower, the NaOH solution is showered down, while the gas mixture flows upward. Boiling must be avoided within the absorption tower. The neutralization heat of dilute strong acid and dilute strong alkali is 57.3 kJ/mol water; this heat must be removed.

A possible conceptual design of the five-step copper-chlorine plant subsystem which performs the chlorination process is shown in Fig. 6.109. It requires both hydrochloric acid recycling and copper particle recycling. The input into the chlorination subsystem are copper particles from the chlorination step—coming

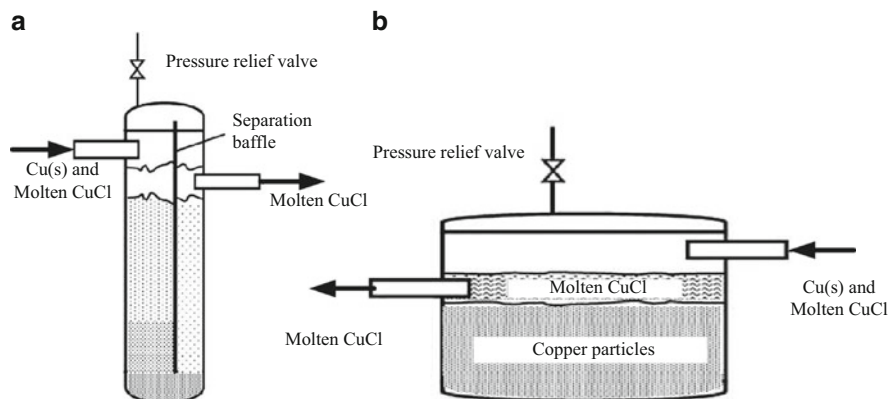


Fig. 6.108 Separation systems of molten cuprous chloride and copper particles: (a) vertical configuration, (b) horizontal configuration [modified from Wang et al. (2008)]

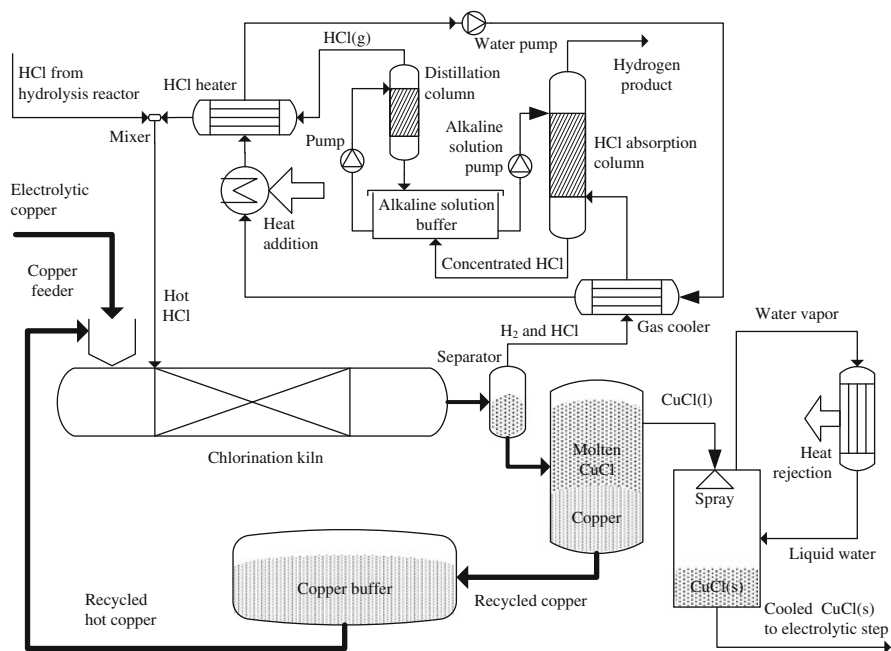


Fig. 6.109 Conceptual design of the chlorination step in Cu-Cl-5 thermochemical cycle [modified from Wang et al. (2008)]

at about 353 K—and hot hydrochloric acid ($T > 600$ K) coming from the hydrolysis subsystem, while the output is a stream of cuprous chloride particles, delivered to the electrolytic process. Unreacted copper particles are first separated by gravitational sedimentation and then recycled at high temperature. The gas phase of the

Table 6.32 Design issues related to the copper oxychloride decomposition step

Category	Technical issues and relevant parameters to consider for design.
Reaction kinetics	Decomposition temperature, activation time and energy of reaction, particle reaction rate/kinetics, residence time (corresponding to each specific particle structure/size, ratios of reactants), heating medium (molten salt/gas/wall/particles).
Flow, phases, mixing	Feeding of reactant particles (hot/cold), size and lifetime of aggregations (particles, molten salt, bubbles). Descent of particles in molten salt. Up-flow of bubbles in molten salt. Velocity, size, volumetric fraction of bubbles at different temperatures. Splashing effect on liquid surface due to the bubbles exiting the chamber. Flooding/overflow of molten salt pushed by bubbles due to sudden pressure decrease. Particle distribution in molten salt. Flow field of molten salt.
Material	Pressure should be lower than 4 atm. Molten CuCl and O ₂ are highly corrosive. Vapor CuCl, chlorine gas, and HCl gas may occur in trace amounts.
Oxygen handling	Oxygen removal rate. Entrainment of reactant particles and molten salt droplets. Heat recovery from oxygen stream must be applied: heat transfer rate, thermal efficiency, type of heat exchanger. Composition of effluent gas to be considered (O ₂ , CuCl vapor, HCl, Cl ₂ , H ₂ O)
Molten CuCl handling	Recover heat from molten CuCl by means of direct contact (over a temperature range). Heat transfer rate between water vapor and CuCl particles (either liquid droplets or solid pellets). Thermal efficiency of direct contact. Maximum ratio of water vapor to CuCl. Type/structure of sprayer. Mixing solid particles and liquid water. Recover heat from CuCl by indirect contact. Thermal efficiency of heat exchanger. Type/structure of shell heat exchanger. Composition of molten CuCl. Solid CuCl ₂ from reaction and side reaction. Reactant particles entrained by molten CuCl. Composition of molten CuCl. Solid CuCl ₂ from reaction and side reaction. Reactant particles entrained by molten CuCl.

Source: Wang et al. (2008)

reaction product is separated in a gravitational separator. Furthermore, the gases are cooled and hydrochloric acid is absorbed in an alkaline solution using an absorption column. The alkaline buffer is maintained at constant pH by continuous removal of hydrochloric acid in a distillation column. The recycled HCl gas is reheated prior to reinjecting it in the chlorination reactor.

Another major subsystem of the copper–chlorine plant is the thermolysis reactor, which is common to all variants of the cycle. As mentioned in prior sections, in this reactor the copper oxychloride is decomposed and oxygen is produced. Three phases coexist in the reactor, namely, oxygen gas (and possible chlorine gas and CuCl vapors), molten cuprous chloride, and solid copper oxychloride. The major design issues of this reaction steps are listed in Table 6.32.

The thermolysis (oxy-decomposer) subsystem must start by preheating cuprous chloride in the reactor until molten state is achieved. Then oxygen is introduced into the molten CuCl to form bubbles, after which the volume and rate of bubble growth,

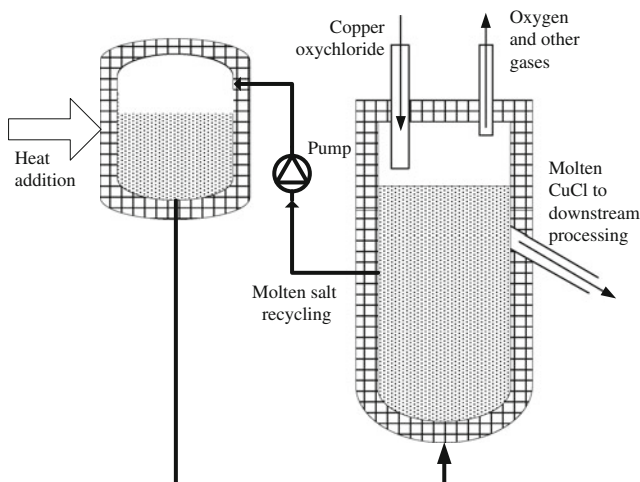


Fig. 6.110 Schematics of the reactor for copper oxychloride decomposition and oxygen generation [modified from Wang et al. (2008)]

as well as the mixing rate of gas and molten salt, can be controlled. Then solid CuCl particles are injected into the reactor to reach the level of overflow after melting, which corresponds to the volume of the reaction zone below the molten salt level. The reactor can then be heated at the reaction temperature and the CuCl melts in the reactor. The reaction starts by feeding copper oxychloride.

For the molten salt reactor, the effective liquid and solid heights should be about ten times the bulk height, since the volumetric ratio of $\text{CuO} \cdot \text{CuCl}_2(\text{s})$ to CuCl is 1/9, excluding the volume occupied by bubbles. The gas bubbles will also occupy a portion of volume. Assuming that the initial size of a gas bubble is about the same as a particle of copper oxychloride, this size will grow when the bubble is ascending to the liquid (molten salt) level.

In the thermolysis reactor, the reactant particles absorb decomposition heat from the surrounding molten bath. While the particles are descending in the molten CuCl bath, oxygen ascends through the molten salt and then leaves the reactor. Simultaneously, another product (liquid CuCl) is formed within the molten bath and exits separately from the reactor. Within the reactor, heat is transferred from liquid (molten CuCl) to solid $\text{CuO} \cdot \text{CuCl}_2$ (reactant) particles and the molten bath can be sustained by the reaction product itself. The oxygen product will leave the reactant particles immediately due to buoyancy of gas in the molten salt. This fast separation aids to minimize heat transfer resistance to the reactant particles, which then helps make the overall reaction rate closer to the intrinsic reaction rate itself. The design of the reactor requires a high efficiency of heat exchange and separation of reactant from products, as well as product (oxygen) from product (molten salt).

A practical and efficient option is to heat the molten salt from the wall with a double-shell structure as indicated in the reactor schematic in Fig. 6.110. Flowing in

Table 6.33 Flow rates of various streams of the copper oxychloride decomposition reactor

H ₂ production		Oxygen at 800 K		CuO·CuCl ₂ (s)		CuCl(l)	
Scale	N m ³ /day	kg/day	m ³ /h	kg/h	m ³ /h	kg/h	m ³ /h
Test-bench	36	0.024	2.1	13.4	0.003	12.4	0.003
Pilot plant	36,000	24	2,100	13,375	2.758	12,400	3.352
Full scale	3,000,000	2,000	175,000	1,114,600	230	1,033,333	280

Source: Wang et al. (2008)

the double shell, a secondary flow of molten salt provides heat to the reactor. The secondary flow of molten salt could be provided from a solar energy storage reservoir or nuclear heat exchanger, which uses molten salt as the heat storage and transferring medium. The cuprous chloride itself can act as a heat storage medium. If necessary, agitation could be introduced into the bath. This approach would take advantage of both free and forced convection with heterogeneous mixing that facilitates both heat and mass transfer. The flow rates of significant streams related to thermolysis reactor are listed in Table 6.33 for three capacities of production of the Cu–Cl plant.

In Lewis et al. (2009b), a conceptual design of a three-reaction-step copper–chlorine cycle was described: (1) an electrolytic cell with AEM ($\text{H}_2\text{--H}^+$, Fig. 6.15); (2) a crystallizer to dehydrate $\text{CuCl}_2 \cdot n\text{H}_2\text{O}$, $n > 1$ to the form $\text{CuCl}_2 \cdot 2\text{H}_2\text{O}$; (3) a spray reactor for hydrolysis (Fig. 6.41); and (4) an oxy-decomposer with bayonet heat exchangers. The overall system is presented in Fig. 6.111 in a modified form which includes a molten salt heat exchanger for heat recovery. The electrolyzer operates at high pressure—24 bar—while the spray reactor operates in a slight vacuum or at 1 atm.

As suggested in Fig. 6.111, water is fed into the anolyte buffer where there is a solution of hydrochloric acid, cuprous chloride, and cupric chloride. This solution is pumped to 24 bar and heated to 373 K when the pressurized solution is still in the liquid phase. The anodic reaction occurs between cuprous chloride and chlorine ions, namely, $2\text{CuCl}(\text{aq}) + 2\text{Cl}^-(\text{aq}) \rightarrow \text{CuCl}_2(\text{aq}) + 2\text{e}^-$. Once formed, cupric chloride complexes with water molecules as $\text{CuCl}_2 \cdot n\text{H}_2\text{O}$, $n \geq 2$.

The anolyte is cooled down to ~303 K and passed to a crystallization unit where it partially dehydrates. Bayonet heat exchangers are used in the crystallization unit to remove heat. Next, cupric chloride in aqueous form is heated such that the aqueous solution can be concentrated in $\text{CuCl}_2 \cdot 2\text{H}_2\text{O}(\text{aq})$. The solution is rapidly expanded in spraying nozzles which form micrometer droplets scattered in steam at 673 K where the hydrolysis reaction occurs with formation of copper oxychloride particles that deposit at the bottom of the reactor. Hydrochloric acid and steam are extracted as gases and cooled to 373 K. A part of the liquid is further condensed and subcooled to ~303 K and further mixed with cooled cuprous chloride particles generated by the molten salt heat exchanger. The particles partially or totally dissolve in the acidic solution. The copper oxychloride solids fall into the oxy-decomposer which is supplied with heat by bayonet heat exchangers sunk into a molten cuprous chloride bath. The decomposition reaction generates oxygen gas

Table 6.34 Stream flow rates of a large-scale copper–chlorine plant with three steps

Stream	H ₂ O	HCl	CuCl	CuO·CuCl ₂	CuCl ₂ ·2H ₂ O	H ₃ O ⁺	Cl [−]	CuCl ⁺	O ₂	H ₂
H ₂ O feed	47	0	0	0	0	0	0	0	0	0
Anode feed	328	3.4	515			40	107	93	0	0
Cathode feed	1,173	0.03	0	0	0	99	184	0	0	0
H ₂ product	0	0	0	0	0	0	0	0	0	5.2
Crystallizer feed	168	0.2	0	0	979	414	91	39	0	0
CuCl ₂ hydrolyzer feed	198	2.5	0	0	0	0	187	519	0	0
H ₂ O hydrolyzer feed	1,153	0	0	0	0	0	0	0	0	0
Oxydecomposer feed	0	0	0	561	0	0	0	0	0	0
O ₂ product	0	0	0	0	0	0	0	0	41.6	0
CuCl recycle	0	0	515	0	0	0	0	0	0	0

Flow rate units: Mt/h

Source: Ferrandon et al. (2008)

of HCl and steam at 373 K are directed toward the catholyte buffer where water condenses and HCl is dissolved. The hot catholyte is pumped to 24 bar and supplied at the cathode.

Hydrochloric acid at high concentration generates protons and chlorine anions according to $\text{HCl} \rightarrow \text{H}^+ + \text{Cl}^-$. The chlorine anions cross the membrane while the protons reduce at the cathode forming hydrogen. A separation unit (not detailed) is used to separate and scrub hydrogen and to return the acidified liquid solution at lower pressure but high temperature to the catholyte buffer.

The calculated data for a copper–chlorine plant of 125,000 kg hydrogen per day operating in a diagram approximately the same as that presented in Fig. 6.111 was reported by Ferrandon et al. (2008). Accordingly, the plant requires 210 MW thermal energy and ~88 MW electric energy. If one assumes that electricity is generated with 40 % efficiency, the total requirement of thermal energy is 430 MW; therefore the energy efficiency is 29 %. In order to generate the same amount of hydrogen with an alkaline electrolysis system of 65 % energy efficiency, one needs ~313 MW of electric power, or an equivalent of ~780 MW electric energy, with an energy overall efficiency of 26 %. The flow rates reported by Ferrandon et al. (2008) are summarized in Table 6.34.

6.13 ASPEN Plus Plant Simulation and Flow Sheets

Aspen Plus simulation software, which predicts the behavior of process reactions and steps using standard engineering relationships, mass and energy balances, as well as phase and chemical equilibrium data, has been used for Cu–Cl plant simulation studies by Serban et al. (2004), Lewis et al. (2005a, b), Ferrandon et al. (2008), Rosen et al. (2010), and Orhan (2011).

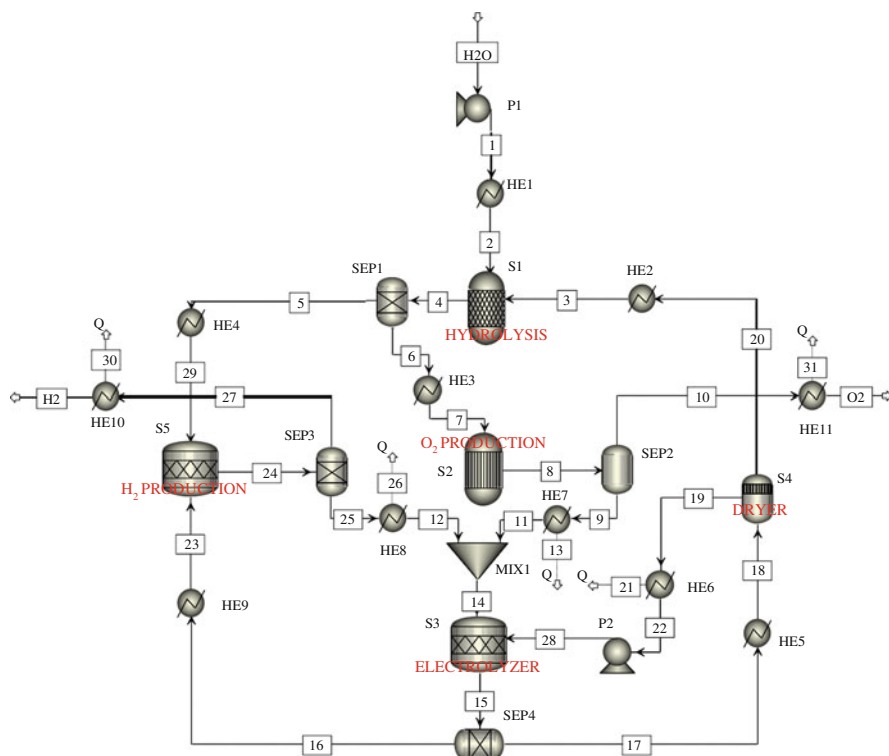


Fig. 6.113 ASPEN Plus flow sheet of a four-step cycle [modified from Orhan (2011)]

pinch analysis and better design of various steps within the Cu–Cl cycle are expected to lead to further efficiency improvements.

Figure 6.112 shows a flow-sheet simulation of a four-step copper–chlorine cycle variant, while the simulation for a five-step cycle is shown in Fig. 6.113. Energy streams resulted from the five-step flow-sheet simulation are listed in Table 6.35.

6.14 Plant Control, Safety, and Reliability

Al-Dabbagh and Lu (2010a, b) reported reliability, control systems, and safety assessments of a nuclear hydrogen plant with the Cu–Cl cycle under various risk scenarios. The studies were developed and analyzed with a dynamic flowgraph methodology (DFM) that provides the capability of modeling the behavior of control systems in the Cu–Cl cycle.

The methodology provides an integrated hardware/software model and also identifies how certain critical events of interest may occur. The DFM model is capable of verifying design requirements, performing failure analysis, and defining

Table 6.35 Energy balance of the five-step Cu–Cl cycle simulation process

Block	Process	ΔH (kJ/mol H ₂)	Block	Process	ΔH (kJ/mol H ₂)	Block	Process	ΔH (kJ/mol H ₂)
S1	T	120.2	S2	T	125.5	S3	E	53.2
S4	M	33.2	S5	T	−41.6	H1	T	80
HE2	T	61.3	HE3	T	20.8	HE4	T	4.0
HE5	T	57.6	HE6	T	−30	HE7	T	−64
HE8	T	−60.6	HE9	T	35.2	HE10	T	−9
HE11	T	−5.6	SEP1	M	0.9	SEP2	M	1.2
SEP3	M	1.8	SEP4	M	2	P1	E	3
P2	E	1.9	MIX1	M	0.4	N/A	N/A	N/S

Processes: *T* thermal; *E* electrical or electrochemical; *M* mechanical.

Source: Orhan (2011)

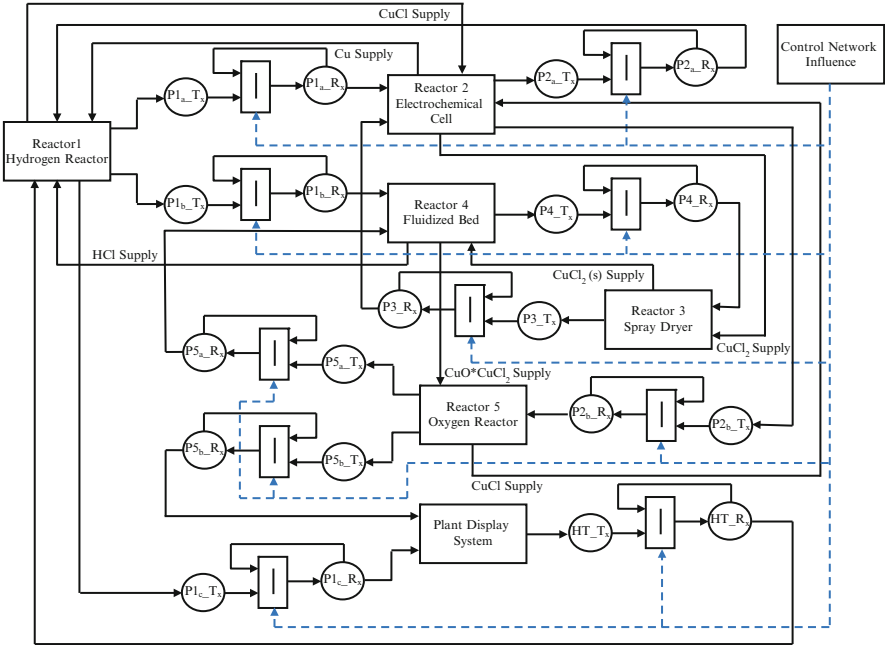


Fig. 6.114 DFM flow sheet of the Cu–Cl cycle [modified from Al-Dabbagh and Lu (2010a)]

test cases. The modeling strategy uses a two-step process, namely, construction and analysis of the model. The construction of the DFM models was performed by using a detailed multistate representation of the cause-and-effect and time-varying relationships within system components.

Figure 6.114 shows a flow sheet of the DFM model of the Cu–Cl cycle. The model is capable of tracing sequences of events inductively and/or deductively to identify paths that result in system events of interest. An inductive analysis was performed by specifying a set of component states and investigating the

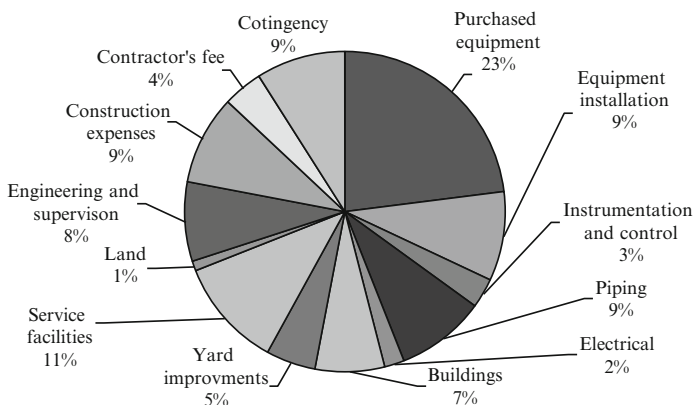


Fig. 6.115 Percentages of cost components for a hybrid Cu–Cl plant [data from Orhan et al. (2008c)]

propagation through the system and the influence on the system state level of interest. Also, a deductive analysis was performed by identifying a state of interest (desirable or undesirable) and finding the combination and sequences of parameters that led to the identified state. The control architecture, communication structure, and configuration of the instrumentation and control systems were developed and the DFM has been successfully applied to the Cu–Cl cycle.

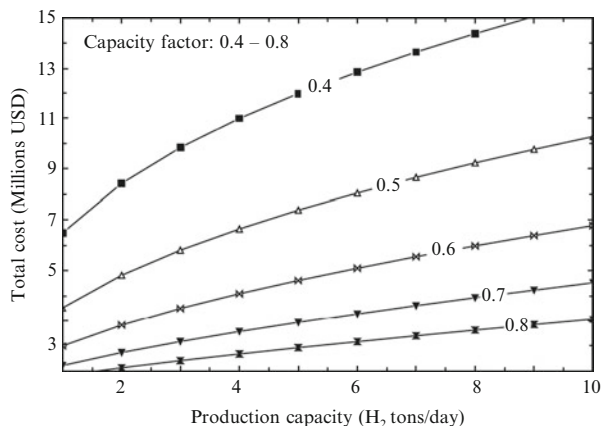
6.15 Cost, Exergo-Economic, and Life Cycle Assessments

A cost analysis of a hybrid Cu–Cl plant was reported by Orhan et al. (2008c) assuming an amortization period of 10 years, 15 % annual return on investment, and an annual capital charge of 20 %. A production cost of \$300/kW for the electrolysis cells was assumed, along with storage costs of \$800,000/t of hydrogen via tube storage. The working capital comprises:

- Raw materials and supplies carried in stock
- Finished products in stock and semifinished products in the process of being manufactured
- Accounts receivable
- Cash kept on hand for monthly payment of operating expenses such as salaries, wages, and raw material purchases
- Accounts payable
- Taxes payable

Figure 6.115 shows percentages of cost components estimated for a hybrid Cu–Cl plant, as reported by Orhan et al. (2008c). Figure 6.116 shows that the total product cost varies in the range of 1–15 million dollars. The costs increase

Fig. 6.116 Variation of total product cost with production capacity and capacity factor [data from Orhan et al. (2008c)]



with plant capacity, according to a concave down logarithmic trend. This shows that the cost of unit capacity decreases with production capacity. With an increasing capacity factor, the costs decrease. The curves for capacity factors of 0.6, 0.7, and 0.8 have close similarity, while greater variation exists for capacity factors of 0.5 and 0.4. This suggests that the capacity factor will lie between 0.6 and 0.8.

Exergo-economic analysis using exergy–cost–energy–mass (EXCEM) provides a quantitative relationship between capital costs and thermodynamic losses. Recent EXCEM studies have examined these features of the Cu–Cl cycle, to determine costs for improving the economic viability of the cycle, as reported by Orhan et al. (2010a). The overall energy and exergy efficiencies of the entire cycle were reported for several different cases, i.e., varying reaction temperatures, environment temperatures, pressures, chemical compositions, etc. In addition, the recent studies compared the Cu–Cl cycle costs against other energy options such as fossil fuels (coal and natural gas), renewable energies (solar, wind, hydro, geothermal, and biomass), and nuclear energy.

A thermodynamic analysis using energy and exergy, as well as several parametric studies, was conducted for various configurations of coupled systems to assess and compare their efficiencies (Orhan et al. 2010b). The methodology provides a useful approach for improving the cost-effectiveness of the Cu–Cl cycle. The hydrogen cost was found to be inversely related to the exergo-economic factor, plant capacity, and exergy efficiency.

Life cycle assessments (LCA) were reported in Ozbilen et al. (2011a, b). The environmental emissions and impacts based on standard categories are shown in Figs. 6.116 and 6.117. Table 6.36 defines the environmental impact categories. Emissions from the overall system are the sum of outputs from a nuclear plant and thermochemical hydrogen plant. The LCA of hydrogen production with the thermochemical Cu–Cl cycle was compared against other hydrogen production methods. The LCA was used to evaluate the total environmental impact of the hydrogen production processes and identify environmentally critical phases.

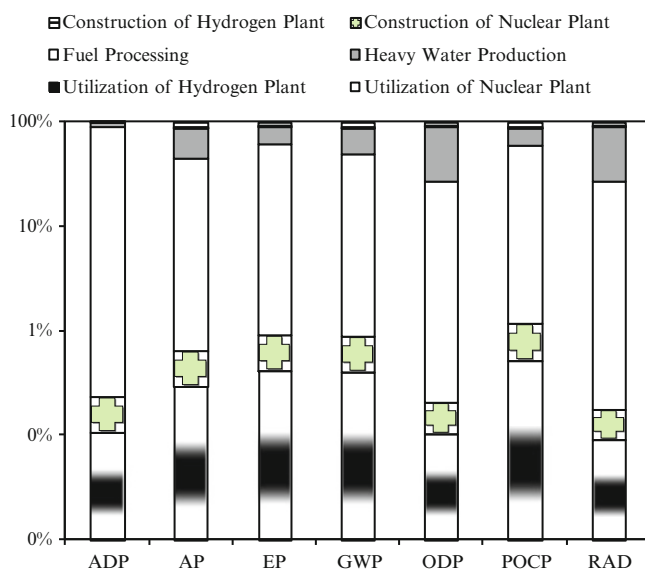


Fig. 6.117 Percentage contributions from different hydrogen generation system processes [data from Ozbilin et al. (2011a)]

Table 6.36 Definitions of environmental impact categories

Environmental impact category	Definition
Abiotic resource depletion potential (ADP) (g extracted element)	Abiotic depletion involves the extraction of nonrenewable raw materials
Global warming potential (GWP) (g CO ₂ -eq)	Amount of CO ₂ in the earth's atmosphere
Ozone depletion potential (ODP) (g CFC-eq)	Depletion of ozone layer leads to an increase in the ultraviolet radiation reaching the earth's surface
Eutrophication potential (EP) (kg phosphate-eq)	Overfertilization or nutrition enrichment at a certain location
Acidification potential (AP) (g SO ₂ -eq)	Acid depletion on soil and into water may lead to changes in the degree of acidity
Photochemical ozone creation potential (POCP) (kg ethene-eq)	Due to volatile organic compounds in the atmosphere
Radioactive radiation (RAD) (disability-adjusted life years, DALY)	Emission and propagation of energy in the form of rays or waves

The “cradle-to-grave” analysis included production, transportation, installment, operation, and disposal phases of the processes. The LCA analysis had four phases: (1) goal and scope definition (objectives, boundaries); (2) life cycle inventory (LCI) analysis (inventory data on energy and material flows); (3) life cycle impact assessment (LCIA; evaluates environmental impacts of material and energy flows); and (4) improvement analysis (results, conclusions, recommendations, and improvements).

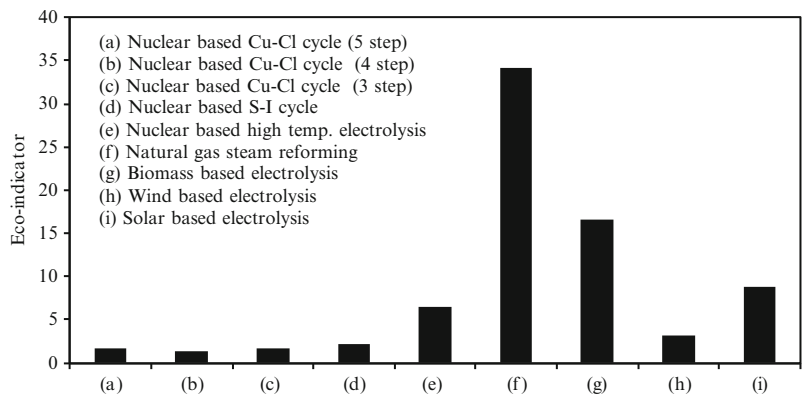


Fig. 6.118 Global warming potential of different hydrogen production methods [data from Ozbilen (2011)]

Table 6.37 Uranium requirements for all stages of the uranium fuel cycle

Fuel cycle stages	Three-step Cu–Cl cycle		Four-step Cu–Cl cycle		Five-step Cu–Cl cycle	
	Input (kg)	Output (kg)	Input (kg)	Output (kg)	Input (kg)	Output (kg)
Mining	6.81×10^{-3}	6.81×10^{-3}	6.00×10^{-3}	6.00×10^{-3}	7.29×10^{-3}	7.29×10^{-3}
Milling	6.81×10^{-3}	3.40×10^{-3}	6.00×10^{-3}	3.00×10^{-3}	7.29×10^{-3}	3.64×10^{-3}
Conversion	3.40×10^{-3}	3.40×10^{-3}	3.00×10^{-3}	3.00×10^{-3}	3.64×10^{-3}	3.64×10^{-3}
Enrichment	3.40×10^{-3}	3.77×10^{-4}	3.00×10^{-3}	3.33×10^{-4}	3.64×10^{-3}	4.04×10^{-4}
Fuel production	3.77×10^{-4}	3.77×10^{-4}	3.33×10^{-3}	3.33×10^{-4}	4.04×10^{-4}	4.04×10^{-4}

Source: Ozbilen et al. (2011a)

Figure 6.118 shows that the four-step Cu–Cl cycle has the lowest environmental impact compared to the three-step and five-step cycles. If the electrical energy output of the nuclear plant is used for all processes, then the global warming potential (GWP) will decrease from 15.8 to 0.56 kg CO₂-equivalent. The primary processes of mining and conversion stages have the highest environmental impact due to the fossil fuel used during those processes. Parametric studies also showed that the increase in plant hydrogen production capacity and lifetime do not have a significant effect on the impact categories if the capacity and lifetime are sufficiently large. It is observed that the nuclear-based S–I cycle and four-step Cu–Cl cycle are the most environmentally benign methods of hydrogen production in terms of GWP.

Table 6.37 shows the uranium requirements for all stages of a fuel cycle for a nuclear hydrogen plant. The assumptions adopted for the reference case have a total lifetime of the system (TLS) of 60 years and a daily hydrogen production capacity of the system (HPC) of 125,000 kg. The heat recovery percentage in the Cu–Cl cycle from exothermic processes is assumed to be 70 %. The functional unit of the system in Table 6.37 is 1 kg of hydrogen production.

6.16 Conclusions

In this chapter, a promising emerging water splitting technology—the hybrid copper–chlorine cycle—is examined and discussed extensively. Seven versions of the cycle were identified and categorized in detail. The three and four-step variants have been actively studied. The cycle versions including a copper electrowinning process had most interest in the period 2003–2008. More recently, AECL demonstrated successfully the hydrogen-evolving electrochemical process and a shift in the research focus toward cycle variants which include this process is observed. UOIT has focused primarily on the development of a four-step process that includes a dehydration system of cupric chloride. ANL has examined a system using a spray reactor with dehydration of copper oxychloride by crystallization. Prediction of thermochemical properties of chemical compounds has significant importance for cycle modeling and design. Electrochemical process and hydrolysis steps are also crucial for cycle development. AECL, UOIT, and PSU developed experimental facilities of electrolysis cells with proton exchange membranes that successfully demonstrate the process. Another crucial reaction step of the cycle is hydrolysis. The parameters were identified based on experiments and scaled-up reactors. It is crucial to set the reaction temperature correctly in order to minimize the side products such as chlorine. At the same time, the amount of excess steam is an important parameter. Dehydration of cupric chloride has been studied extensively with the aim to reduce the temperature level of the input heat and amount of required heat input. It appears that a combination of crystallization and spray drying can efficiently dehydrate the cupric chloride. Alternatively, ANL developed a method of crystallization followed by a spray reactor for hydrolysis with promising results.

An integrated facility of 3 kg hydrogen per day is currently under development at UOIT to establish the large-scale viability of the Cu–Cl cycle. In addition, multiple studies have been dedicated to process scale-up and simulation at an industrial scale, to cost analysis, LCA, and environmental impact, among others. Based on this knowledge developed over the past decade, the copper–chlorine cycle can be considered as the prime competitor of sulfur–iodine and hybrid-sulfur thermochemical cycles, along with high-temperature electrolysis technology for large-scale hydrogen generation with nuclear energy.

Nomenclature

a	Charge transfer coefficient
a	Fluidized bed parameter
a, b	Regression coefficients
A	Area (m^2)
B	Spalding number

Bi	Biot number
c_p	Specific heat (kJ/kg K)
C	Molar concentration (mol/dm ³)
C_d	Drag coefficient
C_P	Molar specific heat at constant pressure (kJ/mol K)
COP	Coefficient of performance
d	Diameter (m)
d_p	Sauter mean diameter (m)
D	Diffusion coefficient (m ² /s)
D_{as}	Damkohler number at reactor scale
E	Molar specific energy (kJ/mol)
\mathbb{E}	Electric potential (V)
f	Fugacity (Pa)
f_p	Friction factor of the bed
F	Faraday constant (C/mol)
g	Gravitational acceleration (m/s ²)
G	Molar Gibbs free energy (kJ/mol)
GHSV	gas hourly space velocity (h ⁻¹)
j	Current density (A/m ²)
k	Thermal conductivity (W/m K)
k	Reaction rate constants
K	Equilibrium constant
\mathcal{K}	Interchange coefficient
h	Heat transfer coefficient (W/m ² K)
h	Specific enthalpy (kJ/kg)
H	Molar enthalpy (kJ/mol)
HR	Hausner ratio
L	Fluidized bed height (m)
m	Mass (kg)
\dot{m}	Mass flow rate (kg/s)
M	Molecular mass (kg/kmol)
n	Order of reaction
\dot{n}	Moles generation rate (mol/s)
n_d	Electro-osmotic drag coefficient
N	Number of atoms
NTU	Number of thermal units
OVP	Total over-potential (V)
P	Pressure (Pa)
Pr	Prandtl number
q	Heat flux (W/m ²)
Q	Heat (kJ)
\dot{Q}	Heat transfer rate (W)
r	Superficial specific resistance (Ω/m^2)
r	Reaction rate (mol/s)

r	Radial coordinate (m)
R	Universal gas constant (kJ/mol K)
ROCV	Reversible open-cell voltage (V)
Re	Reynolds number
S	Molar entropy (kJ/mol K)
Sc	Schmidt number
Sh	Sherwood number
SP	Span
t	Time (s)
T	Temperature (K)
U	Overall heat transfer coefficient (W/m ² K)
v	Molar specific volume (m ³ /mol)
V	Voltage (V)
\mathcal{V}	Velocity (m/s)
W	Work (kJ)
W_b	Bed inventory (kg)
x	Transversal coordinate (m)
x	Conversion of solid particles
x_s	Molar steam fraction
X	Conversion factor
y	Mole fraction
Y	Mass fraction of solid

Greek Letters

α	Volumetric thermal expansion coefficient (1/K)
δ	Thickness (m)
ε	Bubble fraction in the bed
ε	Heat exchanger effectiveness
η	Efficiency
φ	Carnot abatement factor
Φ	Sphericity
μ	Dynamic viscosity (Pa s)
ψ	Exergy efficiency
θ	Dimensionless temperature
ρ	Density (kg/m ³)
ξ	Extent of reaction
σ	Electric conductivity (S/m)
τ	Reaction time (s)
ω	Acentric factor

Subscripts

0	Exchange current
a	Anode
act	Activation
b	Bulk phase
b	Backward
c	Critical
c	Cathode
c	Cold
conc	Concentration
d	Decomposition
d	Droplet
D	Debye
e	Electrolyte
e	Effective
eq	Equilibrium
E	Einstein
f	Fluidized
f	Forward
g	Vapor
gen	Generated
h	Hot
i	General index
l	Liquid
L	Limiting current density
lg	Latent
m	Melting
ohm	Ohmic
p	Particle
r	Reduced
r	Reaction
sat	Saturation
t	Tube
w	Water

Superscripts

0	Reference state
"	Per unit of surface
-	Average value (overbar)

References

- Abanades S, Charvin P, Flamant G, Neveu P (2006) Screening of water-splitting thermo-chemical cycles potentially attractive for hydrogen production by concentrated solar energy. *Energy* 31:2469–2486
- Al-Dabbagh AW, Lu L (2010a) Design and reliability assessment of control systems for a nuclear-based hydrogen production plant with copper–chlorine thermochemical cycle. *Int J Hydrogen Energy* 35:966–977
- Al-Dabbagh AW, Lu L (2010b) Dynamic flowgraph modeling of process and control systems of a nuclear-based hydrogen production plant. *Int J Hydrogen Energy* 35:9569–9580
- Avsec J, Naterer GF, Predin A (2009) Calculation of thermodynamic properties for hydrochloric and copper compounds in a hydrogen production process. *J Energy Technol* 2:47–64
- Balashov VN, Schatz RS, Chalkova E, Akinfiev NN, Fedkin MV, Lvov SN (2011) CuCl electrolysis for hydrogen production in Cu–Cl thermochemical cycle. *J Electrochem Soc* 158: B266–B275
- Carty RH, Mazumder MM, Schreiber JD, Pangborn JB (1981) Thermochemical production of hydrogen. Final report 30517, vol. 1–4. Institute of Gas Technology, Chicago, IL
- Cleary V, Bowen P, Witlox H (2007) Flashing liquid jets and two-phase droplet dispersion I. Experiments for derivation of droplet atomization correlations. *J Hazard Mater* 142:786–96
- Croizé L, Doizi D, Larousse B, Pailloux A, Reaux D, Gallou C, Dauvois V, Roujou JL, Zanella Y, Carles P (2010) Interest of absorption spectroscopy for the control of industrial processes. Application to H₂ massive production. *Appl Phys B* 100:409–415
- Daggupati V, Naterer GF, Gabriel K, Gravelsins R, Wang Z (2009) Equilibrium conversion in Cu–Cl cycle multiphase processes of hydrogen production. *Thermochem Acta* 496:117–123
- Daggupati V, Naterer GF, Gabriel K (2010a) Diffusion of gaseous products through a particle surface layer in a fluidized bed reactor. *Int J Heat Mass Transf* 53:2449–2458
- Daggupati VN, Naterer GF, Gabriel KS, Gravelsins RJ, Wang ZL (2010b) Solid particle decomposition and hydrolysis reaction kinetics in Cu–Cl thermochemical hydrogen production. *Int J Hydrogen Energy* 35:4877–4882
- Daggupati VN, Naterer GF, Dincer I (2011a) Convective heat transfer and solid conversion of reacting particles in a copper(II) chloride fluidized bed. *Chem Eng Sci* 66:460–468
- Daggupati VN, Pope K, Naterer GF, Gabriel KS, Wang ZL (2011b) Conversion of solid cupric chloride in a fluidized bed hydrolysis reactor. Proceedings of international conference of hydrogen production ICH2P-11, Thessaloniki, Greece, 19–22 June, paper #112
- Daggupati VN, Naterer GF, Gabriel KS, Gravelsins RJ, Wang ZL (2011c) Effects of atomization conditions and flow rates on spray drying for cupric chloride particle formation. *Int J Hydrogen Energy* 36:11353–11359
- Dokya M, Kotera Y (1976) Hybrid cycle with electrolysis using Cu–Cl system. *Int J Hydrogen Energy* 1:117–121
- Ferrandon MS, Lewis MA, Tatterson DF, Nankanic RV, Kumarc M, Wedgewood LE, Nitsche LC (2008) The hybrid Cu–Cl thermochemical cycle. I. Conceptual process design and H₂A cost analysis. II. Limiting the formation of CuCl during hydrolysis. In: NHA annual hydrogen conference, Sacramento convention center, CA, 30 March to 3 April
- Ferrandon MS, Lewis MA, Tatterson DF, Gross A, Doizi D, Croizé L, Dauvois V, Roujou JL, Zanella Y, Carles P (2010a) Hydrogen production by the Cu–Cl thermochemical cycle: Investigation of the key step of hydrolysing CuCl₂ to Cu₂OCl₂ and HCl using a spray reactor. *Int J Hydrogen Energy* 35:992–1000
- Ferrandon MS, Lewis MA, Alvarez F, Shafirovich E (2010b) Hydrolysis of CuCl₂ in the Cu–Cl thermochemical cycle for hydrogen production: experimental studies using a spray reactor with an ultrasonic atomizer. *Int J Hydrogen Energy* 35:1895–1904
- Ghandehariun S, Rosen MA, Naterer GF, Wang Z (2011) Comparison of molten salt heat recovery options in the Cu–Cl cycle of hydrogen production. *Int J Hydrogen Energy* 36:11328–11337

- Granovskii M, Dincer I, Rosen MA, Pioro I (2008) Performance assessment of a combined system to link a supercritical water-cooled nuclear reactor and a thermochemical water splitting cycle for hydrogen production. *Energy Conv Manage* 49:1873–1881
- Haseli Y, Dincer I, Naterer GF (2008) Hydrodynamic gas-solid model of cupric chloride particles reacting with superheated steam for thermochemical hydrogen production. *Chem Eng Sci* 63:4596–4604
- Haseli Y, Naterer GF, Dincer I (2009) Fluid-particle mass transport of cupric chloride hydrolysis in a fluidized bed. *Int J Heat Mass Transf* 52:2507–2515
- Haynes WM (2012) CRC handbook of chemistry and physics, 92 (Internet Version)th edn. CRC, Boca Raton, FL
- Ikeda BM, Kaye MH (2008) Thermodynamic properties in the Cu-Cl-O-H system. Seventh international conference on nuclear and radiochemistry, Budapest, Hungary, August
- Jaber O, Naterer GF, Dincer I (2010a) Convective heat transfer from solidified molten salt in a direct contact heat exchanger. *Heat Mass Transf* 46:999–1012
- Jaber O, Naterer GF, Dincer I (2010b) Heat recovery from molten CuCl in the Cu-Cl cycle of hydrogen production. *Int J Hydrogen Energy* 35:6140–6151
- Khan MA, Chen Y (2005) Preliminary process analysis and simulation of the copper-chlorine thermochemical cycle for hydrogen generation. Nuclear hydrogen production, third information exchange meeting, Oarai, Japan, 5–7 October. Nuclear Energy Agency 6122
- Lewis MA, Serban M, Basco J (2003) Hydrogen production at 550 °C using a low temperature thermochemical cycle. Proceedings of the OECD/NEA meeting, Argonne National Laboratory
- Lewis MA, Serban M, Basco JK (2004) A progress report on the chemistry of the low temperature Cu-Cl thermochemical cycle, *Trans Am Nucl Soc* 91:113–114
- Lewis MA, Petri MC, Masin JG. (2005a) A scoping flowsheet methodology for evaluating alternative thermochemical cycles. Nuclear hydrogen production, third information exchange meeting, Oarai, Japan, 5–7 October. Nuclear Energy Agency 6122
- Lewis MA, Masin JG, Vilim RB, Serban M (2005b) Development of the low temperature thermochemical cycle. International congress on advances in nuclear power plants, 15–19 May, Seoul, Korea
- Lewis MA, Masin JG (2009) The evaluation of alternative thermochemical cycles—Part II: the down-selection process. *Int J Hydrogen Energy* 34:4125–4135
- Lewis MA, Masin JG, O'Hare PA (2009a) Evaluation of alternative thermochemical cycles, Part I: the methodology. *Int J Hydrogen Energy* 34:4115–4124
- Lewis MA, Ferrandon MS, Tatterson DF, Mathias P (2009b) Evaluation of alternative thermochemical cycles—Part III further development of the Cu-Cl cycle. *Int J Hydrogen Energy* 34:4136–4145
- Marin GD, Wang Z, Naterer GF, Gabriel K (2010) Chemically reacting and particle-laden multiphase flow in a molten salt vessel. Tenth AIAA/ASME joint thermophysics and heat transfer conference, Chicago, Illinois, 28 June to 1 July, Paper #225388
- Marin GD, Wang Z, Naterer GF, Gabriel K (2011a) X-ray diffraction study of multiphase reverse reaction with molten CuCl and oxygen. *Thermochim Acta* 524:109–116
- Marin GD, Wang Z, Naterer GF, Gabriel K (2011b) Byproducts and reaction pathways for integration of the CuCl cycle of hydrogen production. *Int J Hydrogen Energy* 36:13414–13424
- McQuillan BW, Brown LC, Besenbruch GE, Tolman R, Cramer T, Russ BE, Vermillion BA, Earl B., Hsieh H-T, Chen Y, Kwan K, Diver R, Siegal N, Weimer A, Perkins C, Lewandowski A (2010) High efficiency generation of hydrogen fuels using solar thermal-chemical splitting of water. General Atomics Project 3022
- Miller AI (2005) An update on Canadian activities on hydrogen. Nuclear hydrogen production, 3rd Information Exchange Meeting, Oarai, Japan, 5–7 October. Nuclear Energy Agency 6122
- Naterer GF (2008) Second law viability of upgrading waste heat for thermochemical hydrogen production. *Int J Hydrogen Energy* 33:6037–6045

- Naterer GF, Gabriel K, Wang Z, Daggupati V, Gravelins R (2008a) Thermochemical hydrogen production with a copper-chlorine cycle, I: oxygen release from copper oxychloride decomposition. *Int J Hydrogen Energy* 33:5439–5450
- Naterer GF, Daggupati VN, Marin G, Gabriel KS, Wang ZL (2008b) Thermochemical hydrogen production with a copper-chlorine cycle, II: flashing and drying of aqueous cupric chloride. *Int J Hydrogen Energy* 33:5451–5459
- Naterer GF, Suppiah S, Lewis M, Gabriel K, Dincer I, Rosen MA, Fowler M, Rizvi G, Easton EB, Ikeda BM, Kaye MH, Lu L, Pioro I, Spekkens P, Tremaine P, Mostaghimi J, Avsec A, Jiang J (2009) Recent Canadian advances in nuclear-based hydrogen production and the thermochemical Cu-Cl cycle. *Int J Hydrogen Energy* 34:2901–2917
- Naterer GF, Suppiah S, Stolberg L, Lewis M, Wang Z, Daggupati V, Gabriel K, Dincer I, Rosen MA, Spekkens P, Lvov L, Fowler M, Tremaine P, Mostaghimi J, Easton EB, Trevani L, Rizvi G, Ikeda BM, Kaye MH, Lu L, Pioro I, Smith WR, Secnik E, Jiang J, Avsec J (2010) Canada's program on nuclear hydrogen production and the thermochemical Cu-Cl cycle. *Int J Hydrogen Energy* 35:10905–10926
- Naterer GF, Suppiah S, Stolberg L, Lewis M, Ferrandon M, Wang Z, Dincer I, Gabriel K, Rosen MA, Secnik E, Easton EB, Trevani L, Pioro I, Tremaine P, Lvov S, Jiang J, Rizvi G, Ikeda BM, Luf L, Kaye M, Smith WR, Mostaghimi J, Spekkens P, Fowler M, Avsec J (2011a) Clean hydrogen production with the Cu-Cl cycle—progress of international consortium, I: experimental unit operations. *Int J Hydrogen Energy* 36:15472–15485
- Naterer GF, Suppiah S, Stolberg L, Lewis M, Ferrandon M, Wang Z, Dincer I, Gabriel K, Rosen MA, Secnik E, Easton EB, Trevani L, Pioro I, Tremaine P, Lvov S, Jiang J, Rizvi G, Ikeda BM, Luf L, Kaye M, Smith WR, Mostaghimi J, Spekkens P, Fowler M, Avsec J (2011b) Clean hydrogen production with the Cu-Cl cycle—progress of international consortium, II: simulations, thermochemical data and materials. *Int J Hydrogen Energy* 36:15486–15501
- NIST (2012) Chemistry webbook. National Institute of Standards and Technology. Available from: <http://webbook.nist.gov/chemistry/>
- Nixon A, Ferrandon M, Kaye MH, Trevani L (2011) Thermochemical hydrogen production Synthesis, characterization, and decomposition of copper oxychloride. *J Thermal Anal Calor*. doi:10.1007/s10973-011-1998-3
- Odukoya A, Naterer GF (2011) Electrochemical mass transfer irreversibility of cuprous chloride electrolysis for hydrogen production. *Int J Hydrogen Energy* 36:11345–11352
- Orhan MF (2011) Conceptual design, analysis and optimization of nuclear-based hydrogen production via copper-chloride thermochemical cycles. PhD thesis, University of Ontario Institute of Technology
- Orhan MF, Dincer I, Rosen MA (2008a) Thermodynamic analysis of the copper production step in a copper-chlorine cycle for hydrogen production. *Thermochim Acta* 480:22–29
- Orhan MF, Dincer I, Rosen MA (2008b) Energy and exergy assessments of the hydrogen production step of a copper-chlorine thermochemical water splitting cycle driven by nuclear-based heat. *Int J Hydrogen Energy* 33:6456–6466
- Orhan MF, Dincer I, Naterer GF (2008c) Cost analysis of a thermochemical Cu–Cl pilot plant for nuclear-based hydrogen production. *Int J Hydrogen Energy* 33:6006–6020
- Orhan MF, Dincer I, Rosen MA (2009) Energy and exergy analyses of the fluidized bed of a copper-chlorine cycle for nuclear-based hydrogen production via thermochemical water decomposition. *Chem Eng Res Des* 87:684–694
- Orhan MF, Dincer I, Rosen MA (2010a) An exergy-cost-energy-mass analysis of a hybrid copper-chlorine thermochemical cycle for hydrogen production. *Int J Hydrogen Energy* 35:4831–4838
- Orhan MF, Dincer I, Rosen MA (2010b) Exergoeconomic analysis of a thermochemical copper-chlorine cycle for hydrogen production using specific exergy cost (SPECOC) method. *Thermochim Acta* 497:60–66
- Orhan MF, Dincer I, Rosen MA (2011) Exergy analysis of heat exchangers in the copper-chlorine thermochemical cycle to enhance thermal effectiveness and cycle efficiency. *Int J Low-Carbon Technol* 6:156–164

- Ozbilen A (2011) Life cycle assessment of nuclear-based hydrogen production via thermochemical water splitting using a copper-chlorine (Cu-Cl) cycle. MSc thesis, University of Ontario Institute of Technology
- Ozbilen A, Dincer I, Rosen MA (2011a) Environmental evaluation of hydrogen production via thermochemical water splitting using the Cu-Cl Cycle: a parametric study. *Int J Hydrogen Energy* 36:9514–9528
- Ozbilen A, Dincer I, Rosen MA (2011b) A comparative life cycle analysis of hydrogen production via thermochemical water splitting using a Cu-Cl cycle. *Int J Hydrogen Energy* 36:11321–11327
- Parry T (2008) Thermodynamics and magnetism of copper oxychloride. MSc thesis, Brigham Young University, Provo, UT, USA
- Perret R, Chen Y, Besenbruch G, Diver R, Weimer A, Lewandowski A, Miller E (200). High temperature thermochemical solar hydrogen generation research. UNLV Research Foundation. Report to Department of Energy DE-FG36-03GO13062
- Pope K, Naterer GF, Wang Z (2011) Pressure drop of packed bed vertical flow for multiphase hydrogen production. *Int J Hydrogen Energy* 36:11338–11344
- Ranganathan S, Easton EB (2010a) High performance ceramic carbon electrode-based anodes for use in the Cu-Cl thermochemical cycle for hydrogen production. *Int J Hydrogen Energy* 35:1001–1007
- Ranganathan S, Easton EB (2010b) Ceramic carbon electrode-based anodes for use in the Cu-Cl thermochemical cycle. *Int J Hydrogen Energy* 35:4871–4876
- Rosen MA, Naterer GF, Chukwu CC, Sadhankar R, Suppiah S (2010) Nuclear-based hydrogen production with a thermochemical copper-chlorine cycle and supercritical water reactor: equipment scale-up and process simulation. *Int J Energy Res*. doi:[10.1002/er.1702](https://doi.org/10.1002/er.1702)
- Serban M, Lewis MA, Basco JK (2004) Kinetic study of the hydrogen and oxygen production reactions in the copper-chloride thermochemical cycle. AIChE SPRING NATIONAL MEETING, New Orleans LA, 25–29 April
- Sim K-S, Son Y-M, Kim J-W (1993) Some thermochemical cycles composed of copper compounds with three-step reactions. *Int J Hydrogen Energy* 18:287–290
- Stolberg L, Boniface HA, McMahon S, Suppiah S, York S (2008) Electrolysis of the CuCl/HCl aqueous system for the production of nuclear hydrogen. Proceedings of the fourth international topical meeting on high temperature reactor technology HTR-2008. 28 September to 1 October, Washington, DC
- Suppiah S, Li J, Sadhankar R, Kutchcoskie KJ, Lewis M (2005) Study of the hybrid Cu-Cl cycle for nuclear hydrogen production. Nuclear hydrogen production, third information exchange meeting, Oarai, Japan, 5–7 October. Nuclear Energy Agency 6122
- Suppiah S, Stolberg L, Boniface H, Tan G, McMahon S, York S, Zhang W (2009) Canadian nuclear hydrogen R&D programme: Development of the medium-temperature Cu-Cl cycle and contributions to the high-temperature sulphur-iodine cycle. Forth international exchange meeting on nuclear hydrogen production, Oakbrook IL, USA, 13–16 April. Nuclear Energy Agency and Organization for Economic Co-operation and Development, NEA 6805
- Trevani L, Ehlerova J, Sedlbauer J, Tremaine PR (2010) Complexation in the Cu(II)–LiCl–H₂O system at temperatures to 423 K by UV-visible spectroscopy. *Int J Hydrogen Energy* 35:4893–4900
- Trevani L (2011) The copper-chloride cycle: synthesis and characterization of copper oxychloride. Hydrogen and fuel cells international conference and exhibition, Vancouver, BC, 15–18 May
- Vilim RB (2004) Commodity inventories and equipment sizes for a low temperature nuclear-chemical plant for production of hydrogen. AIChE spring national meeting, conference proceedings. pp 2706–2712
- Wang Z, Naterer GF, Gabriel K (2008) Multiphase reactor scale-up for Cu–Cl thermochemical hydrogen production. *Int J Hydrogen Energy* 33:6934–6946
- Wang ZL, Naterer GF, Gabriel K, Gravelins R, Daggupati V (2009) Comparison of different copper-chlorine thermochemical cycles for hydrogen production. *Int J Hydrogen Energy* 34:3267–3276
- Wentorf RH, Hanneman RE (1974) Thermochemical hydrogen generation. *Science* 185:311–319

- Williams LO (1980) Hydrogen power. An introduction to hydrogen energy and its applications. Pergamon, New York
- Zamfirescu C, Dincer I, Naterer GF (2009) Performance evaluation of organic and titanium based working fluids for high-temperature heat pumps. *Thermochim Acta* 496:18–25
- Zamfirescu C, Dincer I, Naterer GF (2010a) Thermophysical properties of copper compounds in copper-chlorine thermochemical water splitting cycles. *Int J Hydrogen Energy* 35:4839–4852
- Zamfirescu C, Naterer GF, Dincer I (2010b) Kinetics study of the copper/hydrochloric acid reaction for thermochemical hydrogen production. *Int J Hydrogen Energy* 35:4853–4860
- Zamfirescu C, Naterer GF, Dincer I (2010c) Upgrading of waste heat for combined power and hydrogen production with nuclear reactors. *J Eng Gas Turbines Power* 132:102911
- Zamfirescu C, Naterer GF, Dincer I (2011) Vapor compression CuCl heat pump integrated with a thermochemical water splitting cycle. *Thermochim Acta* 512:40–48
- Zamfirescu C, Naterer GF, Dincer I (2012) Photochemical disproportionation of cuprous chloride for electrolytic hydrogen generation. *Int J Hydrogen Energy*. doi:[10.1016/j.ijhydene.2012.01.183](https://doi.org/10.1016/j.ijhydene.2012.01.183)